NEUP Project

Novel Dissimilar Joints Between Alloy 800H and 2.25%Cr and 1%Mo Steel

Project 14-6803 WP: NU-14-PA-PSU-0601-04

Final Report

The Pennsylvania State University

Abstract

Dissimilar metal joints between ferritic steels and nickel base alloys are currently fabricated using conventional arc welding processes with selected filler metal combinations. The dissimilar metal joints contain abrupt changes in composition over a relatively small distance. Many years of service at elevated temperatures has shown that these welds are susceptible to creep and creep fatigue failures. The primary mechanism for these creep failures involves carbon diffusion from the ferritic steel to the nickel base alloy. As a result, a carbon depleted zone is created that contains very few stable carbides. This work used additive manufacturing (AM) technologies as a highly controllable means for reducing carbon migration through theoretically-designed, compositionally graded transition joints guided by appropriate thermodynamic, kinetic and heat transfer and fluid flow modeling. The contents of the report include the objectives and tasks set forth by the PI and collaborators, major technical accomplishments throughout the research and additional details in the form of technical publications resulting from the NEUP grant and reports from the collaborating university and national laboratory.

Objectives and Tasks

Through a collaborative effort from Penn State University, Ohio State University and Oak Ridge National Laboratory researchers, an integrated experimental and theoretical program was undertaken to alleviate carbon migration in dissimilar metal joints between 2.25Cr-1Mo ferritic steels and Alloy 800H nickel base alloys. The program was focused on a novel approach of using AM to develop, fabricate and test highly engineered dissimilar metal transition joints. Penn State was responsible for the overall management of the program, the thermodynamic and heat transfer and fluid flow modeling and the fabrication of test samples. Ohio State provided additional analysis and characterization for the scale up of the sub-size specimens. ORNL was responsible for the creep and creep fatigue testing and coordinating the development of the methodology and data collection supporting code qualification. Specific technical objectives include the following:

1. Minimize carbon diffusion by reduction of carbon potential gradient at typical service temperatures in graded transitional joints and design carbon diffusion barriers by thermodynamic and kinetic modeling.
2. Fabricate transitional joints with additive manufacturing guided by numerical modeling of heat transfer and fluid flow and the carbon potential/diffusion barrier modeling.
3. Examine mechanical properties and creep testing results of the fabricated part with a combination of established and unique methodologies.
4. Perform a series of scaling experiments and modeling to investigate the validity of the graded joints at length scales typical of in-service components.
5. Generate, evaluate and document data that will be helpful for the initiation of the ASME code case for the eventual code qualification of the AM fabricated dissimilar metal joints.

A logical path to accomplishing the objectives of the proposal and the interdependence of the tasks is shown in Figure 1.

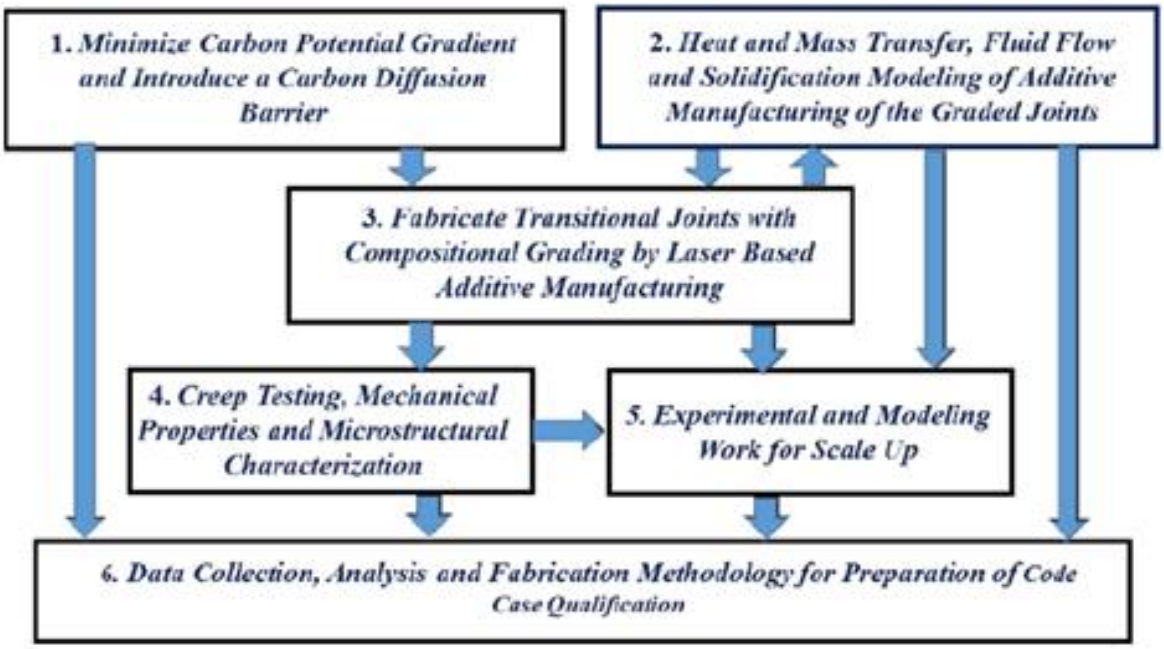

Figure 1. Interdependence of the proposed tasks

Descriptions of the individual tasks are as follows:

Task 1. Minimize Carbon Potential Gradient and Introduce a Carbon Diffusion Barrier

A thermodynamic model will be used to minimize the spatial gradient of chemical potential that drives diffusion of carbon from low Cr to high Cr regions. The model will provide a correlation between the carbon chemical potential and the alloy chemical composition across a graded transitional weld joint between 2.5Cr-1Mo ferritic steels and an 800-H nickel base alloys. The compositional profile in the transition joint will be tailored based on the results of the carbon activity and chemical composition maps developed here. By reducing chemical potential gradient of carbon the driving force for carbon diffusion will be reduced. In addition, thermodynamic and kinetic modeling at typical service temperatures will be undertaken to design a diffusion barrier within the transitional weld joint.

Task 2. Heat and Mass Transfer, Fluid Flow and Solidification Modeling of Additive Manufacturing of the Graded Joints

The geometry of the fusion zone, thermal cycles, solidification parameters and the kinetics of various phase transformations are affected by the process variables which include laser power, power density, fabrication speed, and powder characteristics. The roles of these variables in affecting the melt geometry, heating and cooling rates, temperature gradients and the solidification

parameters will be studied by modeling. The thermo-fluid component of the model will be validated with experimental melt pool shape and size and measured thermal cycles, and used to construct process maps showing the effect of variables on the output variables.

Task 3. Fabricate Transitional Joints with Compositional Grading by Laser Based Additive Manufacturing

Thermodynamic and kinetic modeling results will be used to produce components with continuously varying nonlinear composition profiles obtained by melting continuously changing mixtures of at least two alloys powders by the laser assisted AM process. Designs for a range of sub-scale joints (about 1 to 2 cm in length) will be based on the results of Tasks 1 and 2 and result in a series of test samples that will be characterized using optical and electron microscopic evaluation of microstructure, evaluation of compositional profiles, microhardness profiles, and determination of creep properties from different regions of the joint.

Task 4. Creep Testing and Characterization

Due to varying composition, microstructure and mechanical properties of the fabricated part, it cannot be adequately tested by traditional creep testing. A new creep testing procedure for non-homogeneous alloys that involves high-temperature digital image correlation to measure localized non-uniform deformation under high temperature creep testing conditions, will be utilized for the proposed research. In addition, conventional creep testing data which is an important input data for the initiation of the eventual code compliance will be undertaken.

Task 5. Scale Up

The original sub-size samples of the order of 1 to 2 cm length produced in Task 3 will go through a design and testing phase and scaled up to a sample full-size component of the order of 5 cm or longer. By scaling up to a full size component, the impact of different spatial and temporal scales in the fabrication process can be quantified. Since large components with graded composition often experience residual stress and distortion during fabrication, these will be investigated through modeling. These results will also be an input into the follow on Task 6 on the initiation of the ASME code qualification of the process.

Task 6. Initiation of Code Qualification Activities

Documentation of the successful methodology to fabricate sound transition joint both in laboratory scale and full size component, the mechanical property data and the creep testing results generated

in the proposed research will be helpful for the initiation of the ASME code case for the AM fabricated dissimilar metal joints.

Technical Accomplishments

Task 1. Minimize carbon potential gradient and introduce a carbon diffusion barrier

Thermodynamic calculations were performed to model the carbon potential gradient in compositionally graded transitions between 2.25Cr-1Mo steel and Alloy 800H. While a linear composition gradient can significantly reduce the driving force for carbon diffusion compared to a dissimilar weld, the optimal solution requires a nonlinear composition profile. Lowering the chromium concentration across the joint provides a composition profile that can minimize the driving force for diffusion.

Coupled thermodynamic and kinetic calculations were undertaken to simulate carbon migration over years of service. The numerical modeling demonstrated that carbon diffusion can be drastically reduced by introducing a composition gradient compared to a dissimilar weld. The effects of different compositional profiles on carbon diffusion were studied.

More information on chemical potential calculations and carbon diffusion modeling can be found in Appendices A and B.

Task 2. Heat and mass transfer, fluid flow and solidification modeling of additive manufacturing of the graded joints

Important thermo-physical properties such as surface tension, viscosity, density and thermal conductivity are crucial input variables for heat transfer and fluid flow simulations. However, the necessary experimental data are often not available for compositionally graded alloys. Significant efforts were undertaken to model the thermo-physical properties to create an extensive database. Nonlinear changes in properties that did not exhibit a rule-of-mixtures relationship were uncovered.

An existing model was adapted for the heat transfer, fluid flow and solidification modeling of compositionally graded transition joints between 2.25Cr-1Mo steel and Alloy 800H using AM. The model solves the conservation equations of mass, momentum and energy to calculate thermal cycles, molten pool velocity distributions, temperature gradients, solidification rates and cooling rates. The calculation of these important variables are essential for determining the metallurgical quality for structurally sound and defect free parts.

Further development of the model led to the calculation of the curved surface characteristic of AM deposits. Such calculations allow for more accurate determination of the spatially dependent thermal cycles during fabrication. Additionally, the thermal histories calculated by the model were coupled with a mechanical model for the prediction of residual stresses and distortion.

Details, methodologies and applications of the heat transfer and fluid flow modeling can be found in Appendices C, D, E, F, G and H.

Task 3. Fabricate transitional joints with compositional grading by laser based additive manufacturing

Experiments were undertaken to fabricate compositionally graded test specimens using custom-blended powder mixtures. Laser based directed energy deposition AM was used for fabrication as this process allows for compositional grading compared to other techniques. A custom multiple nozzle, high energy high deposition (HEHD) machine at Penn State University was used for building the samples. The advantage of this machine is its ability to deposit material quickly by using relatively high laser powers and fast travel speeds. The HEHD machine is also capable of operating in a protective argon environment, which is essential to prevent oxidation.

Experimental details can be found in Appendices B and I.

Task 4. Creep testing and characterization

Extensive characterization of compositionally graded specimens was performed to examine chemical composition, microstructure and mechanical properties. Both optical and electron microscopy coupled with microhardness measurements revealed microstructural variations throughout the composition gradients.

The theoretical hypothesis of using compositional grading to reduce carbon diffusion was investigated experimentally through accelerated heat treatments. Carbon diffusion profiles were measured for both a dissimilar weld and compositionally graded alloy subjected to identical heat treatments. Significant diffusion was observed in the dissimilar weld while only small changes in the carbon concentration profile of the compositionally graded alloy were measured. For the first time, it was proved experimentally that carbon diffusion was hindered in the presence of a composition gradient compared to a dissimilar weld.

The evaluation of creep data for compositionally graded transition joints require baseline creep data for comparison. A dissimilar joint between 2.25Cr-1Mo steel and Alloy 800H was welded using IN82 filler metal by collaborators at Ohio State University. Conventional creep testing was performed in the as-welded and post weld heat treatment condition. The time-to-rupture data showed good agreement with previously reported data in the literature.

For non-homogeneous materials, it is often useful to test mechanical properties using techniques that can obtain localized strain rates. Experimental testing of creep properties was undertaken at Oak Ridge National Laboratory using a GleebleTM thermal mechanical simulator and high temperature digital image correlation.

More details on the characterization can be found in Appendix B. A summary of the creep testing performed by the collaborating university and national laboratory is given in Appendix J.

Task 5. Scale up

Multiple test specimens were deposited using laser based AM on many different length scales. Single pass, single layer deposits were used to study the effects of compositional changes on molten pool geometry. Sub-scale test samples on the order of 3-5 cm were fabricated to study carbon diffusion through changes in chemical composition. Large, 150 mm tall walls were fabricated to meet specimen geometry for creep testing at Oak Ridge National Laboratory. Additional details can be found in Appendices B and I.

Publications

The following is a list of publications resulting from the NEUP grant that acknowledge the support from the U.S. Department of Energy:

J.S. Zuback, T.A. Palmer, T. DebRoy, "Additive manufacturing of functionally graded transition joints between ferritic and austenitic alloys", in preparation.

T. Mukherjee, J.S. Zuback, W. Zhang, T. DebRoy, Residual stresses and distortion in additively manufactured compositionally graded and dissimilar joints, *Computational Materials Science,* 143 (2018) 325-337.

T. DebRoy, H.L. Wei, J.S. Zuback, T Mukherjee, J.W. Elmer, J.O. Milewski, A.M. Beese, A. Wilson-Heid, A. De, W. Zhang, Additive manufacturing of metallic components – process, structure and properties, *Progress in Materials Science,* 92 (2018) 112-224.

G.L. Knapp, T. Mukherjee, J.S. Zuback, H.L. Wei, T.A. Palmer, A. De, T. DebRoy, Building blocks for a digital twin of additive manufacturing, *Acta Materialia,* 135 (2017) 390-399.

H.L. Wei, J.W. Elmer, T. DebRoy, Crystal growth during keyhole mode laser welding, *Acta Materialia,* 133 (2017) 10-20.

T. Mukherjee, V. Manvatkar, A. De, T. DebRoy, Dimensionless numbers in additive manufacturing, *Journal of Applied Physics,* 121 (2017) 064904.

T. DebRoy, W. Zhang, J. Turner, S.S. Babu, Building digital twins of 3D printing machines, *Scripta Materialia,* 135 (2017) 119-124.

H.L. Wei, J.W. Elmer, T. DebRoy, Three-dimensional modeling of grain structure evolution during welding of an aluminum alloy, *Acta Materialia,* 126 (2017) 413-425.

T. Mukherjee, W. Zhang, T. DebRoy, An improved prediction of residual stresses and distortion in additive manufacturing, *Computational Materials Science*, 126 (2017) 360-372.

T. Mukhejee, V. Manvatkar, A. De, T. DebRoy, Mitigation of thermal distortion during additive manufacturing, *Scripta Materialia*, 127 (2017) 79-83.

H.L. Wei, T. Mukherjee, T. DebRoy, Grain growth modeling for additive manufacturing of nickel based superalloys, *Proceedings of the 6th Internationl Conference on Recrystallization and Grain Growth*, (2016) 265-269.

H.L. Wei, J.W. Elmer, T. DebRoy, Origin of grain orientation during solidification of an aluminum alloy, *Acta Materialia*, 115 (2016) 123-131.

T. Mukherjee, J.S. Zuback, A. De, T. DebRoy, Printability of alloys for additive manufacturing, *Scientific Reports*, 6 (2016) 19717.

T. Mukherjee, J.S. Zuback, A. De, T. DebRoy, Heat and fluid flow modeling to examine 3D printability of alloys, *7th International Symposium on High-Temperature Metallurgical Processing*, (2016) 469-478.

H.L. Wei, J. Mazumder, T. DebRoy, Evolution of solidification texture during additive manufacturing, *Scientific Reports*, 5 (2015) 16446.

Presentations

T. Mukherjee, V. Manvatkar, A. De, T. DebRoy, A numerical approach to fabricate defect free and structurally sound components by additive manufacturing, AWS Professional Program at FABTECH, November 8, 2017, Chicago, IL.

G.L. Knapp, T. Mukherjee, J.S. Zuback, H.L. Wei, T.A. Palmer, A. De, T. DebRoy, Building a digital twin of additive manufacturing, AWS Professional Program at FABTECH, November 8, 2017, Chicago, IL.

J.S. Zuback, T.A. Palmer, T. DebRoy, Compositionally graded transition joints between 2.25Cr-1Mo steel and Alloy 800H using additive manufacturing, AWS Professional Program at FABTECH, November 6, 2017, Chicago, IL.

H.L. Wei, T. Mukherjee, T. DebRoy, Building blocks for a digital twin of additive manufacturing – a path to understand the most important metallurgical variables, ASM Annual Symposium, Additive Materials Technology, June 6-7, 2017, Niskayuna, NY.

J.S. Zuback, T. Mukherjee, G.L. Knapp, H.L. Wei, T.A. Palmer, T. DebRoy, Novel dissimilar joints between 2.25Cr-1Mo steel and Alloy 800H, DOE Advanced Materials Program Review, June 6-7, 2017, Germantown, MD.

T. Mukherjee, W. Zhang, T. DebRoy, A quantitative approach to fabricate distortion free additively manufactured parts, AWS Professional Program at FABTECH, November 18, 2016, Las Vegas, NV.

J.S. Zuback, T. Mukherjee, T.A. Palmer, T. DebRoy, Novel dissimilar joints between 2.25Cr-1Mo steel and Alloy 800H, AWS Professional Program at FABTECH, November 18, 2016, Las Vegas, NV.

H.L. Wei, T. Mukherjee, T. DebRoy, Grain growth modeling for additive manufacturing of nickel based super alloys, Proceedings of the 6th International Conference on Recrystallization an Grain Growth, July 18, 2016, Pittsburgh, PA.

J.S. Zuback, T. Mukherjee, H.L. Wei, T.A. Palmer, T. DebRoy, Novel dissimilar joints between 2.25Cr-1Mo steel and Alloy 800H, DOE Advanced Materials Program Review, June 7-8, 2016, Germantown, MD.

T. DebRoy, Heat and fluid flow modeling to examine 3D printability of alloys, 7th International Symposium on High Temperature and Metallurgical Processing, February 14-18, 2015, Nashville, TN.

Appendix A:

Minimizing the driving force for carbon diffusion

Genetic Algorithm Optimization Procedure

In nuclear power plants, dissimilar metal welds between 2.25Cr-1Mo steel and Alloy 800H are prone to failure due to carbon migration. After years of service at elevated temperatures, carbon diffuses from 2.25Cr-1Mo steel towards Alloy 800H. Although these alloys initially have similar carbon concentrations, the carbon chemical potentials differ significantly, creating a driving force for diffusion. Due to the differences in carbon potentials and the very small width of the weld, the carbon potential gradient is large.

A way to minimize carbon diffusion is by fabricating a transition joint in which the composition can be varied. However, tailoring the composition of a transition joint which minimizes the carbon potential gradient requires thermodynamic modeling. It is known that the amount of chromium significantly affects the carbon chemical potential. Therefore, it is assumed for simplicity that all compositions will vary linearly, except for chromium. In this methodology, the chromium concentration which minimizes the carbon potential gradient at different locations across the transition joint is determined. To simplify the explanation four equally spaced locations across the transition are chosen. The total number of positions will be equal to the number of layers deposited during the AM process. The compositions of the two alloys are given below in Table 1.

Alloy	**Fe**	**Cr**	**Mo**	**Mn**	**Ni**	**Si**	**C**	**Cu**	**Ti**	**Al**
Steel	Bal.	2.25	1	0.5	0.045	0.5	0.1	-	-	-
800H	39.5	21	-	1.5	34.95	1	0.1	0.75	0.6	0.6

Table 1. Alloy compositions

For this problem, the transition joint is assumed to be in service at a temperature of 500°C, which is included in the typical service range. Using the thermodynamic database JMatPro® V8 the carbon chemical potential for any alloy concentration can be calculated. To start, the compositions of the two end member alloys are entered and carbon chemical potential is calculated. Using these two values, a linear equation in the form of $y=mx+b$ is calculated where y is chemical potential, m is the slope, x is the position and b is the chemical potential at the 0 position. A linear interpolation is chosen since the minimum thermodynamic driving force for carbon diffusion occurs when carbon chemical potential as a function of position is linear. Using the linear equation, the optimal value at each location can be obtained.

The linear change in composition for all elements excluding chromium is shown in Table 2 below for each of the four positions. The question marks in the Cr column are the concentrations that need to be determined in the problem.

Position	Fe	Cr	Mo	Mn	Ni	Si	C	Cu	Ti	Al
1	Bal	???	0.8	0.7	7.03	0.6	0.1	0.15	0.12	0.12
2	Bal	???	0.6	0.9	14.01	0.7	0.1	0.3	0.24	0.24
3	61.94	???	0.3	1.2	Bal	0.8	0.1	0.45	0.36	0.36
4	50.72	???	0.2	1.3	Bal	0.9	0.1	0.6	0.48	0.48

Table 2. Alloy compositions at 4 selected locations

Using JMatPro®, the carbon chemical potential can be calculated as a function of the concentration of any alloying element. Each of the compositions in Table 2 above is entered and the chemical potential of carbon as a function of chromium concentration is calculated for each composition. Using a 4^{th} order polynomial fit, the data in an equation of the form is expressed as,

$$y = ax^4 + bx^3 + cx^2 + dx + e \qquad (1)$$

In summary, there are 4 different equations corresponding to the 4 locations along the transition joint which relate carbon chemical potential to chromium concentration.

At this point, there is now an optimized linear relation between carbon chemical potential and position and 4 polynomial equations relating carbon chemical potential to chromium concentration. Next, a genetic search algorithm is applied to the 4 polynomial equations. The genetic algorithm will create a random population of chromium concentrations and test each value to finally determine the chromium concentration at the 4 positions along the joint which minimize the carbon potential gradient.

Code:

In the input file, the user defines the number of variables, population members and number of generations in the first line. Next, the user defines a weighting factor and crossover ratio. Last, the user specifies the range of values for each variable for the genetic algorithm to operate in. This is useful to decrease the amount of computing time. An example of input file is shown below.

```
4,50,800        !# of variables, population members, generations
0.8, 0.5        !weighting factor, crossover ratio
```

0 21.0 !lower and upper bounds of the first variable

0 21.0 !lower and upper bounds of the second variable

0 21.0 !lower and upper bounds of the third variable

0 21.0 !lower and upper bounds of the fourth variable

The source code is the file that performs the genetic algorithm. The file creates an initial random population based on user inputs. Then, it tests the fitness of each individual in the population. Each of the variables corresponds to a chromium concentration at the selected positions along the transition joint. For example, the first variable is the chromium concentration at position 1, the second variable is the chromium concentration at position 2 and so on. The parameter 'value' is the objective function. Each objective function contains the polynomial equation for the 4 different locations along the joint, as described above. The lines take the form

$$value = \left(1 + \frac{ax^4 + bx^3 + cx^2 + dx + e}{const}\right)^2 \qquad (2)$$

The polynomials in each function correspond to the variables. The term '*const'* in each line is the absolute value of the optimized carbon chemical potential found using the linear relation described in the previous section. The polynomial will give a negative value, since we are simulating in a range of chromium concentrations that can only give negative values. To minimize the objective function, the polynomial should be equal to *const*. If this is the case, then (polynomial/*const*) will equal -1, which gives a value of 0. Ideally, the objective function will equal 0 at the end of the simulation. However, an acceptable fitness value is usually set at which point the simulation will end. The results from the simulation are written in output file. In this file, a table is created showing the initial population and also the values for each of the variables with their corresponding fitness value.

The optimized carbon chemical potential gradient as described above is shown in Figure 1 as a function of arbitrary units. It is observed that a linear variation in all alloying elements from high potential 2.25Cr-1Mo steel to the low potential Alloy 800H significantly deviates from the optimal solution. In other words, a linear composition change is not the optimal solution for limiting carbon migration from the ferritic steel.

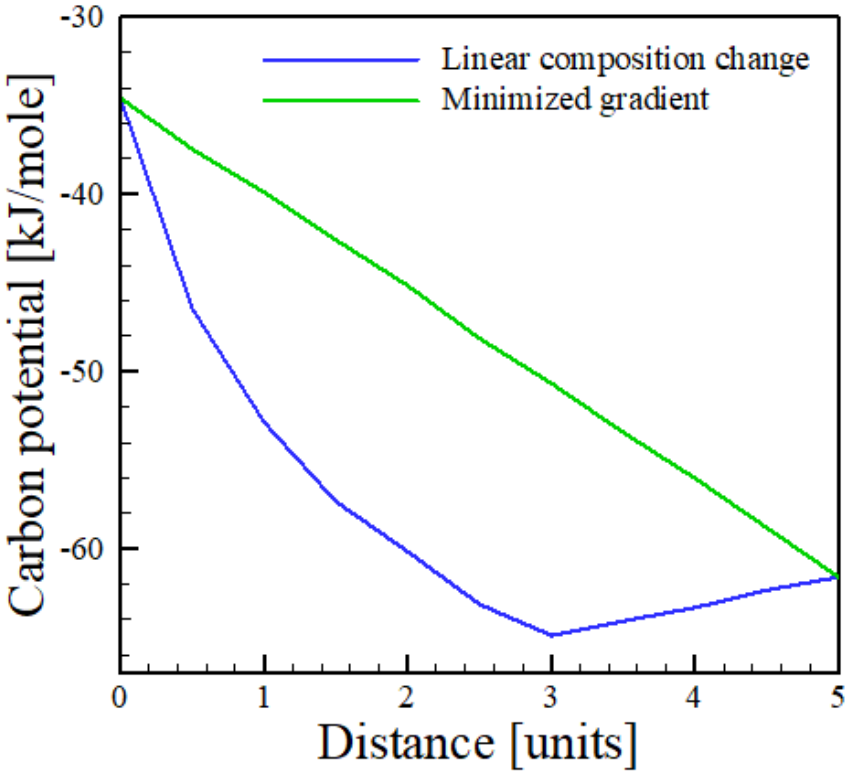

Figure 1. Carbon potential as a function of distance at 500°C for a linear composition change (blue) and a composition change modeled to minimize carbon potential gradient (green) from 2.25Cr-1Mo steel (position=0) to Alloy 800H (position=5)

By controlling the concentration of chromium at various locations while all other elements vary linearly, the optimal solution can be obtained. The results for the genetic search algorithm are shown in Figure 2. Compared to the case where chromium is varied linearly, chromium needs to be significantly lowered in order to minimize the driving force for carbon diffusion at all locations across the graded alloy.

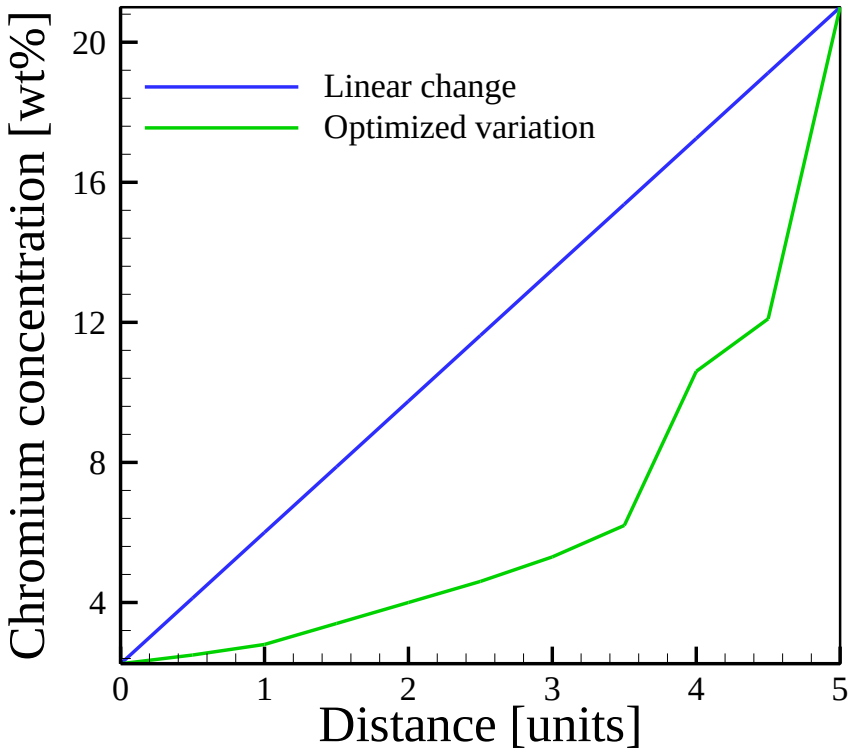

Figure 2. Chromium concentration as a function of distance at 500°C for a linear composition change (blue) and a composition change modeled to minimize carbon potential gradient (green) from 2.25Cr-1Mo steel (position=0) to Alloy 800H (position=5)

In the above calculations, the distance was chosen as arbitrary because the optimal solution is a linear change in the carbon chemical potential with respect to distance regardless of the length. To investigate the dependence on the transition joint length on the minimization of the carbon chemical potential gradient, it assumed that the composition has been chosen such that a linear change in chemical potential results. Then, the carbon potential gradient is calculated as a function of the length of the transition joint. The results show that a joint as small as five centimeters in length is adequate in further reducing the carbon chemical potential gradient, shown in Figure 3.

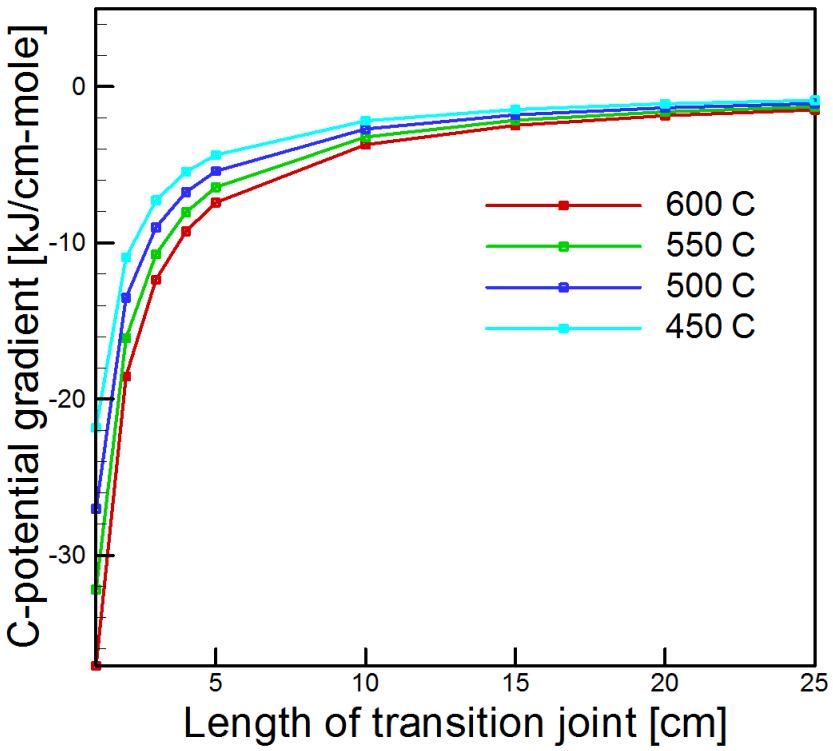

Figure 3. Carbon potential gradient as a function of length of transition joint at four different temperatures within the typical service range.

Appendix B:

Additive manufacturing of functionally graded transition joints between ferritic and austenitic alloys

Additive manufacturing of functionally graded transition joints between ferritic and austenitic alloys

J.S. Zuback[1], T.A. Palmer[1,2] and T. DebRoy[1,*]

[1]Department of Materials Science and Engineering
The Pennsylvania State University, University Park, PA 16802
[2]Department of Engineering Science and Mechanics
The Pennsylvania State University, University Park, PA 16802
(*Corresponding author, email: debroy@psu.edu)

Abstract

Dissimilar metal joints between ferritic and austenitic materials are susceptible to poor creep performance and premature failure due to carbon diffusion driven by abrupt changes in composition and microstructure. Compositional grading using additive manufacturing offers a means for producing functionally graded materials specifically designed to limit carbon diffusion. Using thermodynamic and kinetic calculations, carbon migration can be drastically decreased by controlling the carbon chemical potential through compositional grading between a ferritic steel and austenitic alloy. An appropriately designed graded transition would take 50 years to deplete the same amount of carbon as a dissimilar weld after just 2 years. When the desired joint design was fabricated using laser-based directed energy deposition additive manufacturing, a gradual change in chemical composition between a 2.25Cr-1Mo steel and Alloy 800H was achieved. However, a transition from a bainitic to a martensitic to an austenitic microstructure was observed, highlighting the importance of considering transformation kinetics in the design of ferritic-to-austenitic functionally graded materials. Additionally, there is no benefit to continue compositional grading once the microstructure becomes fully austenitic, at which point changes in chemical composition negligibly affect the driving force for carbon diffusion. For the first time, it was experimentally shown through accelerated heat treatment that a functionally graded material can successfully limit carbon diffusion compared to a dissimilar weld.

1. Introduction

Dissimilar metal joints between ferritic and austenitic materials are commonly found in sector transitions of nuclear energy generation facilities [1-4]. Ferritic low-alloy steels are often used in pressure vessels due to their good strength and corrosion resistance at elevated service temperatures. Austenitic stainless steels and Fe-Ni-Cr alloys offer excellent high temperature strength, resistance to oxidation, and creep rupture properties. Fusion welding between these dissimilar materials is typically performed with a nickel-based filler metal to alleviate the coefficient of thermal expansion. As a consequence, abrupt changes in chemical composition, microstructure, and mechanical properties are observed [2, 4-6], leading to a degradation in the performance of the joint during long-term high temperature service [1].

The overall mechanical performance of ferritic/austenitic dissimilar metal welds (DMWs) is highly dependent on carbide formation. Specifically, resistance to creep in these joints is obtained through the formation of stable carbides rich in Cr or Mo in the service temperature range of 773-973 K (500-700 °C)[7]. The large carbon solubility of the austenite phase and presence of carbide forming elements, such as chromium, create a driving force for carbon diffusion away from the ferritic steel [8, 9]. Although nuclear power plants are designed to last for several decades, after just one to two decades of service, a band of carbides is typically found on the austenitic side of the interface [4] due to carbon accumulation driven by both changes in composition and crystal structure. Consequently, a soft, carbon-depleted zone with few stable carbides forms along the interface in the ferritic steel, leading to premature creep related failures near the fusion line [4, 10, 11]. Carbon diffusion from ferritic to austenitic alloys resulting in carbon depletion has been identified as a major cause for premature failure of DMWs [2, 4, 7].

Functionally graded materials (FGMs) are an alternative method of joining ferritic and austenitic materials to reduce the driving force for carbon diffusion and improve creep performance. FGMs are defined as a class of materials with spatially variable properties tailored to achieve a specific function [12]. Variations in geometry, density, composition, or microstructure are typically designed at specific locations in FGMs to enhance mechanical properties [13], improve service performance [14] or increase compatibility with other systems [15]. A common example of FGMs is found in orthopedic implants, which are designed with gradients in porosity to allow for bone growth while providing load-bearing support [16]. Compositional grading is a frequently used method for producing FGMs, in which the chemical composition is spatially varied

to eliminate the abruptness of certain properties found in dissimilar joints. In this work, compositional grading has the potential for engineering FGMs that reduce the driving force for carbon diffusion using designed chemical composition profiles.

Additive manufacturing (AM) technologies offer an attractive way for producing FGMs in which the chemical composition [17, 18], part density [19], and process parameters [20] can be changed to alter the microstructure and properties with high levels of spatial resolution. Laser-based directed energy deposition (DED) using powder feedstock is a commonly used method for tailoring composition gradients by controlling the powder flow rates of different alloy powders into the molten pool [21]. For example, composition gradients between Ti-6Al-4V and pure V [21], Inconel® (IN) 625 and 304L and 316 stainless steel (SS) [18, 22], pure Fe and Fe-50 at% Al [23], SS 316L and Stellite 6 [24], Ti-6Al-4V and IN 718 [25] and Invar [26], and Ti and Ti-Mo/V [27] have been fabricated. While most of the studies report a smooth, gradual change in chemical composition, inhomogeneities in microstructures and properties are often observed. Even if care is taken in producing smooth compositional transitions, secondary phases, like intermetallic compounds and carbides, are shown to form at specific compositions [18, 26].

A gradual change in composition between ferritic and austenitic alloys can limit carbon diffusion rates by orders of magnitude compared to a conventional dissimilar metal weld [3, 8, 28]. In this work, FGMs between 2.25Cr-1Mo steel and Alloy 800H are designed using theoretical calculations to achieve the goal of reducing carbon diffusion and then fabricated by a laser-based DED AM process using custom-blended metal powder mixtures. No additional benefits in terms of carbon diffusion are achieved in compositional grading once a completely austenitic structure is obtained at a powder blend of 70% 800H. Beyond this point, the driving force for carbon diffusion is not influenced by changes in chemical composition. Additionally, compositional changes impact the formation of other microconstituents and phases. Microstructural evaluation and Vickers hardness measurements revealed the presence of a bainitic region at low levels of 800H additions. However, if the design is altered to exclude this region from the FGM, the driving force for carbon diffusion is increased, resulting in a loss of functionality. In terms of both carbon diffusion and mechanical properties, the presence of stable carbides in the as-deposited microstructure is also important in the design of ferritic to austenitic FGMs. In this case, Ti-rich carbides, which are stable at high temperatures, were present in the as-deposited austenitic region of the FGM.

2. Experimental

A laser-based DED process designed to operate at high laser powers was used to fabricate a series of compositionally graded joints on a normalized and tempered 150 mm x 150 mm x 12.7 mm thick SAE387 Grade 22 steel substrate. During processing, the build chamber was purged with high purity argon, and the oxygen content was held between 300 and 500 ppm to reduce the potential for oxidation of the deposited material. A ytterbium fiber laser (IPG Photonics® YLR-12000-L) with a wavelength ranging from 1070-1080 nm was used at a power of 2000 W and a travel speed of 10.6 mm/s, giving a linear heat input of 189 J/mm. Powder was delivered through four nozzles with 1.6 mm diameter orifices at a total flow rate of approximately 0.25 g/s. Each nozzle was angled to converge the powder streams coaxially with the laser to a spot 10 mm below the point of exit, which corresponds to a laser beam radius of approximately 2 mm. Additional shielding was supplied by argon gas flowing coaxially with the laser beam.

The powder feedstock used during deposition consisted of pre-alloyed Pyromet® 800 (Carpenter Powder Products, Inc.) and commercially pure iron and chromium (Atlantic Equipment Engineers, Micron Metals, Inc.). All powders had a size range from 45 to 145 μm in diameter, and compositions of the substrate and powders are shown in Table 1. In order to obtain a composition replicating the 2.25Cr-1Mo steel, the Fe and Cr powders were blended to the appropriate composition.

Since the DED system is equipped with only one powder feeder, compositional grading was performed by blending Pyromet® 800 (800H) and the custom blended Fe-Cr mixture (Fe-2.25Cr) to produce the desired composition prior to deposition at each height of the gradient. A total of 9 different mixtures from 10% to 90% 800H were blended in increments of 10% 800H using a twin screw mixing method. The compositions, in terms of percent 800H and the corresponding layers, are identified in the schematic diagram shown in Fig. 1. The laser beam remained off for approximately 5 minutes each time that a new powder mixture was switched. While this method added to the overall machine time, discontinuous processes have been shown to be beneficial for reducing residual stresses and distortion [29]. A total of 34 layers were deposited using 5 passes per layer. All passes within a layer were scanned in the same direction, and successive layers were scanned in the opposite direction to produce an alternating layer build path plan.

After deposition, a thin slice was extracted near the middle of the deposit using electrical discharge machining to reveal the transverse cross section. The sample was mounted and ground with a series of silicon carbide papers up to P2000 ISO grit size, polished with 3 μm and 1 μm polycrystalline diamond suspension, and finished with 0.05 μm colloidal silica. The cross section was etched by immersion for approximately 2 s with Marble's reagent, which is a solution of 20 g of copper sulfate ($CuSO_4$), 100 mL of hydrochloric acid (HCl), and 100 mL distilled water (H_20) to reveal grain boundaries as well as sub-grain structures.

Micro-hardness measurements were taken using a LECO M-400-G1 microhardness tester with a Vickers indenter. A 300 g load with a dwell time of 5 s was used for all indentations. Hardness traces were recorded at 1 mm intervals along the build direction starting at the fusion line between the base metal and the first layer of the deposition. This spacing was chosen to coincide with the approximate layer height of 1 mm and to avoid interactions between individual hardness indents. A total of 5 measurements were taken per layer at each height and the standard deviation is reported.

Scanning electron microscopy (SEM) using an FEI Quanta 200 was used to view microstructures along the composition gradient. A 20 kV accelerating voltage and 4 mm spot size were used for both secondary electron and backscatter electron images. The SEM is equipped for use with energy dispersive spectroscopy (EDS), which is capable of providing the spatial intensity of multiple elements simultaneously. EDS composition maps were used to show segregation of important carbide forming elements (Cr, Ti) near dendritic boundaries.

For quantitative, high resolution chemistry measurements, chemical composition along the grading direction was measured by electron probe microanalysis (EPMA) using a CAMECA SXFive. EPMA measurements allow for non-destructive characterization with accurate spatial resolution near specific microstructural features. For analyzing the main alloying elements (Fe, Ni and Cr) in the graded joint, the instrument was operated at a voltage of 20 keV and current of 30 nA. The EPMA trace spanned vertically along the build direction in increments of 1 mm.

To study carbon diffusion, a DMW and FGM were heat treated at 725°C for 235 h. The samples were removed from the furnace and air-cooled. Carbon concentrations before and after heat treatment were measured using EPMA with a 15kV accelerating voltage and 200 nA beam current. A liquid nitrogen cooling trap kept at approximately -190°C was used to limit contamination. A total of three line scans measuring 300 μm each were centered on the interface

of interest in 1 μm steps using a 5 s counting time at each location and the number of counts per second were recorded in each sample. Measurements were taken at the 2.25Cr-1Mo steel/IN82 filler metal interface in the DMW and at the 2.25Cr-1Mo steel/10% 800H interface in the FGM. The number of counts per second were converted to wt% C by calibrating the known carbon concentrations of NIST standard reference materials SRM2159, SRM36b and SRM866 through linear interpolation.

3. Calculations

In the design of alloys, thermodynamic and kinetic data are essential for the prediction of phase stability, phase transformations, micro segregation during solidification, and diffusion processes at high temperatures. Traditionally, thermodynamic and kinetic data for alloys have been simplified to binary and ternary systems which are dominated by one element. During compositional grading, the mixing of different elemental chemistries results in high concentrations of multiple alloying elements outside of common alloy composition ranges. The CALculation of PHase Diagrams (CALPHAD) method is capable of extrapolating Gibbs energy functions into these regions to calculate thermodynamic data. Recent work on FGMs has demonstrated that this approach is capable of determining, to a certain extent, experimentally observed phases [8, 18, 21, 26] and, therefore, will be used. In this work, two separate CALPHAD-based software packages are used for theoretical calculations.

3.1 ***Carbon diffusion calculations***

To assess the functionality of different composition profiles for reducing carbon diffusion, ThermoCalc® and DICTRA® (Thermocalc Software AB, Stockholm, Sweden) are used. The programs are coupled during diffusion simulations to allow for simultaneous thermodynamic and kinetic calculations at each time step. The 1-D calculations allow each grid point to have a specific chemical composition to evaluate the effect of various composition gradients on carbon diffusion during extended times at elevated temperatures. The simulated carbon profiles as functions of both distance and time serve as a first step in the design for the functionality graded transition joints.

Carbon diffusion between 2.25Cr-1Mo steel and Alloy 800H dissimilar welds and graded transition joints are investigated using the thermodynamic TCFE8 and kinetic MOBFE3 databases. The problem is similar to that studied by Helander and Ågren [30] in which an interstitial element

diffuses across a dissimilar alloy steel interface. The total amount of a diffusing element through an area per unit time depends both on the chemical composition of the alloy and the ability of that element to move through the phase in question. In multicomponent diffusion, the flux of a species, *k*, perpendicular to an axis, *z*, is given by [31]

$$J_k = -\sum_{i=1}^{n} L_{ki} \frac{\partial \mu_i}{\partial z} \quad (1)$$

where L_{ki} is a mobility factor and μ_i is the chemical potential of species *i*. The mobility factor, L_{ki}, is related to the interdiffusion coefficients, D_{kj}, for each element of interest as

$$D_{kj} = -\sum_{i=1}^{n} L_{ki} \frac{\partial \mu_i}{\partial c_j} \quad (2)$$

where c_j is the concentration of element *j*. The time evolution of the concentration profile of species *k* is obtained by solving

$$\frac{\partial c_k}{\partial t} = -\frac{\partial}{\partial z}(J_k) \quad (3)$$

in which *t* is time. More details about the calculation procedure in DICTRA simulations can be found elsewhere [31]. In equation (1), the driving force for diffusion is the spatial gradient of chemical potential, $\partial\mu/\partial z$, which is a function of both temperature and chemical composition at a constant pressure. Hence, a reduction in the carbon chemical potential gradient will effectively reduce the amount of carbon diffusion.

To validate the coupled thermodynamic and kinetic model, carbon diffusion between ferritic 5.0Cr-0.5Mo and austenitic 21Cr-12Ni steels is simulated and compared with experimental data [32]. The measured carbon concentrations in the as-welded condition were directly entered into the simulation at the beginning of the same 773 K for 500 h heat treatment and the effects of dilution were accounted for by considering a linear change in chemical composition from the ferritic to austenitic steel over a distance of approximately 20 μm. The ferrite, austenite and $M_{23}C_6$ phases were considered in the calculations and the system was simplified to contain only Fe, Ni, Cr, Mo and C. Although the M_6C carbide was observed experimentally [32], only small amounts were reported, and the effects of excluding this phase in the calculations is assumed to be negligible.

A model system is used to compare carbon diffusion between 2.25Cr-1Mo steel and Alloy 800H in a DMW with a sharp concentration change and across a diffuse compositional gradient

with a linear variation in alloy concentration. The major alloying elements in the material system are Fe, Ni, Cr, Mo, and C. A temperature of 773 K (500°C), which falls within the range of common service conditions, is used for simulations. Ferrite, austenite, sigma, and $M_{23}C_6$ phases are considered. The rule of mixtures homogenization function is employed for the estimation of local kinetic data, and a simulation time of 6.3072 x 10^8 s (20 years) was used in both cases to replicate expected service lifetimes.

In current applications, 2.25Cr-1Mo steel is often fusion welded to Alloy 800H using a Ni-base filler metal (Inconel 82/182), which contains high amounts of Cr, to alleviate the coefficient of thermal expansion mismatch [3]. A schematic diagram of the calculation domain for the dissimilar weld is also shown in Fig. 2a. The simulation contains a total region domain of 500 μm which only includes the interface between the ferritic steel and austenitic filler metal where carbon depletion occurs [11]. To account for dilution, a 40 μm region is defined in which an approximate linear change in chemical composition occurs from 2.25Cr-1Mo (Fe-2.25Cr-1Mo-0.1C) to IN82 (Fe-77Ni-20Cr-0.1C) centered in the middle of the region, as shown in Fig. 2a. A double geometric grid system is used to provide more grid points around the dilution region of the weld with values of 0.85 and 1.15 for the lower and upper parts of the region, respectively.

Similarly, a 10 mm region was chosen for a hypothetical FGM, as shown in Fig. 2b. The entire region contains 2.25Cr-1Mo steel (Fe-2.25Cr-1Mo-0.1C) connected to Alloy 800H (Fe-34Ni-21Cr-0.1C) by a linear composition gradient. The chemical composition for all elements varied linearly from 2.25Cr-1Mo to Alloy 800H over a distance of approximately 6.75 mm centered in the middle of the region as shown in Fig. 2b. A linear grid spacing was used for the composition gradient simulation.

3.2 ***Non-equilibrium microstructure considerations***

During AM of alloys, rapid solidification and heat transfer to surrounding material leads to high cooling rates both upon solidification and through important solid-state transformation temperature ranges [33-35]. As a result, the observed phases can often deviate from equilibrium due to rapid temperature changes, limiting the use of equilibrium thermodynamic calculations for phase predictions. JMatPro® V8 (Sente Software LTD, United Kingdom), which also uses the CALPHAD approach and minimization of the Gibbs energy method, is equipped with modules developed for specific material processing calculations. These material-specific modules can solve for important phase transformations to account for non-equilibrium phases and microconstituents.

Equilibrium phase predictions, martensite formation temperatures, continuous cooling transformation diagrams, and Scheil solidification calculations are performed using the General Steel and NiFe Superalloy databases in JMatPro® for microstructure predictions. Inputs for calculations include chemical composition and temperature ranges of interest, with the expected chemical composition of each powder blend serving as input. The benefit of including non-equilibrium phase considerations in the design of functionally graded materials is the ability to predict the likelihood of forming undesired phases.

In Fe-based alloys, the consideration of non-equilibrium phases becomes increasingly important due to the formation of martensite and bainite microconstituents. The formation of metastable martensite must be considered in the steel rich regions of the composition gradient. For the same chemical composition, martensite can have significantly different mechanical properties than other microconstituents or phases, like bainite, ferrite, or pearlite, which form during relatively slower cooling rates. The martensite start (M_s), 50% completion (M_{50}), and 90% completion (M_f) temperatures are calculated in JMatPro® based on chemical compositions similar to the methods by Ghosh and Olson[36] and Lee and Park[37]. These methods calculate the temperature as a function of alloying elements to determine the critical chemical free energy change required for martensite nucleation. The M_s is often represented as $M_s = \sum_i k_i w_i$ where k_i is a constant coefficient and w_i is weight percent of element i, but the effects of prior austenite grain size are neglected.

Continuous cooling transformation (CCT) calculations are used to determine critical cooling rates needed for the formation of pearlite and bainite in the steel-rich region of the composition gradient. The CCT diagrams are calculated by first developing transformation diagrams under isothermal conditions and transforming data to continuous cooling conditions based on well-established additivity rules [38, 39]. All transformation related data is presented in a semi-quantitative manner, since the time-temperature data was not experimentally measured during DED.

Based on large thermal gradients and high solidification front velocities, solidification morphologies that can promote the formation of secondary phases due to significant amounts of elemental segregation are formed. Since the presence of carbides is important for creep strength of the FGM, the consideration of carbide formation is necessary for the design process. Carbides formed upon solidification that remain stable at the service temperature can significantly alter

carbon migration. Here, the goal is to identify and establish the ability to predict carbides in the as-deposited condition. Scheil-Gulliver calculations [40] are used to demonstrate the effect of elemental segregation during solidification. Scheil solidification follows the basic assumption that perfect mixing occurs in the liquid and no diffusion occurs in the solid. The solidification path is approximated through small discrete temperature intervals at which local equilibrium at the interface between liquid and solid is reached. The calculations are capable of providing mass fractions and compositions of phases during solidification. Due to these basic assumptions, results from simulations should be viewed as upper limits for secondary phase fractions and compositions as less segregation is expected during the actual experiments [41].

4. Results and Discussion

4.1 ***Model validation***

To validate the carbon diffusion modeling, the carbon concentration profiles calculated using DICTRA® simulations were compared with experimental profiles measured using wavelength dispersive spectroscopy [32]. Fig. 3 shows good agreement between the measured and simulated profiles. Non-destructive profile measurements for low carbon concentrations can often be difficult and even measurements with two different techniques on the same material can show different results [42]. However, it is worthwhile to note the trends that the model was able to accurately predict. The maximum peak was located beside the original weld interface just inside the austenitic side of the weld. Furthermore, the width of the carbon enriched zone is approximately 10 to 20 μm. On the ferritic side of the interface, a slight depletion of carbon is observed. In failed dissimilar welds, this region is often the location of failure [4]. The agreement between the predicted and measured values allows for the simulations to be used for the design of FGMs in this study.

4.2 ***Spatial variation of chemical potential and composition***

In order to address the reduction of carbon migration through the use of FGMs, simulations were used to compare carbon diffusion across the sharp composition change of a dissimilar weld and a diffuse composition gradient between 2.25Cr-1Mo steel and Alloy 800H. The carbon chemical potential as a function of distance at the beginning of the simulation for the dissimilar weld and FGM are shown in Figs. 4a and 5a, respectively. A large drop in chemical potential is observed in the DMW in Fig. 4a over a relatively short distance, resulting in a large driving force

for diffusion. The sudden decrease can be attributed to both the increase of chromium, a strong carbide forming element, and the change in microstructure from ferrite to austenite. Since austenite has a higher solubility of carbon, an additional driving force for carbon diffusion is introduced. In contrast, Fig. 5a shows that the driving force is significantly lowered as the change in carbon chemical potential occurs gradually over a much longer distance.

Using these calculated carbon chemical potential gradients, the simulated carbon profiles as a function of time and distance are shown in Figs. 4b and 5b for the weld and FGM, respectively. In the DMW (Fig. 4b), it is clear that a large amount of carbon migrates from the ferritic steel towards the austenitic filler metal. A peak C concentration of 0.446 wt% is reached at approximately the midpoint of the weld, while the carbon content in the ferritic steel is constantly lowered as time increases. The overall trends in the plot are consistent with experimental observations of carbon diffusion in DMWs [32, 42, 43]. The peak carbon concentration and widths of the enriched and depleted zones are highly dependent on the different experimental conditions, such as materials, heat treatment and measurement techniques. In contrast to the DMW, the carbon migration in the compositionally graded joint is drastically hindered, as shown in Fig. 5b. The maximum and minimum carbon concentrations reached in the gradient after a simulated time of 20 years at 773 K are 0.106 and 0.090 wt% C, respectively. These results show that the linear composition gradient of the FGM is effective for significantly slowing carbon diffusion compared to its dissimilar weld counterpart.

With the initial design of the FGM established, a series of compositionally graded builds were fabricated using a laser-based DED AM process. The compositions of the main alloying elements (Fe, Ni and Cr) at locations across the build were measured using an EPMA technique and are shown in Fig. 6 with the expected compositions overlaid for comparison. It can be seen that, overall, the measured compositions closely follow the expected step-wise trend of the chemical compositions. It is observed that the highest deviations, particularly in the Fe concentration, occurred in regions corresponding to the interface between two layers of different compositions, which is likely due to mixing from remelting the previously deposited layers.

4.3 ***Microstructure and microhardness variations***

Although Fig. 6 shows that control over chemical composition during DED is achievable, the overall design of FGMs also requires consideration of the deposited microstructure. To relate chemical composition to microstructure, the Schaeffler constitution diagram, which is commonly

used for determining the main microstructural phases formed during fusion welding of alloy steels, stainless steels, and DMWs [44, 45], is utilized. The measured compositions at each location were converted to nickel and chromium equivalents, as defined in equations (4) and (5) (in wt%), and plotted onto the Schaeffler diagram, as shown in Fig. 7.

$$Ni_{EQ} = \%Ni + 30 * \%C + 0.5 * \%Mn \quad (4)$$

$$Cr_{EQ} = \%Cr + \%Mo + 1.5 * \%Si + 0.5 * \%Nb \quad (5)$$

Due to the relatively low amounts of carbon in the as-received powder, the impact of estimating carbon content in the Ni_{EQ} and Cr_{EQ} values is assumed to be minimal. The expected microstructure is martensitic up to a height of 12 mm (low Ni_{EQ} and Cr_{EQ}) above which there is a transition to austenite at heights from 12 to 18 mm above the base plate. These changes in Ni_{EQ} and Cr_{EQ} values as well as microstructure correspond to an increase in the amount of Alloy 800H added to the graded build. Previous work using arc-based AM processes with a similar alloy system showed microstructural observations consistent with these predictions [17].

To assess the validity of the Schaeffler diagram predictions, the microstructures in the as-deposited condition were examined. Due to the significantly different mechanical properties of austenite and martensite, an approximate indication of microstructure can be obtained through microhardness measurements. Fig. 8 shows Vickers hardness traces taken along the height of the build. Regions of martensite and austenite, as predicted by the Schaeffler diagram, are shown by the dotted lines. Significant differences in Vickers hardness are observed as a function of build height. The highest hardness values fall within the fully martensitic region, and large amounts of scatter in the hardness measurements are observed in the region predicted to contain a combination of martensite and austenite. The lowest Vickers hardness measurements are recorded in the fully austenitic regions.

Within the first 4 mm of the build height, however, the hardness drops to a level of approximately 245 ± 15 HV, which is much lower than the base material hardness of 312 ± 25 HV. The composition in this region corresponds to a powder blend representing 10% 800H and Ni_{EQ} and Cr_{EQ} both approximately equal to 4, which is predicted by the Schaeffler diagram to be martensitic. Fig. 9 shows a micrograph in the region approximately 3 mm above the baseplate. While no observable grain boundaries were revealed after etching, small, plate-like structures with sharp edges were present throughout the region.

To provide insight into this observation, a continuous cooling diagram was calculated for the composition range of interest. Fig. 10 shows the calculated bainite and pearlite curves for the compositions corresponding to 10 and 20% 800H regions of the composition gradient. The bainite peak for the 10% 800H region extends much further into the higher cooling rate region than other peaks, indicating that bainite, rather than martensite, is likely to form during cooling. While no time-temperature data are available, the presence of bainite in the 10% 800H region would explain the unusually low hardness values.

A sudden increase in hardness to about 345 HV is observed as the build height increases, representing composition blends ranging from 20 to 30% 800H. As displayed in Fig. 10, the maximum cooling rate required for the formation of bainite is nearly an order of magnitude lower for 20% 800H compared to 10% 800H. Therefore, even for a cooling rate as slow as 10 K/s, no bainite is likely to form in the 20% 800H region, and the microstructure is expected to be martensitic. Fig. 11a shows the microstructure present at a location 7 mm above the baseplate corresponding to a composition of 20% 800H. The solidification sub-grain structure of dendrite boundaries are easily observable, as further shown in Fig. 11b, and displays large amounts of lath martensite. Smaller regions of austenite appear, as indicated by the white arrows.

With increasing height from 11 to 16 mm (30 to 40% 800H), the hardness measurements gradually decreased, on average, but also displayed a large amount of scatter. The large standard deviations indicate microstructural inhomogeneities consisting of hard regions dispersed in a softer matrix. Figs. 12a and 12b show representative micrographs for regions which correspond to compositions of 30 and 40% 800H graded regions, respectively. Sharp martensitic laths and larger austenitic blocks are present at each location. However, the amount of austenite gradually increased with build height as more austenite forms on the boundaries between cells and dendrites, while the cores remain martensitic.

As the percentage of 800H is increased, less martensite is expected, as was observed experimentally. To explain the varying amounts of austenite and martensite with increasing additions of 800H to the graded structure, it is worthwhile to investigate the martensite transformation temperatures. Fig. 13 shows calculations of M_s, M_{50}, and M_f as a function of 800H additions. At additions up to 30% 800H, both M_s and M_f are above room temperature, meaning that the martensitic transformation is likely to reach completion. At a composition of 40% 800H, M_f drops below room temperature, indicating that although the transformation has started, it does

not reach completion upon cooling to room temperature. After 40% 800H, the calculations show that the M_s values drops below room temperature, prohibiting the martensitic transformation from ever initiating, leading to high amounts of retained austenite.

Above a build height of 16 mm, the compositions correspond to powder blends from 40 to 100% 800H with approximate Cr_{EQ} values ranging from 8.4 to 21 and Ni_{EQ} values ranging from 12.6 to 35. A plateau in Vickers hardness was reached and measurements showed a consistent value slightly below 150 HV and a dendritic microstructure was present, as displayed in Figs. 14a and 14b. No fine features like lath martensite were observed, and the microstructure displayed large, elongated grains with a dendritic sub-structure. However, small particles were present along the grain boundaries and interdendritic regions of the austenitic microstructure, indicating secondary phase formation.

Significant elemental segregation during AM can lead to the formation of both desirable and unwanted phases. The identification of alloying elements in a small particle is a simple, quick way to provide information about secondary phases. A secondary electron image accompanied by elemental distribution maps near a grain boundary in the 90% 800H region of the gradient is shown in Fig. 15. The region along the grain boundary and between dendrite arms showed a significant depletion in iron and accumulation of titanium, while all other elements show no clear segregation. Moreover, the bright spots of titanium in the elemental map correspond to dark, spherical particles on the secondary electron image, indicating carbide formation.

The two carbides existing in the 90% 800H region in equilibrium calculations are of the MC (Ti-rich) and $M_{23}C_6$ type (Cr-rich), as shown in Fig. 16a. In the typical service temperature range of approximately 673-873K (400-600°C), the $M_{23}C_6$ carbide is dominant, while the MC carbide is more stable at higher temperatures. Both $M_{23}C_6$ and MC are predicted to exist at an equilibrium mass percent of less than 1%.The Scheil-Gulliver model of JMatPro® was used to calculate mass fractions and phase compositions during idealized solidification. In Fig. 16b, only MC and austenite form upon solidification, with the Ti-rich MC phase constituting less than 1% of the overall mass. Based on the thermodynamic calculations and experimental observations, it can be concluded that the observed Ti-rich particles are carbides are of the MC type. No Cr-rich carbides were observed in the as-deposited condition.

The presence of carbides in dissimilar ferritic/austenitic joints is essential for creep performance. Many studies have investigated the precipitation and dissolution sequences of

carbides in 2.25Cr-1Mo steel and dissimilar weldments [7, 46]. A common finding is that systems tend towards the formation of Cr-rich $M_{23}C_6$ and Mo-rich M_6C carbides when approaching equilibrium, at the expense of M_2C, M_7C_3 and cementite dissolution [7, 46, 47]. Table 2 shows equilibrium thermodynamic calculations for carbides at different compositions throughout the FGM in this work. Due to the low carbon concentration of the powder and the absence of Mo in the custom blended mixture, the variety of different carbides likely to form through the composition gradient is limited. Furthermore, the formation of the Ti-rich MC carbide during solidification can significantly alter carbon migration through the joint because MC is also stable at service temperatures for many compositions.

4.4 ***Measurements of carbon diffusion profiles***

To test the design of the FGM in limiting carbon diffusion, a DMW and FGM were subjected to the same accelerated heat treatment at 998 K for 235 h (~10 days). The carbon concentration profiles were measured using EPMA via three line scans across the interface for each sample. Figure 17 shows carbon concentration in the DMW in the as-welded condition (Figure 17a) and in the as-deposited FGM (Figure 17b). In both cases, the ferritic steel is located to the left of the interface while the austenitic filler metal is to the right in the DMW and the 10% 800H region is to the right in the FGM. In the as-welded condition in Figure 17a, an approximately downward linear trend is observed near the interface moving from the ferritic steel towards the austenitic filler metal, indicating dilution during welding. Nominally, the ferritic steel contains slightly more carbon than the filler metal, as was measured by EPMA. The points for each location correspond to the average values of the three line scans and the error bars represent the standard deviation.

Carbon accumulation is observed in the heat treated condition on the austenitic side of the interface while the average carbon concentration on the ferritic side is slightly depleted, as shown in Figure 18a. The large amounts of scatter in the enriched region can be attributed to the formation of carbides. The results of the measurements show that significant amounts of carbon diffuses from the ferritic steel towards the austenitic filler metal. However, Figure 18b shows very little changes in the carbon concentration profile when compared to Figure 17b. This finding indicates that carbon diffusion from the ferritic steel is undoubtedly suppressed in the presence of the chemical composition gradient of the FGM.

4.5 ***Tailoring composition gradients to achieve improved performance***

Since most design processes are inherently iterative, it is worthwhile to search for areas of improvement. The primary function of compositional grading in this work is to reduce the driving force for carbon diffusion. In the model system of the graded transition in Fig. 2b, the carbon chemical potential gradient is shown to reach a nearly constant value, as shown in Fig. 5a, after a distance of approximately 6 mm. At this location, the corresponding composition in the model system is 15 wt% Cr, 0.31 wt% Mo, 24 wt% Ni and 0.1 wt% C. Compositional grading beyond this composition has little effect on the driving force for carbon diffusion.

To demonstrate this assertion, a hypothetical case of a partial composition gradient with the same numerical setup described in Figs. 5a and 5b is considered. The composition profiles are shown in Fig. 19a where the compositional grading ends at Fe-15Cr-0.31Mo-24Ni-0.1C and the remainder of the joint has the composition of 800H (Fe-34Ni-21Cr-0.1C). The carbon chemical potential and diffusion profiles are shown in Figs. 19b and 19c, respectively. The dotted line in Fig. 19b represents the carbon potential profile when a full composition gradient is used (Fig. 4a). Since both Figs. 5a and 19b have similar driving forces for carbon diffusion, nearly identical diffusion results are produced with the shorter graded structure.

Additionally, from equations (4) and (5), the end of the partial compositional grading would give a Ni_{EQ} value of 27 and a Cr_{EQ} value of 15.3. Based on the chemical compositions plotted on the Schaeffler diagram in Fig. 7, this approximately corresponds to the 70% 800H region of the graded transition joint in which an austenitic microstructure was observed. As the diagram in Fig. 7 has shown good agreement with experimental observations, it can be assumed that a fully austenitic microstructure would be obtained at the end of the partial composition gradient. It can thus be concluded that no additional benefits are achieved in compositional grading after 70% 800H because the material is no longer effective at serving its designed function and no changes in microstructure would result.

Furthermore, it is desirable to exclude the soft region (245 HV) of the experimental FGM to eliminate abruptness in future builds. By removing the 10% 800H composition from the FGM and starting the grading with 20% 800H, one would effectively eliminate the discontinuity in hardness. However, in order for the removal of the 10% 800H region of the joint to be acceptable for future designs, it must not negatively impact the overall function of the FGM. To investigate

the effect of removing 10% 800H from the composition gradient on carbon diffusion, the model system is revisited using DICTRA® simulations.

Fig. 20a shows a schematic of the calculation setup similar to that in Fig. 20a with the 10% 800H region removed and the composition gradient starting at 20% 800H and ending with 70% 800H. All other simulation parameters, including time, temperature, domain size, and grid spacing are identical. The carbon chemical potential profile as a function of distance is shown in Fig. 20b, in which the dotted line represents the carbon chemical potential of the original profile in Fig. 5a. Calculations show that a steeper gradient is obtained when the 10% 800H region is removed, indicating a larger thermodynamic driving force for carbon diffusion. The carbon diffusion results in Fig. 20c show that by not including the 10% 800H region in the FGM, more carbon migrates from the ferritic steel towards the austenitic alloy. This situation indicates that a tradeoff between function and desired microstructure exists in the design of FGMs between ferritic and austenitic alloys.

The carbon diffusion flux is a measure of the amount of carbon migrating through a unit area per unit time and is dependent on both location and time. To summarize the different types of joints through which carbon diffusion was simulated in this work, Table 3 provides the carbon diffusion fluxes at the location where maximum diffusion occurs after different service times. The calculations take into account the change in driving force with time as the system moves towards equilibrium. A positive value of the diffusion flux indicates carbon migration in the direction away from the ferritic steel towards the austenitic material. A FGM shows a lower flux of carbon throughout the expected service life compared to a DMW and is approximately an order of magnitude smaller. The calculations show that it would take nearly 50 years for an appropriately graded FGM to deplete the same amount of carbon from the ferritic steel as a DMW depletes after just 2 years.

5. Summary and conclusions

Spatial variation of the carbon chemical potential through compositional grading between a ferritic steel and an austenitic alloy was investigated experimentally and theoretically. In order to improve creep performance by reducing carbon loss by diffusion, a coupled thermodynamic and kinetic approach was utilized. Compositionally graded joints were fabricated using additive manufacturing and characterized to understand carbon loss by diffusion. The major findings of this work can be summarized in the following conclusions:

(a) The results show that the carbon chemical potential gradient as well as the carbon diffusion rate is significantly diminished by replacing the dissimilar joints with the compositionally graded joints. In an appropriately graded joint, it would take approximately 50 years to deplete the same amount of carbon as a dissimilar weld in just 2 years. Thus the creep performance of the joints can be significantly improved by the use of functionally graded materials.

(b) The experimentally measured carbon diffusion profiles of a dissimilar weld and functionally graded material provide conclusive evidence for the first time that carbon diffusion can be drastically suppressed. Large amounts of carbon accumulation in the austenitic region of the dissimilar weld were observed after heat treatment. However, only very subtle changes in the carbon concentration profile of the functionally graded material were observed when comparing the as-deposited and heat treated conditions.

(c) The fabricated compositional profile was expected to produce a martensitic to austenitic transition over the first 20 mm. However, in the 10% 800H region an abrupt decrease in microhardness was observed followed by a sharp return to high hardness in the 20% 800H region. As more of the austenitic alloy was added to the joint, a gradual change from a martensitic to a fully austenitic structure was observed. Taking these microstructural changes into account for an improved joint design led to the finding that a shorter joint can be used to achieve the same intended function.

(d) No benefits are gained in compositional grading after 70% 800H, where the microstructure is fully austenitic. Further changes in composition cause no appreciable changes in the driving force for carbon diffusion and DICTRA® simulations show nearly identical carbon profiles. Therefore, the functionality of the graded joint can be achieved by joining 2.25Cr-1Mo steel to Alloy 800H with a composition gradient ranging from 10 to only 70% 800H.

(e) A relatively soft bainitic microstructure was found to exist in the 10% 800H region of the joint, causing an abrupt decrease in microhardness which was followed by a rapid return to high hardness levels in the martensitic 20% 800H region. However, if the 10% 800H region of the graded joint is excluded to avoid bainite formation, an increase in the driving force for carbon migration results, leading to higher amounts of carbon diffusion.

(f) Although both $M_{23}C_6$ and MC carbides exist in equilibrium throughout the graded joint, only Ti-rich MC carbides were observed in the as-deposited microstructure, which are predicted by Scheil calculations to form during solidification. The precipitation of $M_{23}C_6$ when the functionally graded material is placed into service can also retard carbon migration and improve creep performance.

Acknowledgements

The authors would like to thank Mr. Jay Tressler and Mr. Ed Good of the Center for Innovative Materials Processing through Direct Digital Deposition (CIMP-3D) at Penn State University for assistance with sample fabrication and metallographic preparation. This work is supported by the Department of Energy Nuclear Energy University Program under grant number DE-NE0008280.

References

[1] D. Roberts, R. Ryder, R. Viswanathan, Performance of dissimilar welds in service, J. Press. Vess 107(3) (1985) 247-254.
[2] C. Lundin, Dissimilar metal welds-transition joints literature review, Weld. J. 61(2) (1982) 58-63.
[3] J. DuPont, R. Mizia, Review of dissimilar metal welding for the NGNP helical-coil steam generator, Idaho National Laboratory (INL), Idaho Falls, ID, 2010.
[4] J. DuPont, Microstructural evolution and high temperature failure of ferritic to austenitic dissimilar welds, Int. Mater. Rev. 57(4) (2012) 208-234.
[5] M. Sireesha, V. Shankar, S.K. Albert, S. Sundaresan, Microstructural features of dissimilar welds between 316LN austenitic stainless steel and alloy 800, Mater. Sci. Eng. A 292(1) (2000) 74-82.
[6] C. Jang, J. Lee, J.S. Kim, T.E. Jin, Mechanical property variation within Inconel 82/182 dissimilar metal weld between low alloy steel and 316 stainless steel, Int. J. Pres. Ves. Pip. 85(9) (2008) 635-646.
[7] J. Race, H. Bhadeshia, Precipitation sequences during carburisation of Cr–Mo steel, Mater. Sci. Tech. 8(10) (1992) 875-882.
[8] G. Brentrup, B. Snowden, J. DuPont, J. Grenestedt, Design considerations of graded transition joints for welding dissimilar alloys, Weld. J. 91 (2012) 252-59.

[9] H. Wang, G. Wang, F. Xuan, S. Tu, Fracture mechanism of a dissimilar metal welded joint in nuclear power plant, Eng. Fail. Anal. 28 (2013) 134-148.
[10] K. Laha, K. Chandravathi, K.B.S. Rao, S. Mannan, D. Sastry, An assessment of creep deformation and fracture behavior of 2.25 Cr-1Mo similar and dissimilar weld joints, Metall. Mater. Trans. A 32(1) (2001) 115-124.
[11] K. Laha, K.B.S. Rao, S. Mannan, Creep behaviour of post-weld heat-treated 2.25 Cr-1Mo ferritic steel base, weld metal and weldments, Mater. Sci. Eng. A 129(2) (1990) 183-195.
[12] R.M. Mahamood, E.T. Akinlabi, M. Shukla, S. Pityana, Functionally graded material: an overview, Proceedings of the World Congress on Engineering, London, UK, 2012, pp. 2-6.
[13] S. Kapuria, M. Bhattacharyya, A. Kumar, Bending and free vibration response of layered functionally graded beams: A theoretical model and its experimental validation, Compos. Struct. 82(3) (2008) 390-402.
[14] Z.H. Melgarejo, O.M. Suárez, K. Sridharan, Wear resistance of a functionally-graded aluminum matrix composite, Scripta Mater. 55(1) (2006) 95-98.
[15] B.V. Krishna, W. Xue, S. Bose, A. Bandyopadhyay, Functionally graded Co–Cr–Mo coating on Ti–6Al–4V alloy structures, Acta Biomater. 4(3) (2008) 697-706.
[16] A. Bandyopadhyay, B. Krishna, W. Xue, S. Bose, Application of laser engineered net shaping (LENS) to manufacture porous and functionally graded structures for load bearing implants, J. Mater. Sci-mater. M. 20 (2009) 29-34.
[17] G. Brentrup, J. DuPont, Fabrication and characterization of graded transition joints for welding dissimilar alloys, Weld. J. 92 (2013) 72-79.
[18] B.E. Carroll, R.A. Otis, J.P. Borgonia, J.-o. Suh, R.P. Dillon, A.A. Shapiro, D.C. Hofmann, Z.-K. Liu, A.M. Beese, Functionally graded material of 304L stainless steel and inconel 625 fabricated by directed energy deposition: Characterization and thermodynamic modeling, Acta Mater. 108 (2016) 46-54.
[19] L. Murr, S. Gaytan, F. Medina, H. Lopez, E. Martinez, B. Machado, D. Hernandez, L. Martinez, M. Lopez, R. Wicker, Next-generation biomedical implants using additive manufacturing of complex, cellular and functional mesh arrays, Philos. T. Roy. Soc. A 368(1917) (2010) 1999-2032.
[20] R. Dehoff, M. Kirka, W. Sames, H. Bilheux, A. Tremsin, L. Lowe, S. Babu, Site specific control of crystallographic grain orientation through electron beam additive manufacturing, Mater. Sci. Tech. 31(8) (2015) 931-938.
[21] D.C. Hofmann, S. Roberts, R. Otis, J. Kolodziejska, R.P. Dillon, J.-o. Suh, A.A. Shapiro, Z.-K. Liu, J.-P. Borgonia, Developing gradient metal alloys through radial deposition additive manufacturing, Sci. Rep. 4 (2014) 5357.
[22] U. Savitha, G.J. Reddy, A. Venkataramana, A.S. Rao, A. Gokhale, M. Sundararaman, Chemical analysis, structure and mechanical properties of discrete and compositionally graded SS316–IN625 dual materials, Mater. Sci. Eng. A 647 (2015) 344-352.
[23] C. Shen, Z. Pan, D. Cuiuri, J. Roberts, H. Li, Fabrication of Fe-FeAl functionally graded material using the wire-arc additive manufacturing process, Metall. Mater. Trans. B 47(1) (2016) 763-772.
[24] P. Muller, P. Mognol, J.-Y. Hascoet, Modeling and control of a direct laser powder deposition process for Functionally Graded Materials (FGM) parts manufacturing, J. Mater. Process. Technol. 213(5) (2013) 685-692.
[25] M. Domack, J. Baughman, Development of nickel-titanium graded composition components, Rapid Prototyp. J. 11(1) (2005) 41-51.

[26] L.D. Bobbio, R.A. Otis, J.P. Borgonia, R.P. Dillon, A.A. Shapiro, Z.-K. Liu, A.M. Beese, Additive manufacturing of a functionally graded material from Ti-6Al-4V to Invar: Experimental characterization and thermodynamic calculations, Acta Mater. 127 (2017) 133-142.
[27] P. Collins, R. Banerjee, S. Banerjee, H. Fraser, Laser deposition of compositionally graded titanium–vanadium and titanium–molybdenum alloys, Mater. Sci. Eng. A 352(1) (2003) 118-128.
[28] G.J. Brentrup, Design and fabrication of functionally graded transition joints to replace failure-prone dissimilar metal welds, Mater. Sci. Eng., Lehigh University, Ann Arbor, 2011, p. 110.
[29] E.R. Denlinger, J.C. Heigel, P. Michaleris, T. Palmer, Effect of inter-layer dwell time on distortion and residual stress in additive manufacturing of titanium and nickel alloys, J. Mater. Process. Technol. 215 (2015) 123-131.
[30] T. Helander, J. Ågren, Computer simulation of multicomponent diffusion in joints of dissimilar steels, Metall. Mater. Trans. A 28(2) (1997) 303-308.
[31] A. Borgenstam, L. Höglund, J. Ågren, A. Engström, DICTRA, a tool for simulation of diffusional transformations in alloys, J. Phase Equilib. 21(3) (2000) 269.
[32] M. Huang, d.L. Wang, Carbon migration in 5Cr-0.5 Mo/21Cr-12Ni dissimilar metal welds, Metall. Mater. Trans. A 29(12) (1998) 3037-3046.
[33] V. Manvatkar, A. De, T. DebRoy, Heat transfer and material flow during laser assisted multi-layer additive manufacturing, J. Appl. Phys. 116(12) (2014) 124905.
[34] G. Knapp, T. Mukherjee, J. Zuback, H. Wei, T. Palmer, A. De, T. DebRoy, Building blocks for a digital twin of additive manufacturing, Acta Mater. 135 (2017) 390-399.
[35] A. Raghavan, H. Wei, T. Palmer, T. DebRoy, Heat transfer and fluid flow in additive manufacturing, Journal of Laser Applications 25(5) (2013) 052006.
[36] G. Ghosh, G. Olson, Computational thermodynamics and the kinetics of martensitic transformation, J. Phase Equilib. 22(3) (2001) 199.
[37] S.-J. Lee, K.-S. Park, Prediction of martensite start temperature in alloy steels with different grain sizes, Metall. Mater. Trans. A 44(8) (2013) 3423-3427.
[38] N. Saunders, Z. Guo, X. Li, A. Miodownik, J.P. Schillé, The calculation of TTT and CCT diagrams for general steels, JMatPro Software Literature (2004).
[39] J. Kirkaldy, Diffusion-controlled phase transformations in steels. Theory and applications, Scand. J. Metall. 20(1) (1991) 50-61.
[40] E. Scheil, Bemerkungen zur schichtkristallbildung, Z. Metallkd. 34(3) (1942) 70-72.
[41] T. Keller, G. Lindwall, S. Ghosh, L. Ma, B.M. Lane, F. Zhang, U.R. Kattner, E.A. Lass, J.C. Heigel, Y. Idell, M.E. Williams, A.J. Allen, J.E. Guyer, L.E. Levine, Application of finite element, phase-field, and CALPHAD-based methods to additive manufacturing of Ni-based superalloys, Acta Mater. 139(Supplement C) (2017) 244-253.
[42] F. Mas, C. Tassin, N. Valle, F. Robaut, F. Charlot, M. Yescas, F. Roch, P. Todeschini, Y. Bréchet, Metallurgical characterization of coupled carbon diffusion and precipitation in dissimilar steel welds, J. Mater. Sci. 51(10) (2016) 4864-4879.
[43] R. Ryder, C. Li, R. Viswanathan, J. Dimmer, Dissimilar metal weld failures in power plants—Causes and remedies, Trends in electric utility research (1984) 137.
[44] J.N. DuPont, J.C. Lippold, S.D. Kiser, Welding metallurgy and weldability of nickel-base alloys, John Wiley & Sons, Hoboken, NJ, 2009.
[45] A. Schaeffler, Constitution diagram for stainless steel weld metal, Metal Prog. 56(11) (1949) 680.

[46] R. Baker, J. Nutting, The tempering of 2.25 Cr%–1% Mo steel after quenching and normalizing, J. Iron Steel Inst. 202 (1959) 257-68.
[47] J. Yang, C. Huang, C. Yang, J. Horng, Microstructural examination of 2.25 Cr 1Mo Steel Steam pipes after extended service, Mater. Charact. 30(2) (1993) 75-88.

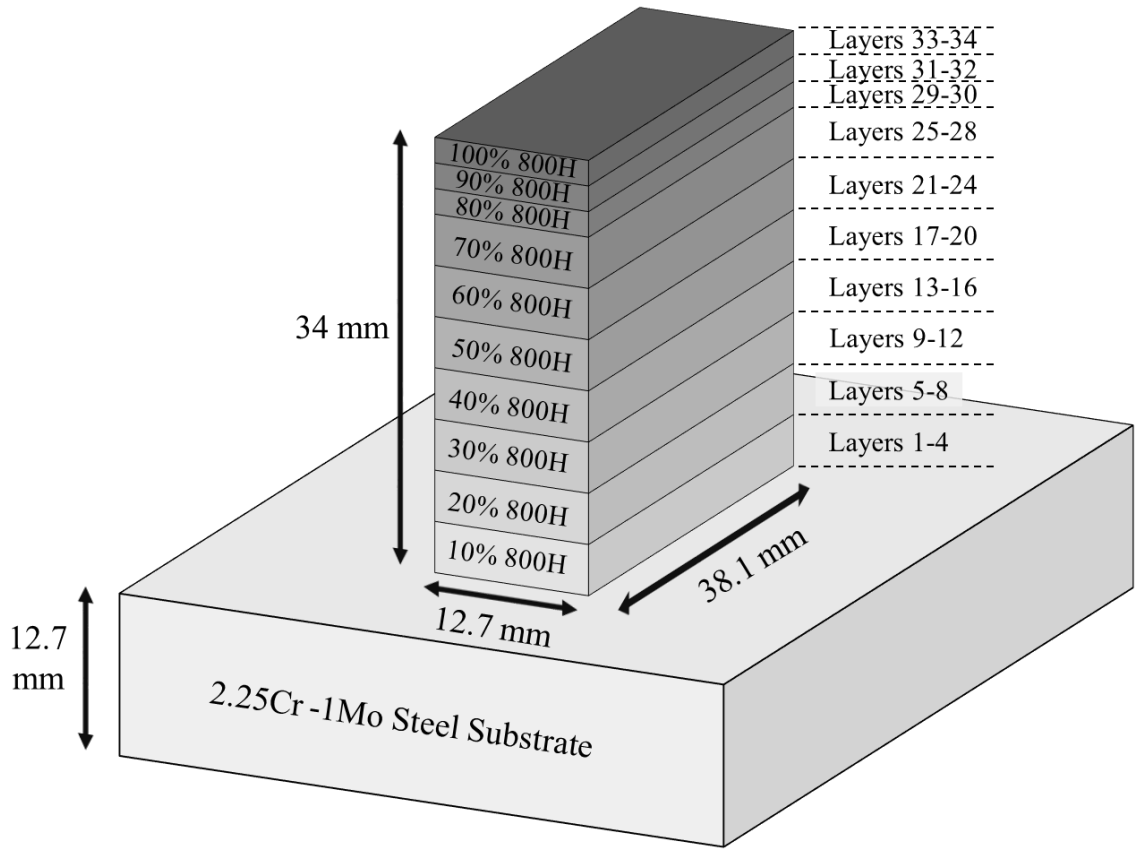

Fig. 1. Schematic diagram of the compositionally graded deposit showing target dimensions and regions of different compositions

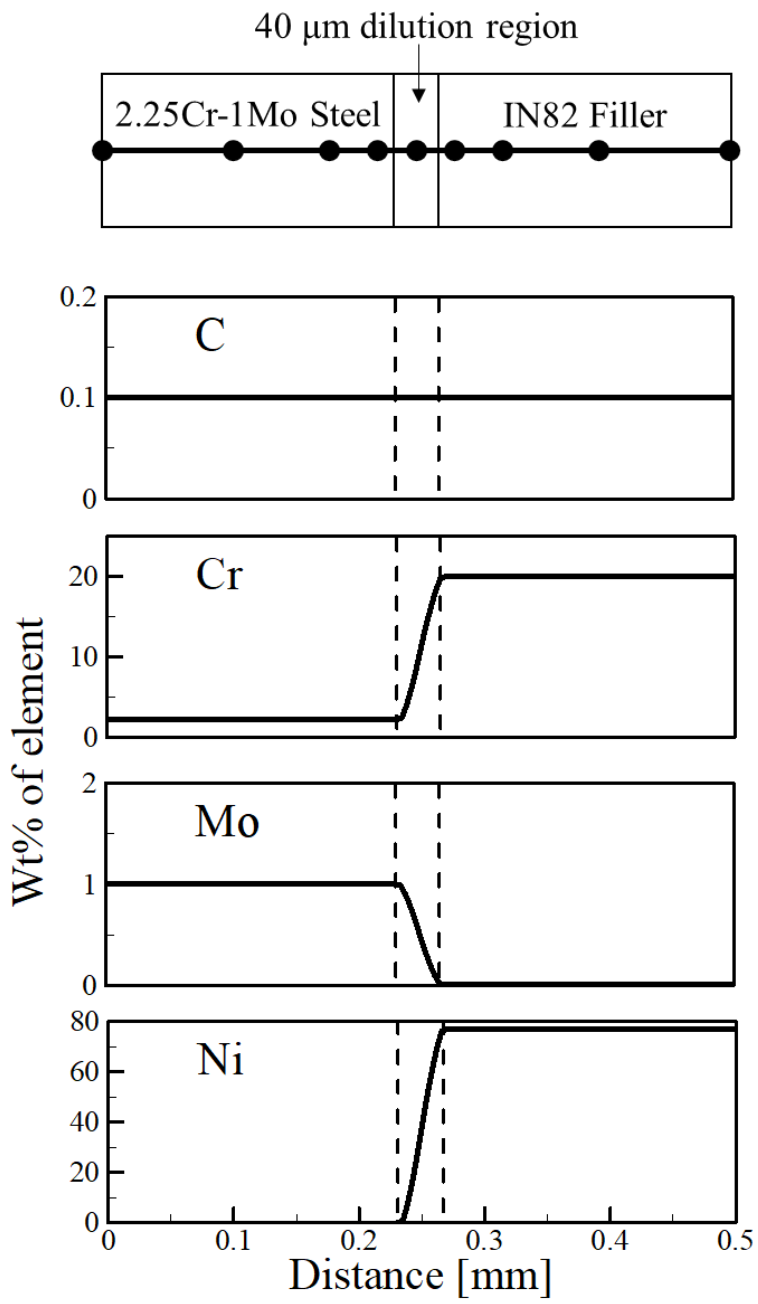
40 μm dilution region
2.25Cr-1Mo Steel
IN82 Filler
C
Cr
Mo
Ni
Wt% of element
Distance [mm]
0.2
0.1
0
20
10
2
1
80
60
40
20
0.1
0.2
0.3
0.4
0.5

(a)

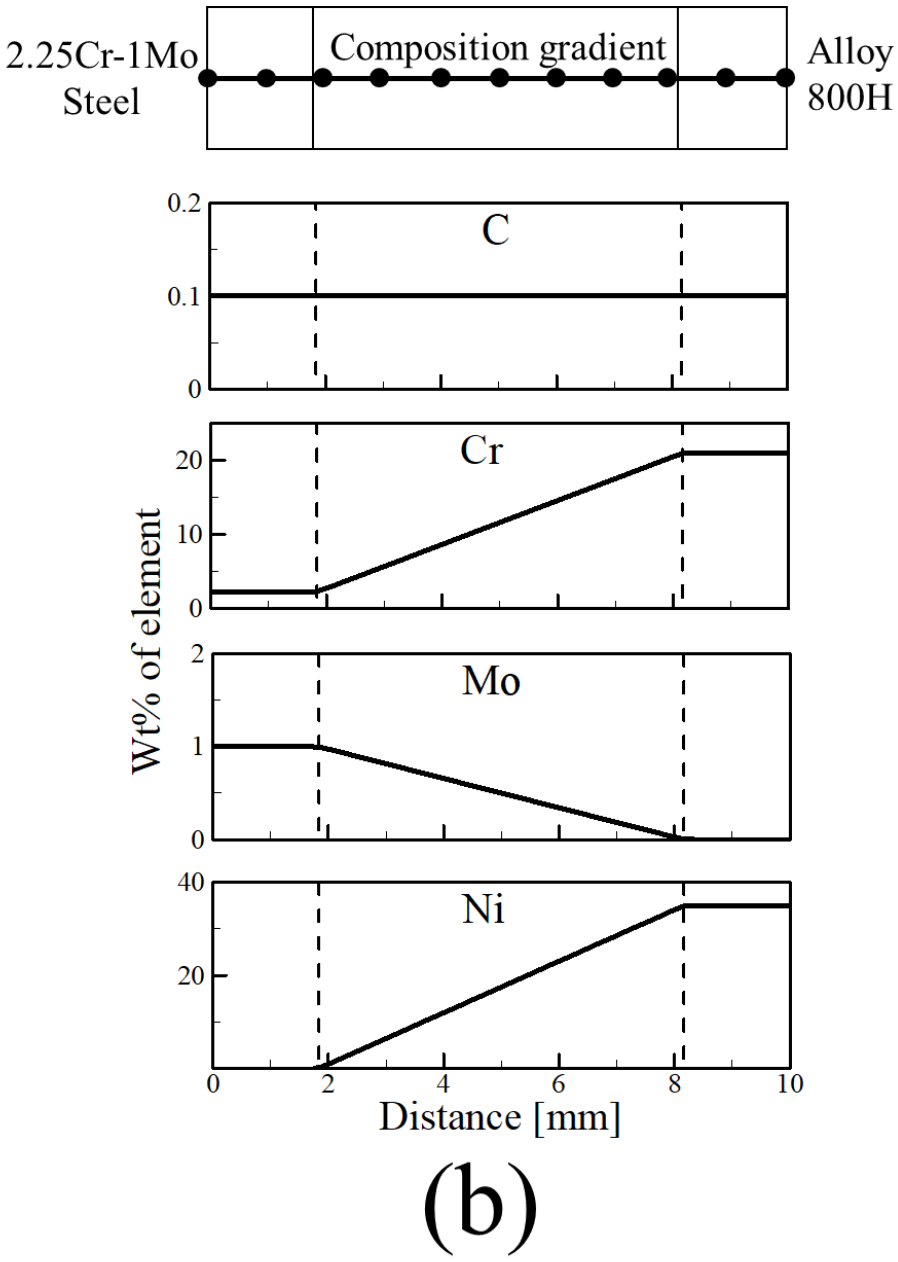

Fig. 2. Schematic diagram of the calculation region for carbon diffusion calculations and initial composition profiles for C, Cr, Mo and Ni in (a) a DMW and (b) a graded transition joint between 2.25Cr-1Mo steel and Alloy 800H. The (a) double geometric and (b) linear grid spacings are shown by the solid black dots.

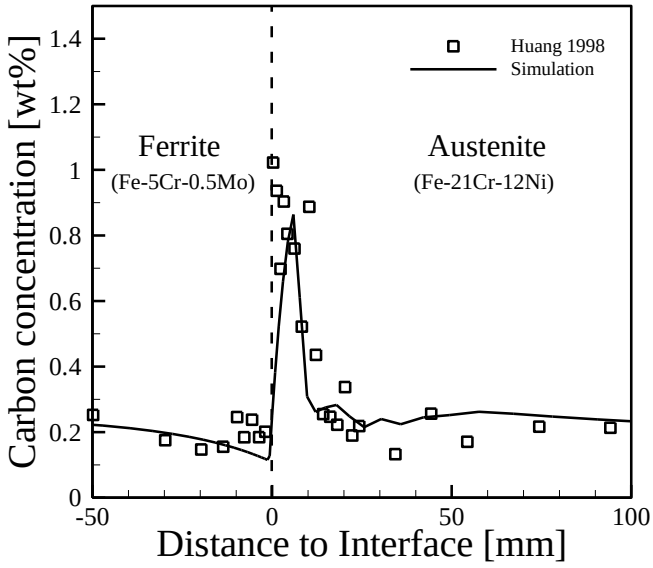

Fig. 3. Comparison between simulated carbon diffusion profiles with experimental measurements between a 5Cr-0.5Mo/21Cr-12Ni weld heat treated at 773 K for 500 h.

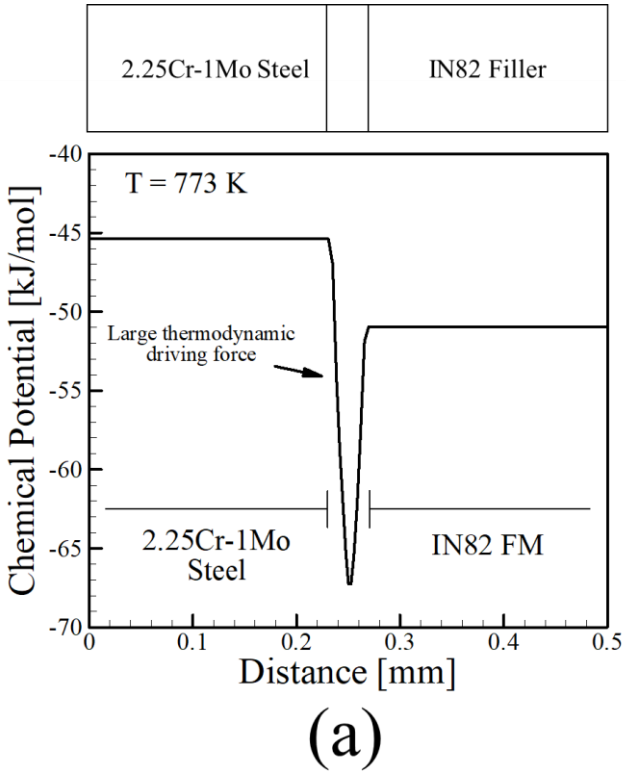

(a)

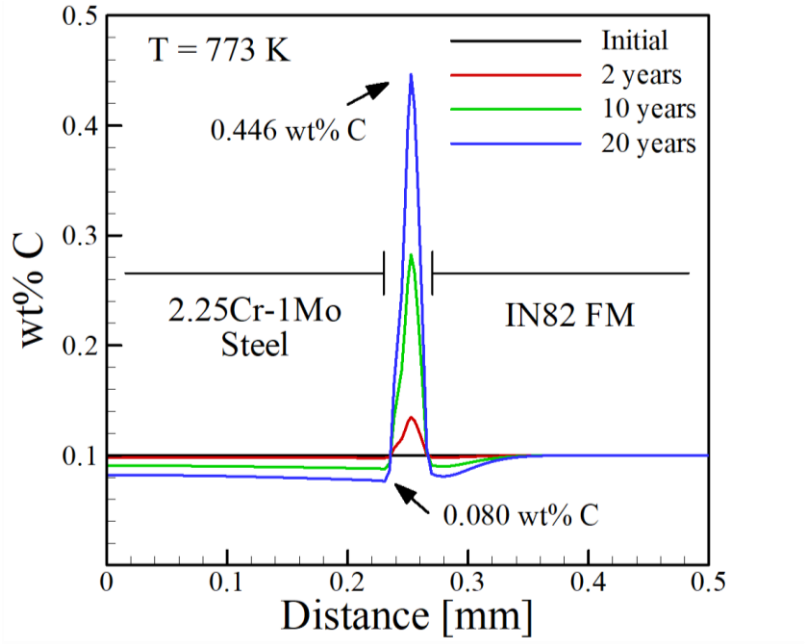

(b)

Fig. 4. Results from DICTRA simulations showing (a) carbon chemical potential as a function of distance at the beginning of the simulation and (b) carbon diffusion profiles as a function of time and distance for a DMW between 2.25Cr-1Mo steel and Alloy 800H at 773 K

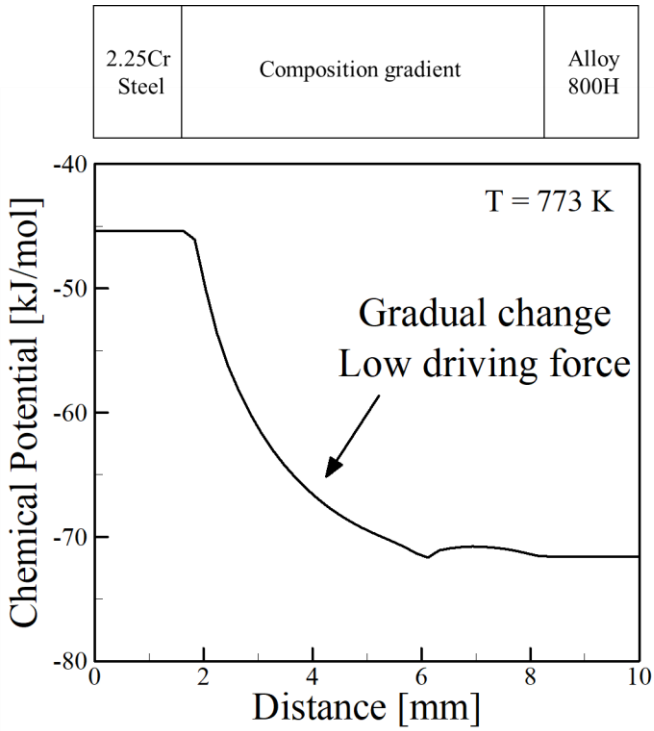

(a)

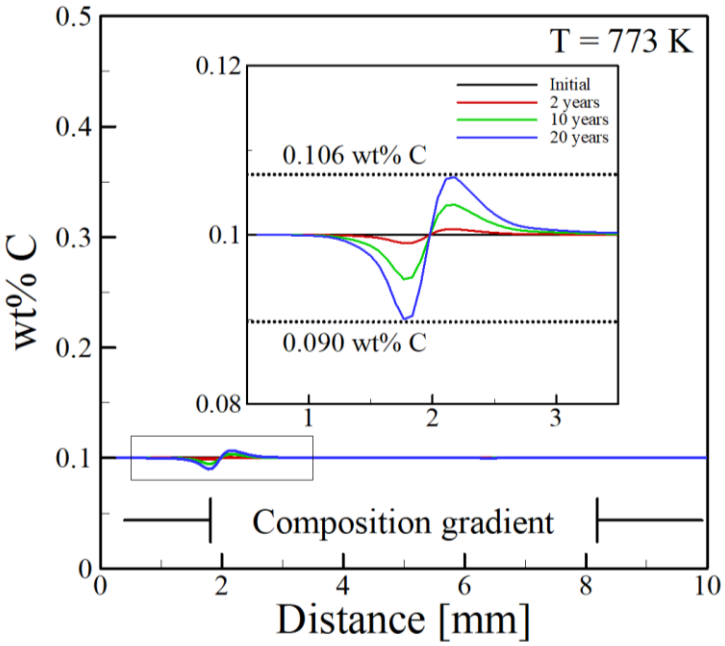

(b)

Fig. 5. Results from DICTRA simulations showing (a) carbon chemical potential as a function of distance at the beginning of the simulation and (b) carbon diffusion profiles as a function of time and distance for a composition gradient between 2.25Cr-1Mo steel and Alloy 800H at 773 K

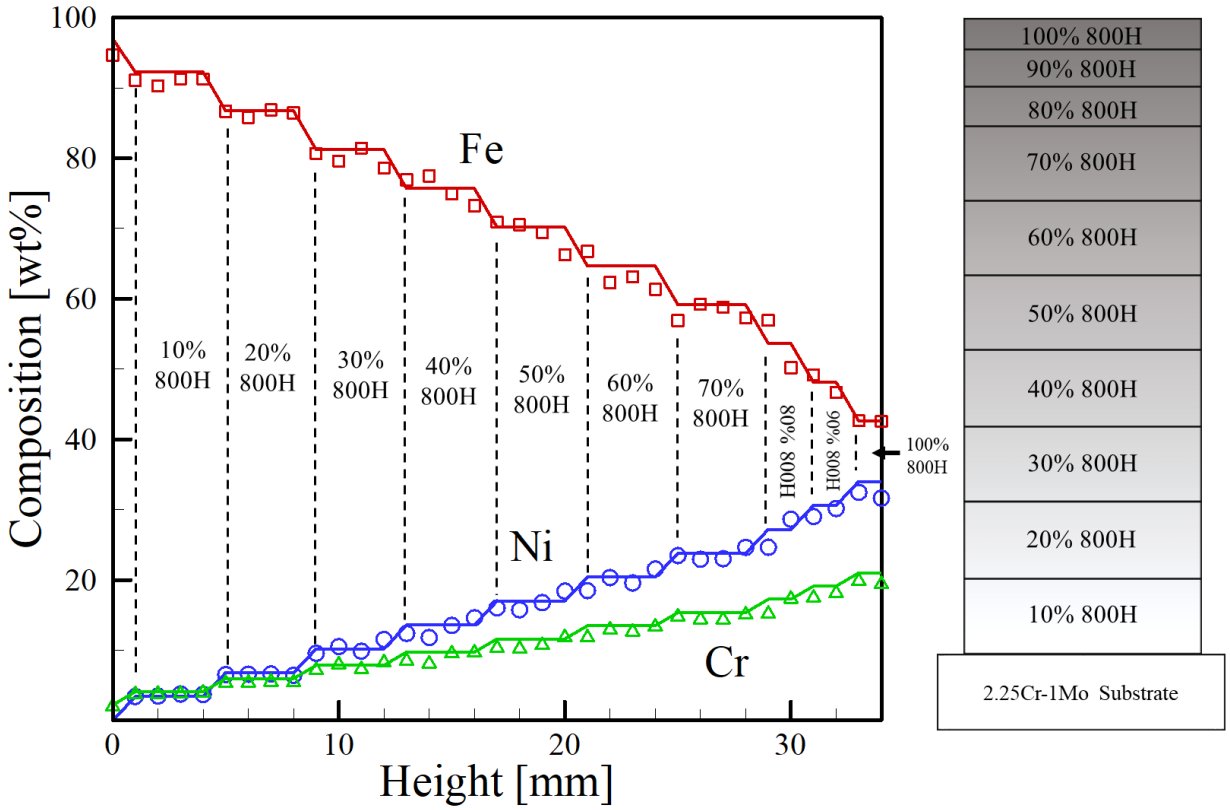

Fig. 6. Expected and measured chemical composition as a function along the build height

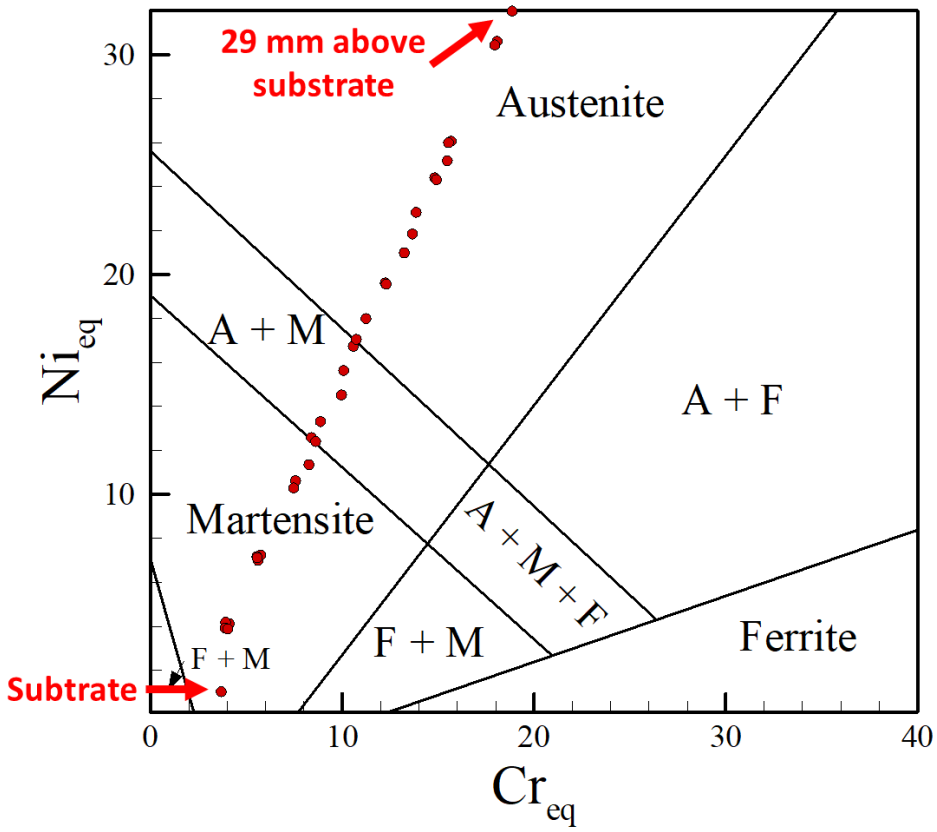

Fig. 7. EPMA data converted to nickel and chromium equivalents and plotted on the Schaeffler constitution diagram to determine the main microstructural phases across the gradient

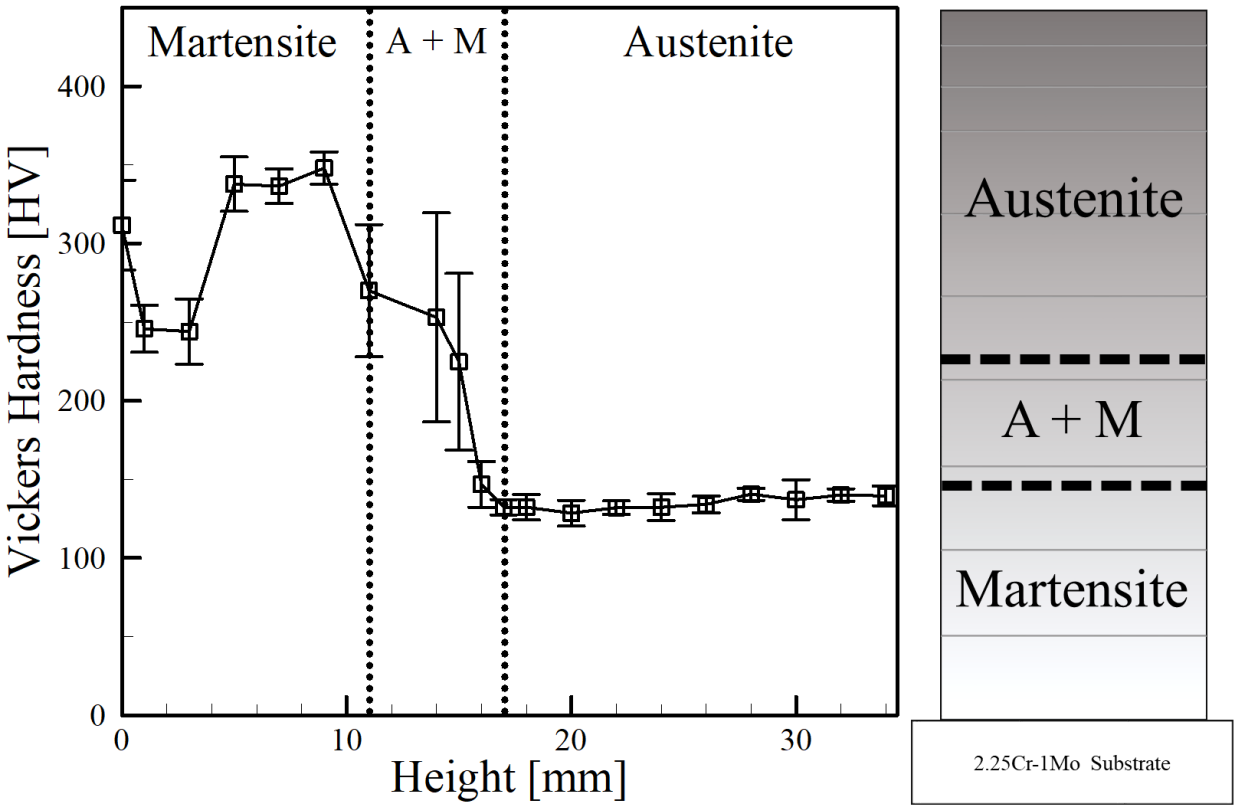

Fig. 8. Vickers hardness measurements along the compositionally graded sample. Regions of martensite, austenite and a mixture of austenite and martensite predicted by the Schaeffler diagram are separated by dotted lines.

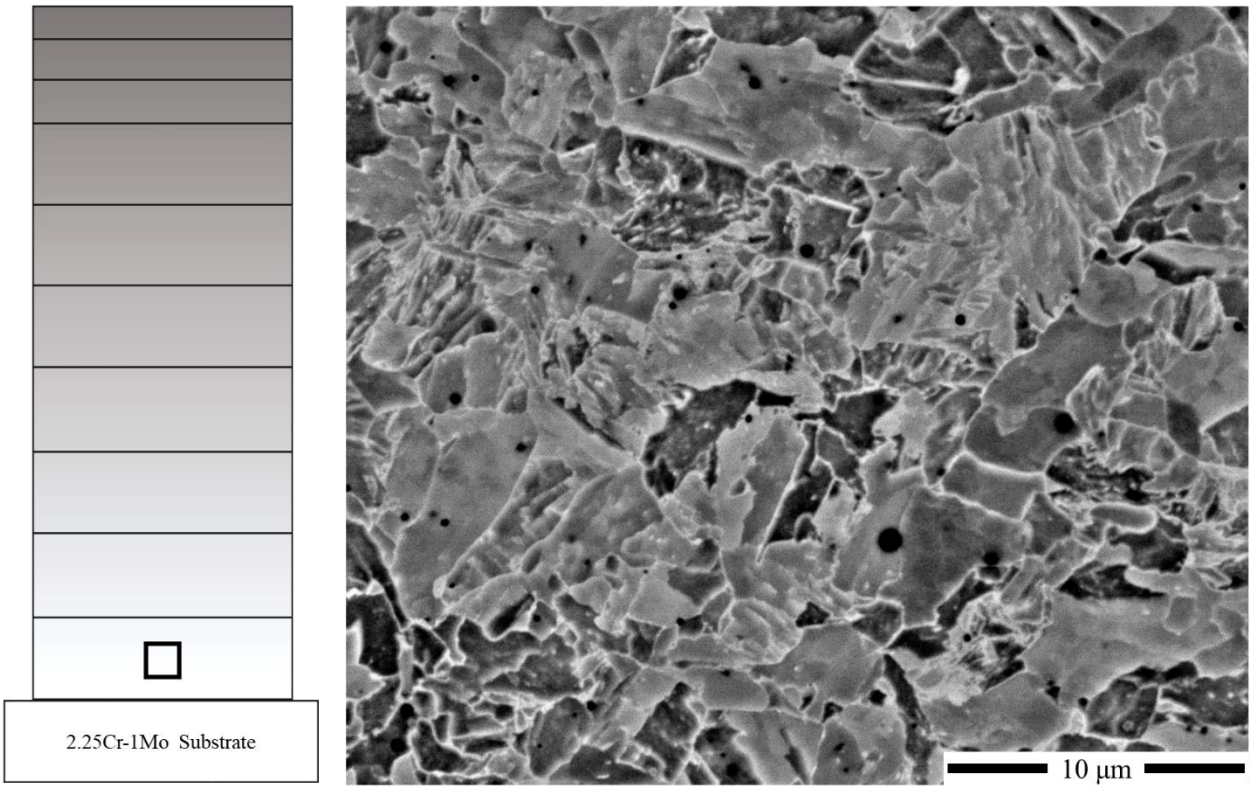

Fig. 9. SEM micrograph approximately 3 mm from the baseplate in the build direction, corresponding to the 3rd deposited layer and a composition of 10% 800H

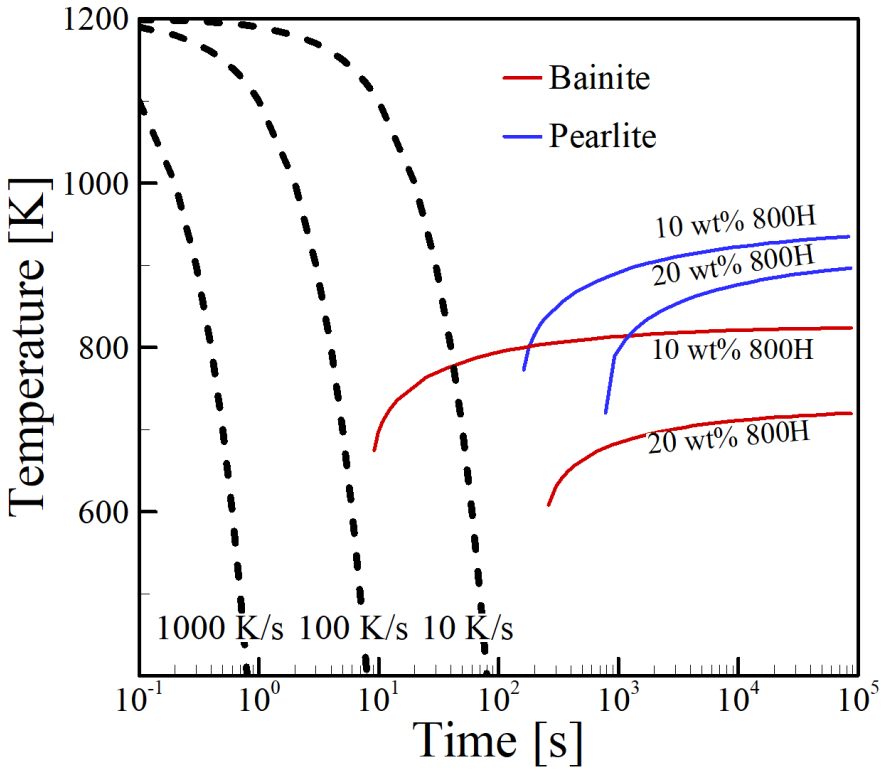

Fig. 10. Continuous cooling diagram for the austenite transformation of steel-rich compositions within the compositionally graded sample

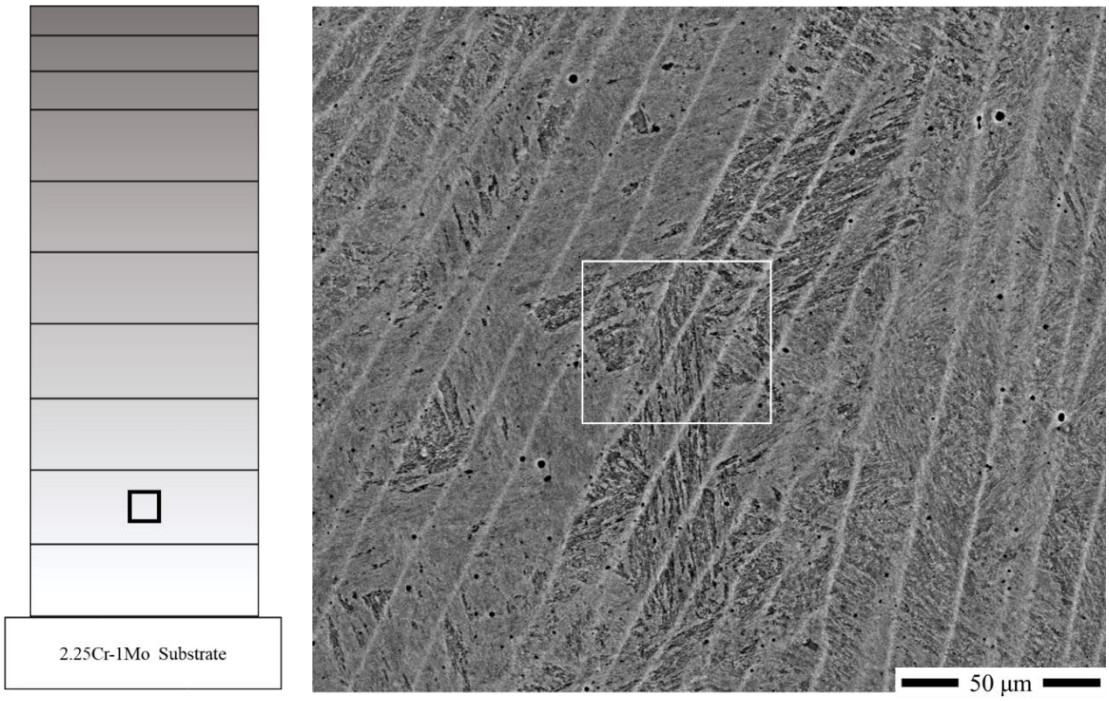

(a)

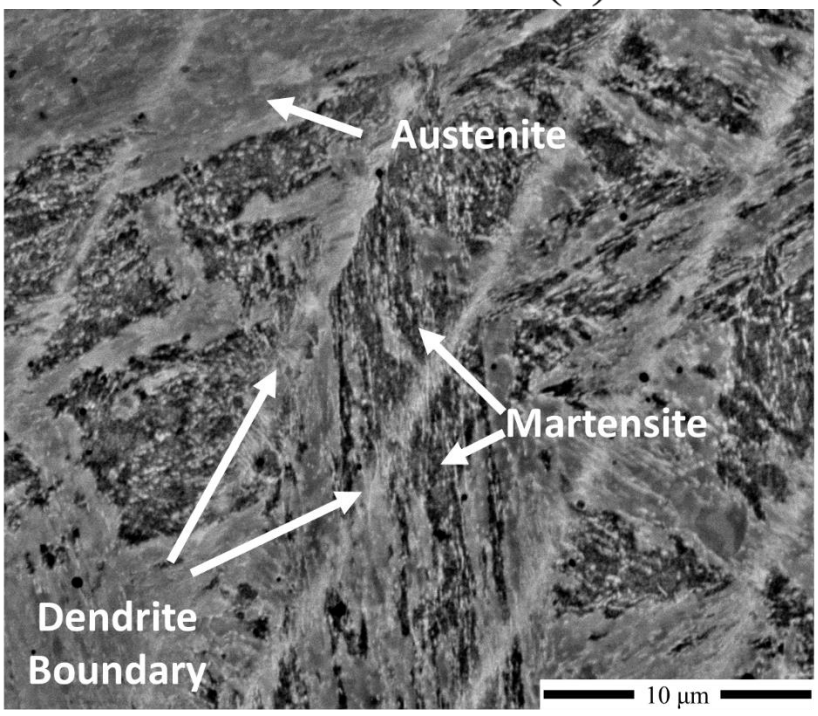

(b)

Fig. 11. (a) SEM micrograph approximately 7 mm from the baseplate in the build direction, corresponding to the 7th deposited layer and a composition of 20% 800H and (b) a higher magnification image outlined by the white box in (a) showing martensite and austenite

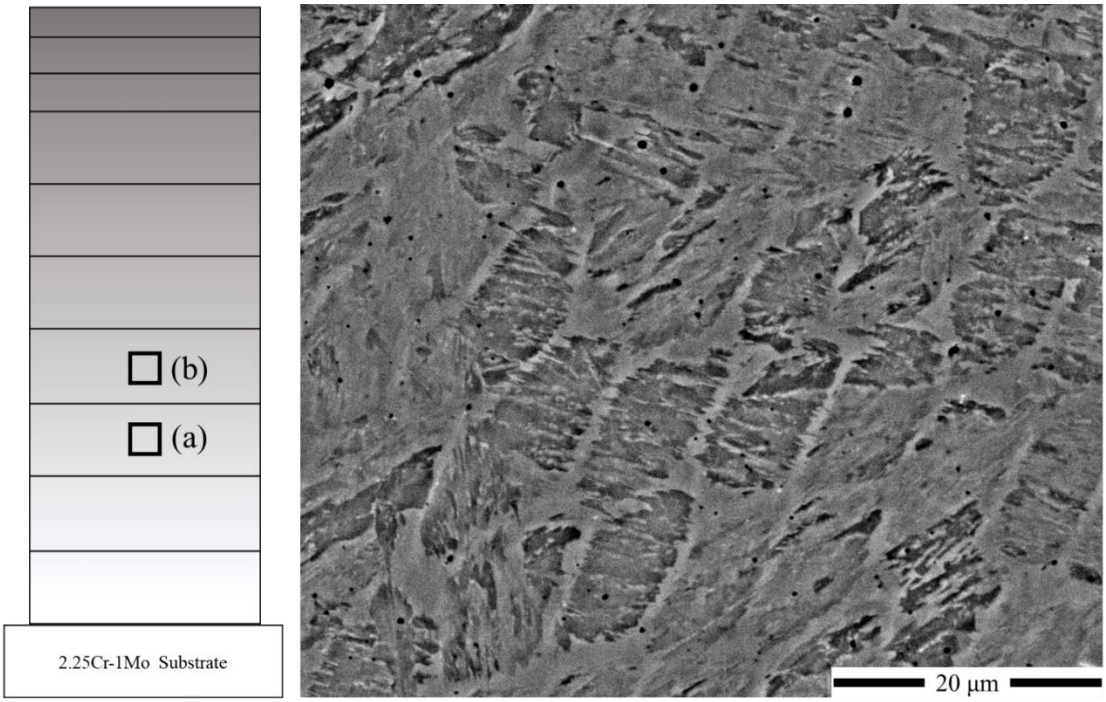

(a)

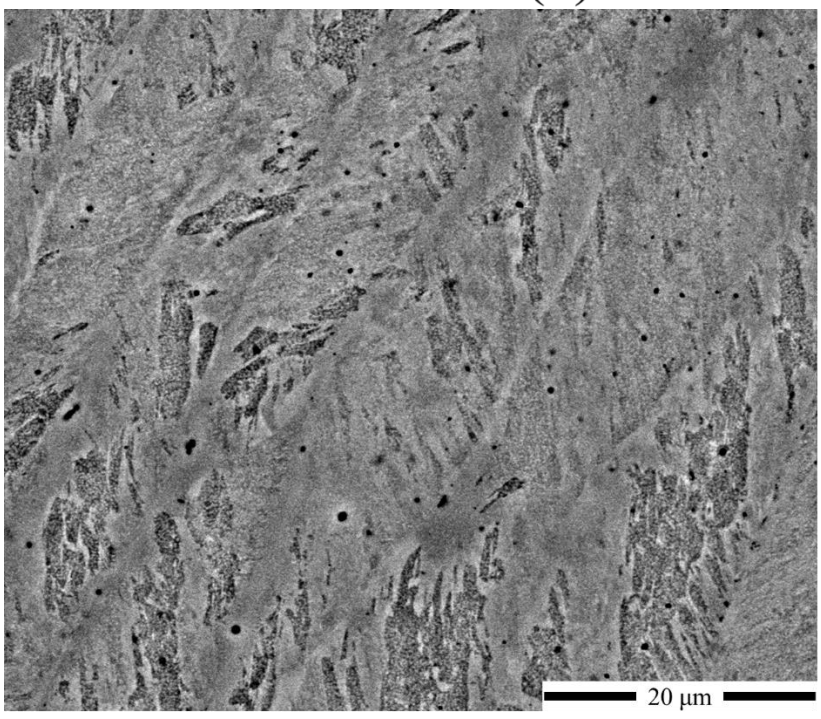

(b)

Fig. 12. SEM micrographs approximately (a) 11 mm and (b) 15 mm from the baseplate in the build direction. The microstructures correspond to the 11^{th} and 15^{th} deposited layers and compositions of 30 and 40% 800H, respectively

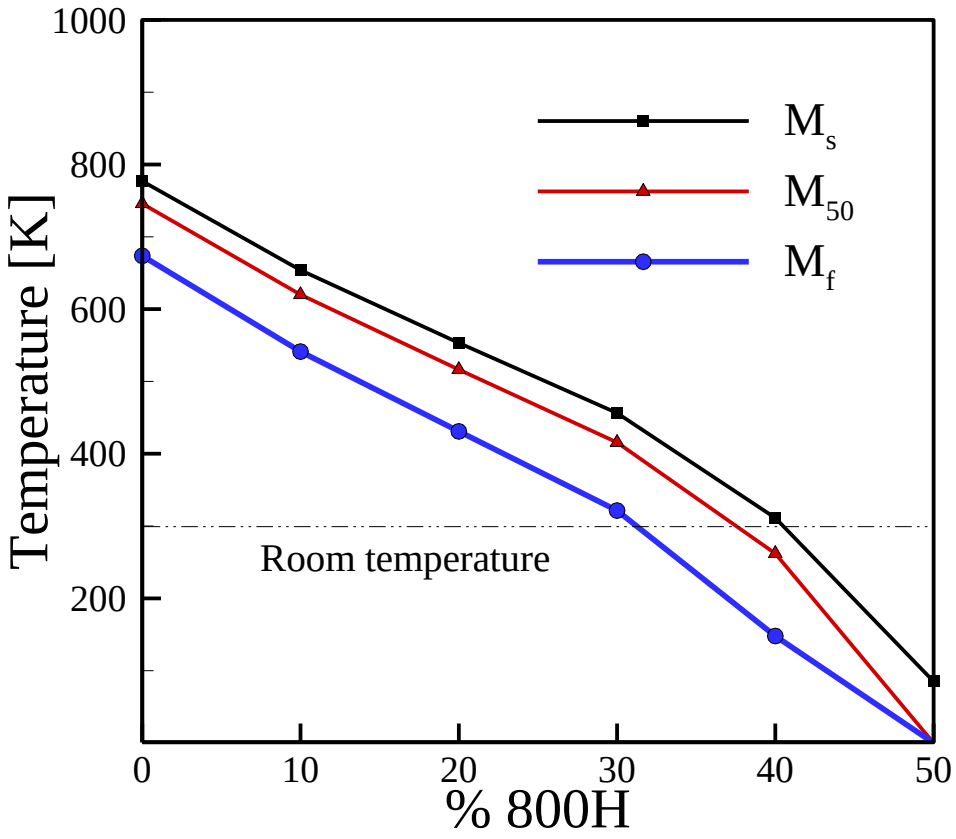

Fig. 13. Martensite start (M_s), 50% completion (M_{50}) and finish (M_f) temperatures for the martensite transformation as a function of composition in terms of percent 800H.

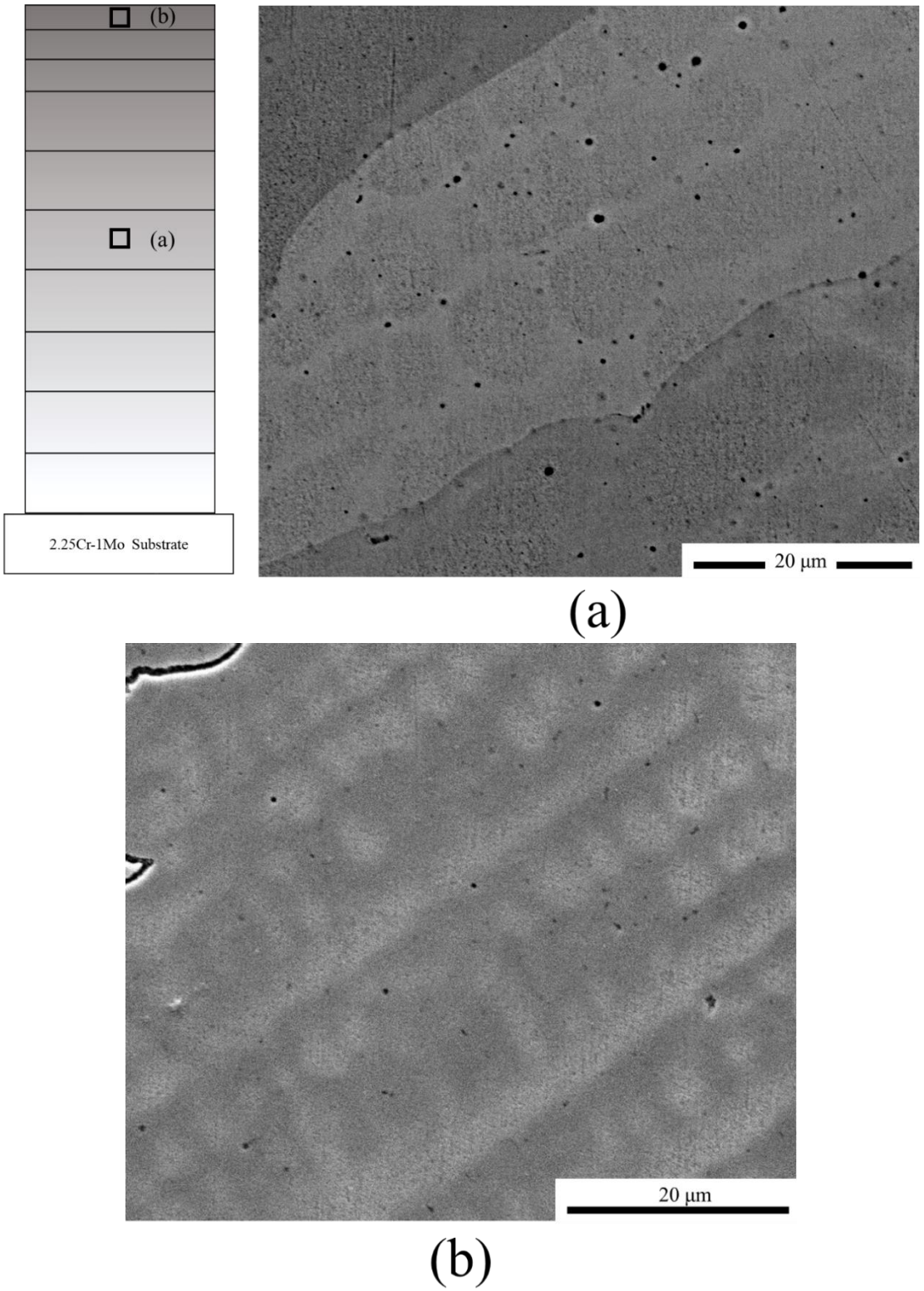

Fig. 14. SEM micrographs approximately (a) 19 mm and (b) 34 mm from the baseplate in the build direction. The microstructures correspond to the 19th and 34th deposited layer, and compositions of 50 and 100% 800H, respectively

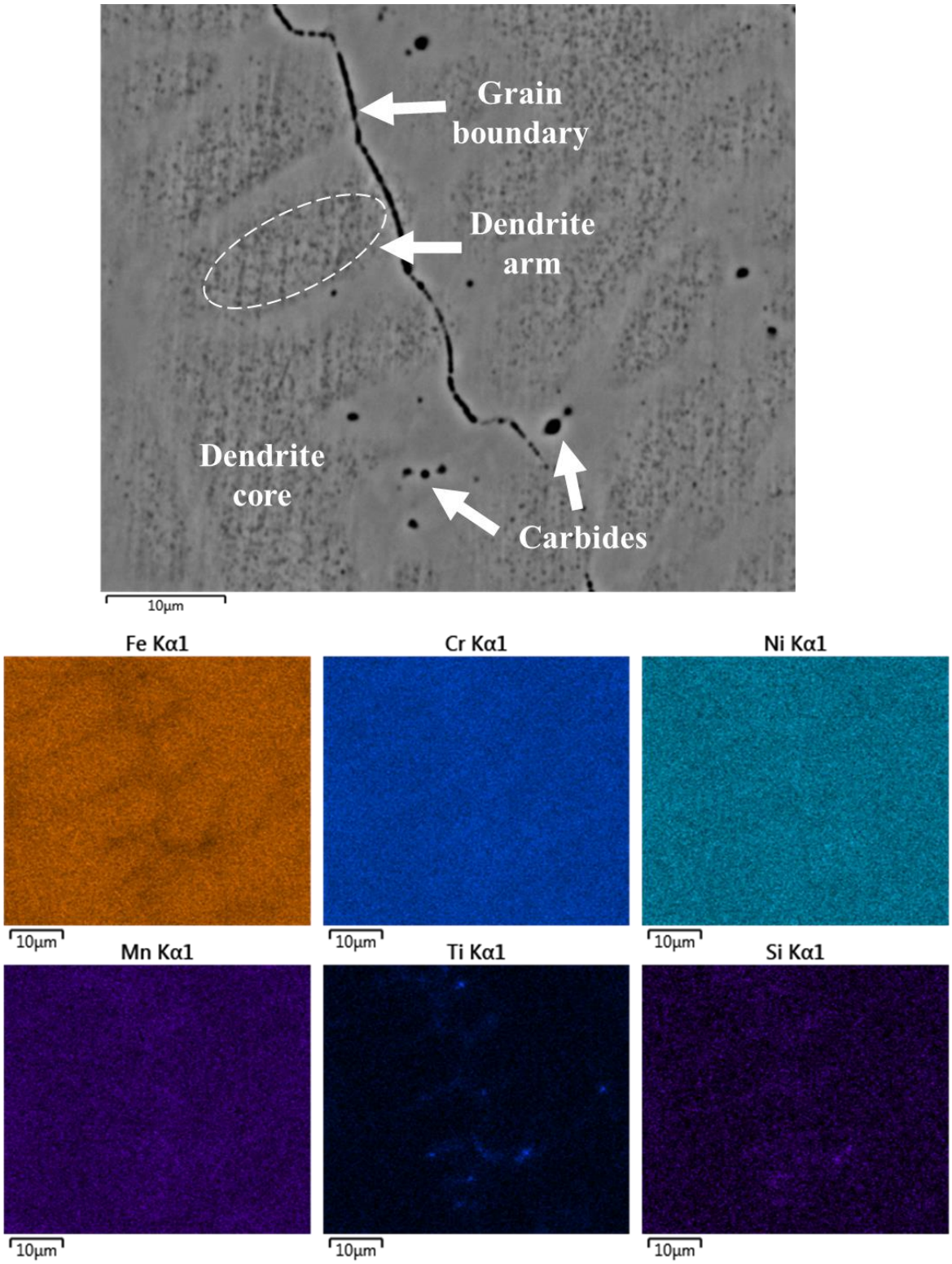

Fig. 15. EDS map showing elemental segregation along the grain boundaries and interdendritic regions in the 90% 800H region of the composition gradient

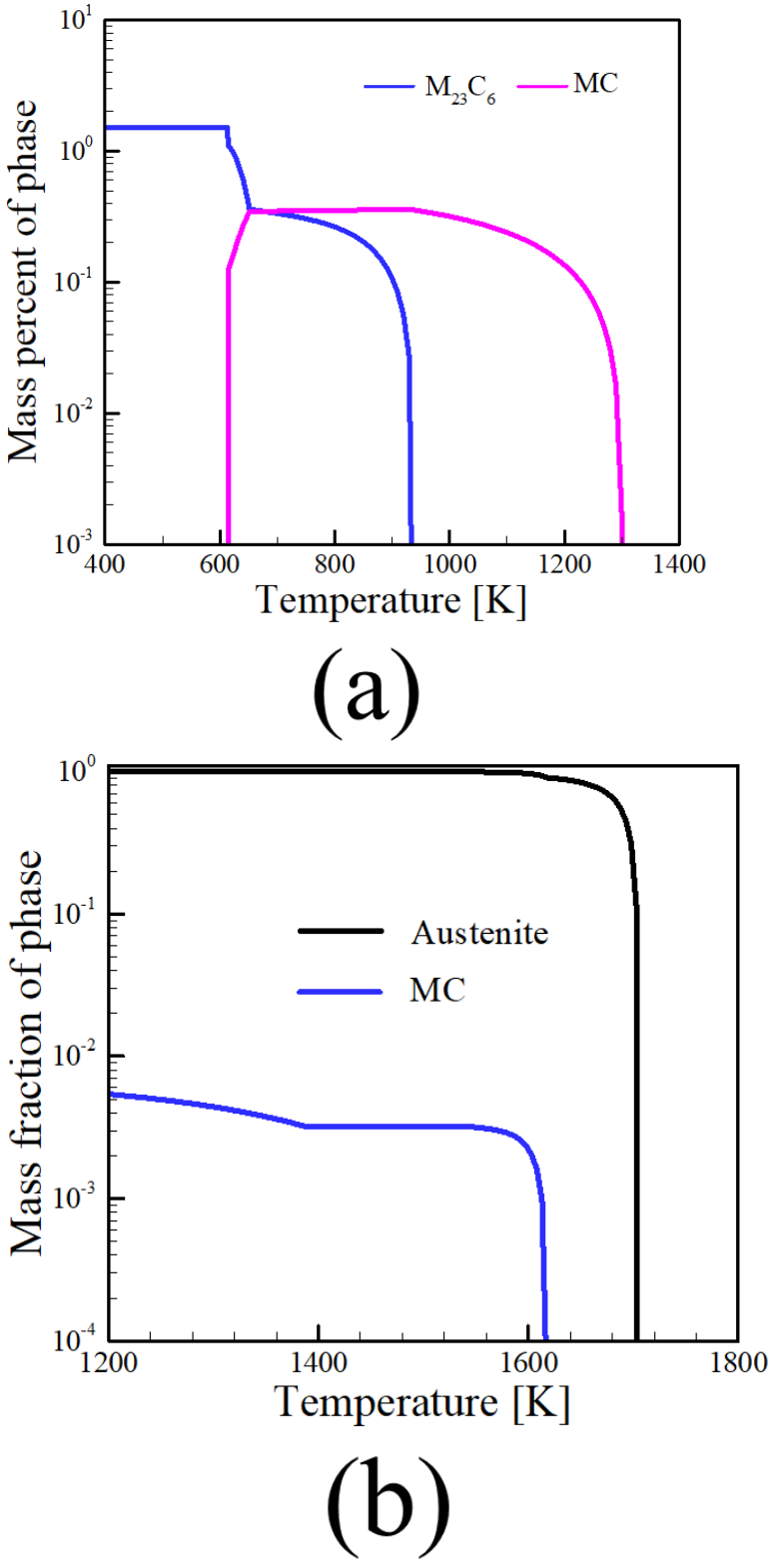

Fig. 16. Thermodynamic calculations in the 90% 800H region showing (a) stable carbides as a function of temperature and (b) mass fractions of solidified phases from Scheil simulation

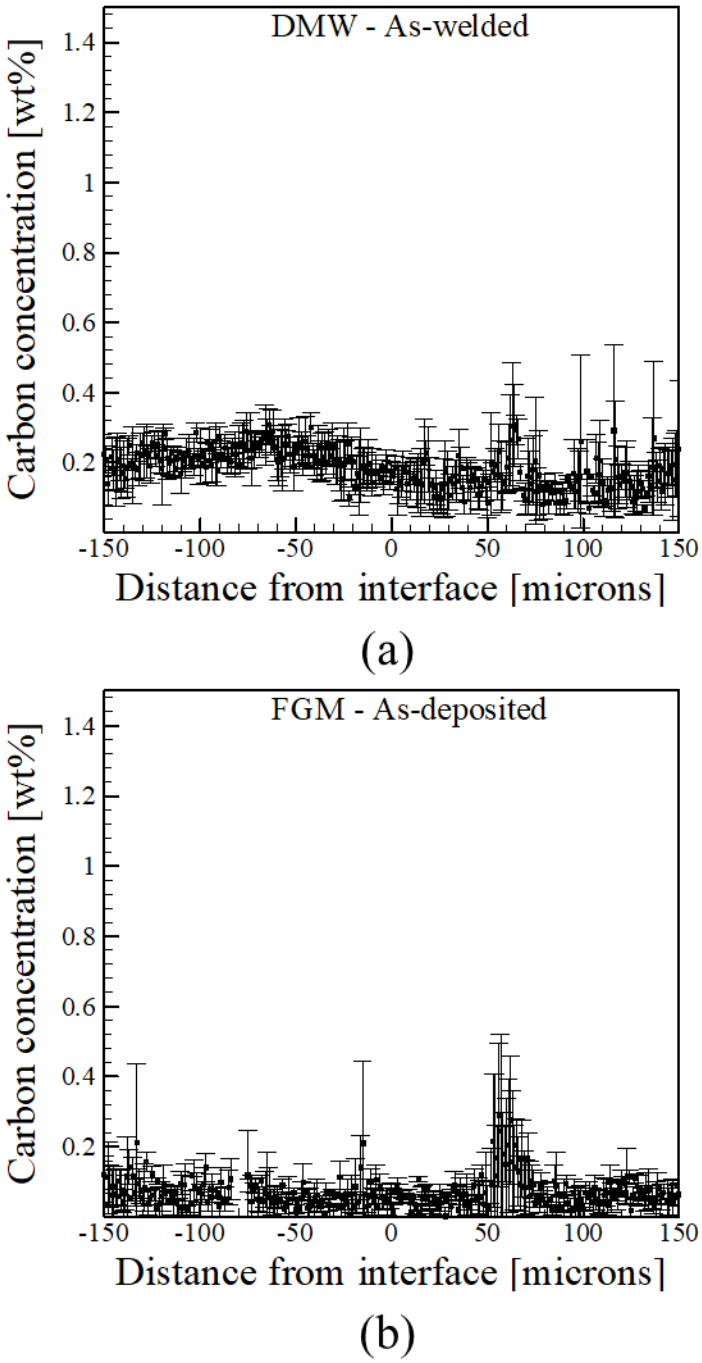

Figure 17. Measured carbon concentration profiles for (a) a DMW in the as-welded condition and (b) a FGM in the as-deposited condition. All negative distance correspond to the ferritic steel side of the interface.

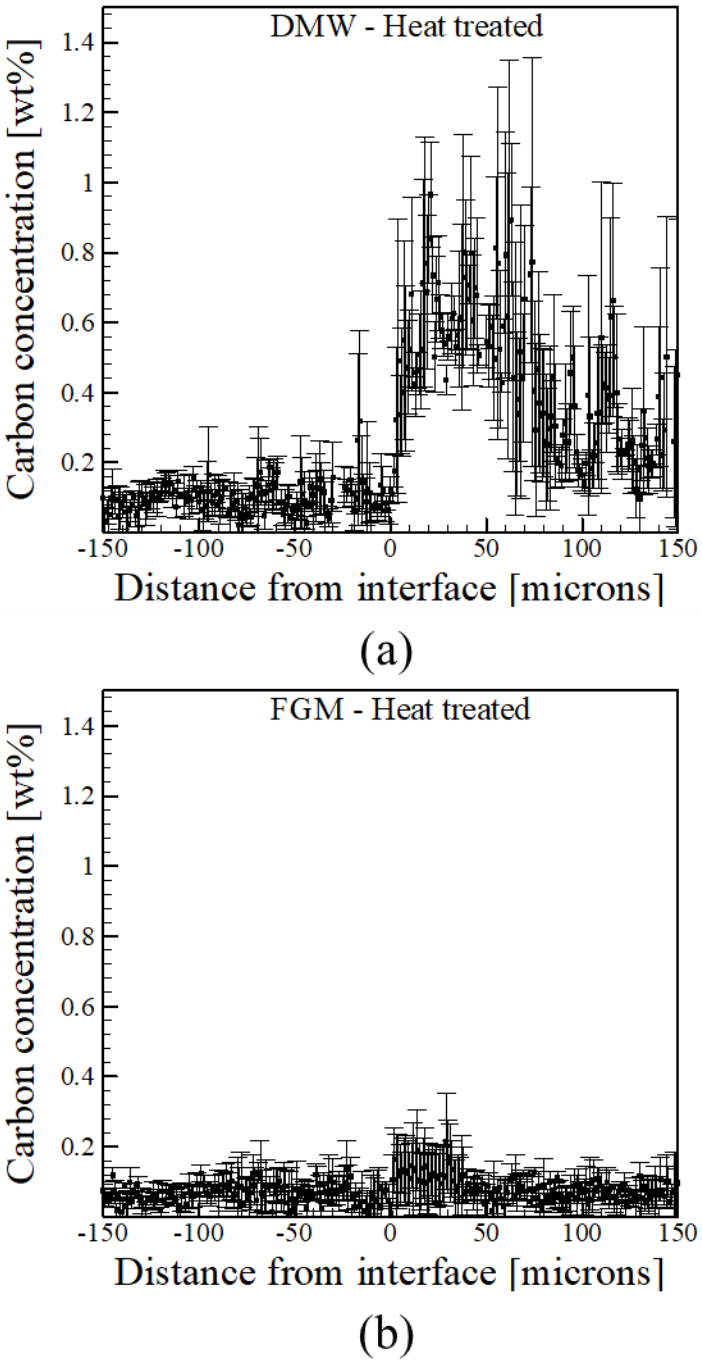

Figure 18. Measured carbon concentration profiles after heat treatment at 998 K for 235 h for (a) a DMW and (b) a FGM. All negative distance correspond to the ferritic steel side of the interface.

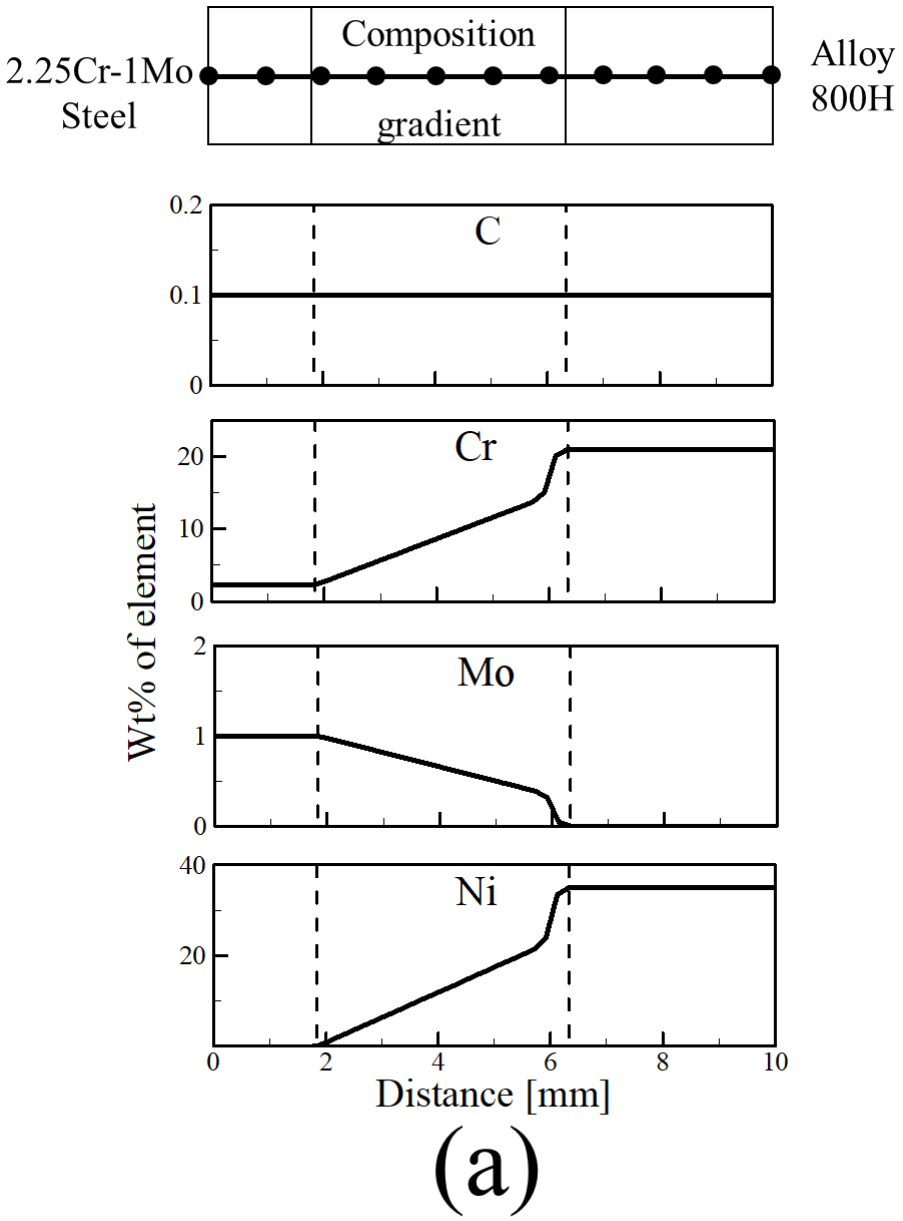
2.25Cr-1Mo
Steel
Composition
gradient
Alloy
800H
C
Cr
Mo
Ni
Wt% of element
Distance [mm]
0.2
0.1
0
20
10
2
1
40
20
0
2
4
6
8
10

(a)

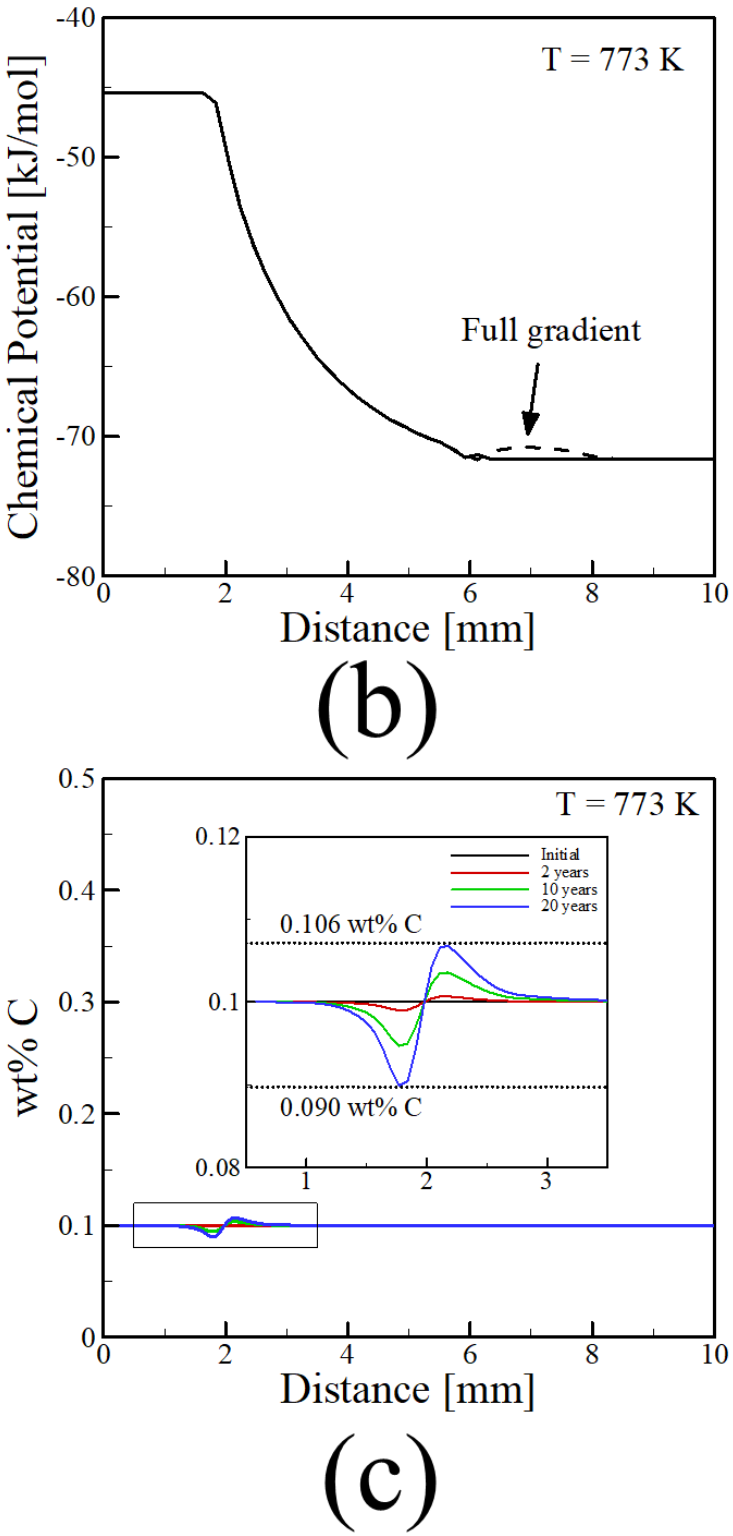

Fig. 19. The corresponding (a) compositional variations (b) carbon chemical potential and (c) carbon diffusion profiles where only a *partial* composition gradient from 10% to 70% 800H is used between 2.25Cr-1Mo steel and Alloy 800H

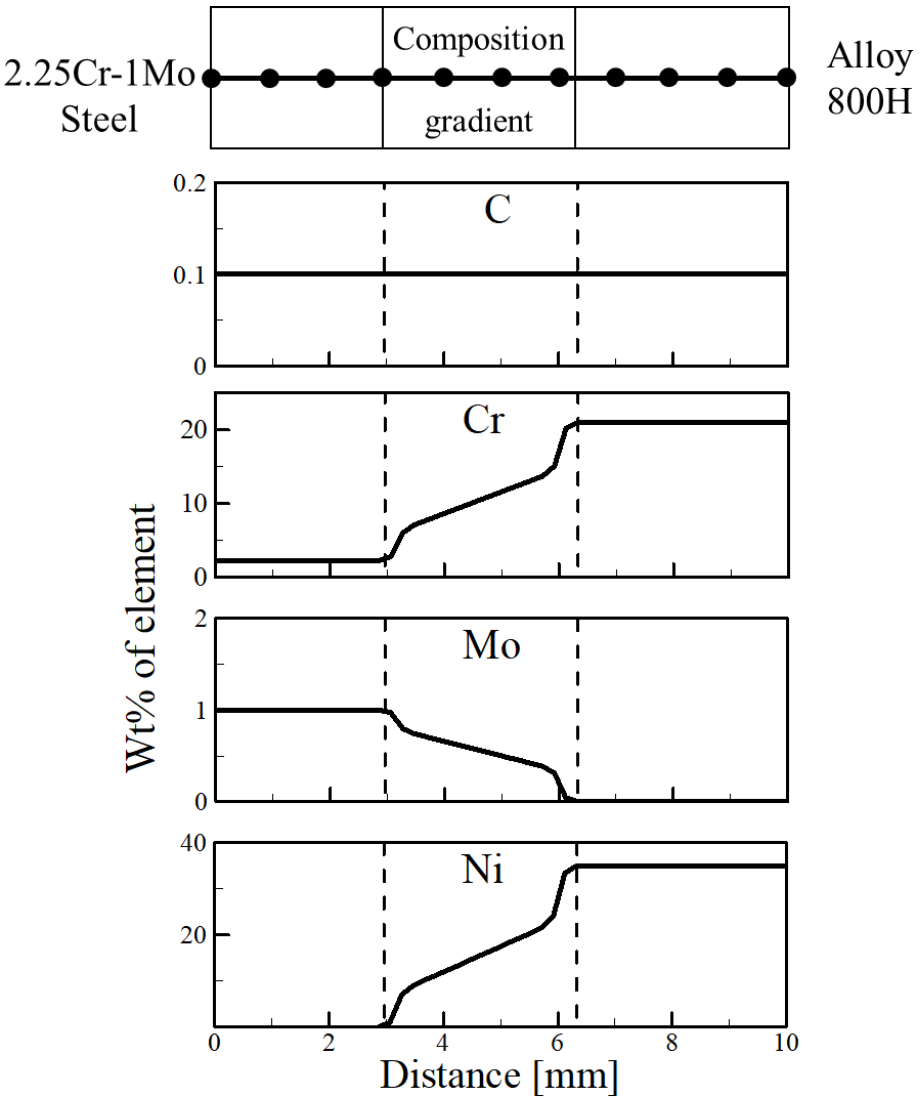
2.25Cr-1Mo
Steel
Composition
gradient
Alloy
800H
C
Cr
Mo
Ni
Wt% of element
Distance [mm]

(a)

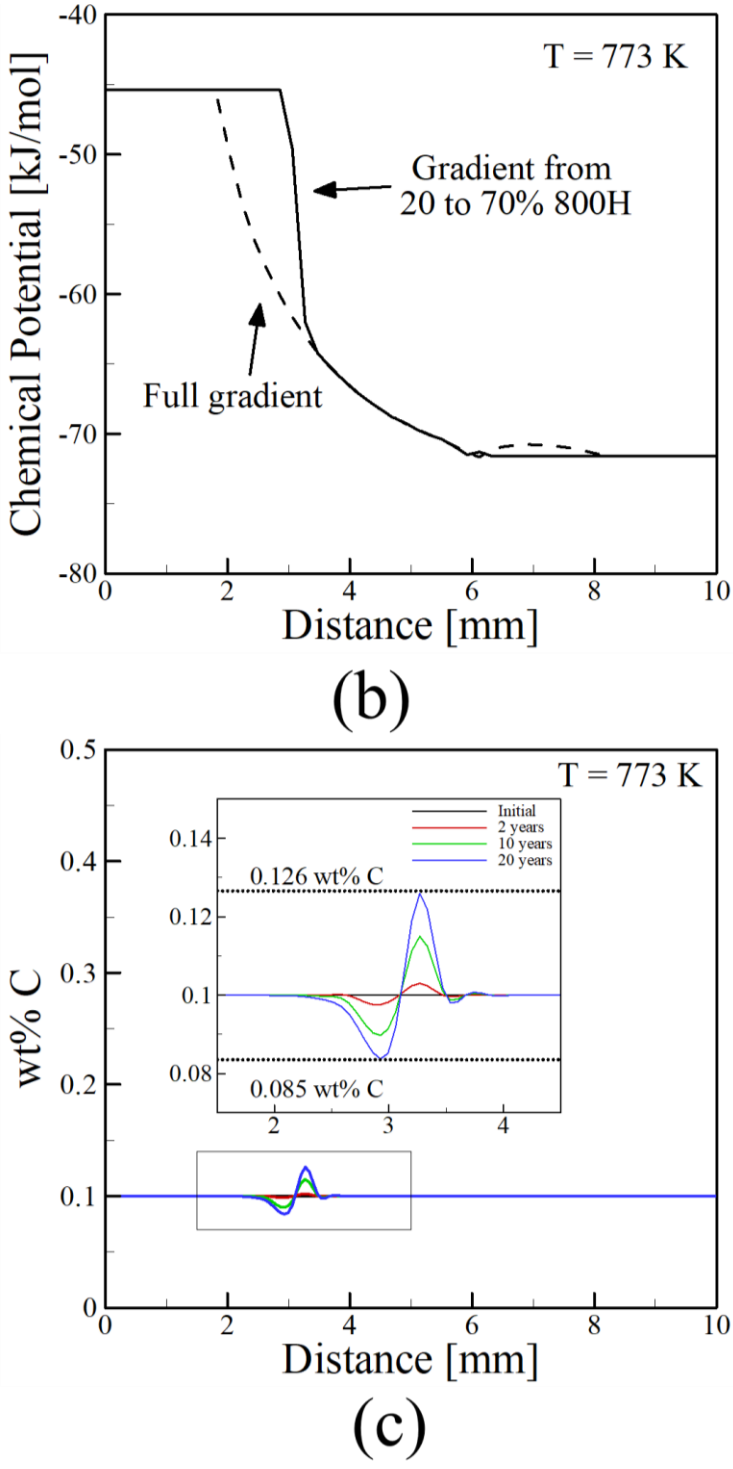

Fig. 20. The corresponding (a) compositional variations (b) carbon chemical potential and (c) carbon diffusion profiles where only a *partial* composition gradient from 20% to 70% 800H is used between 2.25Cr-1Mo steel and Alloy 800H

Table 1. Chemical compositions of powder used for deposition

	Wt% of element										
Powder	Al	Cr	Fe	Mn	Ni	Si	Ti	C	O	P	S
Pyromet® 800	0.38	21.0	Bal.	0.88	34.0	0.62	0.41	0.095	0.015	0.003	0.006
Fe	-	-	Bal.	-	-	-	-	0.005	-	-	0.016
Cr	<0.01	Bal.	0.07	-	-	<0.01	-	0.004	0.43	0.0013	0.023

Table 2. Carbides in equilibrium for different compositions at 773 K

Composition (% 800H)	Stable carbides	Equilibrium mass percent
10	$M_{23}C_6$	0.16
20	$M_{23}C_6$	0.15
30	MC + $M_{23}C_6$	0.10 + 0.14
40	MC + $M_{23}C_6$	0.15 + 0.13
50	MC + $M_{23}C_6$	0.24 + 0.069
60	MC + $M_{23}C_6$	0.29 + 0.077
70	$M_{23}C_6$	1.20
80	$M_{23}C_6$	1.36
90	$M_{23}C_6$	1.52
100	$M_{23}C_6$	1.68

Table 3. Comparison of average computed carbon diffusion fluxes and depletion in the ferritic steel at different service times at 773 K in dissimilar joints between 2.25Cr-1Mo steel and alloy 800H

Type of joint		2 years	5 years	10 years	20 years	50 years	100 years
DMW	Avg. Flux	1.97×10^{-13}	4.94×10^{-13}	9.87×10^{-13}	1.96×10^{-12}	1.52×10^{-12}	7.85×10^{-13}
	Depletion	2%	5%	10%	20%	25%	29%
FGM	Avg. Flux	1.57×10^{-14}	3.92×10^{-14}	7.85×10^{-14}	1.57×10^{-13}	3.92×10^{-13}	7.85×10^{-13}
	Depletion	0.12%	0.5%	0.9%	1.5%	2%	2.7%

Appendix C:

Residual stresses and distortion in additively manufactured compositionally graded and dissimilar joints

Computational Materials Science 143 (2018) 325–337

Contents lists available at ScienceDirect

Computational Materials Science

journal homepage: www.elsevier.com/locate/commatsci

Residual stresses and distortion in additively manufactured compositionally graded and dissimilar joints

T. Mukherjee [a], J.S. Zuback [a], W. Zhang [b], T. DebRoy [a,*]

[a] Department of Materials Science and Engineering, The Pennsylvania State University, University Park, PA 16801, United States
[b] Department of Materials Science and Engineering, The Ohio State University, Columbus, OH 43221, United States

ARTICLE INFO

Article history:
Received 19 October 2017
Received in revised form 11 November 2017
Accepted 13 November 2017

Keywords:
Additive manufacturing
3D printing
Transition joint
Thermo-mechanical modeling
Finite element analysis
Thermodynamic calculations

ABSTRACT

Additively manufactured compositionally graded joints are potentially attractive to minimize abrupt changes in residual stresses and distortion of dissimilar alloy joints. Performance of these graded joints depends on the residual stresses and distortion governed by the transient temperature field during additive manufacturing and local mechanical properties of the joint. Here we develop, validate and utilize a thermo-mechanical model to provide a definitive way to additively manufacture sound graded joints for minimizing abrupt changes in residual stresses and distortion of the dissimilar joints. This model calculates residual stresses and distortion from accurate temperature fields calculated using a well-tested heat transfer and fluid flow model and temperature dependent alloy properties estimated by thermodynamic calculations. Both graded and dissimilar joints of 2.25Cr-1Mo steel to alloy 800H and Ti-6Al-4V to 800H, fabricated using laser-assisted powder based direct energy deposition process are examined. It is found that the sharp changes in residual stresses in dissimilar joints between Ti-6Al-4V and 800H can be effectively minimized by fabricating a graded joint between them. Although the magnitudes of residual stresses in Ti-6Al-4V to 800H joint are higher than that in 2.25Cr-1Mo steel to 800H joint, the former is less susceptible to warping, buckling and delamination due to the high room temperature yield strength of the Ti-6Al-4V substrate.

1. Introduction

Dissimilar metal joints are used in aerospace, nuclear power generation, marine and automobile industries [1,2]. However, dissimilar joints often fail because of the distortion and high gradient of residual stresses generated due to the sharp changes in chemical composition and properties across the joint interface [2–5]. These difficulties can be minimized by the development of compositionally graded transition joints where the variations of chemical composition and properties occur smoothly across the joint over a large distance [6,7]. Additive manufacturing (AM) is a practical choice to fabricate compositionally graded transition joints by adding materials of varying compositions in a layer-by-layer manner [8–12]. AM has already been used to fabricate transition joints between stainless steels and nickel base superalloys for nuclear applications [10,11] and between titanium alloys and iron-nickel alloys for aerospace applications [12]. However, additively manufactured compositionally graded components also encounter residual stresses and distortion because of the spatially non-uniform and transient temperature field during the process. Depending on the local room temperature yield strength of the graded components, these residual stresses and distortion may result in premature fatigue failure, delamination, warping and buckling. Therefore, accurate estimations of residual stresses and distortion are necessary for both dissimilar and graded joints to fabricate sound compositionally graded components by AM for minimizing abrupt change in residual stresses and distortion of the dissimilar joints.

There are two main differences in residual stresses and distortion between compositionally graded and single alloy components. First, the evolution of residual stresses depends on the cooling process of the component at the end of the deposition. In graded components, the difference in the thermo-physical properties between the two end alloys governs the cooling process and thus the evolution of the residual stresses and distortion. Second, susceptibilities to warping, buckling and delamination depend not only on the magnitudes of the residual stresses but also on the local room temperature yield strength of the graded component. Since, the yield strength varies spatially in many compositionally graded components, two regions with the same magnitude of residual stresses

* Corresponding author.
E-mail address: debroy@psu.edu (T. DebRoy).

https://doi.org/10.1016/j.commatsci.2017.11.026
0927-0256/

can have different susceptibilities to delamination, buckling and warping.

Experimental measurements of residual stresses and distortion of AM components are time consuming and expensive [13]. These measurements also depend on sample preparation, shape and size of the components and accuracy of the experimental methods such as X-ray or neutron diffraction [14–16]. For both compositionally graded and dissimilar metal joints, use of non-destructive measurement techniques are restricted by the limited availability of strain free lattice spacing for all compositions [4,17]. A recourse is to calculate residual stresses and distortion in all locations of the component using numerical models. However, most of the existing numerical models of AM residual stresses neglect the convective flow of liquid metal inside the molten pool that often dominates the heat transfer during AM [18]. This simplification may result in inaccuracy in temperature field calculations, [19] and as a result, residual stresses and strain calculated based on such inaccurate temperatures can become unreliable [18]. Another difficulty in these calculations is the limited availability of the temperature dependent thermo-physical and mechanical properties data for different alloy compositions used in the graded components [20]. In the literature, thermodynamic calculations have been done to estimate the alloy properties for graded joints between titanium alloys, nickel base superalloys and steels [11,12]. However, so far the estimated properties have not been used to calculate residual stresses and distortion of the compositionally graded transition joints. Because of the challenges mentioned above, literature on the estimation of residual stresses and distortion of additively manufactured compositionally graded components is scarce.

Here, we calculate, for the first time, the residual stresses and distortion of compositionally graded joints as well as dissimilar joints of (a) 2.25Cr-1Mo steel to an iron-nickel alloy (800H) and (b) a titanium alloy (Ti-6Al-4V) to 800H, fabricated using laser assisted powder based direct energy deposition process. In these graded joints, alloy composition changes with layers along the build height direction. A thermo-mechanical model is used to calculate residual stresses and distortion from the transient temperature field accurately estimated using a heat transfer and fluid flow model that considers the effects of convective flow of liquid metal. The temperature and composition dependent thermo-physical and mechanical properties are estimated by thermodynamic calculations using a commercial program, JMatPro®. This program calculates different alloy properties for a specified temperature range based on the chemical composition of the alloy. The thermo-mechanical model is rigorously tested and validated against independent experimental data. The spatial variation of the residual stresses and distortion for the two types of graded joints is compared based on their alloy properties, transient temperature fields and molten pool dimensions. The relative advantages of fabricating graded joints over dissimilar joints for minimizing the abrupt changes in residual stresses and distortion are examined for the two types of joints.

2. Theoretical investigation

2.1. Modeling assumptions

The calculations of the residual stresses and distortion are performed in two steps. First, a well-tested three-dimensional heat transfer and fluid flow model [21–23] is used to calculate transient temperature fields. Second, based on the calculated temperature fields, residual stresses and distortion are predicted using a commercial finite element analysis (FEA) code, Abaqus® [24]. The following simplified assumptions are made in both the heat transfer and fluid flow model and the FEA mechanical model.

(1) Densities of the solid and liquid alloys are considered as temperature independent.
(2) The surfaces of the deposited layers are assumed to be flat.
(3) The effects of strains induced by solid-state phase transformation and creep are neglected to make the calculations tractable.
(4) Each layer is assigned to a pre-defined composition and the effect of dilution due to re-melting of the substrate or previous layers on the layer composition is not considered.

2.2. Thermodynamic calculations for alloy properties

Temperature and composition dependent thermo-physical and mechanical properties of alloys are needed for the heat transfer and fluid flow calculations as well as the finite element based mechanical model. During the fabrication of compositionally graded joints, the mixing of chemistries often leads to high alloying element concentrations. Local chemical compositions can extend into regions where experimental property data are not available and approximations such as simplified phase diagrams, stress-strain plots and dilute alloy properties are not applicable. An alternative for determining important material properties is through numerical modeling based on elemental mixing interactions. JMatPro® is a thermodynamic program designed for materials processing applications that models important alloy properties such as equilibrium phases, phase transformations, thermo-physical properties and mechanical behavior [25]. The CALculation of PHAse Diagrams (CALPHAD) method, which is widely established in the literature [26], is used to determine phase fractions and compositions for a given alloy concentration and temperature or temperature range.

The modeling of thermo-physical and mechanical properties using JMatPro® involves the following sequential steps. First, the equilibrium fraction of phases is determined through the minimization of the total Gibbs energy method using thermodynamic excess functions to account for the mixing of elements. The property, P, of interest for each phase is expressed as [27],

$$P = \sum_i x_i P_i^0 + \sum_i \sum_{j>1} x_i x_j \sum_v \Omega_{ij}^v (x_i - x_j)^v \quad (1)$$

where P_i^0 is the property of the phase in the pure element, Ω_{ij}^v is a binary interaction parameter between elements i and j dependent on an integer, v. x_i and x_j are the mole fractions of i and j in the phase, respectively. The effects of temperature on the property of a phase are taken into account through both P_i^0 and Ω_{ij}^v, which are function of temperature. The total property of the alloy is then determined from the phase fractions and properties of each phase using the general law of mixtures [28]. The use of this type of model allows for the approximation of both thermo-physical and mechanical properties as functions of composition and temperature and accounts for effects of multi-phase microstructure. The thermo-physical and mechanical properties of different alloy compositions are provided in Tables 1–5 and in Supplementary document.

2.3. Governing equations and boundary conditions

Detailed description of the thermo-mechanical model is available in a previous publication [18]. For completeness, a few salient features of the model are provided as follows. The heat transfer and fluid flow model solves the equations of conservation of mass, momentum and energy [29], as given below, respectively.

$$\frac{\partial (\rho u_i)}{\partial x_i} = 0 \quad (2)$$

Table 1
Thermo-physical properties of SS 410, 2.25Cr-1Mo steel, Ti-6Al-4V and 800H. Here 'T' represents temperature in K.

Properties	SS 410	2.25Cr-1Mo steel	Ti-6Al-4V	800H
Liquidus temperature (K)	1749	1787	1928	1675
Solidus temperature (K)	1640	1740	1878	1608
Thermal conductivity (W/m K)	14.0 + 0.0125 T	11.82 + 0.0106 T	$1.57 + 0.016\ T - 1 \times 10^{-6}\ T^2$	8.54 + 0.0167 T
Specific heat (J/kg K)	$447.2 + 0.041\ T - 4.18 \times 10^{-6}\ T^2$	461.4 + 0.1338 T	$492.4 + 0.025\ T - 4.18 \times 10^{-6}\ T^2$	309.2 + 0.5104 T
Density (kg/m^3)	7160	7270	4000	7870
dγ/dT (N/m K)	-0.40×10^{-3}	-0.44×10^{-3}	-0.26×10^{-3}	-0.24×10^{-3}

Table 2
Temperature dependent mechanical properties of SS 410 in annealed condition.

Temperature (K)	Young's modulus (GPa)	Temperature (K)	Volumetric expansion co-efficient (/K)	Temperature (K)	Yield stress (MPa)
300	191.2	300	21.93E−06	300	284.0
400	183.6	400	22.07E−06	700	164.0
500	175.9	500	22.21E−06	1100	150.0
600	168.1	600	22.37E−06	1300	77.2
700	160.1	700	22.53E−06	1500	22.3
800	152.0	800	22.70E−06		
900	143.8	900	22.88E−06		
1000	135.5	1000	23.07E−06		
1100	127.0	1100	23.27E−06		
1200	118.1	1200	23.53E−06		
1300	108.4	1300	23.94E−06		
1400	99.7	1400	24.14E−06		
1500	89.6	1500	24.50E−06		
1640	59.5	1640	25.52E−06		

Table 3
Temperature dependent mechanical properties of 2.25Cr-1Mo steel.

Temperature (K)	Young's modulus (GPa)	Temperature (K)	Volumetric expansion co-efficient (/K)	Temperature (K)	Yield stress (MPa)
300	211.3	300	12.39E−06	300	312.5
400	206.4	400	12.76E−06	700	156.9
500	200.0	500	13.12E−06	1100	88.1
600	191.5	600	13.49E−06	1300	57.7
700	181.0	700	13.85E−06	1500	42.4
800	168.8	800	14.22E−06		
900	155.2	900	14.59E−06		
1000	140.4	1000	14.98E−06		
1100	124.2	1500	15.22E−06		
1200	109.1	1600	16.01E−06		
1300	98.3	1700	17.13E−06		
1400	81.36				
1500	61.31				
1600	34.12				
1700	8.79				

Table 4
Temperature dependent mechanical properties of Ti-6Al-4V.

Temperature (K)	Young's modulus (GPa)	Temperature (K)	Volumetric expansion co-efficient (/K)	Temperature (K)	Yield stress (MPa)
300	125	300	8.78E−06	300	955
533	110	533	9.83E−06	573	836
589	100	589	10.0E−06	773	732
700	93	700	10.7E−06	1023	581
755	80	755	11.1E−06	1073	547
811	74	811	11.2E−06	1173	480
923	55	923	11.7E−06	1273	405
1073	27	1073	12.2E−06	1373	330
1098	22	1098	12.3E−06		
1123	18	1123	12.4E−06		
1573	12	1573	13.0E−06		
1873	9	1873	16.3E−06		

$$\frac{\partial(\rho u_j)}{\partial t} + \frac{\partial(\rho u_j u_i)}{\partial x_i} = \frac{\partial}{\partial x_i}\left(\mu \frac{\partial u_j}{\partial x_i}\right) + S_j \quad (3)$$

$$\rho \frac{\partial h}{\partial t} + \frac{\partial(\rho u_i h)}{\partial x_i} = \frac{\partial}{\partial x_i}\left(\frac{k}{C_p}\frac{\partial h}{\partial x_i}\right) - \rho \frac{\partial \Delta H}{\partial t} - \rho \frac{\partial(u_i \Delta H)}{\partial x_i} \quad (4)$$

where ρ is the density, u_i and u_j are the velocity components along the i and j directions, respectively, and x_i is the distance along the i direction, t is the time, μ is the effective viscosity, and S_j is a source term for the momentum equation. h is the sensible heat, C_p is the specific heat, k is the thermal conductivity, and ΔH is the latent heat content.

Table 5
Temperature dependent mechanical properties of 800H.

Temperature (K)	Young's modulus (GPa)	Temperature (K)	Volumetric expansion co-efficient (/K)	Temperature (K)	Yield stress (MPa)
300	200.7	300	15.68E−06	300	272.3
400	194.5	400	16.01E−06	500	157.7
500	188.0	500	16.34E−06	700	139.3
600	181.3	600	16.68E−06	1500	50.8
700	174.4	700	17.02E−06		
800	167.3	800	17.35E−06		
900	158.8	900	17.71E−06		
1000	148.4	1000	18.18E−06		
1100	139.1	1100	19.10E−06		
1200	131.2	1200	19.47E−06		
1300	113.1	1300	19.85E−06		
1400	94.7	1400	20.24E−06		
1500	76.0	1500	20.65E−06		
1600	37.1	1600	21.05E−06		

The Abaqus® based finite element analysis (FEA) code solves the constitutive equations for elastic, plastic and thermal strains where the total strain increment ($\Delta\varepsilon_{lm}^{tot}$) with respect to time is represented as,

$$\Delta\varepsilon_{lm}^{tot} = \Delta\varepsilon_{lm}^{E} + \Delta\varepsilon_{lm}^{P} + \Delta\varepsilon_{lm}^{Th} + \Delta\varepsilon_{lm}^{V} \quad (5)$$

where $\Delta\varepsilon_{lm}^{E}$, $\Delta\varepsilon_{lm}^{P}$ and $\Delta\varepsilon_{lm}^{Th}$ are the elastic, plastic and thermal strain increments respectively. $\Delta\varepsilon_{lm}^{V}$ is the strain induced due to the solid state phase transformation and creep, which is assumed to be zero in the present model [18].

Convective and radiative heat losses to the surroundings [21,22] are applied on the walls of the deposit and the substrate as boundary conditions in heat transfer and fluid flow model. Liquid metal convection inside the molten pool driven by the spatial gradient of surface tension due to the temperature gradient on the top surface of the pool, known as Marangoni convection [23,30,31], governs the temperature distribution. To consider this effect in the calculation, Marangoni shear stress (τ) is applied as a boundary condition to calculate the velocities of the molten metal and is expressed as [30]:

$$\tau = \frac{d\gamma}{dT}\frac{dT}{dr} = \mu\frac{du}{dz} \quad (6)$$

where T is the temperature, u is velocity of the liquid metal on the top surface of the molten pool, γ is the surface tension, μ is the viscosity and r is the radial distance from the axis of the heat source. The boundary conditions for the FEA mechanical model include fixed bottom surface, i.e., the displacements of all nodes of the bottom surface along the x, y and z directions are zero.

2.4. Algorithm of the thermo-mechanical model

A Python script is utilized to export the mesh and the transient temperature fields from the heat transfer and fluid flow model to the Abaqus-based FEA model. This script creates a database file containing the nodes, elements and transient temperature fields using the Abaqus Scripting Interface. This database file is imported to the FEA mechanical model to calculate residual stresses, strain and distortion incorporating the temperature dependent mechanical properties estimated using JMatPro®. The detailed algorithm of the thermo-mechanical model is summarized in Fig. 1.

2.5. Utilization of the model for graded and dissimilar joints

In this research, two types of graded joints are considered, 2.25Cr-1Mo steel to 800H joint and Ti-6Al-4V to 800H joint. Substrates for these two graded joints are 2.25Cr-1Mo steel and

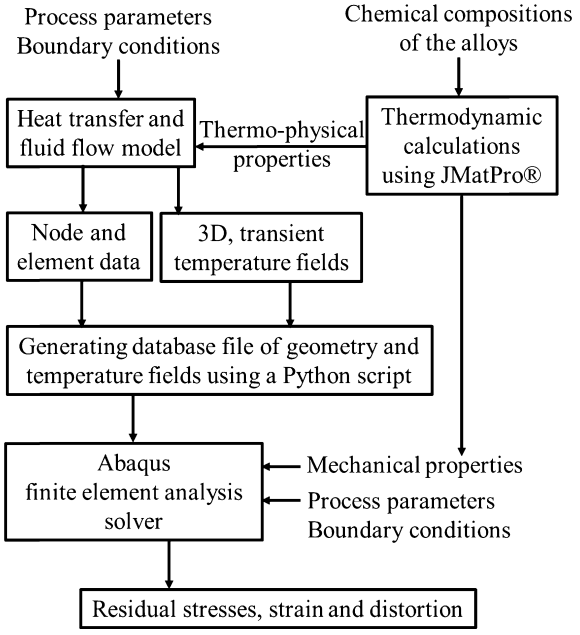

Fig. 1. Outline of the thermo-mechanical model combining the heat transfer and fluid flow model with the FEA mechanical model.

Ti-6Al-4V, respectively. For both joints, the 10th layer is made by 100% alloy 800H. From the 1st layer to the 9th layer, the composition is changed linearly with an increment of 10 wt% of 800H. For instance, the composition of the 1st layer is 10% 800H and 90% Ti-6Al-4V or 2.25Cr-1Mo steel and composition of the 9th layer is 90% 800H and 10% Ti-6Al-4V or 2.25Cr-1Mo steel. For the dissimilar joints, substrate and layer 1 to layer 5 are made of Ti-6Al-4V or 2.25Cr-1Mo steel and 6th to 10th layer are made of 800H. Therefore, sharp change in composition occurs at the interface of 5th and 6th layer of the dissimilar joints. Schematic representations of both graded and dissimilar joints are given in Fig. 2. For the purpose of model validation, a build-up of 10 layer, single pass wall made of entirely stainless steel 410 (SS 410) is also studied.

Fig. 3 represents the solution domain, and the detailed dimensions are provided in Table 6. Half of the solution domain is considered by taking advantage of the y-symmetry. The laser beam travels along the positive x-axis. The component is built vertically upward along the positive z-axis with the deposition of 10 layers. The residual stress along x-direction (σ_x) is referred as longitudinal stress and is primarily responsible for crack propagation, buckling and warping [18]. The through-thickness

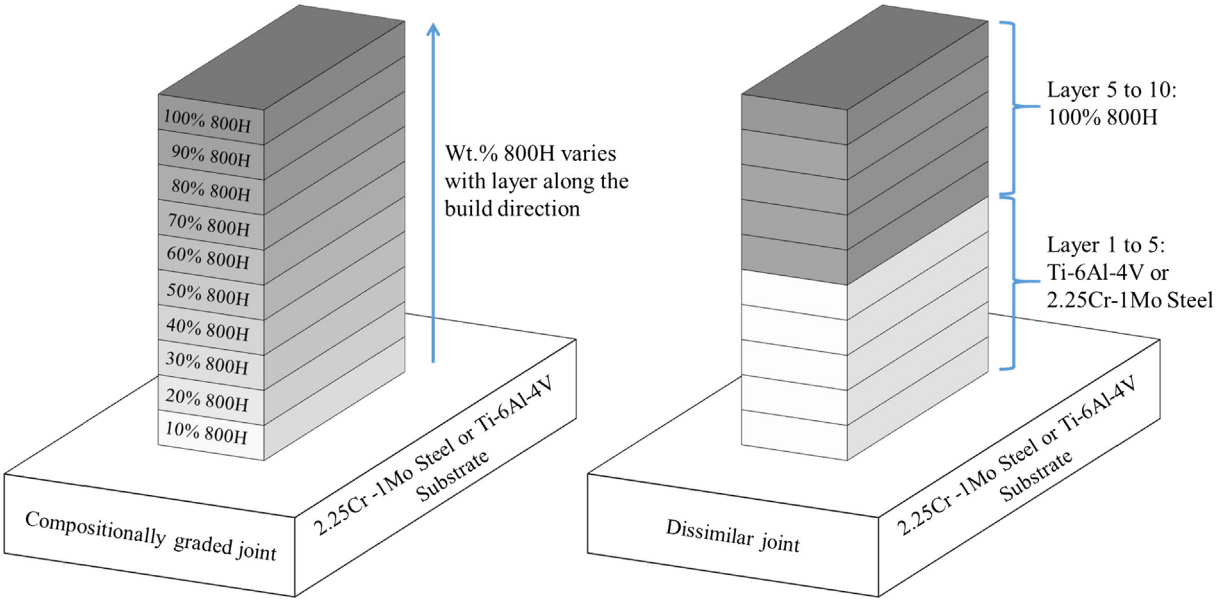

Fig. 2. Schematic representation of the compositionally graded and the dissimilar joints fabricated using additive manufacturing.

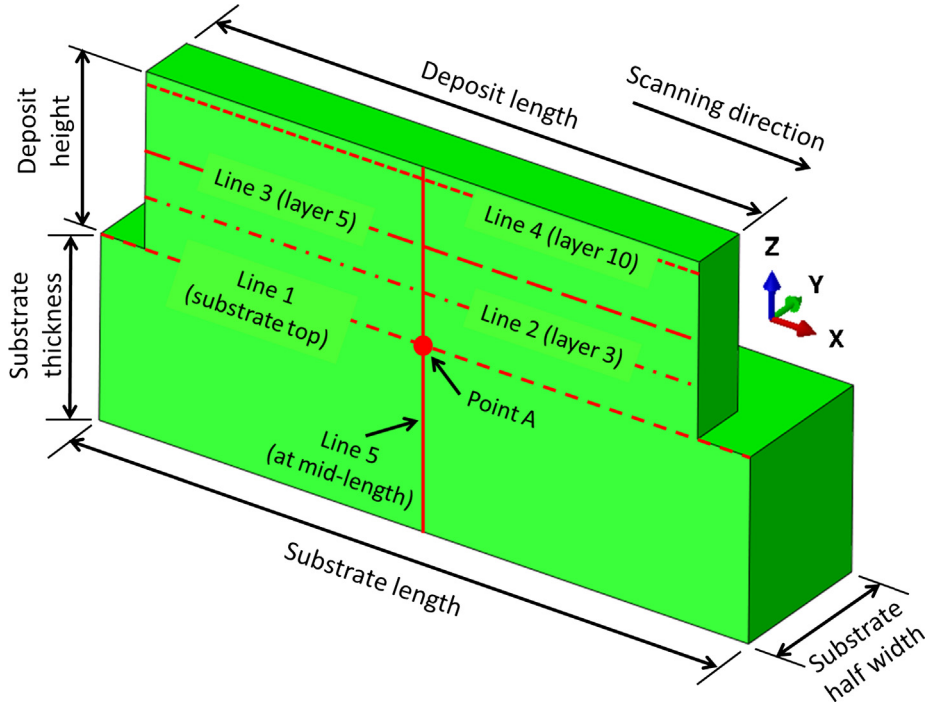

Fig. 3. Solution domain for the heat transfer and fluid flow calculations and the subsequent mechanical analysis. Due to the y-symmetry, a half of the solution domain is considered to reduce time and computer memory requirements for the analysis. The five lines along which residual stress values are surveyed and the one point at which temperature variation with time is monitored are shown. The values of the dimensions are provided in Table 6.

Table 6
Process parameters used for calculations.

Parameter set	Laser power (W)	Scanning speed (mm/s)	Powder flow rate (gm/s)	Deposit height (mm)	Deposit length (mm)	Substrate dimension (mm)
1	300, 600	2.5, 4.2	0.358	5	10	$10 \times 4 \times 1$
2	300	10	0.432	3.8	12	$14 \times 5 \times 4$

residual stress along z-direction (σ_z) may cause delamination and detachment of the component from the substrate [18]. Residual stress and strain distributions are spatially non-uniform depending on the local material properties. To capture this non-uniformity, residual stress distributions are plotted along five lines shown in Fig. 3.

3. Results and discussions

3.1. Model validation

Fig. 4 shows fair agreements between the calculated through-thickness residual stresses (σ_z) and the corresponding experimentally measured values [32] for a 10 layer laser-assisted SS 410 deposit. Fig. 4(a) and (b) shows the through-thickness residual stresses along 'line 2' (in Fig. 3) for two different scanning speeds and 300 W laser power. Through-thickness residual stresses along the 'line 5' (in Fig. 3) are plotted for two different scanning speeds and 600 W laser power in Fig. 4(c) and (d). Several measurements were taken to estimate the error bars as shown in Fig. 4. The slight mismatch between the experimental and calculated values could be caused by both the measurement difficulties and the assumptions used in numerical calculations. Validity of the numerical model provides us the confidence to apply the model for compositionally graded transition joints.

3.2. Temperature and velocity distributions in graded joints

Fig. 5 shows the temperature and velocity fields when the laser beam is at the mid-length of the deposit during the deposition of 1st, 5th and 10th layers. Fig. 5(a)–(c) and (d)–(f) are for 2.25Cr-1Mo steel to 800H joint and Ti-6Al-4V to 800H joint, respectively. The zones marked by red color and bounded by the liquidus temperature isotherm of the corresponding alloy, represent the fusion zone. The length of the fusion zones (molten pool length) are mentioned in the figures. The arrows shown in the figures represent the velocity vectors of the liquid metal inside the molten pool. The magnitude of the velocities can be read by comparing the length of these arrows with the length of the reference vector provided. In AM, most of the heat is transferred downwards through the substrate [33]. Therefore, during the deposition of the upper layers, heat transfer from the molten pool through the substrate decreases [33]. That results in larger molten pool for upper layers in 2.25Cr-1Mo steel to 800H joint as shown in Fig. 5(a)–(c). However, in Ti-6Al-4V to 800H joint, the density of 800H is almost twice than that of Ti-6Al-4V (see Table 1). Therefore, under the same processing conditions, Ti-6Al-4V exhibits larger molten pool than 800 H. Therefore, in Ti-6Al-4V to 800H joint, the molten pool size is decided by trading off two opposing factors, (1) reduction in pool size for upper layers due to increasing density from Ti-6Al-4V to 800H and (2) increase in pool size for upper layers due to reduced heat transfer through the substrate. As a result, the molten pool size does not change significantly as shown in Fig. 5(d)–(f).

3.3. Residual stresses and distortion in graded joints

These spatially non-uniform temperature and velocity fields, shown in Fig. 5, result in thermal distortion. For quantitative understanding of thermal distortion, we have recently proposed [34,35] a strain parameter (ε^*) as an indicator of the susceptibility to distortion.

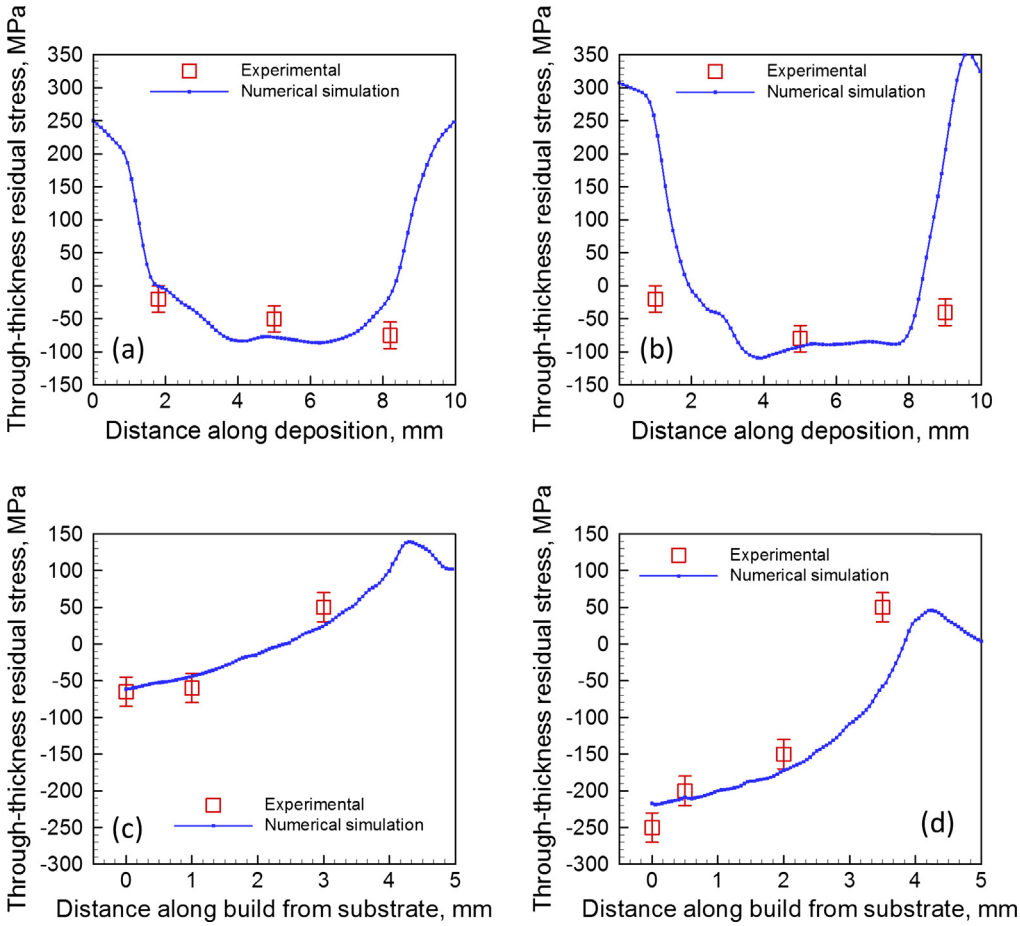

Fig. 4. Comparison between experimentally measured [32] and numerically computed through-thickness residual stress profiles for a 10 layers SS 410 deposit along deposition/travel direction (along line 2) using a laser power of 300 W and scanning speed of (a) 2.5 and (b) 4.2 mm/s and along build direction (along line 5) using a laser power of 600 W and scanning speed of (c) 2.5 and (d) 4.2 mm/s. Other process conditions are given as process parameter set 1 in Table 6.

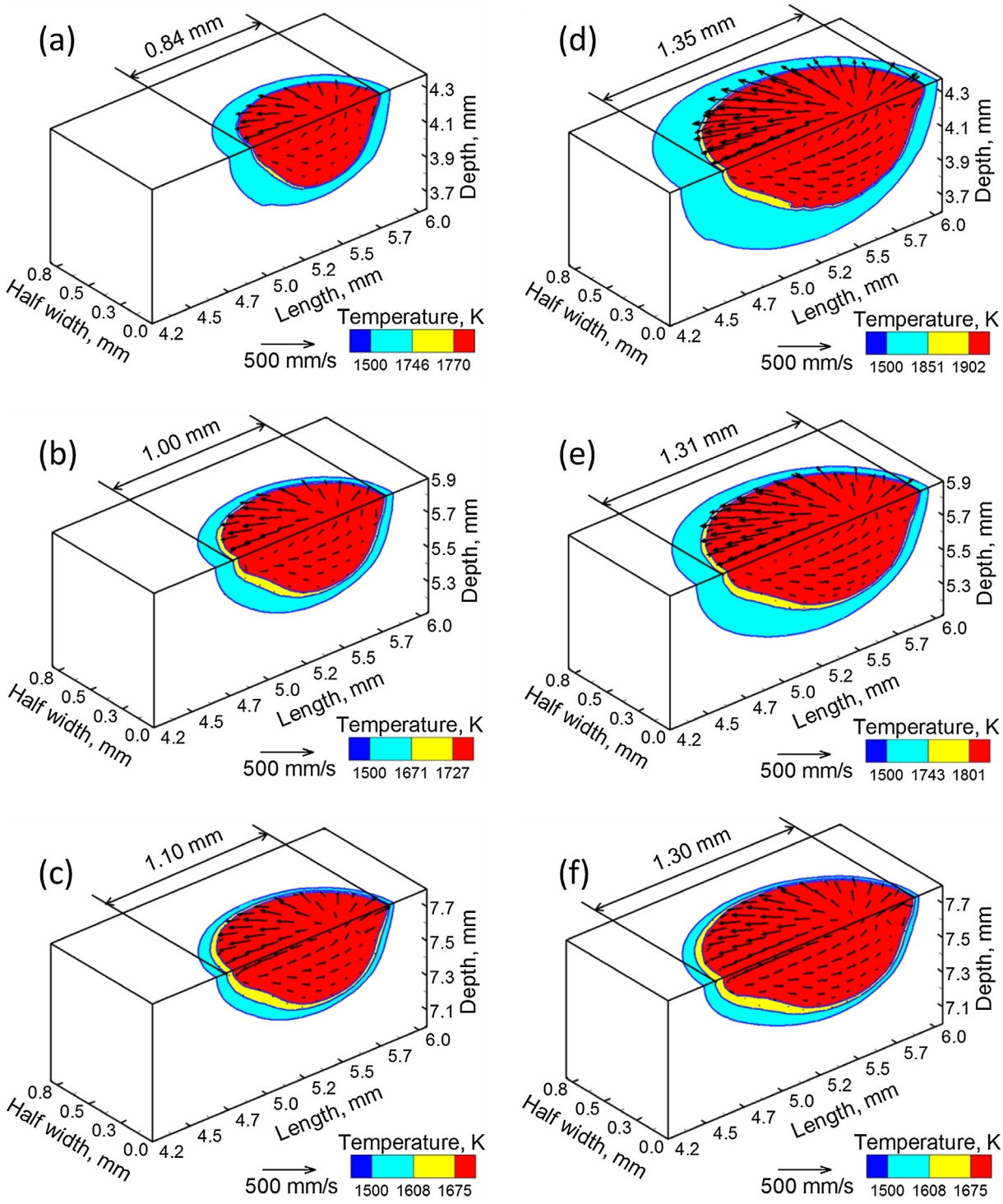

Fig. 5. Temperature and velocity distributions for 2.25Cr-1Mo steel to 800H joint during the deposition of (a) 1st (b) 5th and (c) 10th layer and for Ti-6Al-4V to 800H joint during the deposition of (d) 1st (e) 5th and (f) 10th layer using process parameter set 2 in Table 6.

$$\varepsilon^* = \frac{\beta \Delta T}{EI} \frac{t\, H^{3/2}}{F_o \sqrt{\rho}} \tag{7}$$

where β and ρ are the volumetric coefficient of thermal expansion and density of the alloy, respectively. ΔT is the maximum rise in temperature during the process, t is the characteristic time and H is the heat input per unit length. E and I are the elastic modulus and moment of inertia of the substrate, the product, EI, is the flexural rigidity of the structure. The Fourier number, F_o is the ratio of heat dissipation rate to heat storage rate [33]. The Fourier number and the maximum temperature rise are calculated using the heat transfer and fluid flow model. In 2.25Cr-1Mo steel to 800H joint, pool size increases with layers, as shown in Fig. 5(a)–(c). A large molten pool shrinks more during solidification and results in higher distortion. Therefore, in 2.25Cr-1Mo steel to 800H joint, the strain parameter, a measure of the peak thermal strain, increases with layers as shown in Fig. 6. In Ti-6Al-4V to 800H joint, the molten pool size does not change significantly with layers, as shown in Fig. 5

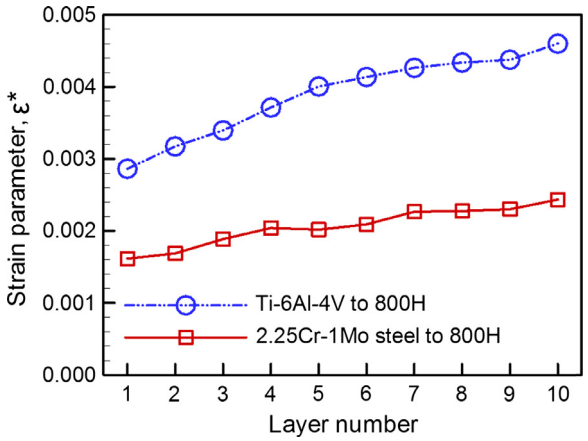

Fig. 6. Variation of strain parameter with number of layer for both 2.25Cr-1Mo steel to 800H and Ti-6Al-4V to 800H joints for the process parameter set 2 in Table 6.

(d)–(f). However, the volumetric thermal expansion coefficient of 800H is almost twice of that of Ti-6Al-4V. Therefore, also in Ti-6Al-4V to 800H joint, the strain parameter increases with layers, as shown in Fig. 6.

Fig. 7 shows the longitudinal stress distribution at the end of 2nd and 10th layer depositions. Longitudinal stress is the component of the residual stress along the scanning direction (x-direction). The positive and the negative values of the stresses in the figures represent the tensile and the compressive residual stresses, respectively. Two important observations can be made from these figures.

1. Magnitudes of the residual stresses vary with the progress of the deposition process. For example, at the end of the deposition of the 2nd layer, the highest magnitude of the longitudinal residual stress is observed near the 2nd layer (see Fig. 7 (a) and (b)). However, with the progress of the deposition process this high residual stress near the 2nd layer is partially alleviated.
2. The residual stresses are spatially non-uniform depending on the varying material properties of the graded joints. For example, Fig. 7(c) and (d) show that after deposition of all 10 layers, the maximum value of the longitudinal stress is near the top of the deposit for both types of joints. However, in Ti-6Al-4V to 800H joint, a high accumulation of tensile residual stress is also observed near the substrate deposit interface.

Figs. 8 and 9 provide detailed explanations of these two observations, respectively. During AM, the previously deposited layers experience reheating and cooling during the deposition of upper layers [21]. Fig. 8(a) and (b) shows the temperature variation with time at Point A (at mid-length of line 1, see Fig. 3) during the fabrication of 2.25Cr-1Mo to 800H joint and Ti-6Al-4V to 800H joint, respectively. Ti-6Al-4V substrate has lower thermal conductivity than 2.25Cr-1Mo steel substrate (Table 1). Therefore, in Ti-6Al-4V to 800H joint, less heat can be transferred through the Ti-6Al-4V substrate. That is why the peak temperatures monitored in Fig. 8 (b) are higher than those in Fig. 8(a) for the same layer. This repetitive heating and cooling partially alleviate the residual stresses for both types of the joints. Fig. 8(c) and (d) shows the longitudinal stress distribution along line 1 (see Fig. 3) after the deposition of 1st, 3rd, 6th and 10th layers, for 2.25Cr-1Mo to 800H joint and Ti-6Al-4V to 800H joint, respectively. For both types of the joints, the magnitude of the residual stress near the center along line 1

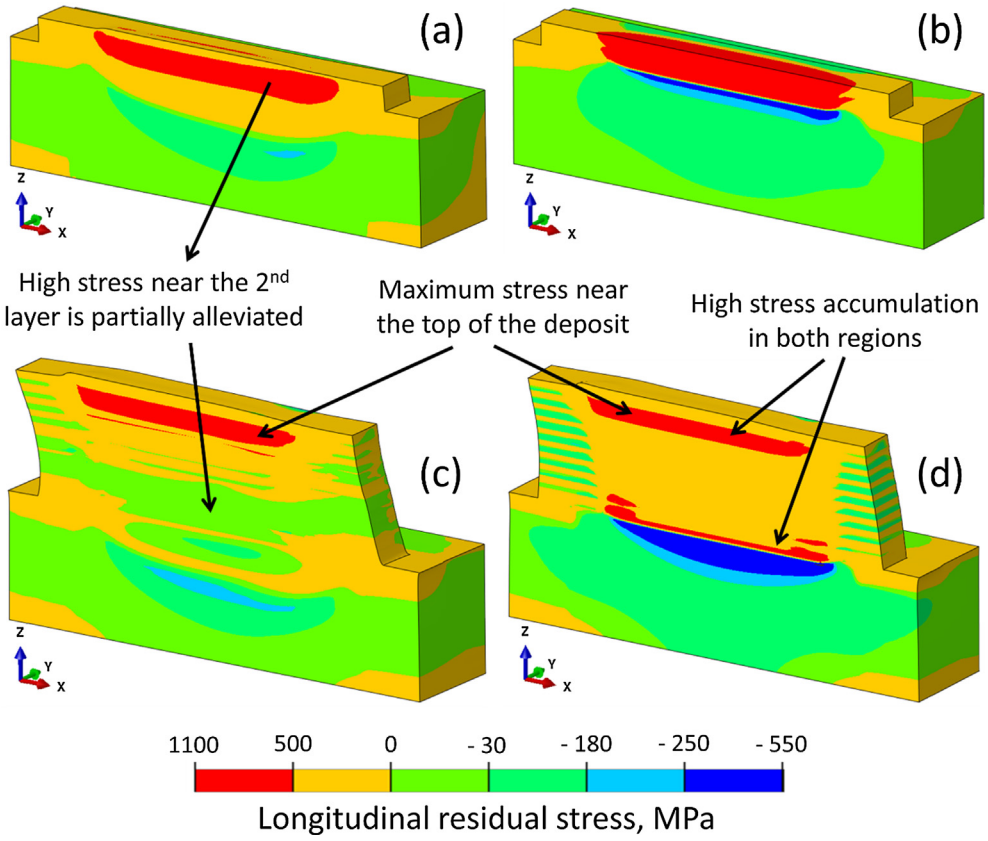

Fig. 7. Longitudinal residual stress (σ_x) distribution at the end of 2nd layer for (a) 2.25Cr-1Mo steel to 800H and (b) Ti-6Al-4V to 800H joints and at the end of 10th layer for (c) 2.25Cr-1Mo steel to 800H and (d) Ti-6Al-4V to 800H joints using process parameter set 2 in Table 6. Scanning direction is along the positive x-axis.

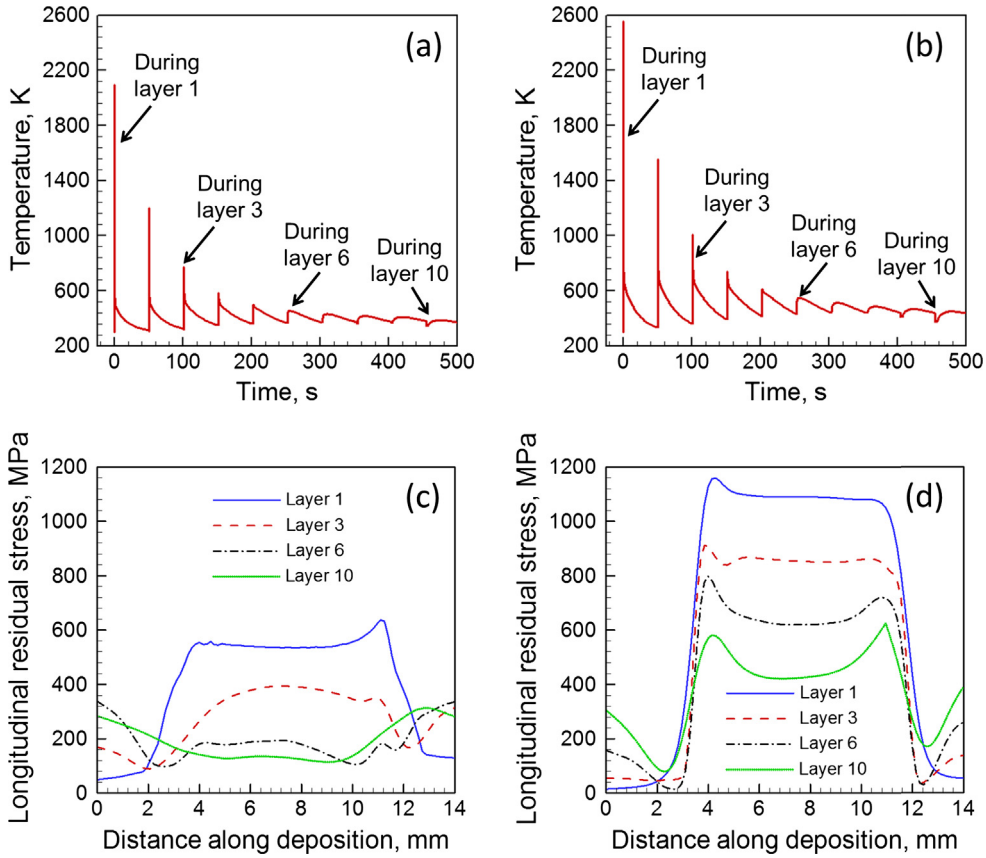

Fig. 8. Variation of the temperature with time monitored at 'point A' (Fig. 3) for (a) 2.25Cr-1Mo steel to 800H and (b) Ti-6Al-4V to 800H joints. Longitudinal residual stress distribution along 'line 1' (Fig. 3) for (c) 2.25Cr-1Mo steel to 800H and (d) Ti-6Al-4V to 800H joints after the deposition of 1st, 3rd, 6th and 10th layer. All results are for the process parameter set 2 in Table 6.

(shown in Fig. 3) decreases with the progress of the deposition process due to the repetitive heating and cooling. However, longitudinal residual stress along line 1 in Ti-6Al-4V to 800 H joint is always higher than that in 2.25Cr-1Mo to 800H joint, due to higher room temperature yield strength and lower thermal expansion coefficient of Ti-6Al-4V substrate compared to those of 2.25Cr-1Mo steel substrate.

In a compositionally graded joint, the residual stresses are spatially non-uniform depending on the local thermo-physical and mechanical properties. Fig. 9(a) and (b) represent the longitudinal residual stress distributions along three lines (line 1, 3 and 4 shown in Fig. 3) for 2.25Cr-1Mo to 800H joint and Ti-6Al-4V to 800H joint, respectively. For 'line 1', only the residual stress along the length of the deposit (12 mm) is plotted to compare the stress profiles inside the deposit. These residual stresses are plotted at the end of the deposition of the 10th layer when the part cools down to the room temperature. 'Line 4' is near the top free end of the wall and cools down to room temperature at the very end. That is why the residual stress along 'line 4' is the highest. Magnitude of the residual stress decreases with the distance from the free end (i.e. moving toward substrate). That is why longitudinal stresses along 'line 1' and 'line 3' are less than that along 'line 4'. However, in Ti-6Al-4V to 800H joint (Fig. 9b), room temperature yield strength near 'line 1' is significantly higher than that along 'line 3' (see Supplementary document for material properties). Therefore, longitudinal stress along 'line 1' is higher than that along 'line 3', as shown in Fig. 9(b). Because of that, in Ti-6Al-4V to 800H joint, large longitudinal residual stresses accumulate both near the top free end (line 4) as well as at the substrate deposit interface (line 1), as shown in Fig. 7(d).

Susceptibility to warping, buckling and delamination depends not only on the magnitude of the residual stresses but also the local room temperature yield strength of the graded joint [18]. Therefore, a normalized residual stress expressed as the ratio of the longitudinal residual stress to the local room temperature yield strength is used for assessment of such problems [18,36]. For 2.25Cr-1Mo to 800H joint (Fig. 9(c)), the normalized residual stresses follow the similar distribution as the longitudinal residual stress (Fig. 9(a)) since the room temperature yield strength does not change significantly along the height of the joint (see Supplementary document for material properties). However, for the Ti-6Al-4V to 800H joint (Fig. 9(d)), due to the higher room temperature yield strength near 'line 1' than that near 'line 3', the values of normalized stresses along 'line 1' and 'line 3' are nearly identical. Therefore, even if the magnitude of the residual stress along 'line 1' is higher than that along 'line 3', the susceptibilities to warping and delamination along these two lines are similar.

Fig. 10 shows the three-dimensional distribution of through-thickness component (along the build direction, σ_z, shown in Fig. 3) of the residual stress for the two types of the graded joints after the deposition of 2nd layer (Fig. 10(a) and (b)) and 10th layer (Fig. 10(c) and (d)). At the end of the deposition process, the top free end of the deposit cools down to the room temperature at the very end. Because of that, tensile stress accumulates near the top free end. That results in the accumulation of large compressive stress near the substrate-deposit interface. The magnitude of the compressive stress at the substrate-deposit interface is maximum at the mid-length of the deposit and the stress quickly transitions into high tensile stress at the two ends. This non-uniformity may result in detachment of the component from the substrate [18].

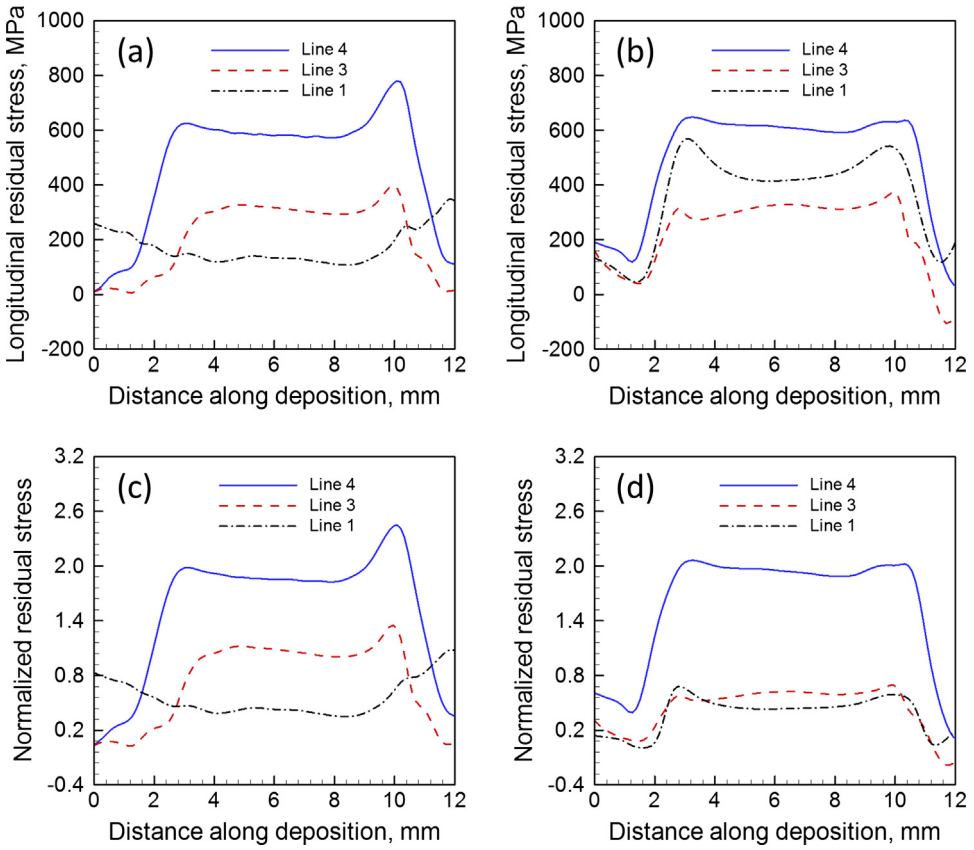

Fig. 9. Longitudinal residual stress distributions for (a) 2.25Cr-1Mo steel to 800H and (b) Ti-6Al-4V to 800H joints and normalized residual stress distributions for (c) 2.25Cr-1Mo steel to 800H and (d) Ti-6Al-4V to 800H joints along 'line 1', 'line 3' and 'line 4' (Fig. 3) at the end of 10 layers deposition when the component cools down to the room temperature. All results are for the process parameter set 2 in Table 6.

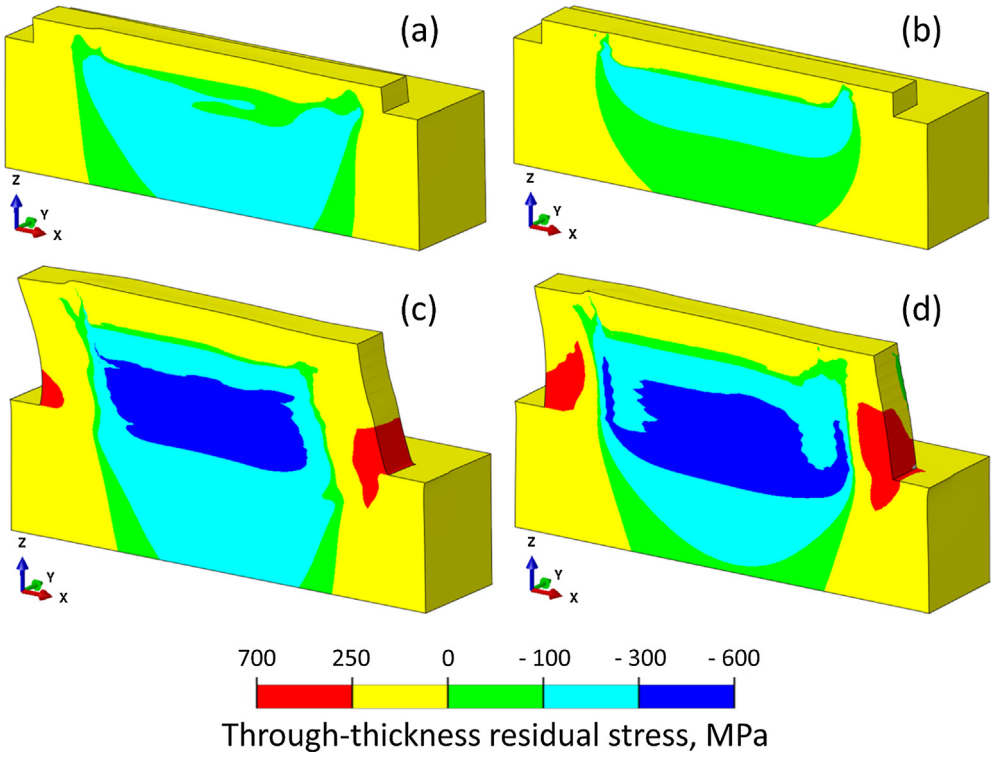

Fig. 10. Through-thickness residual stress distribution at the end of 2nd layer for (a) 2.25Cr-1Mo steel to 800H and (b) Ti-6Al-4V to 800H joints and at the end of 10th layer for (c) 2.25Cr-1Mo steel to 800H and (d) Ti-6Al-4V to 800H joints using process parameter set 2 in Table 6. Scanning direction is along the positive x-axis.

3.4. Graded joints versus dissimilar joints

Fig. 11 explains the benefits of fabricating graded joints over dissimilar joints for minimizing residual stresses and distortion. The results for 2.25Cr-1Mo to 800H joint and Ti-6Al-4V to 800H joint are shown in Fig. 11(a)–(c) and (d)–(f), respectively. In graded joints, the substrate is Ti-6Al-4V or 2.25Cr-1Mo steel and the 10th layer is 800 H, as described before. From the 1st to 9th layer the composition changes with a step of 10 wt% of 800H. On the other hand, for the dissimilar joints, substrate and layer 1 to layer 5 are made of Ti-6Al-4V or 2.25Cr-1Mo steel and 6th to 10th layer are made of 800H, as shown in Fig. 2. Therefore, sharp change in composition occurs at the interface of 5th and 6th layer of the dissimilar joints. All plots in Fig. 11 are made after the end of 10 layers deposition when the component cools down to the room temperature. Longitudinal residual stresses are plotted along the 'line 1' for the entire length of the substrate (14 mm) and through-thickness residual stress and strain are plotted along 'line 5'. Lines 1 and 5 show the entire transition of stresses from substrate to deposit along the laser travel and build height directions, respectively.

The mechanical properties of 2.25Cr-1Mo steel and alloy 800H are similar (see Tables 3 and 5). As a result, no sharp changes in residual stresses and strain at the joint interface are observed. Therefore, graded joint between these two alloys provides marginal benefit over the dissimilar joint for minimizing residual stress

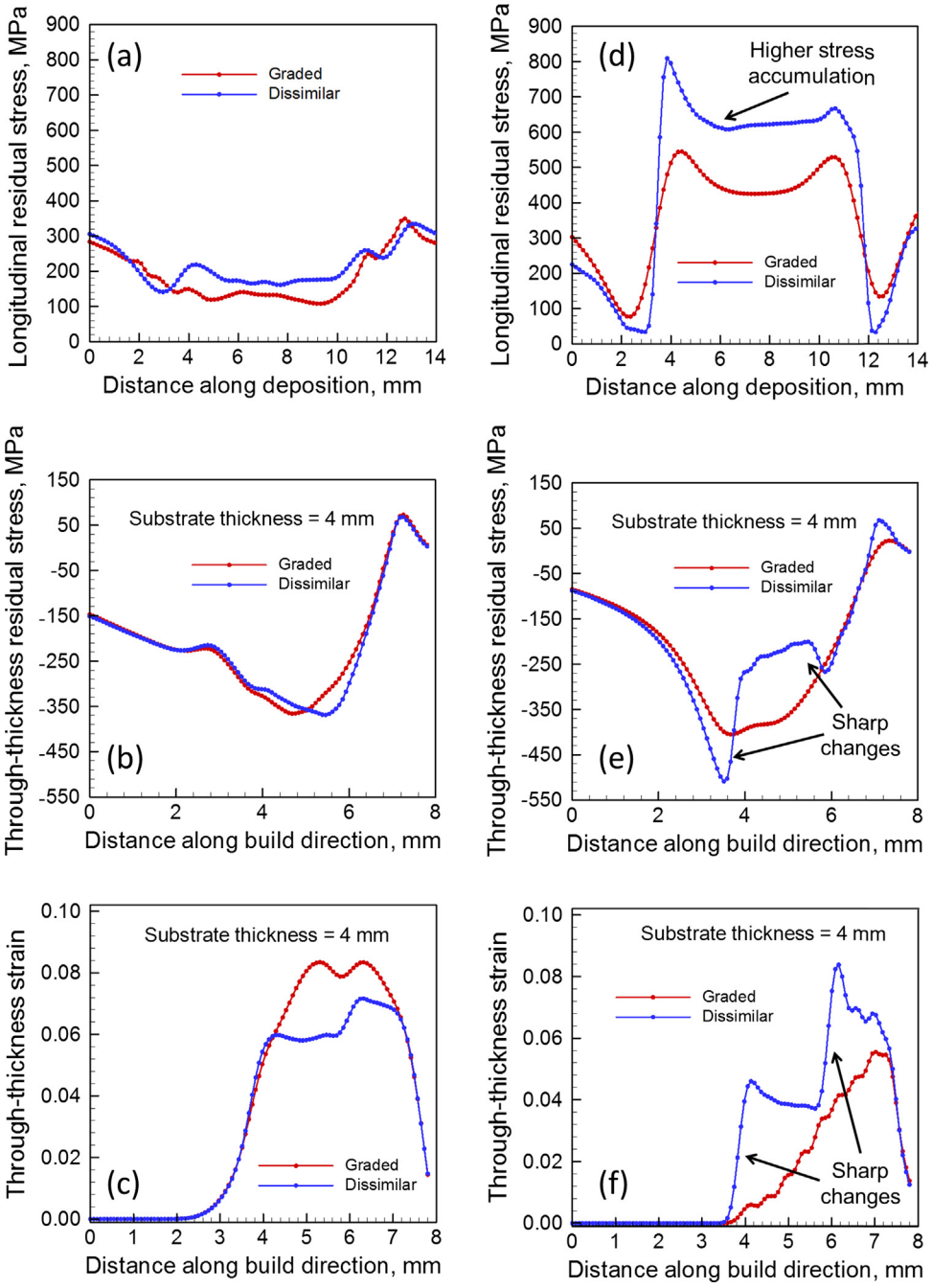

Fig. 11. (a) Longitudinal residual stress along 'line 1', through-thickness (b) stress and (c) strain along 'line 5' for 2.25Cr-1Mo steel to 800H joint and (d) longitudinal residual stress along 'line 1', through-thickness (e) stress and (f) strain along 'line 5' Ti-6Al-4V to 800H joints using process parameter set 2 in Table 6.

and distortion in this pair of dissimilar metals. However, mechanical properties of Ti-6Al-4V are significantly different from those of alloy 800H (see Tables 4 and 5). For example, room temperature yield strength of Ti-6Al-4V is about four times higher than that of 800H. However, room temperature Young's modulus and volumetric expansion coefficient of Ti-6Al-4V are almost half of 800H. Sharp changes in residual stresses and strain in the dissimilar joints due to these differences in mechanical properties can be minimized by fabrication of compositionally graded joints between these two alloys, as shown in Fig. 11(d)–(f). These findings are consistent with the observations made by Williamson et al. [37] where, sharp changes in residual stresses were minimized by fabricating graded joints between pure nickel and alumina by powder metallurgy process.

4. Summary and conclusions

A thermo-mechanical model is developed, validated and utilized to predict residual stresses and distortion based on the accurate temperature field calculated using a well tested heat transfer and fluid flow model and temperature and composition dependent alloy properties estimated using thermodynamic calculations. Residual stresses and distortion are calculated and compared for both compositionally graded as well as dissimilar alloy joints of 2.25Cr-1Mo steel to alloy 800H and Ti-6Al-4V to 800H. The main findings are indicated below.

1. Since, the mechanical properties of Ti-6Al-4V and 800H are significantly different, dissimilar joints between these two alloys exhibited sharp changes in residual stresses and strains at the interface between the two alloys. These sharp changes in residual stresses and strains have been proved to minimize by fabricating a graded joint between these two alloys.
2. Because of the similar mechanical properties of 2.25Cr-1Mo steel and 800H, graded joints between these two alloys provided relatively lower benefits for minimizing residual stresses and distortion compared to the dissimilar joints between them.
3. Residual stresses near the substrate-deposit interface were partially alleviated due to the reheating and cooling during the deposition of the upper layers for all cases studied. However, longitudinal residual stress near the substrate-deposit interface in Ti-6Al-4V to 800H joints was higher than that for 2.25Cr-1Mo steel to 800H joints. This behavior is consistent with the higher room temperature yield strength and lower thermal expansion coefficient of Ti-6Al-4V substrate than 2.25Cr-1Mo steel substrate.
4. The computed ratio of the longitudinal residual stress at the substrate-deposit interface to the room temperature yield strength of the substrate provided information about the susceptibilities to warping, buckling and detachment of deposit from its substrate. A graded joint between 800H and Ti-6Al-4V on Ti-6Al-4V substrate was less susceptible to these defects than a joint between 800H and 2.25Cr-1Mo steel on 2.25Cr-1Mo steel substrate because of the higher room temperature yield strength of the Ti-6Al-4V substrate than 2.25Cr-1Mo steel.
5. The thermal strain during deposition increases with layers for both graded joints of Ti-6Al-4V to 800H and 2.25Cr-1Mo steel to 800H. For the former, this is mainly because of the increasing heat accumulation during the deposition of upper layers. For the latter, the rising strain results largely from the increase in volumetric expansion coefficient as more 800H is added into Ti-6Al-4V in the upper layers. Moreover, for a particular layer, the value of the strain for Ti-6Al-4V to 800H joint is higher than that for 2.25Cr-1Mo steel to 800H joint mainly due to the low elastic modulus and density of the Ti-6Al-4V substrate.

Acknowledgement

We acknowledge the support from US Department of Energy NEUP Grant [DE-NE0008280]. One of the authors (T.M.) also acknowledges the support from American Welding Society research fellowship grant [179466]. Finally, W.Z. acknowledges the support from US Department of Energy NEUP Grant [DE-NE0000708].

Appendix A. Supplementary material

Supplementary data associated with this article can be found, in the online version, at https://doi.org/10.1016/j.commatsci.2017.11.026.

References

[1] C.D. Lundin, Dissimilar metal welds-transition joints literature review, Weld. J. 61 (2) (1982) 58–63.
[2] D. Deng, K. Ogawa, S. Kiyoshima, N. Yanagida, K. Saito, Prediction of residual stresses in a dissimilar metal welded pipe with considering cladding, buttering and post weld heat treatment, Comput. Mater. Sci. 47 (2009) 398–408.
[3] Z. Zeng, X. Li, Y. Miao, G. Wu, Z. Zhao, Numerical and experiment analysis of residual stress on magnesium alloy and steel butt joint by hybrid laser-TIG welding, Comput. Mater. Sci. 50 (5) (2011) 1763–1769.
[4] D. Delfosse, N. Cherradi, B. Ilschner, Numerical and experimental determination of residual stresses in graded materials, Compos. Part B: Eng. 28 (1-2) (1997) 127–141.
[5] D. Qiao, W. Zhang, T.Y. Pan, P. Crooker, S.A. David, Z. Feng, Evaluation of residual plastic strain distribution in dissimilar metal weld by hardness mapping, Sci. Technol. Weld Join. 18 (7) (2013) 624–630.
[6] G.J. Brentrup, J.N. DuPont, Fabrication and characterization of graded transition joints for welding dissimilar alloys, Weld. J. 92 (2013) 72–79.
[7] T. DebRoy, H.L. Wei, J.S. Zuback, T. Mukherjee, J.W. Elmer, J.O. Milewski, A.M. Beese, A. Wilson-Heid, A. De, W. Zhang, Additive manufacturing of metallic components – process, structure and properties, Prog. Mater. Sci. 92 (2018) 112–224.
[8] G.K. Lewis, E. Schlienger, Practical considerations and capabilities for laser assisted direct metal deposition, Mater. Des. 21 (4) (2000) 417–423.
[9] A. Reichardt, R.P. Dillon, J.P. Borgonia, A.A. Shapiro, B.W. McEnerney, T. Momose, P. Hosemann, Development and characterization of Ti-6Al-4V to 304L stainless steel gradient components fabricated with laser deposition additive manufacturing, Mater. Des. 104 (2016) 404–413.
[10] A. Hinojos, J. Mireles, A. Reichardt, P. Frigola, P. Hosemann, L.E. Murr, R.B. Wicker, Joining of Inconel 718 and 316 Stainless Steel using electron beam melting additive manufacturing technology, Mater. Des. 94 (2016) 17–27.
[11] B.E. Carroll, R.A. Otis, J.P. Borgonia, J. Suh, R.P. Dillon, A.A. Shapiro, D.C. Hofmann, Z.K. Liu, A.M. Beese, Functionally graded material of 304L stainless steel and Inconel 625 fabricated by directed energy deposition: characterization and thermodynamic modeling, Acta Mater. 108 (2016) 46–54.
[12] L.D. Bobbio, R.A. Otis, J.P. Borgonia, R.P. Dillon, A.A. Shapiro, Z.K. Liu, A.M. Beese, Additive manufacturing of a functionally graded material from Ti-6Al-4V to Invar: experimental characterization and thermodynamic calculations, Acta Mater. 127 (2017) 133–142.
[13] P.H. Chang, T.L. Teng, Numerical and experimental investigations on the residual stresses of the butt-welded joints, Comput. Mater. Sci. 29 (2004) 511–522.
[14] P.J. Withers, H.K.D.H. Bhadeshia, Residual stress. Part 1–Measurement techniques, Mater. Sci. Technol. 17 (4) (2001) 355–365.
[15] Z. Wang, E. Denlinger, P. Michaleris, A.D. Stoica, D. Ma, A.M. Beese, Residual stress mapping in Inconel 625 fabricated through additive manufacturing: Method for neutron diffraction measurements to validate thermomechanical model predictions, Mater. Des. 113 (2017) 169–177.
[16] A.S. Wu, D.W. Brown, M. Kumar, G.F. Gallegos, W.E. King, An experimental investigation into additive manufacturing-induced residual stresses in 316L stainless steel, Metal. Mater. Trans. A 45 (13) (2014) 6260–6270.
[17] W. Zhang, Z. Feng, P. Crooker, Improved procedure for computing residual stresses from neutron diffraction data and its application to multipass dissimilar welds, Sci. Technol. Weld Join. 16 (3) (2011) 254–260.
[18] T. Mukherjee, W. Zhang, T. DebRoy, An improved prediction of residual stresses and distortion in additive manufacturing, Comput. Mater. Sci. 126 (2017) 360–372.
[19] L.E. Svensson, B. Gretoft, H.K.D.H. Bhadeshia, An analysis of cooling curves from the fusion zone of steel weld deposits, Scand. J. Metall. 15 (1986) 97–103.
[20] B.H. Rabin, R.L. Williamson, S.M.R.S. Suresh, Fundamentals of residual stresses in joints between dissimilar materials, MRS Bull. 20 (1) (1995) 37–39.
[21] V. Manvatkar, A. De, T. DebRoy, Heat transfer and material flow during laser assisted multi-layer additive manufacturing, J. Appl. Phys. 116 (12) (2014) 124905.

[22] V. Manvatkar, A. De, T. DebRoy, Spatial variation of melt pool geometry, peak temperature and solidification parameters during laser assisted additive manufacturing process, Mater. Sci. Technol. 31 (8) (2015) 924–930.
[23] G.L. Knapp, T. Mukherjee, J.S. Zuback, H.L. Wei, T.A. Palmer, A. De, T. DebRoy, Building blocks for a digital twin of additive manufacturing, Acta Mater. 135 (2017) 390–399.
[24] Abaqus Documentation, Version 6.14, Dassault Systems, 2015.
[25] N. Saunders, Z. Guo, X. Li, A.P. Miodownik, J.P. Schille, Using JMatPro to model materials properties and behavior, JOM 55 (12) (2003) 60–65.
[26] N. Saunders, A.P. Miodownik, CALPHAD: A comprehensive guide, vol. 1, Elsevier, 1998.
[27] N. Saunders, Z. Guo, X. Li, A.P. Miodownik, J.P. Schille, Modelling the material properties and behavior of Ni-based superalloys, Superalloys (2004) 849–858.
[28] Z. Fan, P. Tsakiropoulos, A.P. Miodownik, A generalized law of mixtures, J. Mater. Sci. 29 (1994) 141–150.
[29] A. Raghavan, H.L. Wei, T.A. Palmer, T. DebRoy, Heat transfer and fluid flow in additive manufacturing, J. Laser Appl. 25 (5) (2013) 052006.
[30] T. DebRoy, S.A. David, Physical processes in fusion welding, Rev. Mod. Phys. 67 (1) (1995) 85.
[31] Y.S. Lee, W. Zhang, Modeling of heat transfer, fluid flow and solidification microstructure of nickel-base superalloy fabricated by laser powder bed fusion, Addit. Manufact. 12 (2016) 178–188.
[32] L. Wang, S.D. Felicelli, P. Pratt, Residual stresses in LENS-deposited AISI 410 stainless steel plates, Mater. Sci. Eng. A 496 (1) (2008) 234–241.
[33] T. Mukherjee, V. Manvatkar, A. De, T. DebRoy, Dimensionless numbers in additive manufacturing, J. Appl. Phys. 121 (6) (2017) 064904.
[34] T. Mukherjee, J.S. Zuback, A. De, T. DebRoy, Printability of alloys for additive manufacturing, Sci. Rep. 6 (2016).
[35] T. Mukherjee, V. Manvatkar, A. De, T. DebRoy, Mitigation of thermal distortion during additive manufacturing, Scripta Mater. 127 (2017) 79–83.
[36] R. Jackson, I. Chusoipin, I. Green, A finite element study of the residual stress and deformation in hemispherical contacts, Trans. ASME J. Tribol. 127 (3) (2005) 484–493.
[37] R.L. Williamson, B.H. Rabin, J.T. Drake, Finite element analysis of thermal residual stresses at graded ceramic-metal interfaces. Part I. Model description and geometrical effects, J. Appl. Phys. 74 (2) (1993) 1310–1320.

Appendix D:

Building blocks for a digital twin of additive manufacturing

Acta Materialia 135 (2017) 390–399

Contents lists available at ScienceDirect

Acta Materialia

journal homepage: www.elsevier.com/locate/actamat

Full length article

Building blocks for a digital twin of additive manufacturing

G.L. Knapp [a], T. Mukherjee [a], J.S. Zuback [a], H.L. Wei [a], T.A. Palmer [a], A. De [b], T. DebRoy [a, *]

[a] Department of Materials Science and Engineering, The Pennsylvania State University, University Park, PA, 16802, USA
[b] Department of Mechanical Engineering, Indian Institute of Technology, Bombay, 400076, India

ARTICLE INFO

Article history:
Received 11 April 2017
Received in revised form
20 June 2017
Accepted 20 June 2017
Available online 22 June 2017

Keywords:
3D printing
Deposit geometry
Solidification parameters
Secondary dendrite arm spacing
Micro-hardness

ABSTRACT

Properties and serviceability of additively manufactured components are affected by their geometry, microstructure and defects. These important attributes are now optimized by trial and error because the essential process variables cannot currently be selected from scientific principles. A recourse is to build and rigorously validate a digital twin of the additive manufacturing process that can provide accurate predictions of the spatial and temporal variations of metallurgical parameters that affect the structure and properties of components. Key building blocks of a computationally efficient first-generation digital twin of laser-based directed energy deposition additive manufacturing utilize a transient, three-dimensional model that calculates temperature and velocity fields, cooling rates, solidification parameters and deposit geometry. The measured profiles of stainless steel 316L and Alloy 800H deposits as well as the secondary dendrite arm spacing (SDAS) and Vickers hardness measurements are used to validate the proposed digital twin. The predicted cooling rates, temperature gradients, solidification rates, SDAS and micro-hardness values are shown to be more accurate than those obtained from a commonly used heat conduction calculation. These metallurgical building blocks serve as a phenomenological framework for the development of a digital twin that will make the expanding knowledge base of additive manufacturing usable in a practical way for all scientists and engineers.

1. Introduction

Properties and serviceability of metallic components produced by laser-assisted additive manufacturing (AM) depend on their geometry, microstructure and defects [1–5]. The evolution of microstructure and geometry is affected by the transient temperature fields, cooling rates and solidification parameters [6,7], which, in turn, depend on the process variables, alloy and specific AM process. Building a structurally sound and reliable component requires specification of an optimum set of process variables that affect the transient temperature fields, geometry and cooling rates.

Since there are many interrelated process variables, the selection of an optimized combination capable of producing a structurally sound, reliable component is challenging. The temperature fields and molten pool geometry are difficult to monitor and control in real time during AM. As a result, the structure and properties of components are routinely optimized by adjustment of many process variables by trial and error without any guiding scientific framework. Nearly all of the previous studies rely purely on empirical techniques in which select process parameters are varied while all others are held constant for achieving acceptable properties [8]. Post-process analyses determine the geometry, microstructure and mechanical properties of the as-built component. This approach is time consuming, expensive, and provides no assurance of attaining the optimal structure and properties of the component.

A recourse is to develop a phenomenological framework, or a digital twin [1], capable of predicting the most important variables that affect the metallurgical structure and properties of the components based on scientific principles. Ideally, the framework would enable users to specify any combination of AM process parameters and obtain the important metallurgical variables such as the transient temperature fields, molten pool geometry, temporal and spatial variations of cooling rates and solidification parameters rapidly. In principle, this digital twin of the AM process, when adequately validated with experimental data, would replace or reduce expensive, time-consuming physical experiments with rapid, inexpensive 'numerical experiments'. In the initial phase, such a model would consider all of the important AM process variables as input and provide the transient, three dimensional,

* Corresponding author.
E-mail address: debroy@psu.edu (T. DebRoy).

http://dx.doi.org/10.1016/j.actamat.2017.06.039
1359-6454/

temperature and velocity fields, cooling rates, solidification parameters and geometry of the deposit as output. From these outputs, non-dimensional numbers, such as the thermal strain parameter, would be computed for further insight into the process [9–11].

Existing AM process models have their inherent advantages and disadvantages for specific applications. Finite element method based heat conduction models [12–14] are able to calculate deposit geometry and temperature distributions, from which heating and cooling rates can be extracted. However, these models neglect the effects of convective flow of molten metal inside the pool during the calculations of temperature distributions. This causes inaccurate predictions of melt pool shape, which leads to inaccuracies in cooling rates. For example, Manvatkar et al. [15] showed that by ignoring the effect of convection, the cooling rates in AM were overestimated by a factor of two. Svensson et al. [16] also noted that the use of a heat conduction equation did not adequately represent experimental cooling curves. Current heat transfer and fluid flow models [15,17] consider the Marangoni convection inside the pool by using a flat-surface assumption, allowing accurate estimation of the temperature and velocity distributions, cooling rates and solidification parameters. However, this assumption causes the predicted deposit geometry to deviate from experimental data. Level Set Method (LSM) [18] and Volume of Fluid (VOF) [19] method both track the evolution of the free surface of the deposit, thus, calculate the bead geometry. This advantage is offset by the fact that they are computationally intensive and often used for only two-dimensional calculations.

Here, we seek to develop and experimentally verify important building blocks for a first-generation digital twin of AM by developing a computationally efficient, comprehensive model with abilities to predict deposit geometry, transient temperature, velocity distributions and solidification parameters in three dimensions. An analytical sub-model based on mass conservation combined with consideration of powder catchment efficiency obtains an initial prediction of the deposit geometry with curved surfaces. A 3D transient heat transfer and fluid flow model provides a crucial building block needed for the prediction of all the important metallurgical variables that affect the structure and properties of the components. This model calculates temperature and velocity distributions, cooling rate and solidification parameters for a single-layer deposit. Experimental validation of the computed deposit geometry is undertaken for stainless steel 316L and Alloy 800H to demonstrate the applicability of the phenomenological digital twin to both alloy systems. Based on the calculated cooling rates, secondary dendritic arm spacing and hardness of SS 316L are calculated and compared with the corresponding experimental results. The actual tailoring of the final component's properties based on the predictive model is still a long way in the future and is outside the scope of this manuscript.

2. Theoretical calculations

2.1. Analytical calculations of the deposit geometry

Previous research on predicting single layer cladding geometry includes the use of parabolic and sinusoidal curves fitting [20], numerical algorithms [21], in-situ sensing [22], neural networks [20,23] and ANOVA techniques [24]. However, the curve-fitting calculations often rely solely on experimental observations and do not consider relevant phenomena such as mass conservation and material properties. In order to model the directed energy deposition (DED) process, the surface of the front edge of the deposit must be considered in three-dimensions. Experimentally, the leading edge of the deposit is located in front of the laser beam axis, which is likely due to a combination of powder-stream distribution and molten liquid spreading. Based on the success of parabolic function fits to 2D clad surfaces [20], an ellipsoidal function seems a natural extension for a 3D deposit surface. Behind the leading edge of the deposit, this profile reduces to an elliptical surface, such that the surface shape can be described for leading edge as,

$$\frac{x^2}{a^2}+\frac{y^2}{b^2}+\frac{z^2}{c^2}=1 \tag{1}$$

and behind the leading edge as,

$$\frac{y^2}{b^2}+\frac{z^2}{c^2}=1 \tag{2}$$

where a, b, and c are the principal axes of the ellipsoid, as depicted in Fig. 1. Taking advantage of the symmetry of the deposit along the x-z plane, half of the ellipsoid is used in the calculations to reduce computational costs. Physically, the values of b and c represent the deposit half-width and height, respectively, as shown in Fig. 1.

To calculate the values of a, b, and c, several simplifying assumptions are made:

1) The distribution of the blown powder stream is radially symmetric, and hence the values of a and b are equivalent.
2) For a particular alloy, the contact angle and the ratio of the height to half width (c/b) is constant.
3) The maximum deposit half-width is a fraction, f_m, of the laser beam radius, r_b. The value of f_m is calculated using heat balance,

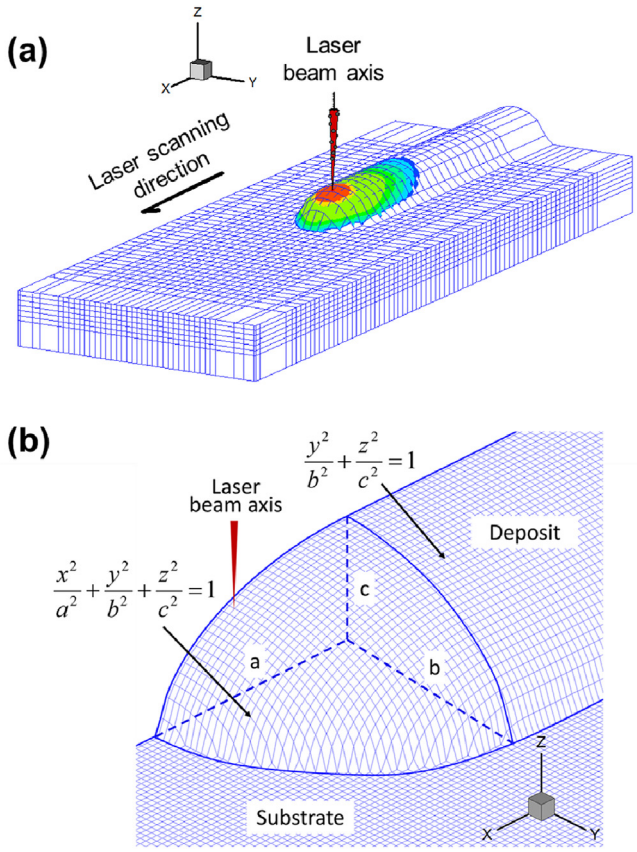

Fig. 1. (a) Schematic overview of the digital twin model. (b) Details of solution domain for the half-ellipsoid deposit indicating the position of the laser beam axis. Deposit is split along the symmetry plane for computational efficiency.

and its value typically varies between 0.75 and 1.0. If all of the supplied powders are included in the deposit, for example if the catchment efficiency is equal to 1.0, the value of f_m is also 1.0, and the half-width of the deposit is equal to r_b.

4) The radius of the powder stream is approximately equal to the laser beam radius at the substrate surface, which is typical of DED processes.

Considering the deposited mass must equal the mass of the deposited volume,

$$\eta_c \dot{m} = \frac{\pi}{2} b\, c v_s\, \rho \tag{3}$$

where η_c is the fractional mass catchment of powder into the pool, $\dot{m}$ is the powder mass flow rate from the nozzle, v_s is the scanning speed of the heat source, and ρ is the density of the deposit material. By assumption (3), $\dot{m}$ from Equation (3) can be rewritten as,

$$\dot{m} = \frac{\pi}{2} f_m\, r_b\, c_0\, v_s\, \rho \tag{4}$$

where, c_0 and $f_m r_b$ (*i.e.* b_0) are the maximum values of deposit height and half-width, respectively. By assumption (2) it is apparent that,

$$\frac{c}{b} = \frac{c_0}{f_m r_b} = \text{constant} \tag{5}$$

Therefore, Equation (3) can be solved for b and c as,

$$b = f_m\, r_b\, \sqrt{\eta_c} \tag{6}$$

$$c = \frac{2\,\dot{m}\,\sqrt{\eta_c}}{\pi\, f_m\, r_b\, v\, \rho} \tag{7}$$

From Equations (6) and (7), there is a clear need for an expression of the fractional mass catchment η_c. Previous studies of mass catchment into single bead deposits for powder-blown laser cladding [25–27] did not yield an analytical expression of η_c based on process parameters and material properties. However, intuition of the processes involved in powder entering the molten pool allows for the derivation of such an expression.

Huang et al. [28] have shown the catchment efficiency to be a function of the top surface area of the pool. Since pool size will grow with an increasing ratio of input energy to the amount of energy it takes to melt the material, catchment efficiency may be expressed as a function of a parameter Q,

$$Q = \frac{\left(P/v_s\right)^{2/3}}{\left(C_P \Delta T + L\right)^{2/3}} \tag{8}$$

where P is laser power, v_s is scanning speed, C_p is specific heat, ΔT is the difference between the solidus temperature of the alloy and ambient temperature, and L is the latent heat of fusion of the alloy. To compare various experiments, it is preferable to take a normalized value of this parameter, Q^*, found by dividing Q by Q_{max} for the ensemble of data used. Therefore, η_c is calculated using a second order polynomial regression from both internal experimental data (see Section 3) and independent data from the literature [29] (Fig. 2), as,

$$\eta_c = -1.5\left(Q^*\right)^2 + 2.8\left(Q^*\right) - 0.3 \tag{9}$$

Using this value of the catchment efficiency, the magnitude of errors for the calculated width and height were 11.0% and 3.7%, respectively, when compared to corresponding experimental data (detailed results for geometry fitting are located in the Appendix). Minimal error in the calculation of the width and height of the beads for two different materials yielded a 95% confidence interval of ±15% for the value of η_c. While it is likely possible to refine the expression for η_c by adding more material parameters and experimental data to the model, the current form is applicable for practical estimations of mass catchment efficiency into the molten pool.

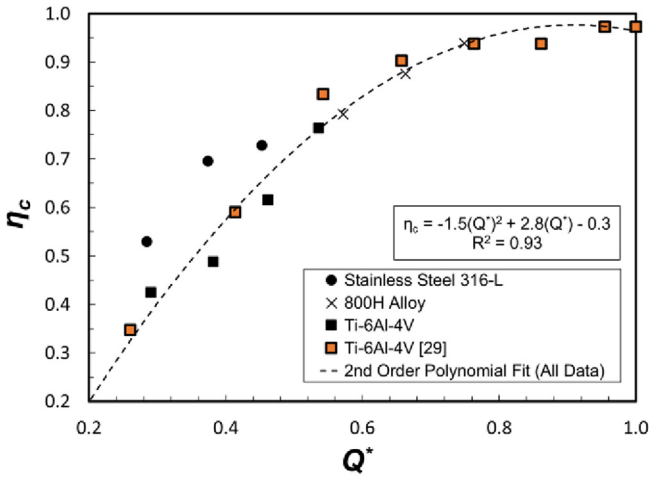

Fig. 2. Fitting of parameter Q^* to experimental data for the fractional mass catchment efficiency, η_c, into the molten pool [29].

2.2. Temperature and velocity field calculations

A three-dimensional numerical heat transfer and fluid flow model solves the enthalpy, three velocity components, and pressure fields for the geometry defined by Equations (6) and (7). The main assumptions of the model are the following. The density of the liquid metal has been assumed to be a constant except for the calculation of the buoyancy force in the momentum equation. This approximation, known as the Boussinesq approximation is widely used for the calculation of buoyancy driven flow [30,31]. Furthermore, the magnitude of the Marangoni force is higher than the buoyancy force by a factor of about 3000 [32]. In addition, the loss of alloying elements due to vaporization [33,34] and the resulting effect on both heat loss and composition change is ignored. The heat loss due to vaporization of alloying elements is a small fraction of the heat supplied by the laser beam for the conditions investigated in this paper. A short description of the calculation procedure is outlined in the supplementary materials.

The model is defined by the governing equations,

$$\frac{\partial(\rho u_i)}{\partial x_i} = 0 \tag{10}$$

$$\frac{\partial(\rho u_j)}{\partial t} + \frac{\partial(\rho u_j u_i)}{\partial x_i} = \frac{\partial}{\partial x_i}\left(\mu \frac{\partial u_j}{\partial x_i}\right) + S_j \tag{11}$$

where, ρ is the density, u_i and u_j are the velocity components along the i and j directions, respectively, and x_i is the distance along the i direction, t is the time, μ is the effective viscosity, and S_j is a source term for the momentum equation. In addition, the energy conservation equation is applied,

$$\rho\frac{\partial h}{\partial t}+\frac{\partial(\rho u_i h)}{\partial x_i}=\frac{\partial}{\partial x_i}\left(\frac{k}{C_p}\frac{\partial h}{\partial x_i}\right)-\rho\frac{\partial \Delta H}{\partial t}-\rho\frac{\partial(u_i\Delta H)}{\partial x_i} \quad (12)$$

where, h is the sensible heat, C_p is the specific heat, k is the thermal conductivity, and ΔH is the latent heat content. Table 1 shows the thermo-physical properties of the alloys used for the calculations. Constant effective viscosity and effective thermal conductivity are taken as 2.0 and 3.0 times the nominal values, respectfully, to account for turbulence effects. Process parameters from Table 2 directly apply to the relevant simulations. A control volume method discretizes the governing equations by dividing the solution domain into small grids, with a total volume of 580 × 50 × 95 (length × width × height) grid points. The discretized equations are solved iteratively using the tri-diagonal matrix algorithm, and the calculations are completed using an in-house Fortran code. Typically, around 3.5 billion linear equations are solved for the deposition of one layer, which takes approximately 50 min in a personal computer with 3.40 Gigahertz i7 processor and 8 Gigabyte RAM (random access memory).

The model considers the laser as a Gaussian-distributed heat source centered at a distance of ½a from the leading edge of the deposit, as shown in Fig. 1. In DED, the powder particles absorb heat during their flight from the nozzle to the substrate, so the applied energy density consists of a volumetric flux term and a surface flux term. The volumetric term, distributed from the surface of the deposit down to the top of the substrate, represents the heat absorbed by the powder during flight.

$$S_V=\frac{Q_V d}{\pi r_b^2 c}\exp\left(-d\frac{r^2}{r_b^2}\right) \quad (13)$$

where Q_v is the total heat absorbed by the powder per unit time during their flight, d is the laser beam intensity distribution factor, c is the height of the deposit (see Fig. 1), r_b is the focused laser beam radius, and r is the radial distance from the beam axis. It is assumed that, on average, the powder particles are heated to solidus temperature during flight, such that:

$$Q_V=\dot{m}c_p(T_{solidus}-T_{ambient}) \quad (14)$$

The remaining energy is applied as a surface flux term, S_s, as shown below:

$$S_S=\frac{Q_S d}{\pi r_b^2 c}\exp\left(-d\frac{r^2}{r_b^2}\right) \quad (15)$$

where Q_s is the net available power that is applied on the deposit surface. Energy conservation is observed such that:

$$Q_V+Q_S=\eta P \quad (16)$$

where P is the nominal laser power and η is the absorptivity of the powder particles that varies between 0.3 and 0.7 [35].

The boundary conditions for the thermal analysis include heat loss by convection and radiation to the surroundings. Spatial variation in pool surface temperature creates a surface tension gradient that drives the convective flow of molten metal inside the pool. The temperature gradient along the 3D curved surface (G) has three components along the x–, y–, and z–directions (G_x, G_y, G_z, respectively). The Marangoni stress at any point on the curved surface along the x–, y–, and z–directions, respectively, is,

$$\tau_x=\mu\frac{du}{dz}=\frac{d\gamma}{dT}G_x \quad (17)$$

$$\tau_y=\mu\frac{dv}{dz}=\frac{d\gamma}{dT}G_y \quad (18)$$

$$\tau_z=\mu\frac{dw}{dr}=\frac{d\gamma}{dT}G_z \quad (19)$$

where T is the temperature, γ is the surface tension, μ is the viscosity of the liquid metal, r is the radial distance from the central axis of the heat source, and u, v, and w are the velocities of the liquid metal along the x–, y–, and z–directions, respectively.

During the calculation of the temperature fields, the molten pool geometry and peak temperature are extracted, which allows for the calculation of the non-dimensional thermal strain parameter described by Mukherjee et al. [10]. This parameter allows for the comparison of the relative amount of thermal distortion between materials and processes.

3. Experimental investigations

A series of 76 mm long single pass, single layer builds were deposited using pre-alloyed SS 316L and 800H powders (Carpenter Powder Products, Inc.) on a 150 mm × 150 mm x 12.7 mm annealed substrate of similar alloy as that of the powder. The powders were gas atomized in nitrogen and had a mesh size range of −100/+325, meaning that the diameter of each powder particle was between 45 and 145 μm. Laser powers ranging from 1000 to 3000 W were used to deposit the builds while all other parameters were kept constant. The process parameters used for the depositions are given in Table 2. The specimens were fabricated using a custom-designed, in-house laser assisted directed energy deposition (DED-L) system with a controlled environment. The build chamber was purged with high purity argon to reduce oxygen levels during experiments. A ytterbium fiber laser (IPG Photonics® YLR-12000-L) with a wavelength of approximately 1080 nm was supplied to the

Table 1
Thermo-physical properties of SS 316L and Alloy 800H.

Properties	SS 316L	800H
Liquidus temperature (K)	1733	1607
Solidus temperature (K)	1693	1674
Thermal conductivity (W/m K)	11.82 + 0.0106 T	8.54 + 0.0167 T
Specific heat (J/kg K)	330.9 + 0.563 T − 4.015 × 10^{-4} T^2 + 9.465 × 10^{-8} T^3	309.2 + 0.5104 T
Density (kg/m^3)	7800	7870
Volumetric expansion co-efficient (/K)	5.85 × 10^{-5}	1.02 × 10^{-5}
Viscosity (kg/m s)	7 × 10^{-3}	7.4 × 10^{-3}
dγ/dT (N/m K)	−0.40 × 10^{-3}	−0.24 × 10^{-3}
Surface tension (N/m)	1.50	1.69
Latent heat of fusion (J/kg)	2.72 × 10^5	2.65 × 10^5

Table 2
Key experimental and simulation process parameters.

Alloy	Laser power (W)	Beam radius (mm)	Scanning speed (mm/s)	Substrate thickness (mm)	Powder flow rate (g/s)
SS 316L	1000–2500	2.0	10.6	10	0.25
Alloy 800H	1500–3000	2.0	10.6	10	0.25

chamber through a reflective optics system. Powder was delivered through four separate nozzles, each of which measuring approximately 1.6 mm in diameter at the point of exit.

A transverse cross section approximately 4 mm thick was removed near the middle of each deposit using an abrasive cutting wheel with a silicon carbide blade. A series of silicon carbide papers up to 1200 grit and metallographic polishing with 3 and 1 μm polycrystalline diamond suspension followed by a final polishing with 0.05 μm colloidal silica was used to obtain a mirror finish. Electrolytic etching was performed on the SS 316L samples with 10% oxalic acid at 5 V for approximately 3 s to reveal grain boundaries and sub-grain structure.

Micro-hardness measurements were taken using a Vickers indenter on a LECO M-400-G1 machine. Each indentation was subjected to a 300 g load at a dwell time of 5 s. Hardness measurements were spaced uniformly throughout the deposit, including the dilution region into the substrate. Light optical microscopy and scanning electron microscopy (SEM) on an FEI Quanta 200 machine were used to view the deposit geometry and grain structure of the transverse cross sections. SEM images were taken in both secondary electron and backscatter electron modes using a 20 kV accelerating voltage and 4 mm spot size. Secondary dendritic arm spacing (SDAS) was measured by image analysis techniques using ImageJ. Grayscale values were measured along a linear path intersecting multiple secondary dendrites. A peak value corresponded to the inter-dendritic regions that were shown in bright contrast on SEM images due to the elemental redistribution of heavier elements. The distance between each peak was then used to determine the approximate center of a secondary dendrite arm, which was ultimately used to calculate the SDAS.

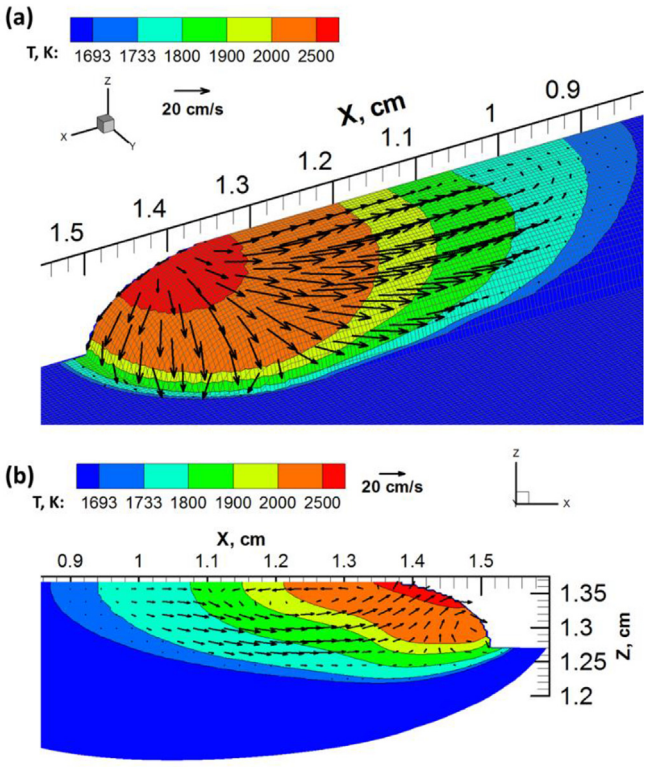

Fig. 3. Temperature and velocity distributions on the curved shaped deposit for stainless steel 316L at 2500 W laser power (a) 3D isometric view and (b) longitudinal sectional view, where the scanning direction is along the positive x-axis.

4. Results and discussion

Fig. 3(a) and (b) show the computed temperature and the velocity distributions on the three-dimensional curved surface and along the longitudinal section of the SS 316L deposit, respectively. The color bands represent the ranges of temperatures corresponding to the figure legend. The location of the peak temperature is near the laser beam axis. The scanning direction is along the positive x-axis. Due to the rapid scanning of the heat source, the isotherms behind the laser beam axis are elongated while the isotherms ahead of the laser beam are compressed. The velocity vectors of the molten metal inside the pool are shown by arrows. A reference vector is shown by an arrow and a comparison of the length of this arrow with the vectors in the plots indicates the relative magnitudes of the computed velocities. The convective flow of liquid metal is primarily driven by the Marangoni stresses caused by the surface tension gradient due to the temperature difference on the surface of the molten pool. Therefore, on the top surface of the deposit the molten metal flows from the high temperature region to the low temperature region along the curved surface as shown in Fig. 3(a). This fluid flow is responsible for enthalpy transport from the front of the pool to the rear, elongating the thermal contours at the back of the pool. Calculated Peclet numbers ranged from 6.3 at 1000 W to 13.4 at 2500 W for SS 316L, showing the increasing role of convective heat transport as heat input, and therefore the magnitude of the Marangoni stresses, increases.

Fig. 3(b) shows that the pool is deeper and has higher temperature and velocities towards the front. Towards the trailing edge of the pool, velocities decrease and the direction of flow is no longer dominated by Marangoni stresses since the temperature gradients are lower at these locations. As velocity diverges from the location of the heat source, separate convective loops are formed, as seen in the front, side, and back of the pool in Fig. 4(a–d). Because of this divergence from the heat source center, the assumed geometry of the deposit and heat source are important in determining the path of fluid convection.

Fig. 5(a) and (b) show the comparisons between the computed transverse section of the deposit with the corresponding experimentally measured macrograph of SS 316L deposits using 1500 W and 2500 W laser powers, respectively. In both figures, the pool boundary is shown as the solidus temperature contour of 1693 K, the mushy zone is shown in orange for temperatures between solidus and liquidus (1733 K) temperatures, and the fusion zone of the deposit is depicted in red for the region heated above the liquidus temperature. Both figures show fair agreements between the computed and the corresponding experimentally measured results. The temperature at the center of the deposit is higher than that of the sides, so molten metal flows from the center of the deposit to the sides along the curved top surface, as shown in Fig. 5. Higher laser power can melt more powders. Therefore, the deposit

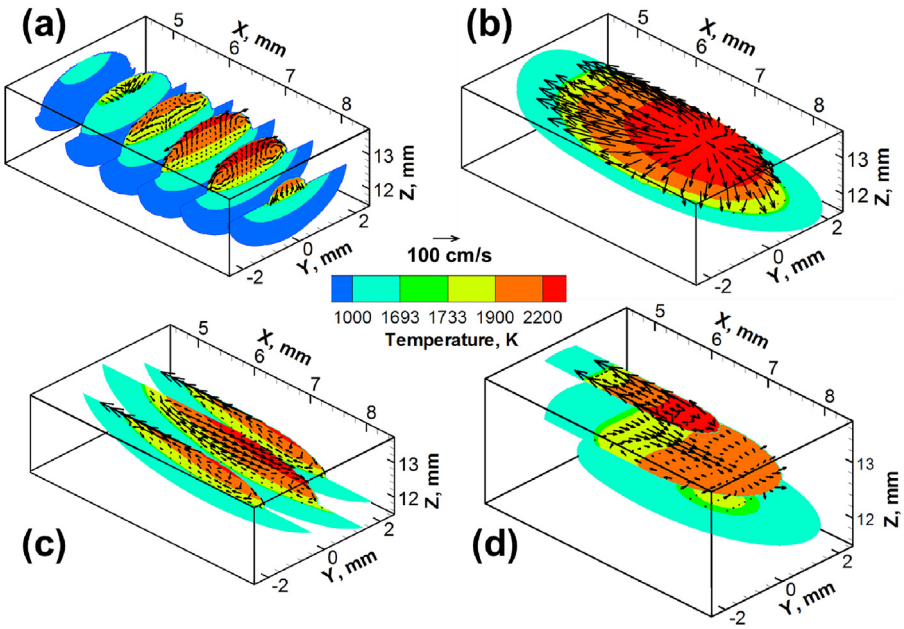

Fig. 4. An instantaneous view of multiple sections through the deposit from simulated stainless steel 316-L at 2500 W laser power: (a) horizontal sections, (b) top-surface, (c) longitudinal sections, and (d) transverse sections. The leading edge of the bead is at x = 8.5 mm.

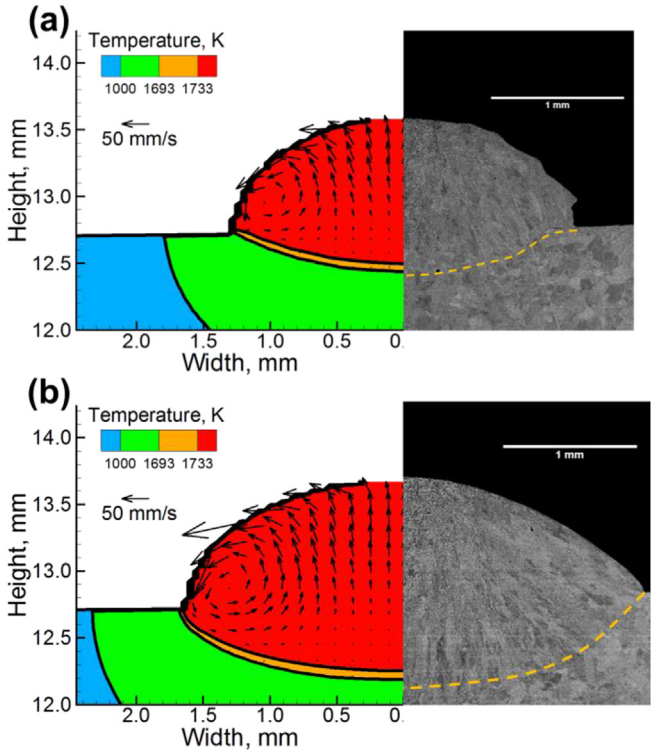

Fig. 5. Comparison of the calculated deposit shape and size with experimental macrograph at the transverse cross section of the build for stainless steel 316L at (a) 1500 W and (b) 2500 W laser power. The dotted lines indicates the edge of the dilution region.

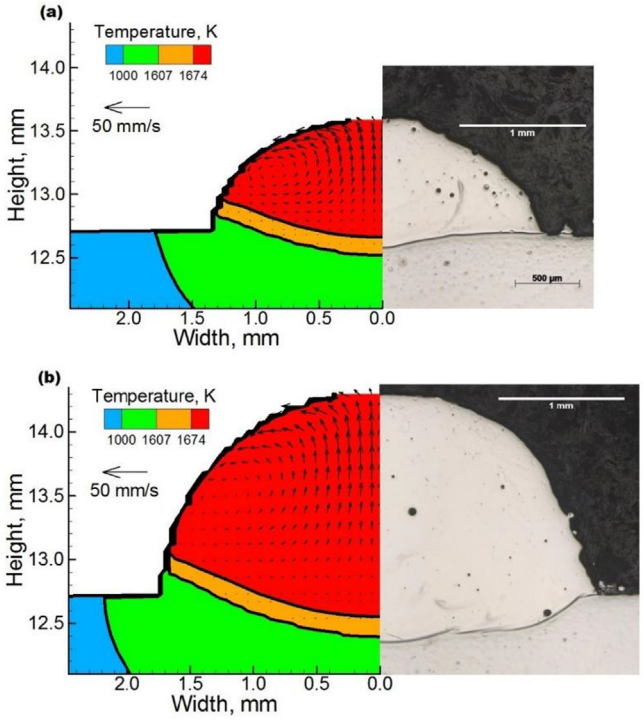

Fig. 6. Comparison of the calculated deposit shape and size with experimental macrograph at the transverse cross section of the build for Alloy 800H at (a) 1500 W and (b) 2500 W laser power.

fabricated using 2500 W laser power is larger than that produced with 1500 W. Fig. 6(a) and (b) also show the comparisons between the computed transverse section of the deposit with the corresponding macrograph using 1500 W and 2500 W laser powers, respectively, for Alloy 800H deposits. Similar observations can be made in these figures. However, Alloy 800H has a lower liquidus temperature than that of SS 316L. Under the same heat input, the amount of the molten material will be more for Alloy 800H, resulting in a larger deposit for Alloy 800H.

Fig. 7 shows the computed variation of the temperature with respect to time, as monitored at the mid height of the deposit center while fabricating 1 cm long SS 316L and Alloy 800H samples

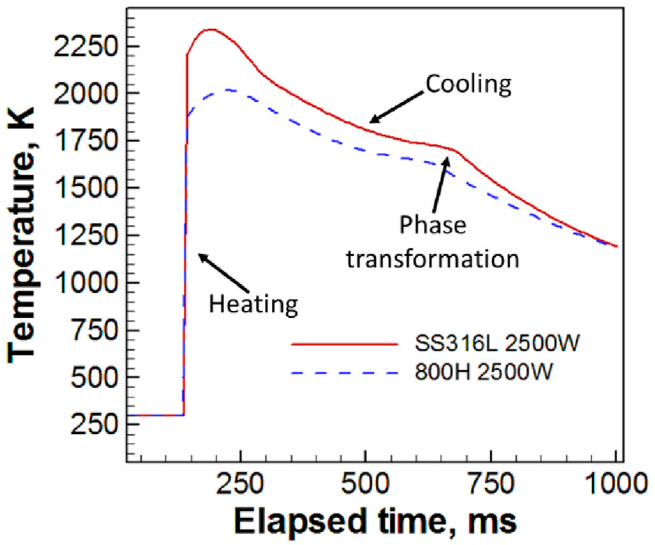

Fig. 7. Simulated thermal history for a location approximately a fifth of the way along the 1.0 cm long deposit length of SS 316L at 2500 W.

using 2500 W laser power. Alloy 800H has higher thermal diffusivity than that of SS 316L, so the peak temperature attained by the SS 316L deposit is higher than that of Alloy 800H. From this figure, it can be observed that heating occurs very rapidly, however the cooling is relatively slower. During the cooling, there is a sudden change in the slope of the curve, representing the solid-to-liquid phase transformation. The slope of the curve during the cooling represents the cooling rate as the build solidifies. For example, in Fig. 7, the calculated cooling rates during solidification are the slope of the curve between the liquidus and solidus temperature. As temperature histories can be stored for any arbitrary point in the model, cooling rates can be determined both spatially and temporally.

Fig. 8(a) and (b) show the comparison of the current model with a heat conduction model and a model with flat a surface assumption, in terms of predicting cooling rate and G/R ratio at different laser powers. With the increase of laser power, pool size increases, which causes the temperature gradients to decrease due to the spreading of isotherms. Therefore, for the same material subjected to similar process parameters, cooling rate and G/R values decrease with higher power. A reduced G/R value indicates that the solidification front will be less stable and columnar to equiaxed transition may occur. As the heat conduction model neglects the mixing of hot and cold liquid by convection, it overestimates the temperature gradient. Therefore, the calculated cooling rate using the heat conduction model is about twice of that calculated using the current model.

Experimental SDAS and hardness measurements of the SS 316L, found in Table 3, show an increase in arm spacing, from 2.51 ± 0.67 μm at 1000 W to 3.27 ± 0.65 μm at 2500 W, and decrease in Vickers hardness as laser power increases, from 214.6 ± 2.2 HV at 1000 W to 205.3 ± 3.2 HV at 2500 W. SEM imaging of the SDAS in Fig. 9 shows the increased arm spacing when using 2500 W compared to 1500 W. To compare the experimental results to the simulated cooling rates, empirical equations for deriving micro-hardness values from cooling rate are taken from literature. First, SDAS is calculated from cooling rate, followed by yield strength calculated from SDAS. Finally, an average micro-hardness is calculated from yield strength. The average magnitude of SDAS of powder-blown AM stainless steel components can be represented as [36],

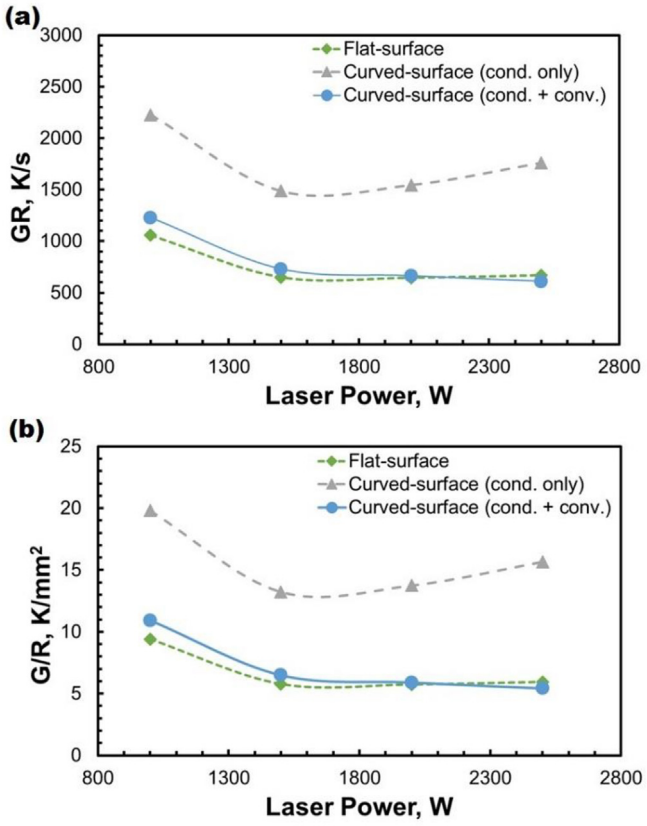

Fig. 8. Comparison of the calculations of (a) cooling rate and (b) temperature gradient to growth rate ratio (G/R) using the current model, flat surface model and heat conduction model for DED of SS 316L at different laser power.

$$\lambda = 50(GR)^{-0.4} \tag{20}$$

where, λ is the SDAS in μm, and GR is the cooling rate in K/s. For very fine columnar dendritic structure, the yield strength can be correlated with SDAS as [15],

$$\sigma_y = \sigma_0 + K_y(\lambda)^{-0.5} \tag{21}$$

Where σ_0 and K_y are constants whose values for SS 316L are 240 MPa and 279 MPa $(\mu m)^{0.5}$, respectively [37]. The average microhardness of SS 316 is related to the yield strength as [15],

$$H_v = 3\sigma_y(0.1)^{-0.25} \tag{22}$$

Applying simulated values of GR from Fig. 8 to Equations (20)–(22) yields the average micro-hardness values presented in Fig. 10, which agree with experimentally measured values, within experimental error. Calculated hardness values for the curved-surface model without fluid convection are significantly higher than the measured experimental values, confirming that fluid convection is a necessary phenomenon to consider when modeling additive manufacturing processes. Without it, the cooling rates become significantly greater due to lack of heat transfer from the front of the pool to the rear, and any properties calculated based on cooling rates will be erroneous.

Finally, the analysis of the thermal strain parameter, ε^*, was carried out in the manner recently proposed by Mukherjee et al. [5]. The thermal strain parameter is stated to be a function of laser speed, laser power, and deposit geometry as [5].

Table 3
Experimental measurements of secondary dendritic arm spacing and Vickers hardness for SS 316L samples.

Laser Power (W)	SDAS (μm)	SDAS Standard Deviation (μm)	Vickers Hardness (HV)	Vickers Hardness Standard Deviation (HV)
1000	2.51	0.67	214.6	2.24
1500	3.19	0.73	211.4	1.85
2000	3.01	0.93	211.2	2.79
2500	3.27	0.65	205.3	3.23

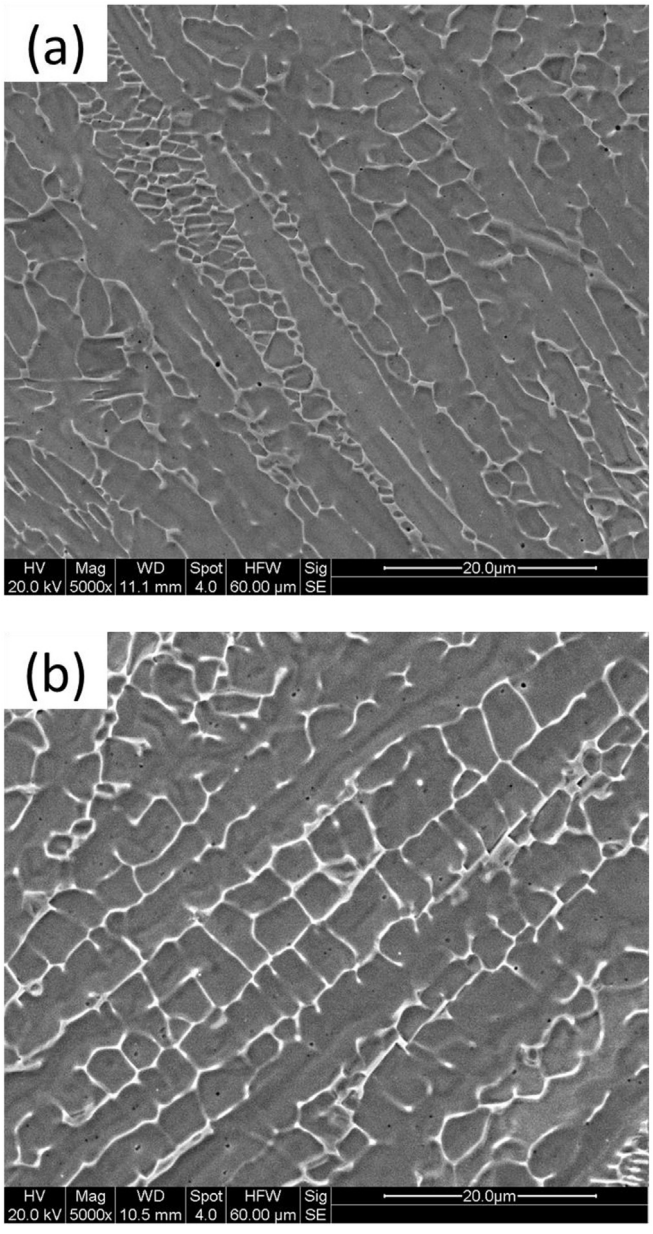

Fig. 9. Scanning electron microscopy image at the transverse cross section of SS 316L build using (a) 1500 W and (b) 2500 W laser power.

$$\varepsilon^* = \frac{\beta \Delta T}{EI} \frac{t}{F\sqrt{\rho}} H^{3/2} \tag{23}$$

where EI is the flexural rigidity of the substrate plate, $\beta\Delta T$ is the volumetric change, t is the deposition time, ρ is the density, F is the Fourier number, and H is the heat input per unit length. Applying

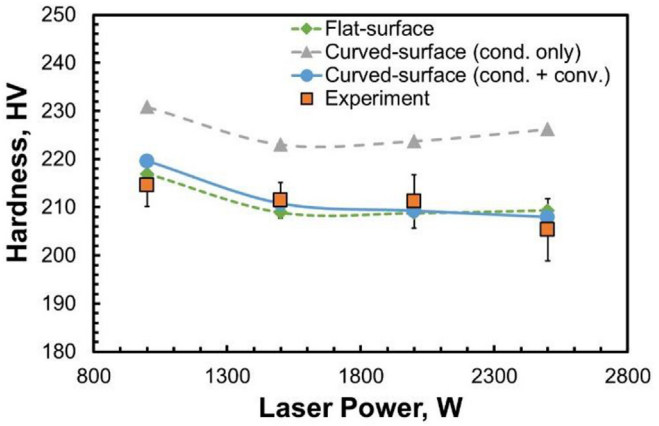

Fig. 10. Comparison of calculated average micro-hardness of stainless steel 316L at various laser powers with experimental data. Error bars are two of the standard deviations calculated for each dataset, in each direction.

Equation (23) to SS 316L and Alloy 800H (Fig. 11) revealed that for both increasing laser powers and scanning speeds, Alloy 800H has a lower ε^* than SS 316L. This is a qualitative result, showing that Alloy 800H is less susceptible to thermal distortion and dimensional inconsistency defects than SS 316L. The sharp increase in ε^* for SS 316L at lower scanning speeds indicates a higher potential for defects with decreasing scanning speed, while Alloy 800H appears to be more resilient to changes in scanning speed. These results show the usefulness of being able to compute the thermal strain parameter for various materials, as the appropriateness of various processing parameters can be determined for each material. While the exact amount of thermal distortion requires more complex modeling, calculations of ε^* allow precautions to be taken to prevent thermal distortion by proper material and/or parameter selection.

5. Summary and conclusions

Building blocks for developing a digital twin of the AM process will utilize a transient, three-dimensional model that calculates temperature and velocity fields, cooling rates, solidification parameters and deposit geometry. This model is proposed, then validated with experimental data of single-pass, single-layer deposits. The following are the most important findings.

(1) The proposed building blocks of a first-generation digital twin of AM have been assembled to accurately estimate 3D curved surface deposit geometry for single-pass deposits, transient temperature and velocity distributions, cooling rates, solidification parameters, secondary dendrite arm spacing and micro-hardness in a computationally efficient manner. Use of the proposed framework will minimize the time consuming and expensive empirical tests to evaluate the effects of the process variables on cooling rates, single-layer deposit geometry and some structural features.

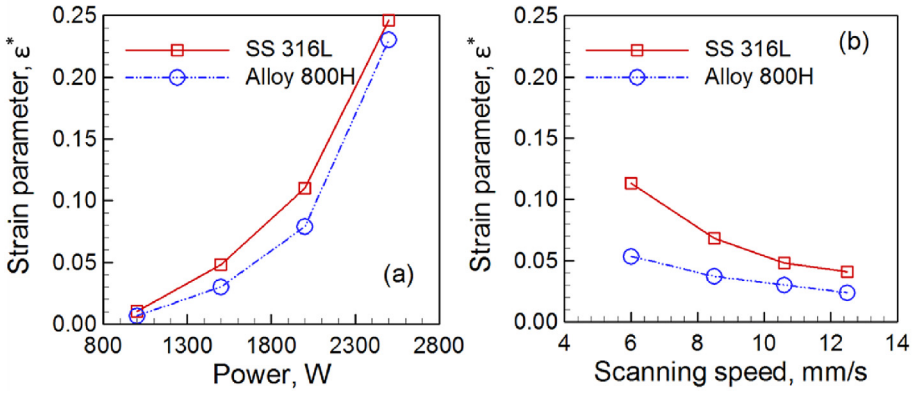

Fig. 11. Calculated thermal strain parameter for SS 316L and Alloy 800H with varying (a) laser power and (b) laser scanning speed.

Table A1
Comparison between estimated and calculated width and height of the deposit.

Material	Laser Power, W	f_m	Calculated width, mm (% error from measured value)	Calculated height, mm (% error from measured value)
SS 316L	1000	0.82	2.23 (−20%)	0.85 (0%)
SS 316L	1500	0.87	2.64 (+4%)	0.90 (+1%)
SS 316L	2000	0.91	2.96 (+16%)	0.92 (+4%)
SS 316L	2500	0.94	3.19 (−16%)	0.93 (−4%)
800H	2000	0.945	3.38 (+12%)	1.44 (−6%)
800H	2500	0.97	3.65 (+6%)	1.48 (−7%)
800H	3000	0.99	3.84 (−3%)	1.49 (−4%)
Average Magnitude of Error:			11.0%	3.7%

Further work could extend these results into a true digital twin capable of accounting for larger-scale factors, such as part geometry.

(2) It is found that the catchment efficiency of the powders increases with higher heat input owing to an increase in molten pool top surface area. A simple analytical model is proposed to predict the catchment efficiency based solely on process parameters and the material properties, enabling back-of-the-envelope calculations that were previously absent in literature.

(3) The convective flow of the molten metal driven by the Marangoni stresses along the curved surface of the deposit significantly changes the temperature distribution, cooling rates and solidification parameters. Mechanical properties such as micro-hardness and secondary dendritic arm spacing can be predicted from the calculated solidification parameters.

(4) Calculation of pool geometry, temperature and velocity fields, and solidification parameters allows for the calculation of many dimensionless numbers. These provide insight into the relative differences of structure, property, and defects expected while doing additive manufacturing of different materials. As an example, calculation of the dimensionless thermal strain parameter, ε^*, shows that SS 316L is more susceptible to thermal distortion defects than Alloy 800H.

Acknowledgements

We acknowledge the support from the Department of Energy Nuclear Energy University Program grant number DE-NE0008280. One of the authors acknowledges support of an American Welding Society research fellowship, grant number 179466.

Appendix A. Supplementary data

Supplementary data related to this article can be found at http://dx.doi.org/10.1016/j.actamat.2017.06.039.

Appendix B. Calculation of maximum deposit width

This appendix details how to calculate the maximum deposit half-width as a fraction, f_m, of the laser beam radius, r_b. The value of f_m is calculated using heat balance, assuming that for a laser with a Gaussian distribution there is some point along the beam radius where the energy density is too small to melt the powder being placed on the substrate.

The upper limit of the value of f_m is 1.0, as the effective energy density outside of the beam radius is zero. Within the laser radius, the power distribution of a laser of nominal power P can be defined as $f(x,y)$, which is typically a bivariate normal distribution function (*i.e.* Gaussian distribution). The limiting factor for laser energy density is that the total energy incident on any one particle of deposit material is greater than or equal to the amount of energy required to melt the particle. The total energy deposited on the particle is expressed as,

$$E_p = (\Delta t^* P)\left(\frac{l}{2r_b}\right)\int_{r}^{r+l}\int_{-r_b}^{r_b} f(x,y)\,dx\,dy \tag{A1}$$

where, laser travel is along the x-axis at scanning speed v_s, r is the distance from the center of the beam, Δt is the total time the laser beam is incident on the particle, and l is the side-length of a small square area the laser is incident upon. As particles are generally spherical, l is a function of particle diameter D_p as,

$$l = \sqrt{\pi}\left(\frac{D_p}{2}\right) \tag{A2}$$

In this scenario, the time Δt it takes the entire laser to pass over one particle is,

$$\Delta t = \frac{2r_b}{v_s} \tag{A3}$$

The amount of energy required to melt a single spherical particle is,

$$E_{req} = \frac{4}{3}\pi\left(\frac{D_p}{2}\right)^3 \rho\left(C_p\left(T_s - T_p\right) + L\right) \tag{A4}$$

where T_s is the solidus temperature and T_p is the preheat temperature. By using a graphical approach to solve $E_P = E_{req}$ for the critical radius $r = r_{crit}$ the maximum deposit width is,

$$r_{crit} = r_b f_m \rightarrow f_m = \frac{r}{r_b} \tag{A5}$$

Now using Equations (6) and (7) the half width b and the height c are calculated for each experimental trial and compared to the experimental measurements. Table A1 presents the results of those calculations, showing that on average the width deviated by 11.0% of the measured experimental value while the height deviated by approximately 3.7%.

References

[1] T. DebRoy, W. Zhang, J. Turner, S.S. Babu, Building digital twins of 3D printing machines, Scr. Mater. 134 (2017) 61–65.
[2] D.D. Gu, W. Meiners, K. Wissenbach, R. Poprawe, Laser additive manufacturing of metallic components: materials, processes and mechanisms, Int. Mater. Rev. 57 (3) (2012) 133–164.
[3] B.E. Carroll, T.A. Palmer, A.M. Beese, Anisotropic tensile behavior of Ti-6Al-4V components fabricated with directed energy deposition additive manufacturing, Acta Mater. 87 (2015) 309–320.
[4] Z. Wang, T.A. Palmer, A.M. Beese, Effect of processing parameters on microstructure and tensile properties of austenitic stainless steel 304L made by directed energy deposition additive manufacturing, Acta Mater. 110 (2016) 226–235.
[5] T. Mukherjee, J.S. Zuback, A. De, T. DebRoy, Printability of alloys for additive manufacturing, Sci. Rep. 6 (2016) 19717.
[6] H.L. Wei, J.W. Elmer, T. DebRoy, Three-dimensional modeling of grain structure evolution during welding of an aluminum alloy, Acta Mater. 126 (2017) 413–425.
[7] H.L. Wei, J.W. Elmer, T. DebRoy, Origin of grain orientation during solidification of an aluminum alloy, Acta Mater. 115 (2016) 123–131.
[8] H. Gong, K. Rafi, H. Gu, T. Starr, B. Stucker, Analysis of defect generation in Ti-6Al-4V parts made using powder bed fusion additive manufacturing processes, Addit. Manuf. 1 (2014) 87–98.
[9] T. Mukherjee, W. Zhang, T. DebRoy, An improved prediction of residual stresses and distortion in additive manufacturing, Comp. Mater. Sci. 126 (2017) 360–372.
[10] T. Mukherjee, V. Manvatkar, A. De, T. DebRoy, Mitigation of thermal distortion during additive manufacturing, Scr. Mater. 127 (2017) 79–83.
[11] T. Mukherjee, V. Manvatkar, A. De, T. DebRoy, Dimensionless numbers in additive manufacturing, J. Appl. Phys. 121 (6) (2017) 064904.
[12] N.E. Hodge, R.M. Ferencz, J.M. Solberg, Implementation of a thermomechanical model for the simulation of selective laser melting, Comp. Mech. 54 (1) (2014) 33–51.
[13] P. Prabhakar, W.J. Sames, R. Dehoff, S.S. Babu, Computational modeling of residual stress formation during the electron beam melting process for Inconel 718, Addit. Manuf. 7 (2015) 83–91.
[14] K. Zeng, D. Pal, H.J. Gong, N. Patil, B. Stucker, Comparison of 3DSIM thermal modelling of selective laser melting using new dynamic meshing method to ANSYS, Mater. Sci. Technol. 31 (8) (2015) 945–956.
[15] V. Manvatkar, A. De, T. DebRoy, Heat transfer and material flow during laser assisted multi-layer additive manufacturing, J. Appl. Phys. 116 (12) (2014) 124905.
[16] L.E. Svensson, B. Gretoft, H.K.D.H. Bhadeshia, An analysis of cooling curves from the fusion zone of steel weld deposits, Scand. J. Metall. 15 (1986) 97–103.
[17] V. Manvatkar, A. De, T. DebRoy, Spatial variation of melt pool geometry, peak temperature and solidification parameters during laser assisted additive manufacturing process, Mater. Sci. Technol. 31 (8) (2015) 924–930.
[18] H. Qi, J. Mazumder, H. Ki, Numerical simulation of heat transfer and fluid flow in coaxial laser cladding process for direct metal deposition, J. Appl. Phys. 100 (2) (2006) 024903.
[19] Y. Lee, M. Nordin, S.S. Babu, D.F. Farson, Effect of fluid convection on dendrite arm spacing in laser deposition, Metall. Mater. Trans. B 45 (4) (2014) 1520–1529.
[20] Y. Cao, S. Zhu, X. Liang, W. Wang, Overlapping model of beads and curve fitting of bead section for rapid manufacturing by robotic MAG welding process, Robot. CIM-Int. Manuf. 27 (3) (2011) 641–645.
[21] M. Alimardani, E. Toyserkani, J.P. Huissoon, Three-dimensional numerical approach for geometrical prediction of multilayer laser solid freeform fabrication process, J. Laser Appl. 19 (1) (2006) 14–25.
[22] C. Doumanidis, Y.-M. Kwak, Multivariable adaptive control of the bead profile geometry in gas metal arc welding with thermal scanning, Int. J. Pres. Ves. Pip. 79 (4) (2002) 251–262.
[23] J. Xiong, G. Zhang, J. Hu, L. Wu, Bead geometry prediction for robotic GMAW-based rapid manufacturing through a neural network and a second-order regression analysis, J. Intell. Manuf. 25 (1) (2014) 157–163.
[24] D.J. Corbin, A.R. Nassar, E.W. Reutzel, A.M. Beese, N.A. Kistler, Effect of directed energy deposition processing parameters on laser deposited Inconel® 718: external morphology, J. Laser Appl. 29 (2) (2017) 022001.
[25] S. Carty, I. Owen, W.M. Steen, B. Bastow, J.T. Spencer, Catchment efficiency for novel nozzle designs used in laser cladding and alloying, in: J. Mazumder, O. Conde, R. Villar, W. Steen (Eds.), Laser Processing: Surface Treatment and Film Deposition, Springer, Netherlands, 1996, pp. 395–410.
[26] K. Partes, Analytical model of the catchment efficiency in high speed laser cladding, Surf. Coat. Technol. 204 (3) (2009) 366–371.
[27] H.K. Lee, Effects of the cladding parameters on the deposition efficiency in pulsed Nd:YAG laser cladding, J. Mater. Process. Tech 202 (1–3) (2008) 321–327.
[28] Y. Huang, M.B. Khamesee, E. Toyserkani, A comprehensive analytical model for laser powder-fed additive manufacturing, Addit. Manuf. 12 (2016) 90–99.
[29] R.M. Mahamood, E.T. Akinlabi, M. Shukla, S. Pityana, Material efficiency of laser metal deposited Ti6Al4V: effect of laser power, Eng. Lett. 21 (1) (2013).
[30] J.S. Turner, Buoyancy Effects in Fluids, Cambridge University Press, 1979.
[31] Z. Fan, F. Liou, Numerical modeling of the additive manufacturing (AM) process of titanium alloy, in: A.K.M. Nural Amin (Ed.), Titanium Alloys–towards Achieving Enhanced Properties for Diversified Applications, InTech, Croatia, 2012, pp. 3–28.
[32] W. Zhang, Probing Heat Transfer, Fluid Flow and Microstructural Evolution during Fusion Welding of Alloys, Department of Materials Science and Engineering, The Pennsylvania State University, 2004.
[33] P.A.A. Khan, T. Debroy, Alloying element vaporization and weld pool temperature during laser welding of AISI 202 stainless steel, Metall. Trans. B 15 (1984) 641–644.
[34] M. Collur, A. Paul, T. DebRoy, Mechanism of alloying element vaporization during laser welding, Metall. Trans. B 18 (1987) 733–740.
[35] A. Raghavan, H.L. Wei, T.A. Palmer, T. DebRoy, Heat transfer and fluid flow in additive manufacturing, J. Laser Appl. 25 (5) (2013) 052006.
[36] H. Yin, S.D. Felicelli, Dendrite growth simulation during solidification in the LENS process, Acta Mater. 58 (4) (2010) 1455–1465.
[37] B.P. Kashyap, K. Tangri, On the Hall-Petch relationship and substructural evolution in type 316L stainless steel, Acta Metall. Mater. 43 (11) (1995) 3971–3981.

Appendix E:

Dimensionless numbers in additive manufacturing

Dimensionless numbers in additive manufacturing

T. Mukherjee, V. Manvatkar, A. De, and T. DebRoy

Citation: J. Appl. Phys. **121**, 064904 (2017); doi: 10.1063/1.4976006
View online: http://dx.doi.org/10.1063/1.4976006
View Table of Contents: http://aip.scitation.org/toc/jap/121/6
Published by the American Institute of Physics

Dimensionless numbers in additive manufacturing

T. Mukherjee, V. Manvatkar, A. De, and T. DebRoy[a)]
Department of Materials Science and Engineering, The Pennsylvania State University, University Park, Pennsylvania 16802, USA

(Received 14 November 2016; accepted 28 January 2017; published online 13 February 2017)

The effects of many process variables and alloy properties on the structure and properties of additively manufactured parts are examined using four dimensionless numbers. The structure and properties of components made from 316 Stainless steel, Ti-6Al-4V, and Inconel 718 powders for various dimensionless heat inputs, Peclet numbers, Marangoni numbers, and Fourier numbers are studied. Temperature fields, cooling rates, solidification parameters, lack of fusion defects, and thermal strains are examined using a well-tested three-dimensional transient heat transfer and fluid flow model. The results show that lack of fusion defects in the fabricated parts can be minimized by strengthening interlayer bonding using high values of dimensionless heat input. The formation of harmful intermetallics such as laves phases in Inconel 718 can be suppressed using low heat input that results in a small molten pool, a steep temperature gradient, and a fast cooling rate. Improved interlayer bonding can be achieved at high Marangoni numbers, which results in vigorous circulation of liquid metal, larger pool dimensions, and greater depth of penetration. A high Fourier number ensures rapid cooling, low thermal distortion, and a high ratio of temperature gradient to the solidification growth rate with a greater tendency of plane front solidification. *Published by AIP Publishing*. [http://dx.doi.org/10.1063/1.4976006]

I. INTRODUCTION

The microstructure and properties of components made by additive manufacturing (AM) vary widely depending on the process parameters selected. These variations originate from the differences in the heat and mass transfer, fluid flow, and solidification during AM, which are influenced by a large number of variables.[1–5] In the laser assisted AM, the variables include laser power, scanning speed, power density, powder flow rate, gas flow conditions, beam traverse path, hatch spacing, layer thickness, and many thermo-physical properties including thermal conductivity, specific heat, density, and solidus and liquidus temperatures of the alloy.[6–9] Achieving structurally sound and reliable components by AM involves understanding and controlling many process variables individually and in appropriate combinations.

There are three main reasons why groups of variables rather than individual variables are of interest in understanding the evolution of the structure and properties of the components made by AM. First, it reduces the number of parameters that need to be investigated in a multi-variable and complex system such as AM. Second, when a group of variables are combined in a non-dimensional form with important physical meanings, such groups of variables, and not the individual constituent variables, express the behavior of the system such as AM. Third, important insights can be totally missed when systematic experiments are conducted by varying one individual variable at a time because such results rarely provide any clue about the influence of the interdependence of a group of variables on the structure and properties of the components.

There are four groups of non-dimensional variables that are of specific interest in AM. First, the non-dimensional heat input represents the ratio of the laser power to scanning speed and is responsible for cooling rates, solidification parameters, fusion zone shape and size, and several other important effects. Second, the Peclet number (Pe) indicates the relative importance of convection and conduction in heat transfer within the melt pool and determines the very mechanism by which the heat is transported within the fusion zone. Third, the Marangoni number (Ma) depicts the magnitude of surface tension force relative to viscous force in the melt pool and is a measure of the strength of the convective transport of heat. By influencing the magnitudes of liquid metal velocities within the melt pool, it affects the geometry of the pool, which is responsible for the solidification structure, thermal distortion, microstructure, and mechanical properties. Finally, the Fourier number (Fo) is the ratio of the rate of diffusive heat transport to the rate of heat storage and critical in understanding the damage heat can do to the components produced by AM. Taken as a whole, these four non-dimensional parameters affect the structure and properties of components built by AM like no individual AM variable.

Because AM is an emerging field, the influential literature in the field is growing, but there is already unmistakable proof about the influence of the four aforementioned non-dimensional numbers in welding and casting. Wei *et al.*[10] showed that in conduction mode laser welding, the Peclet number, Marangoni number, and dimensionless heat input control the shape of the fusion boundary, which in turn affects the solidification process, microstructure, and properties of the weld. Lu *et al.*[11] utilized both the Marangoni number and the Peclet number to explain the variation of the weld pool aspect ratio with respect to heat input and

[a)]Author to whom correspondence should be addressed. Electronic mail: debroy@psu.edu

shielding gas type for gas tungsten arc welding (GTAW) of stainless steel. Robert and DebRoy[12] showed that the unusual shapes of the fusion zone could be correlated using Pe and Ma in laser spot welding. Wei *et al.*[13] explained the difference in the weld pool shape based on the magnitude of the Marangoni number. Weckman *et al.*[14] showed that higher values of Fo slowed down the growth of the melt pool in pulsed laser welding of AISI 409 and AA 1100. Mukherjee *et al.*[15] presented correlations between the thermal strain and Fourier number for the AM of several alloys. Elsen *et al.*[16] and Mazumder[17] used a set of non-dimensional variables to explain the collective influence of process parameters and material behavior during laser processing. The non-dimensional variables correlated processing conditions and alloy properties with heat transfer and fluid flow phenomena and their influence on the structure and properties of the AM components.

Here, we investigate the roles of four well-established dimensionless numbers,[16] non-dimensional heat input, Peclet number, Marangoni number, and Fourier number in the laser based directed energy deposition of three widely used alloys, SS 316, IN 718, and Ti-6Al-4V. A well-tested, three dimensional, transient model is used to compute heat transfer and fluid flow in laser assisted AM. The computed results are examined to understand the role of non-dimensional parameters on the geometry of the fusion zone, solidification parameters, cooling rates, thermal distortion, and other attributes of the AM parts. Although the results presented here are for the laser based directed energy deposition AM process, this approach can be useful for understanding other AM processes.

II. NON-DIMENSIONAL NUMBERS AND THEIR CALCULATIONS

Heat input, which is the ratio of laser power to scanning speed, profoundly affects the structure and properties of the components in both meso and micro-scales. Macro-porosity (pores of equivalent diameters greater than 10 μm), morphology of the solidification front, scale of microstructures, phase compositions, and mechanical properties are affected by heat input like no other variable in 3D printing because they significantly affect temperature fields, thermal cycles, and solidification parameters. A non-dimensional heat input (Q^*) is considered as

$$Q^* = (P/V)/(P_R/V_R), \tag{1}$$

where P and V refer to the laser power and the scanning speed, respectively. P_R and V_R represent the reference laser power and scanning speed that provide the lowest heat input per unit length among the range of process parameters. The non-dimensional heat input, Q^*, therefore provides a measure of the energy deposited per unit length of the deposit.

The convective heat flow inside the molten pool controls the local cooling rate, the G/R ratio, and the solidification process. The relative importance of heat transfer by convection and conduction can be determined from the Peclet number[16]

$$Pe = \frac{UL}{\alpha}, \tag{2}$$

where U is the characteristic velocity, α is the thermal diffusivity of the alloy, and L is the characteristic length. The velocities at the molten pool surface are higher than those in the interior of the pool. The maximum velocity of the molten metal is considered as the characteristic velocity to calculate Pe. The characteristic length in Eq. (2) is considered as the length of the molten pool. A high value of the Peclet number indicates that convective heat transfer is the main mechanism of heat transfer within the liquid metal pool.

The shape and size of the build and the aspect ratio of the molten pool depend on the flow of liquid metal driven primarily by the spatial variation of interfacial tension, also known as the Marangoni stress. Effects of the Marangoni stress on the molten metal velocity is quantified by the Marangoni number[16]

$$Ma = -\frac{d\gamma}{dT}\frac{w\Delta T}{\mu\alpha}, \tag{3}$$

where μ is the dynamic viscosity, α is the thermal diffusivity of the alloy, w is the characteristic length of the molten pool, which is taken as the width of the molten pool, ΔT is the difference between the maximum temperature inside the pool and the solidus temperature of an alloy, and $\frac{d\gamma}{dT}$ is the sensitivity of surface tension gradient with respect to temperature (Table I). For most alloys that do not contain any surface active elements, this quantity is negative.[18] Higher heat input

TABLE I. Thermo-physical properties of SS 316, Ti-6Al-4V, and IN 718.[3,24]

Properties	SS 316	Ti-6Al-4V	IN 718
Liquidus temperature (K)	1733	1928	1609
Solidus temperature (K)	1693	1878	1533
Thermal conductivity (W/m K)	$11.82 + 0.0106\ T$	$1.57 + 1.6 \times 10^{-2}\ T - 1 \times 10^{-6}\ T^2$	$0.56 + 2.9 \times 10^{-2}\ T - 7 \times 10^{-6}\ T^2$
Specific heat (J/kg K)	$330.9 + 0.563\ T - 4.015 \times 10^{-4}\ T^2 + 9.465 \times 10^{-8}\ T^3$	$492.4 + 0.025\ T - 4.18 \times 10^{-6}\ T^2$	$360.4 + 0.026\ T - 4 \times 10^{-6}\ T^2$
Density (kg/m^3)	7800	4000	8100
Volumetric expansion co-efficient (/K)	5.85×10^{-5}	2.5×10^{-5}	4.8×10^{-5}
Viscosity (kg/m s)	7×10^{-3}	4×10^{-3}	5×10^{-3}
$d\gamma/dT$ (N/m K)	-0.40×10^{-3}	-0.37×10^{-3}	-0.26×10^{-3}
Absorption coefficient in liquid (η_l)	0.3	0.3	0.3
Absorption coefficient in powder (η_P)	0.7	0.7	0.7

during AM increases both the peak temperature and the pool dimensions and results in larger values of *Ma*.

Residual stress and distortion are important considerations in AM since multiple cycles of heating, melting, and solidification take place over a prolonged time period. It is the portion of the laser energy that fails to dissipate rapidly and leads to accumulation of heat, large pool size, high thermal strain and distortion, and residual stresses. The Fourier number (F_o) is a relative measure of the heat dissipation rate to the heat storage rate[19]

$$F_o = \alpha\tau/L^2, \tag{4}$$

where α, τ, and L refer to thermal diffusivity, characteristic time scale, and length, respectively. The Fourier number is an inverse measure of how much heat is stored within the component in relation to heat dissipation, and therefore, a higher Fo is desirable. The characteristic time can be expressed as L/V, where L and V are the pool length and scanning speed, respectively. The length of the molten pool is calculated using the heat transfer and fluid flow model. So, Eq. (4) can be re-written as follows:

$$F_o = \alpha/VL. \tag{5}$$

Higher heat input results in a larger molten pool, higher peak temperature, and reduced temperature gradient. As a result, the heat dissipation from the molten pool slows down.

III. HEAT TRANSFER AND FLUID FLOW MODEL

A well tested, three dimensional, transient, heat transfer, and fluid flow model for AM[3,20] is used to compute temperature and liquid metal velocity fields. The model solves the following equations of conservation of mass, momentum, and energy[21,22] in three dimensions

$$\frac{\partial(\rho u_i)}{\partial x_i} = 0, \tag{6}$$

$$\frac{\partial(\rho u_j)}{\partial t} + \frac{\partial(\rho u_j u_i)}{\partial x_i} = \frac{\partial}{\partial x_i}\left(\mu\frac{\partial u_j}{\partial x_i}\right) + S_j, \tag{7}$$

where ρ is the density, u_i and u_j are the velocity components along the i and j directions, respectively, and x_i is the distance along the i direction, t is the time, μ is the dynamic viscosity, and S_j is a source term for the momentum equation. The energy conservation equation[8] is

$$\rho\frac{\partial h}{\partial t} + \frac{\partial(\rho u_i h)}{\partial x_i} = \frac{\partial}{\partial x_i}\left(\frac{k}{C_p}\frac{\partial h}{\partial x_i}\right) - \rho\frac{\partial\Delta H}{\partial t} - \rho\frac{\partial(u_i\Delta H)}{\partial x_i}, \tag{8}$$

where h is the sensible heat, C_p is the specific heat, k is the thermal conductivity, and ΔH is the latent heat content.

The simulations are carried out for the deposition of multilayer structures. The solution domain represents the substrate, deposited layers, and the surrounding gas. Calculations are done over half of the geometry taking advantage of symmetry in many small time steps. Transfer of laser beam energy to the system is defined through a volumetric heat source term. This heat source accounts for the laser energy transfer to powder while in flight from the powder nozzle to the substrate and also after the material reaches the substrate. The volumetric heat source is expressed by the following equation:[23]

$$S_i = \frac{Pd}{\pi r_b^2 t}[\eta_P + (1-\eta_P)\eta_l]\exp\left(-d\frac{r^2}{r_b^2}\right), \tag{9}$$

where η_p is the fraction of laser energy absorbed by the powder during flight from the nozzle to the substrate, P is the nominal laser power, d is the laser beam intensity distribution factor, t is the layer thickness, r_b is the focused beam radius, and r is the radial distance from the beam axis. The first term within the bracket accounts for laser beam energy transferred to the particles during their flight, and second term considers the energy absorbed by the growing layer due to irradiation of the laser beam on the depositing surface. The term η_l refers to the absorption coefficient of the growing layer. The absorption coefficients in Eq. (9) are provided in Table I. The boundary conditions for the thermal analysis include heat loss by convection and radiation with the surroundings. The velocities assigned at the top free surface as boundary conditions are estimated based on surface tension variation due to temperature gradient.

To ensure that there is no energy and mass transfer across the symmetry plane, the spatial gradients of temperature and velocities at the plane of symmetry are set to zero. The initial temperature of the solution domain is considered to be known. Analysis starts with the assignment of substrate properties to all grid points within the substrate. At all grids outside the substrate, the grids are assigned properties of the gas that surrounds the substrate, i.e., argon. For each small stepwise movement of the laser beam, properties of a set of cells under the beam are updated from gas properties to properties of the alloy at the local temperature. After a layer is deposited, an idle time is considered when the laser is switched off. The deposition of a new layer starts from the initial location above the previously deposited layer. The procedure is repeated until the simulation of all the layers is completed. Calculations are continued until the specimen cools to ambient temperature. Simultaneously, the boundary conditions and initial temperature of the solution domain are updated after every time step.

More details about the modeling of powder injection and the solution methodology for AM are described in our previous publications[3,20] and are not repeated here. Only the salient features are indicated here. A control volume method is implemented to discretize the governing equations by dividing the solution domain into small volumes. The discretized equations are solved iteratively using the tri-diagonal matrix algorithm.[3,20] The calculations are performed using an in-house Fortran code compiled using an Intel Fortran compiler. Non-uniform fixed grids are used in the solution domain with finer grid points within the layers and coarser ones in the substrate to achieve a good resolution of variable values and computational accuracy. A solution domain of 20 mm × 3.5 mm × 7.8 mm (length × width × height) is divided into 2,755,000

$(580 \times 50 \times 95)$ grid points. At each time-step, the iterative calculations are continued till the sum of accumulation and heat loss is almost equal to heat input with an imbalance of less than 0.5%, and also, the temperature and velocity components at all grid points satisfy the respective discretized equations within a pre-set error limit of $\pm 0.1\%$. Typically, a total of about 3.5×10^9 linear equations are solved cumulatively to obtain temperature and velocity components for all the time-steps along one layer that takes approximately 28 min in a personal computer with a 3.40 GHz i7 processor and 8 GB RAM.

IV. RESULTS AND DISCUSSION

A. Deposition of SS 316, Ti-6Al-4V, and IN 718 alloys

Figures 1(a)–1(c) show the computed melt pool geometry for the deposition of SS 316, Ti-6Al-4V, and IN 718 for a constant laser power and scanning speed. The red and green bands in the figures indicate the liquid and two phase solid-liquid regions, respectively. The arrows represent velocity vectors in the melt pool, and a reference vector is shown to indicate the magnitudes of the velocities in the melt pool. The bigger pool size for Ti-6Al-4V is attributed to its lower density and thermal diffusivity compared to that for the other two alloys. As expected, higher power results in larger pools for each of the alloys as observed from Figures 1(d)–1(f). The results clearly show that both the processing conditions and the thermo-physical properties of the alloy significantly influence the geometry of the melt pool.

Figure 2 shows a fair agreement between the numerically computed and the corresponding experimentally measured melt pool widths for various layers in a seven layer SS 316 component. Both the computed and the measured results show progressively larger melt pools as the deposition moves to upper layers. However, the increase in pool size is less pronounced in the upper layers. The heat loss from the melt pool to the substrate decreases as more layers are deposited. A slight over-estimation of the computed pool size in Figure 2 is attributed to the uncertainty in the actual rates of heat input and heat loss in the presence of a stream of alloy powder. The agreement between the computed and the experimental results indicates that the model can be used for the calculation of cooling rates, solidification parameters, and the non-dimensional numbers with confidence.

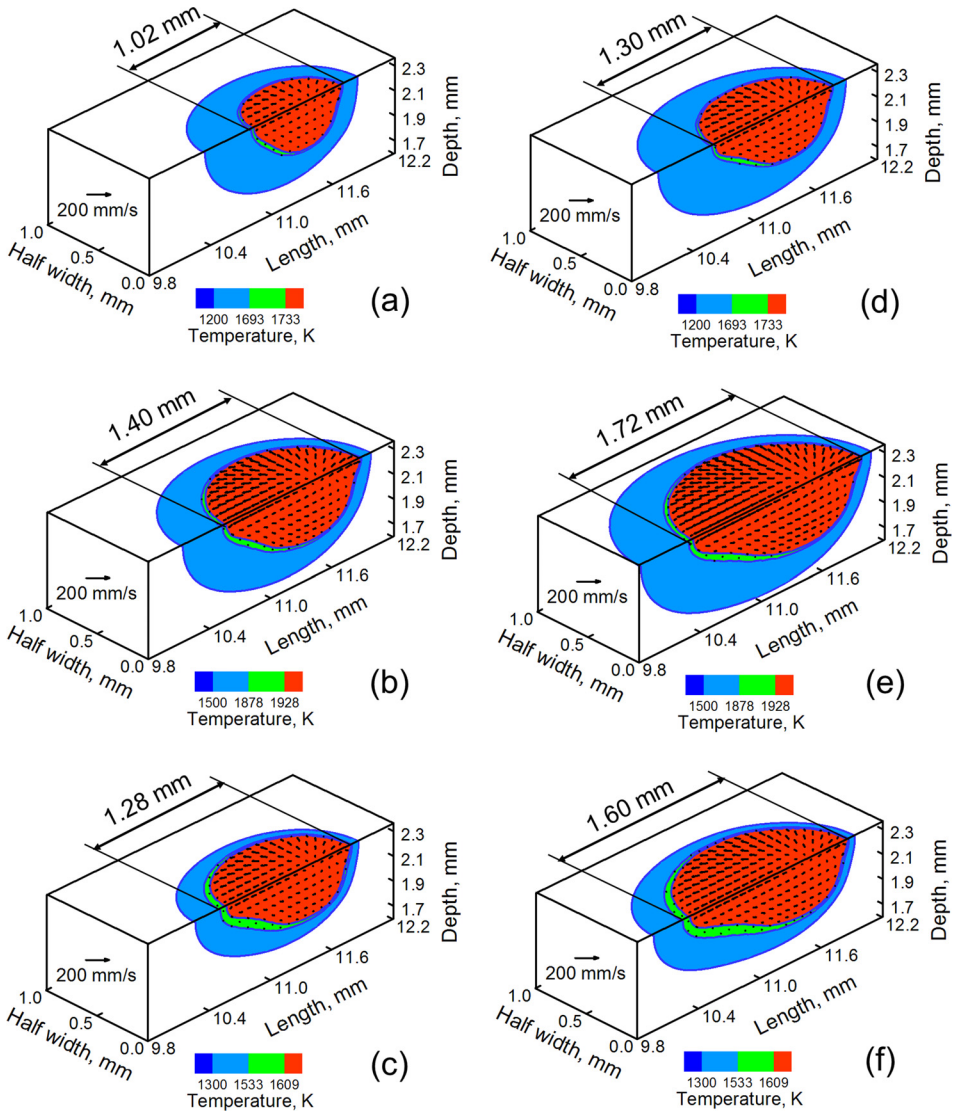

FIG. 1. Temperature and velocity field for a laser power of 190 W for (a) SS 316, (b) Ti-6Al-4V, and (c) IN 718 and of 230 W for (d) SS 316, (e) Ti-6Al-4V, and (f) IN 718. All data are for 15 mm/s scanning speed and at the mid length of the 5th layer.

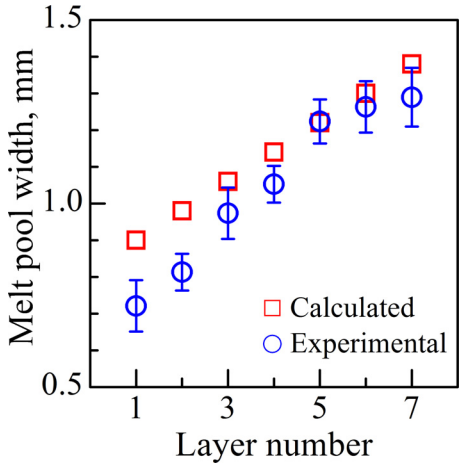

FIG. 2. Comparison of calculated and experimentally measured[25] pool widths for a 7 layer deposition of SS 316. The errors in the experimental measurements are estimated from several readings taken along the layer thickness.

B. Non-dimensional heat input

Figure 3 shows the variation of non-dimensional peak temperature, which is the ratio of the peak temperature, T_P, to the liquidus temperature, T_L, as a function of the non-dimensional heat input, Q^*. As anticipated, the ratio T_P/T_L increases with the increase in Q^* for all three alloys. The reference heat input for Eq. (1) is estimated considering 190 W laser power and 15 mm/s scanning speed, which results in the minimum heat input among the processing conditions listed in Table II. The same heat input is used for all subsequent calculations of non-dimensional heat input unless otherwise specified. Figure 4(a) shows the variations of computed melt pool length in non-dimensional form as a function of non-dimensional heat input Q^* for the three alloy powders. The computed melt pool lengths are the highest for Ti-6Al-4V, which is attributed to its lowest density. Alloys IN 718 and SS 316 have nearly the same density, but the lower liquidus temperature of the former results in greater melt pool size for the same heat input Q^*. Higher heat input can ensure larger melt pools to ensure adequate re-melting of the previously deposited layer to achieve good interlayer

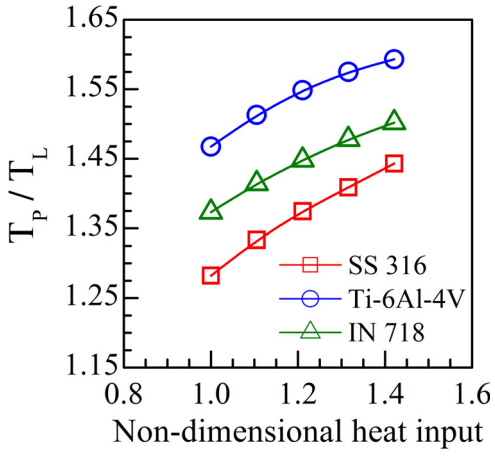

FIG. 3. Effects of the non-dimensional heat input on non-dimensional peak temperature for three alloys.

TABLE II. Process parameters used for calculations.

Laser power (W)	Beam radius (mm)	Scanning speed (mm/s)	Layer thickness (mm)	Substrate thickness (mm)	Powder flow rate (gm/s)
190–270	0.5	15	0.38	4	0.416

bonding. Lack of fusion between two successively deposited layers results in porosity,[9] which adversely affects mechanical properties.[9,15] The porosity due to the lack of fusion between two successively deposited layers can be minimized by increasing heat input. Figure 4(b) shows that the heat input can be correlated with the experimentally measured volume percentage of pores for five different alloys.[26–30] The reference heat input for Figure 4(b) is estimated considering the 175 W laser power and 70 mm/s scanning speed, which provide the minimum heat input among all the process parameter data obtained from the literature.[26–30]

The temperature gradient, G, and the solidification growth rate, R, provide useful information about the evolution of the solidification structure. In particular, GR gives the local cooling rate and G/R influences the morphology of the solidification front.[31,32] Figure 5(a) shows that the calculated cooling rate for a laser assisted AM of SS 316 agrees well with the experimental data.[33] However, errors in the cooling rate estimation are not available in the literature. The reduction of the cooling rate with the heat input (Q^*) is attributed to slower cooling of larger melt pools for high values of Q^*. The variations of the cooling rates are also shown in Figures 5(b) as a function of Q^* for the three alloys. The cooling rates are calculated between the liquidus and solidus temperatures of the alloys at a height of 3.8 mm from the substrate in the mid point of a 20 mm long track. The Ti-6Al-4V deposit attains a higher peak temperature than SS 316 because of its lower density. Ti-6Al-4V also cools slower than SS 316 because of its lower thermal conductivity. However, the slower cooling rate of IN 718 than that of SS 316 can be attributed to its larger pool volume.

For the laser assisted AM of SS 316, a columnar dendritic microstructure secondary arm spacing, d, in the range of 3–10 μm is observed[3,25,34] depending on the cooling rate, CR. The interdependence between the two variables is given by[3]

$$d = A(CR)^{-n}, \tag{10}$$

where d is in μm, CR is the cooling rate in K/s, and A and n are material specific constants having values of 25 and 0.28, respectively.[35] Previous research studies[3,25,36] have shown that for a very fine columnar dendritic structure, the yield strength (σ_y) can be correlated with the secondary dendritic arm spacing[3]

$$\sigma_y = \sigma_0 + K_y\,(d)^{-0.5}, \tag{11}$$

where σ_0 and K_y are constants whose values for SS 316[3] are 150 MPa and 575 MPa $(\mu m)^{0.5}$, respectively. The hardness is related to the yield strength[3]

$$H_v = 3\sigma_y\,(0.1)^{-0.25}. \tag{12}$$

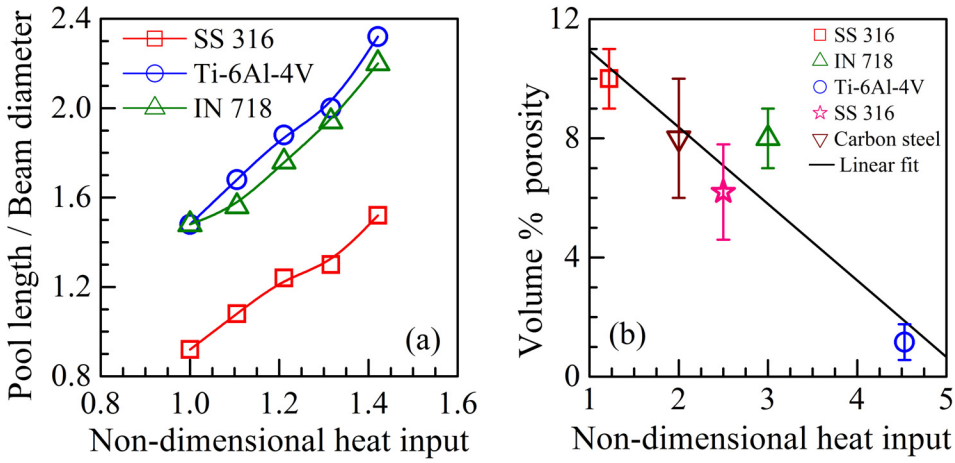

FIG. 4. Effects of the non-dimensional heat input on (a) non-dimensional pool length and (b) volume percentage of lack of fusion porosity for Ti-6Al-4V,[26] IN 718,[27] SS 316,[28] carbon steel,[29] and SS 316.[30] The errors shown are rough estimates based on the data provided in the literature.

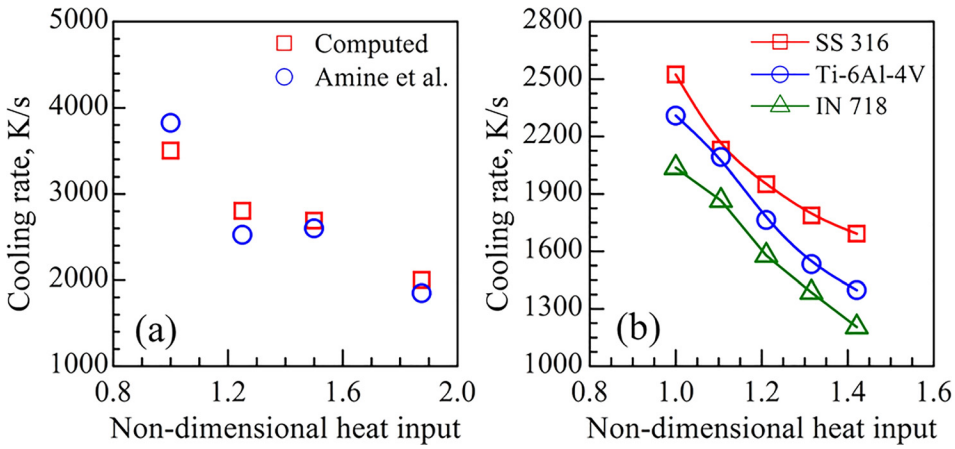

FIG. 5. Effects of the non-dimensional heat input on (a) the cooling rate validated using the data from the literature[33] and (b) the cooling rate for three alloys.

From Eqs. (10)–(12), it is clear that the smaller secondary dendrite arm spacing due to rapid cooling results in higher hardness. Therefore, low heat input results in harder deposits owing to faster cooling as shown in Figure 6(a). This figure also indicates that the calculated hardness for SS 316 agrees well with the experimental data. The presence of laves phases can be detrimental to the mechanical properties of the nickel base superalloys such as IN 718.[37] Formation of these intermetallic compounds can be suppressed by increasing the cooling rate. For example, Nie *et al.*[7] reported a decrease in the volume fraction of the laves phase from 16% to 4% due to an increase in the cooling rate from 500 K/s to 4000 K/s. Parimi *et al.*[38] reported that the parts having the laves phase of 20–30 μm size exhibited worse mechanical properties than that having 1–2 μm size. A rapid cooling due to low heat input can effectively reduce the size of the laves phase as shown in Figure 6(b). This figure is plotted by considering the data from different sources in the literature[38–41] on laser based AM of IN 718. The error values shown are roughly estimated based on the data reported in the literature.

The effect of heat input on the ratio G/R is shown in Figure 7. The temperature gradient in the melt pool is the smallest with IN 718 deposits followed by that in Ti-6Al-4V

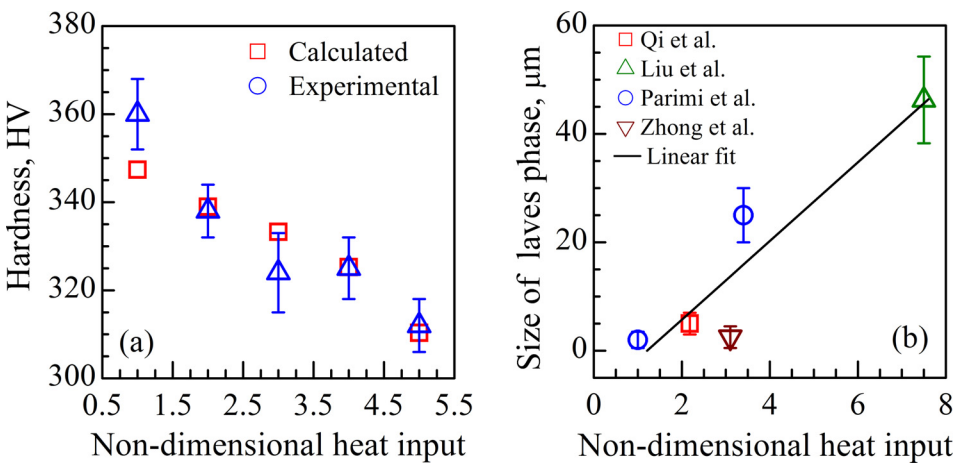

FIG. 6. Effects of the non-dimensional heat input on (a) Vicker's hardness validated using experimental data[35] and (b) size of the laves phase for laser assisted AM of IN 718.[38–41]

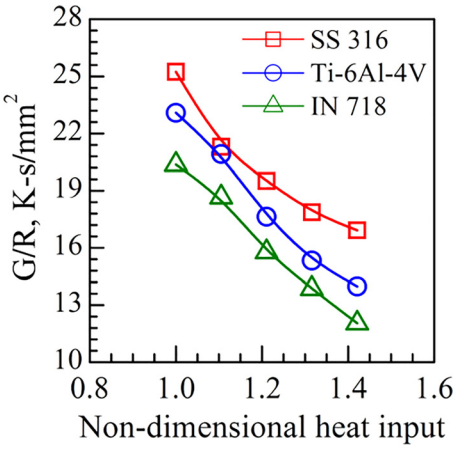

FIG. 7. Variation of the G/R ratio with respect to the heat input for three alloys.

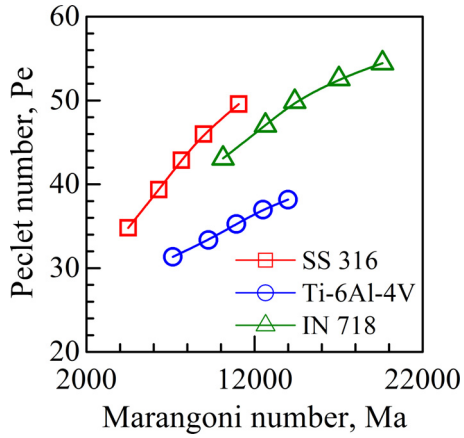

FIG. 9. Relation between the Peclet number and Marangoni number.

and SS 316 alloy deposits. As a result, the SS 316 deposits exhibit the highest G/R followed by that of Ti-6Al-4V and IN 718 alloy deposits.

C. Peclet and Marangoni numbers

Higher heat input increases both the pool length and the velocity of the liquid metal in the melt pool. Therefore, the Peclet number increases with heat input as shown in Figure 8(a) and its value is much higher than 10 for all the cases considered here. These high values indicate that convective heat transfer is the main mechanism of heat transfer within the melt pool. Of the three alloys, Ti-6Al-4V and IN 718 have the highest and the lowest values of thermal diffusivity, respectively (Table I). Therefore, the role of convective heat transfer is the most and the least pronounced for IN 718 and Ti-6Al-4V, respectively, as shown in Figure 8(a).

The Marangoni number, Ma, increases with heat input as shown in Figure 8(b). For a specific heat input, the molten pool volumes of both Ti-6Al-4V and IN 718 deposits are higher than that of SS 316. As a result, both Ti-6Al-4V and IN 718 exhibit higher Marangoni numbers than SS 316. Higher values of the Marangoni number indicate larger velocities of liquid metal in the molten pool. Figure 9 shows that an increase in the Marangoni number also results in higher values of the Peclet number and a more pronounced convective heat transfer within the molten pool.

Higher Ma indicates larger liquid metal velocity and more efficient convective heat transfer, which, in turn, results in a larger liquid metal pool. Lighter alloys also result in a larger molten pool since a smaller weight of alloys is contained in a given volume. Therefore, a combined effect of density and Ma is examined in Figure 10. Both the length and the aspect ratio of the melt pool are enhanced due to higher Ma and lower density of the alloy powder.

D. Fourier number

Susceptibility of alloys to thermomechanical damage (residual stress and distortion) is influenced by their ability to diffuse heat rapidly. The thermal diffusivity of Ti-6Al-4V is higher than those of the other two alloys, and it has the highest Fourier number because of its ability to diffuse heat most efficiently as shown in Figure 11(a). The figure also shows that the Fourier number decreases with an increase in heat input as anticipated. Both slow dissipation and high accumulation of heat result in a large molten pool. Large pools shrink more during solidification and exhibit pronounced thermal distortion. Therefore, a lower Fourier number enhances thermal distortion. In contrast, flexural rigidity of the substrate can resist thermal distortion in AM.[15] The flexural rigidity is defined as a product of elastic modulus, *E*,

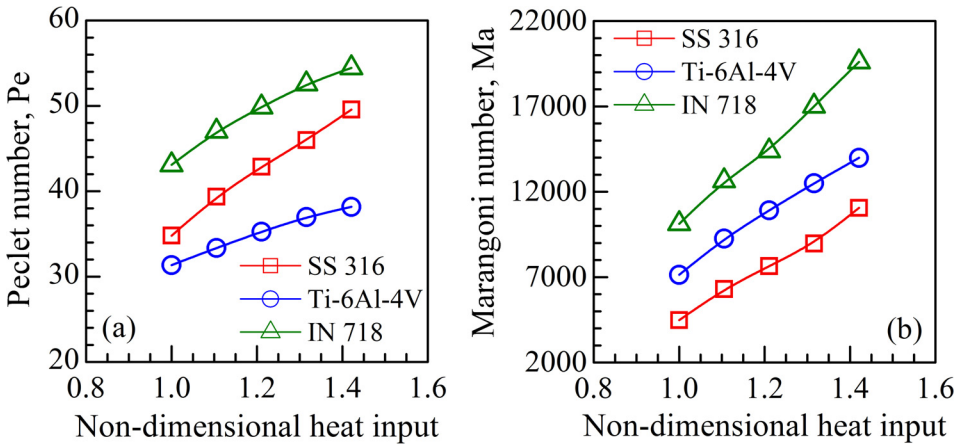

FIG. 8. Effect of linear heat input on the (a) Peclet number and (b) Marangoni number.

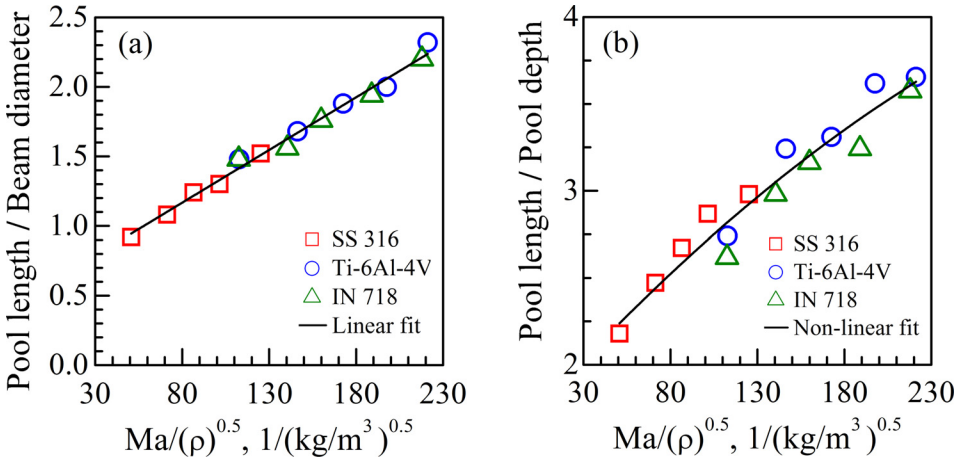

FIG. 10. Effects of the Marangoni number on (a) pool length and (b) aspect ratio of the pool.

of the alloy and the second moment of area, I, of the cross-section of the part geometry. It is recently shown that the following thermal strain parameter, ε^*, is directly related to distortion during solidification of alloys[15,19]

$$\varepsilon* = \frac{\beta \Delta T}{EI} \frac{t H^{3/2}}{F_o \sqrt{\rho}}, \tag{13}$$

where β is the volumetric coefficient of thermal expansion, ΔT is the maximum rise in temperature during the process, E is the elastic modulus, and I is the moment of inertia of the substrate, the product, EI, is the flexural rigidity of the structure, t is the characteristic time, H is the heat input per unit length, F_o is the Fourier number, and ρ is the density of the alloy powder. Figure 11(b) shows the combined effect of both the Fourier number and the flexural rigidity on the thermal strain parameter.[15] It is evident from Figure 11(b) that maintaining a high Fourier number by lowering the heat input is always an effective way to minimize thermal distortion during AM. Figure 11(c) also supports this fact for welding, which is similar to AM for the deposition of a single layer. This figure shows a direct correlation between thermal strain and heat input for three common alloys based on independent experimental data.[42,43] Therefore, a high Fo signifies rapid heat dissipation and low heat storage is desirable to mitigate the thermo-mechanical damage of the fabricated part.

Cooling rates between the liquidus and solidus temperatures of all alloys can be directly correlated with Fo as shown in Figure 12(a). Lower heat accumulation in smaller molten

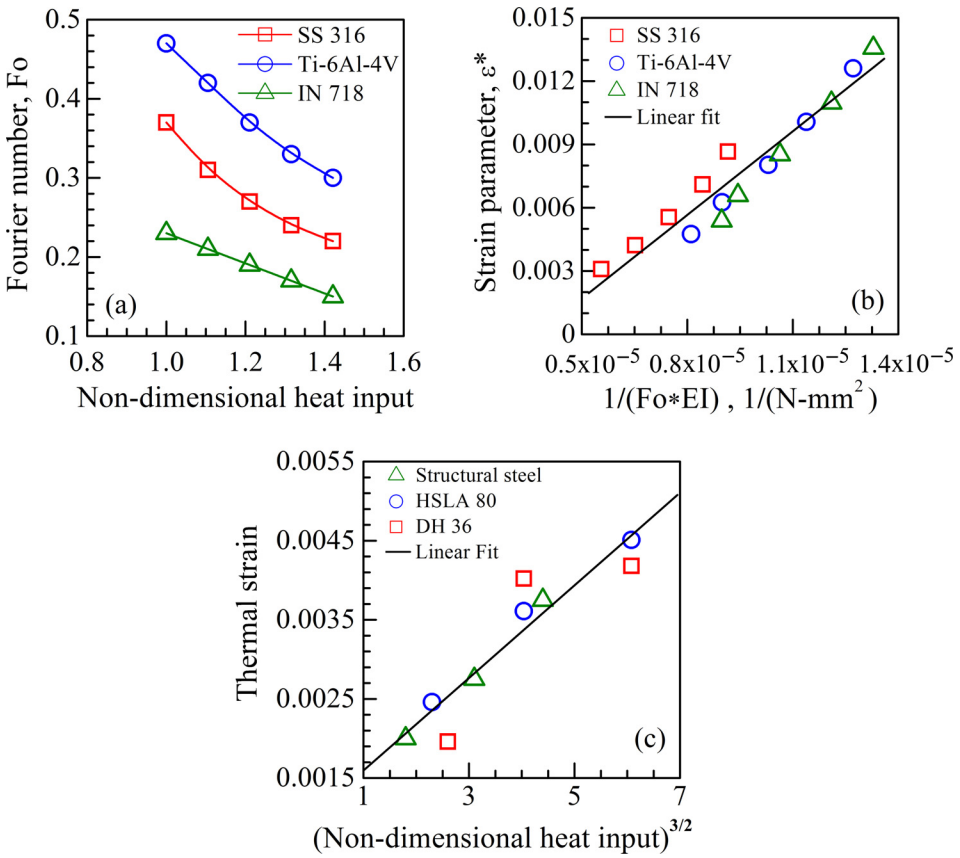

FIG. 11. (a) Fourier number as functions of linear heat input for three alloys, (b) effect of the Fourier number on the thermal strain parameter, and (c) effect of heat input on the thermal strain for structural steel,[42] tool steel,[43] and high strength low alloys steel[43] in welding.

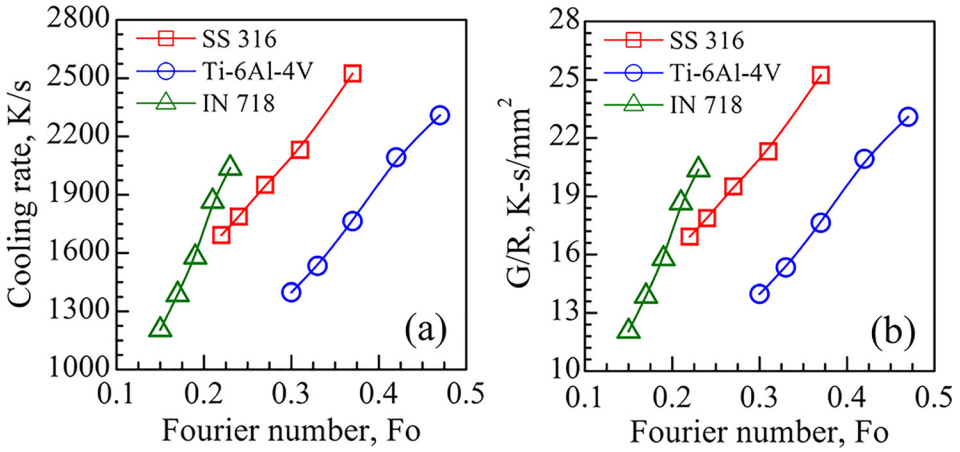

FIG. 12. Effect of the Fourier number on the (a) cooling rate and (b) G/R ratio.

pools results in a higher temperature gradient. Furthermore, a large Fourier number enhances the ratio of temperature gradient (G) to the solidification growth rate (R). Figure 12(b) indicates that the G/R ratio increases with the Fourier number for all alloys. The solid-liquid interface morphology tends to change from cellular, cellular-dendritic to equiaxed dendritic as the value of G/R decreases with a decrease in the Fourier number.

V. SUMMARY AND CONCLUSIONS

The role of non-dimensional numbers in the laser assisted AM of three commonly used engineering alloys, stainless steel 316, Ti-6Al-4V, and a nickel base super alloy IN 718, is examined using a well-tested 3D transient heat transfer and fluid flow model. In particular, the roles of a dimensionless heat input variable, Peclet number, Marangoni number, and Fourier number on temperature and velocity distribution, cooling rate, solidification parameters, hardness, amount of porosity, size of intermetallic compounds, and thermal distortion are evaluated. Below are the specific findings.

1. Higher heat input enhances the peak temperature and pool dimensions. The large pools ensure a stronger interlayer bonding that minimizes the porosity in the fabricated parts.
2. Cooling rates are enhanced for low heat inputs. Formation of the laves phases that are detrimental to the mechanical properties can be suppressed by enhancing the cooling rate in typical AM processing of IN 718 alloy powder.
3. For the conditions of laser assisted AM investigated in this paper, the Peclet numbers are greater than 10. These high values of Pe indicate that convective heat transfer is the main mechanism of heat transfer within the liquid metal pool.
4. A high Marangoni number indicates large velocities inside the molten pool. The rapid movement of the liquid metal inside the pool increases the pool dimensions and aspect ratio. Larger pools with a high aspect ratio promote sound inter layer bonding. Therefore, a high Marangoni number can reduce porosities formed by lack of fusion defects. However, very high Marangoni number may promote instability of the molten pool and increase the susceptibility to defect formation.
5. A high Fourier number can provide a rapid cooling rate and a high G/R ratio. An increase in the Fourier number can also reduce the thermal distortion during AM.

ACKNOWLEDGMENTS

We acknowledge the support from the U.S. Department of Energy NEUP under Grant No. DE-NE0008280. T.M. acknowledges the support from the American Welding Society research fellowship under Grant No. 179466.

[1]D. D. Gu, W. Meiners, K. Wissenbach, and R. Poprawe, Int. Mater. Rev. **57**, 133 (2012).
[2]T. DebRoy, W. Zhang, J. Turner, and S. S. Babu, Building digital twins of 3D printing machines, Scr. Mater. (2017).
[3]V. Manvatkar, A. De, and T. DebRoy, J. Appl. Phys. **116**, 1249051 (2014).
[4]H. Qi, J. Mazumder, and H. Ki, J. Appl. Phys. **100**, 024903 (2006).
[5]X. He and J. Mazumder, J. Appl. Phys. **101**, 053113 (2007).
[6]D. D. Gu and P. Yuan, J. Appl. Phys. **118**, 233109 (2015).
[7]P. Nie, O. A. Ojo, and Z. Li, Acta Mater. **77**, 85 (2014).
[8]A. Raghavan, H. L. Wei, T. A. Palmer, and T. DebRoy, J. Laser Appl. **25**, 052006 (2013).
[9]I. Gibson, D. Rosen, and B. Stucker, *Additive Manufacturing Technologies: 3D Printing, Rapid Prototyping and Direct Digital Manufacturing Ch.10* (Springer, New York, 2015).
[10]P. S. Wei, C. N. Ting, J. S. Yeh, T. DebRoy, F. K. Chung, and G. H. Yan, J Appl. Phys. **105**, 053508 (2009).
[11]S. Lu, H. Fujii, and K. Nogi, Scr. Mater. **51**, 271 (2004).
[12]A. Robert and T. DebRoy, Metall. Mater. Trans. B **32**, 941 (2001).
[13]P. S. Wei, J. S. Yeh, C. N. Ting, T. DebRoy, F. K. Chung, and C. L. Lin, Int. J Heat Mass Transfer **52**, 3790 (2009).
[14]D. C. Weckman, H. W. Kerr, and J. T. Liu, Metall. Mater. Trans. B **28**, 687 (1997).
[15]T. Mukherjee, J. S. Zuback, A. De, and T. DebRoy, Sci. Rep. **6**, 19717 (2016).
[16]M. Elsen, F. Al-Bender, and J.-P. Kruth, Rapid Prototyping J. **14**, 15 (2008).
[17]J. Mazumder, Opt. Eng. **30**, 1208 (1991).
[18]P. Sahoo, T. DebRoy, and M. J. McNallan, Metall. Trans. B **19**, 483 (1988).
[19]T. Mukherjee, V. Manvatkar, A. De, and T. DebRoy, Scr. Mater. **127**, 79 (2017).
[20]V. Manvatkar, A. De, and T. DebRoy, Mater. Sci. Technol. **31**, 924 (2015).
[21]S. A. David and T. DebRoy, Science **257**, 497 (1992).
[22]T. DebRoy and S. A. David, Rev. Mod. Phys. **67**, 85 (1995).
[23]T. Mukherjee, W. Zhang, and T. DebRoy, Comput. Mater. Sci. **126**, 360 (2017).
[24]K. C. Mills, *Recommended Values of Thermophysical Properties for Selected Commercial Alloys* (Cambridge, England, 2002).
[25]V. D. Manvatkar, A. A. Gokhale, G. J. Reddy, A. Venkataramana, and A. De, Metall. Mater. Trans. A **42**, 4080 (2011).

[26]C. J. Kong, C. J. Tuck, I. A. Ashcroft, R. D. Wildman, and R. Hague, in *Proceedings of the Solid Freeform Fabrication Symposium*, Austin, Texas, USA (2011), p. 475.
[27]Q. Jia and D. D. Gu, J. Alloys Compd. **585**, 713 (2014).
[28]A. B. Spierings, M. Schneider, and R. Eggenberger, Rapid Prototyping J. **17**, 380 (2011).
[29]M. A. Taha, A. F. Yousef, K. A. Gany, and H. A. Sabour, Materialwissenschaft und Werkstofftechnik **43**, 913 (2012).
[30]A. Mertens, S. Reginster, Q. Contrepois, T. Dormal, O. Lemaire, and J. Lecomte-Beckers, Int. Mater. Sci. Forum **783–786**, 898 (2014).
[31]H. L. Wei, J. Mazumder, and T. DebRoy, Sci. Rep. **5**, 16446 (2015).
[32]H. L. Wei, J. W. Elmer, and T. DebRoy, Acta Mater. **115**, 123 (2016).
[33]T. Amine, J. W. Newkirk, and F. Liou, Appl. Therm. Eng. **73**, 500 (2014).
[34]B. Zheng, Y. Zhou, J. E. Smugeresky, J. M. Schoenung, and E. J. Lavernia, Metall. Mater. Trans. A **39**, 2228 (2008).
[35]K. Zhang, S. Wang, W. Liu, and X. Shang, Mater. Des. **55**, 104 (2014).
[36]Z. Guo, N. Saunders, P. Miodownik, and J. P. Schillé, in *Proceedings of the ICAA11* (2008), Vol. 22, p. 26.
[37]G. D. Janaki Ram, A. V. Reddy, K. P. Rao, and G. M. Reddy, Sci. Technol. Weld. Joining **9**, 390 (2004).
[38]L. L. Parimi, G. A. Ravi, D. Clark, and M. M. Attallah, Mater. Charact. **89**, 102 (2014).
[39]H. Qi, M. Azer, and A. Ritter, Metal. Mater. Trans. A **40**, 2410 (2009).
[40]F. Liu, X. Lin, H. Leng, J. Cao, Q. Liu, C. Huang, and W. Huang, Opt. Laser Technol. **45**, 330 (2013).
[41]C. Zhong, A. Gasser, J. Kittel, J. Fu, Y. Ding, and R. Poprawe, J. Laser Appl. **28**, 022010 (2016).
[42]S. Okano, M. Mochizuki, M. Toyoda, and T. Ueyama, Sci. Technol. Weld. Joining **17**, 264 (2012).
[43]Y. P. Yang, R. Dull, H. Castner, T. D. Huang, and D. Fanguy, Weld. J. **93**, 421s (2014).

Appendix F:

An improved prediction of residual stresses and distortion in additive manufacturing

Computational Materials Science 126 (2017) 360–372

Contents lists available at ScienceDirect

Computational Materials Science

journal homepage: www.elsevier.com/locate/commatsci

An improved prediction of residual stresses and distortion in additive manufacturing

T. Mukherjee [a], W. Zhang [b], T. DebRoy [a,*]

[a] Department of Materials Science and Engineering, The Pennsylvania State University, University Park, PA 16802, USA
[b] Department of Materials Science and Engineering, The Ohio State University, Columbus, OH 43221, USA

ARTICLE INFO

Article history:
Received 6 September 2016
Received in revised form 30 September 2016
Accepted 1 October 2016
Available online 20 October 2016

Keywords:
Additive manufacturing
3D printing
Laser deposition
Fatigue failure
Thermo-mechanical modeling
Finite element analysis

ABSTRACT

In laser assisted additive manufacturing (AM) an accurate estimation of residual stresses and distortion is necessary to achieve dimensional accuracy and prevent premature fatigue failure, delamination and buckling of components. Since many process variables affect AM, experimental measurements of residual stresses and distortion are time consuming and expensive. Numerical thermo-mechanical models can be used for their estimation, but the quality of calculations depends critically on the accurate transient temperature field which affects both the residual stresses and distortion. In this study, a well-tested, three-dimensional, transient heat transfer and fluid flow model is used to accurately calculate transient temperature field for the residual stress and distortion modeling. The calculated residual stress distributions are compared with independent experimental results. It is shown that the residual stresses can be significantly minimized by reducing the layer thickness during AM. Inconel 718 components are found to be more susceptible to delamination than Ti-6Al-4V parts because they encounter higher residual stresses compared to their yield strength.

1. Introduction

The additive manufacturing (AM) process involves heating, melting and solidification of an alloy by a moving heat source such as a laser or an electron beam in a layer by layer manner [1,2]. As a result, different regions of the work piece experience repeated heating and cooling [2]. The spatially varied thermal cycles result in residual stresses and distortion in the additively manufactured components [3]. The residual stresses, whose magnitude can exceed the yield strength of the alloy, affect corrosion resistance, fracture toughness, crack growth behavior and fatigue performance [4–8]. Moreover, the residual stresses are associated with pronounced deformations especially for thin-walled features [9–13]. Because AM involves many process variables as is the case with fusion welding, experimental measurements of stresses and strains are expensive and time consuming [4,14]. Moreover, experimental measurements depend on the shape and size of the components, nature of the stresses measured, sample preparation and accuracy of X-ray or neutron diffraction [7,14]. A recourse is to undertake calculations of residual stresses and strains in all locations of the work piece [15]. These calculations are often done in two steps in sequence. First, the transient temperature field in the entire work piece is calculated. The computed temperature results are then used for the mechanical calculations. Such sequential calculations of temperatures and stresses make the computations tractable but the accuracy of the calculations depends critically on the quality of the transient temperature field and the thermo-physical property data of the alloy.

As the laser or electron beam energy impinges on the work piece surface, the powder melts quickly to form a molten pool. The highest temperature on the molten pool surface is attained directly below the heat source and the temperature decreases with distance away from this location [16,17]. Inside the molten pool, the liquid alloy recirculates rapidly at very high velocities driven by the spatial gradient of surface tension. The convective flow mixes the liquid metal in different regions and enhances the transport of heat within the molten pool. The circulation pattern strongly affects the temperature distribution in the liquid alloy, heating and cooling rates, solidification pattern, and subsequently the evolution of various solid phases that make up the final microstructure of the part [18,19].

Simulation of complex physical processes that affect the temperature field is computationally intensive, and many of the previous calculations of the temperature field involved various simplifications and assumptions to make the calculations tractable. These include several two-dimensional models [20,21], or an

* Corresponding author.
E-mail address: debroy@psu.edu (T. DebRoy).

http://dx.doi.org/10.1016/j.commatsci.2016.10.003
0927-0256/

Table 1
Thermo-physical properties of Ti-6Al-4V and IN 718 [30].

Properties	Ti-6Al-4V	IN 718
Liquidus temperature (K)	1928	1609
Solidus temperature (K)	1878	1533
Thermal conductivity (W/m K)	$1.57 + 1.6 \times 10^{-2}\,T - 1 \times 10^{-6}\,T^2$	$0.56 + 2.9 \times 10^{-2}\,T - 7 \times 10^{-6}\,T^2$
Specific heat (J/kg K)	$492.4 + 0.025\,T - 4.18 \times 10^{-6}\,T^2$	$360.24 + 0.026\,T - 4 \times 10^{-6}\,T^2$
Density (kg/m^3)	4000	8100
Viscosity (kg/m s)	4×10^{-3}	5×10^{-3}
$d\gamma/dT$ (N/m K)	-0.37×10^{-3}	-0.26×10^{-3}

assumption that the entire deposit is heated and then cooled [22], or building a part by a single layer deposition [23]. In some instances, heat sources have been simplified as surface flux to achieve computational speed [3,23–25]. Another common difficulty is that the calculations ignore the convective heat transfer which is the main mechanism of heat transfer within the liquid, as discussed previously [16–19]. This simplification can lead to the use of inaccurate temperature field for thermo-mechanical calculations [26–28], and the computed residual stress and strain fields do not always agree well with the corresponding experimental data.

The errors in the transient temperature fields and heating and cooling rates resulting from heat conduction calculations that ignore the molten metal convection are well documented in the literature. Svensson et al. noted that "…the heat conduction equation has been found to be inadequate in representing experimental cooling curves" [29]. Manvatkar et al. [16] showed that by ignoring the effect of convection, the cooling rates in additive manufacturing were over-estimated by about twice of the correct values. Therefore, the temperature distribution calculated using heat conduction models without extensive experimental calibrations is not accurate, which in turn, can adversely affect the accuracy in calculations of residual stresses and distortion. What is needed and not currently available is a numerical model that calculates residual stress and strain fields from the transient temperature distribution considering convective heat transfer.

Here we combine a well-tested three-dimensional transient heat transfer and fluid flow model of additive manufacturing with a thermo-mechanical model to accurately calculate the temperature fields, residual stresses and distortion. The calculated temperature and residual stress distributions are tested using independent experimental results. After validation, the model is used to quantitatively study the effect of a wide variety of AM variables such as heat input and layer thickness on residual stresses and distortion. Although the results shown in this article are for direct energy deposition process, the findings will be useful to make dimensionally compliant components and assess residual stresses for all laser assisted powder based AM processes.

2. Modeling

2.1. Assumptions

Some simplified assumptions are made in both the heat transfer and fluid flow model and the thermo-mechanical model. The densities of the solid and liquid metals are assumed to be constant. The surfaces of the deposited layers are considered to be flat. The loss of alloying elements due to vaporization and its effects on both the heat loss and composition change are not incorporated in the present calculations. Finally, the effects of strains induced by solid-state phase transformation and creep are also neglected.

2.2. Governing equations

A well tested, three dimensional, transient, heat transfer and fluid flow model for AM [16,17] is used to compute temperature and liquid metal velocity fields. The model solves the following equations of conservation of mass, momentum and energy [18,19] in three dimensions.

$$\frac{\partial(\rho u_i)}{\partial x_i} = 0 \tag{1}$$

$$\frac{\partial(\rho u_j)}{\partial t} + \frac{\partial(\rho u_j u_i)}{\partial x_i} = \frac{\partial}{\partial x_i}\left(\mu \frac{\partial u_j}{\partial x_i}\right) + S_j \tag{2}$$

where ρ is the density, u_i and u_j are the velocity components along the i and j directions, respectively, and x_i is the distance along the i direction, t is the time, μ is the effective viscosity, and S_j is a source term for the momentum equation. The energy conservation equation is:

$$\rho \frac{\partial h}{\partial t} + \frac{\partial(\rho u_i h)}{\partial x_i} = \frac{\partial}{\partial x_i}\left(\frac{k}{C_p}\frac{\partial h}{\partial x_i}\right) - \rho \frac{\partial \Delta H}{\partial t} - \rho \frac{\partial(u_i \Delta H)}{\partial x_i} \tag{3}$$

where h is the sensible heat, C_p is the specific heat, k is the thermal conductivity, and ΔH is the latent heat content. Table 1 shows the thermo-physical properties of the alloys used for the calculations.

The temperature field as a function of time calculated from the heat transfer and fluid flow model is then imported to a mechanical model based on Abaqus®, a commercial finite element analysis (FEA) code [31]. The total strain increment ($\Delta\varepsilon_{lm}^{tot}$) with respect to time is contributed by the several effects shown below:

$$\Delta\varepsilon_{lm}^{tot} = \Delta\varepsilon_{lm}^{E} + \Delta\varepsilon_{lm}^{P} + \Delta\varepsilon_{lm}^{Th} + \Delta\varepsilon_{lm}^{V} \tag{4}$$

where $\Delta\varepsilon_{lm}^{E}$, $\Delta\varepsilon_{lm}^{P}$ and $\Delta\varepsilon_{lm}^{Th}$ are the elastic, plastic and thermal strain increments respectively. $\Delta\varepsilon_{lm}^{V}$ is the strain induced due to the solid state phase transformation and creep, which is assumed to be zero in the present model. The resulting stress increment estimated from the elastic strain as [5]:

$$\Delta\sigma_{ij}^{E} = D_{ijlm} \cdot \Delta\varepsilon_{lm}^{E} \tag{5}$$

where D_{ijlm} is the elastic stiffness matrix calculated from Young's modulus (E) and Poisson's ratio (υ) as,

$$D_{ijlm} = \frac{E}{1+\nu}\left[\frac{1}{2}(\delta_{ij}\delta_{lm} + \delta_{il}\delta_{jm}) + \frac{\nu}{1-2\nu}\delta_{ij}\delta_{lm}\right] \tag{6}$$

where δ is a Dirac delta function [32] whose value is one only for $i = j$ and $l = m$, and is zero otherwise. Temperature-dependent plasticity with the von Mises yield criterion [5] is utilized to model the flow stress and plastic strain. The thermal strain increment is calculated as:

$$\Delta\varepsilon_{lm}^{Th} = \beta\delta_{lm}\Delta T \tag{7}$$

where β is the volumetric thermal expansion coefficient and ΔT is the temperature increment. The temperature-dependent mechanical properties used for the calculations for Inconel 718 and Ti-6Al-4V are given in Tables 2 and 3, respectively. The step-by-step procedure for calculating temperature distribution, residual stresses and distortion is illustrated in Table 4. A Python script was developed to facilitate mapping the transient temperature fields from the heat transfer and fluid flow model to the Abaqus-based

Table 2
Temperature dependent mechanical properties of IN 718 [33].

Temperature (K)	Young's modulus (GPa)	Temperature (K)	Volumetric expansion co-efficient (/K)	Temperature (K)	Yield stress (MPa)
300	156.3	300	1.17E−05	300	308.9
366.5	151.8	477.6	1.28E−05	588.7	246.3
477.6	144.9	588.7	1.34E−05	810.9	226.1
588.7	138	922	1.46E−05	1033.2	207.7
699.8	131.4	1033.2	1.51E−05	1255.4	114
810.9	124.7	1144.3	1.57E−05		
922	124	1366.5	1.66E−05		
1033.2	123.4	1672	1.66E−05		
1144.3	107.7	1900	1.42E−05		
1255.4	92.05	2400	1.08E−05		
1366.5	68.95	2700	9.47E−06		
1672	23.79	3200	7.84E−06		

Table 3
Temperature dependent mechanical properties of Ti-6Al-4V [34,35].

Temperature (K)	Young's modulus (GPa)	Temperature (K)	Volumetric expansion co-efficient (/K)	Temperature (K)	Yield stress (MPa)
300	125	300	8.78E−06	300	955
533	110	533	9.83E−06	573	836
589	100	589	1.00E−05	773	732
700	93	700	1.07E−05	1023	581
755	80	755	1.11E−05	1073	547
811	74	811	1.12E−05	1173	480
923	55	923	1.17E−05	1273	405
1073	27	1073	1.22E−05	1373	330
1098	22	1098	1.23E−05		
1123	18	1123	1.24E−05		
1573	12	1573	1.30E−05		
1873	9	1873	1.63E−05		

Table 4
Outline of the sequentially-coupled model combining the heat transfer and fluid flow model with the FEA model.

Computational model	Inputs	Outputs	Description
3D transient heat transfer and fluid flow model	Process parameters and temperature dependent thermo-physical properties of the alloys	Temperature and velocity fields	The model solves the equations of conservation of mass, momentum and energy in a 3D discretized solution domain consisted of the substrate, and deposited layers
Importing the nodes, elements and temperature data to the FEA model	Nodes, elements and temperature data from the heat transfer and fluid flow model	A temperature field data file (ODB) that can be imported in the FEA solver for mechanical analysis	A Python script that combines all nodes, elements and corresponding transient temperature data and generates an ODB file that can be directly used in the Abaqus-based FEA solver to calculate stress and strain fields
Abaqus-based FEA model for stress and strain calculations	Nodes, elements, boundary conditions, transient temperature data, and temperature-dependent mechanical properties of the alloys	Transient stress and strain fields	Finite element solution of static force equilibrium equations in the discretized solution domain for the temperature data calculated using the heat transfer and fluid flow model

FEA model. The script used the Abaqus Scripting Interface, an application programming interface (API), to create an ODB file that contained the transient temperature fields. Compared to the other option using Abaqus user subroutine UTEMP to load temperature fields into the stress model, the ODB file had the advantage of more easily handling large dataset of temperature fields.

2.3. Heat source model and boundary conditions

The volumetric heat source term for laser beam used in the heat transfer and fluid flow model is expressed by the following equation [16]:

$$S_i = \frac{Pd}{\pi r_b^2 \lambda}[\eta_P + (1-\eta_P)\eta_l]\exp\left(-d\frac{r^2}{r_b^2}\right) \quad (8)$$

where η_p is the fraction of laser energy absorbed by the powder during flight from nozzle to substrate, η_l refers to the absorption coefficient of the deposited layer, P is the laser power, d is the laser

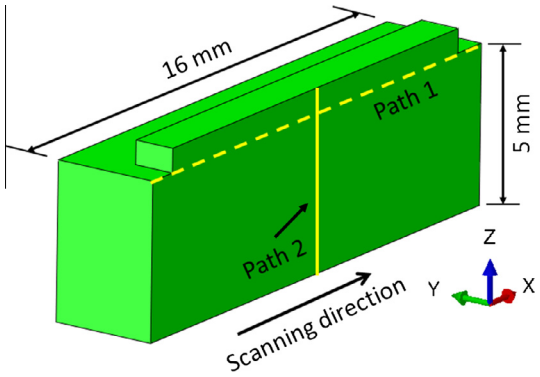

Fig. 1. Solution domain for the heat transfer and fluid flow and mechanical analysis. Due to the symmetry, a half of the solution domain is considered to reduce time and computer memory requirements for the analysis. The two path along which residual stress values are calculated are shown.

Table 5
Process parameters used for calculations.

Parameter set	Laser power (W)	Beam radius (mm)	Scanning speed (mm/s)	Layer thickness (mm)	Substrate thickness (mm)	Powder flow rate (g/s)
1	2000	1.5	10.5	0.90	10	0.432
2	600	0.8	4	0.67	11	0.358
3	200–400	0.5	15	0.4–0.8	4	0.416

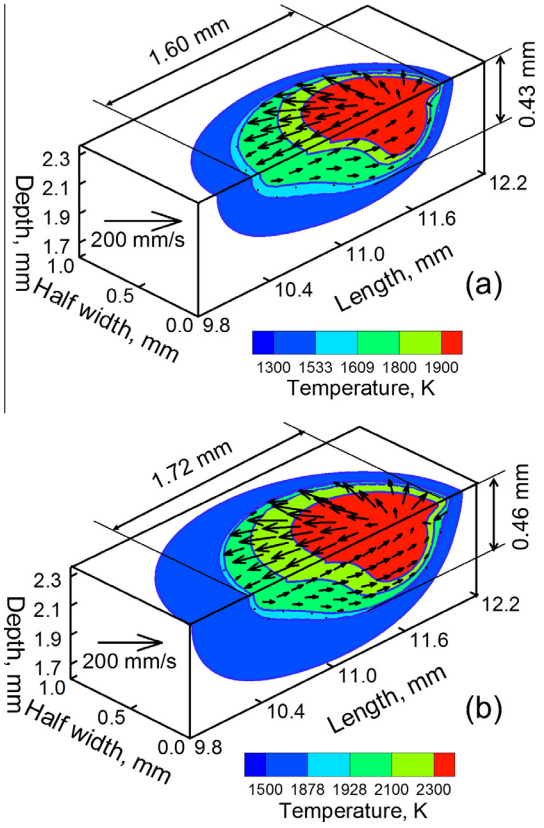

Fig. 2. Temperature and velocity distributions during the deposition of the 2nd layer for (a) IN 718 and (b) Ti-6Al-4V. The simulation is done for 250 W laser power, 15 mm/s scanning speed and 0.4 mm layer thickness.

beam intensity distribution factor, λ is the layer thickness, r_b is the focused beam radius and r is the radial distance from the beam axis. Other boundary conditions for the thermal analysis include heat loss by convection and radiation to the surroundings. The convective flow of molten metal inside the pool is driven by the surface tension gradient on the top surface of the pool resulting from the spatial variation of temperature [18,19]. The resulting Marangoni stress can be expressed as [19]:

$$\tau = \frac{d\gamma}{dT}\frac{dT}{dr} = \mu\frac{du}{dz} \tag{9}$$

where T is the temperature, γ is the surface tension, τ is the Marangoni stress, and r is the radial distance from the axis of the heat source. Fig. 1 represents the solution domain of a 14-mm-long deposit on a 5-mm-thick and 16-mm-long substrate. Calculations are done over a half of the geometry taking advantage of symmetry. The laser beam travels along the positive x-axis. Positive z-axis represents the build direction vertically upward. The boundary conditions for the Abaqus-based mechanical analysis include fixed bottom surface, i.e., the displacements of all nodes of the bottom surface along the x, y and z directions are zero. Table 5 summarizes the additive manufacturing process parameters used in the calculations.

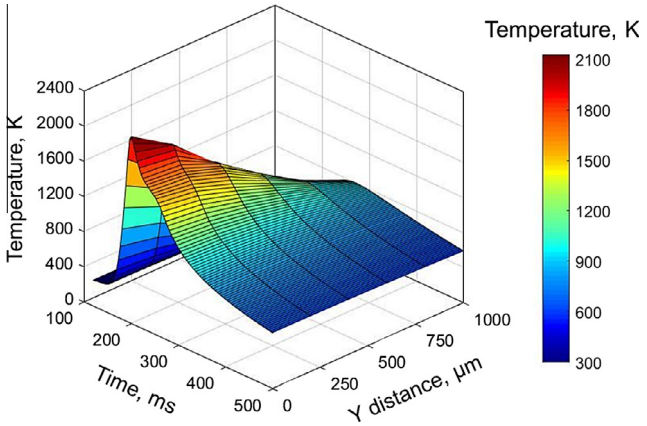

Fig. 3. Temperature variation with time at different locations on the top surface for different y-values but at x = 4.5 mm. This temperature distribution is for a single layer laser assisted deposition of IN 718 powder on IN 718 substrate using the power of 250 W and 15 mm/s scanning speed.

The stresses along x, y and z directions are referred to as the longitudinal, transverse and through-thickness stresses, respectively. From the calculated stress field, these individual residual stress components are extracted along paths 1 and the 2, as shown in Fig. 1. The longitudinal residual stress along path 1 is important because it is a driving force for crack propagation, buckling and distortion. The through-thickness stress along path 2 can be responsible for delamination [23–25].

3. Results and discussions

Fig. 2 shows the computed temperature and velocity fields, and the shape and size of molten pool for IN 718 and Ti-6Al-4V during deposition of the second layer. Each color[1] band in Fig. 2 represents a temperature range shown in the legend and the molten pool lengths are indicated in the figures. It shows that the molten pool size for Ti-6Al-4V is slightly larger than that for IN 718 for the same laser power and scanning speed mainly because of the lower density of Ti-6Al-4V as shown in Table 1. The computed velocity fields in Fig. 2 result from the spatial gradient of surface tension on the top surface of the molten pool. A reference vector is shown by an arrow and a comparison of the length of this arrow with the vectors in the plots indicates the magnitudes of the computed velocities. The results show a strong recirculatory flow of liquid metal from the middle of the pool to the periphery. For the processing conditions considered here, the values of Peclet numbers are significantly higher than 1 (between 9 and 13). Therefore, the calculated Peclet numbers and the magnitude of the velocities clearly show the dominance of convective heat transfer over heat transfer by conduction.

The temperature field in AM is highly transient as well as spatially non-uniform. Fig. 3 represents the temperature variation as a function of time for different locations along the deposit width (y-distance) starting from the pool center (y = 0) for IN 718 deposit.

[1] For interpretation of color in Fig. 2, the reader is referred to the web version of this article.

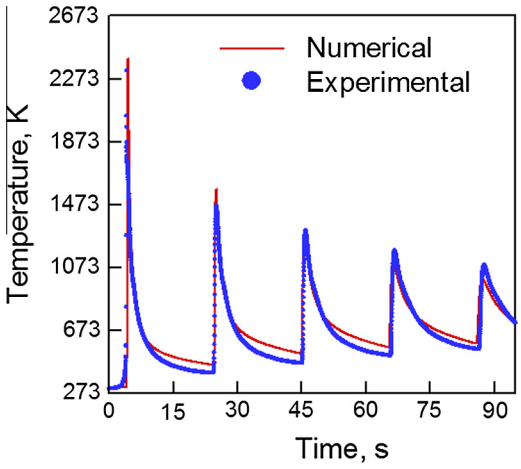

Fig. 4. Comparison of experimentally measured [36] and numerically computed thermal cycle for a 5 layers laser assisted deposition of 150 mm long Ti-6Al-4V deposit on Ti-6Al-4V substrate using process parameter set 1 in Table 5. The monitoring location is at the mid length of the deposit on the top surface of the substrate.

The peak temperature is the highest at the pool center and decreases gradually with distance away from the center. The variation of the temperature with respect to time represents the thermal cycle. Fig. 4 shows that the calculated thermal cycle agrees well with the experimentally measured values [36] for a 5-layer-high deposition of a 150-mm-long Ti-6Al-4V build. The temperature was experimentally measured using a thermocouple located on the top of the substrate at the mid length of the deposit. Thermal cycles are simulated for the entire build using a corresponding solution domain of 150 mm length. The excellent agreement between the experimental and theoretical calculations shows the importance of considering both conduction and convection in the simulation. The agreement also indicates that the computed transient temperature field can be used for the residual stress and strain calculations with confidence.

Fig. 5 shows the temperature distribution for different layers during a 10-layer-high deposition of IN 718 powder. In AM, the substrate acts as a heat sink. Therefore, for the upper layers, heat transfer through the substrate decreases, which in turn, effectively increases the peak temperature for the upper layers. Because of the rapid scanning of laser beam the temperature contours are elongated behind the heat source and compressed in front of the beam. The highly transient and spatially non-uniform temperature distribution, such as that shown in Fig. 5, is responsible for the generation of the stress and strain fields.

Fig. 6 shows the evolution of the longitudinal strain field during the deposition of IN 718. With the progress of the deposition process, more heat accumulates in the work piece. Also, both the peak temperature and the pool volume increase slightly while at the same time the stiffness drops for the upper layers because of

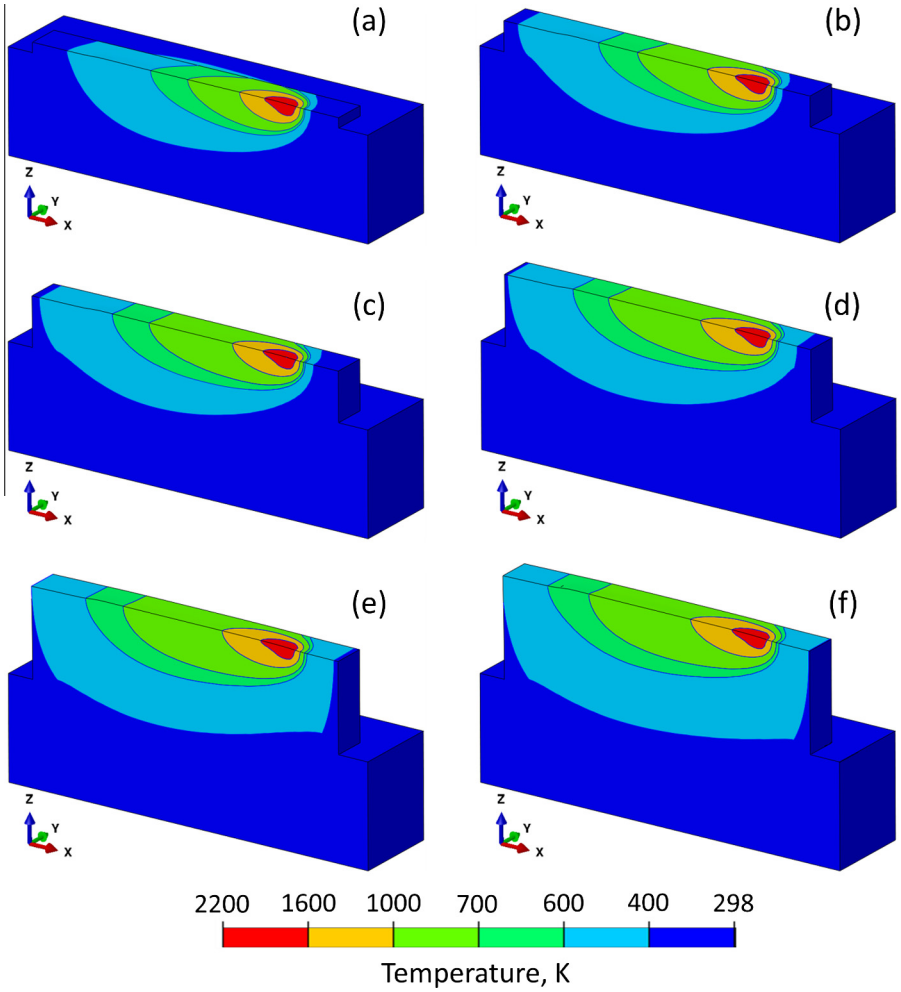

Fig. 5. Temperature distribution during the deposition of (a) 1st (b) 3rd (c) 5th (d) 7th (e) 9th and (f) 10th layer deposition of IN 718 powder on IN 718 substrate. The laser beam position is 10 mm from the starting point of the deposition. Laser beam scanning direction is along the positive x-axis. This simulation is done for 300 W laser power and 15 mm/s scanning speed for the solution domain in Fig. 1.

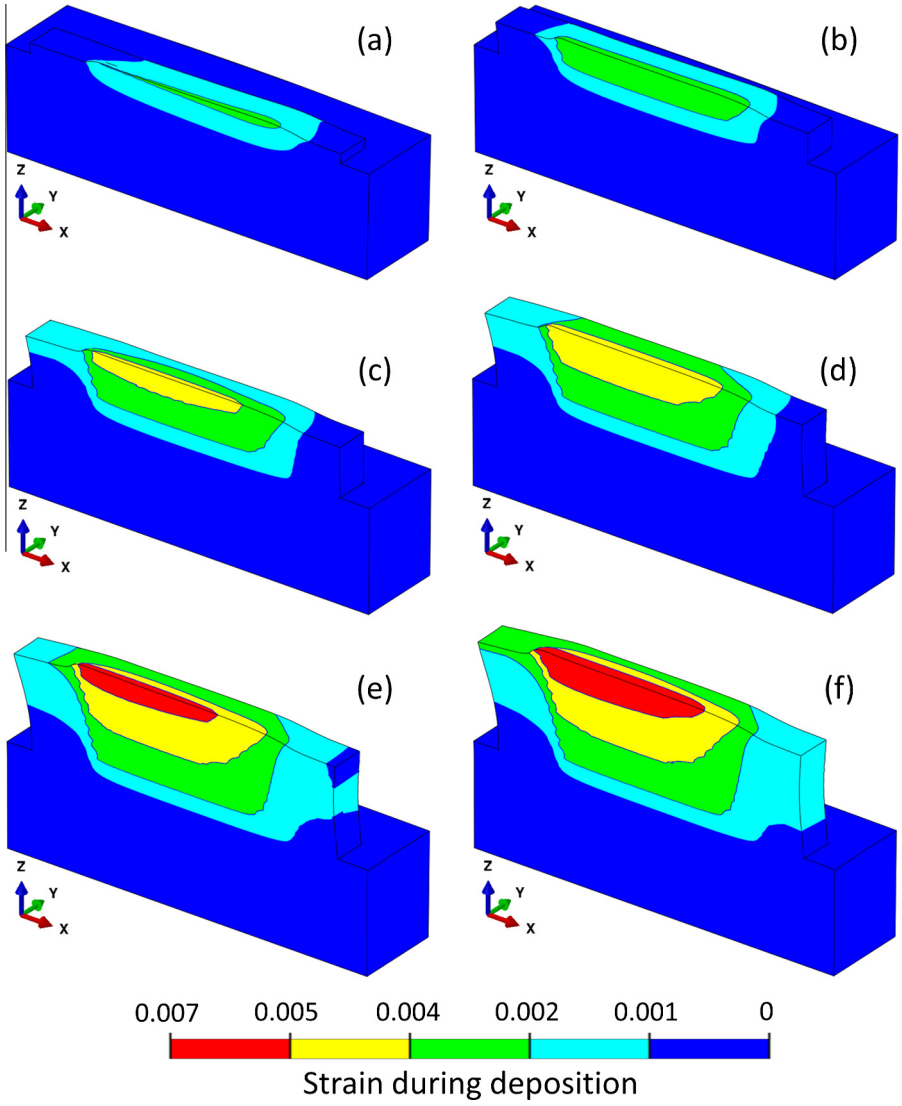

Fig. 6. Longitudinal strain field at the end of depositing (a) 1st (b) 3rd (c) 5th (d) 7th (e) 9th and (f) 10th layer deposition of IN 718 powder on IN 718 substrate. Laser beam scanning direction is along the positive x-axis. This simulation is done for 300 W laser power and 15 mm/s scanning speed for the solution domain in Fig. 1. Deformation is magnified by 10×.

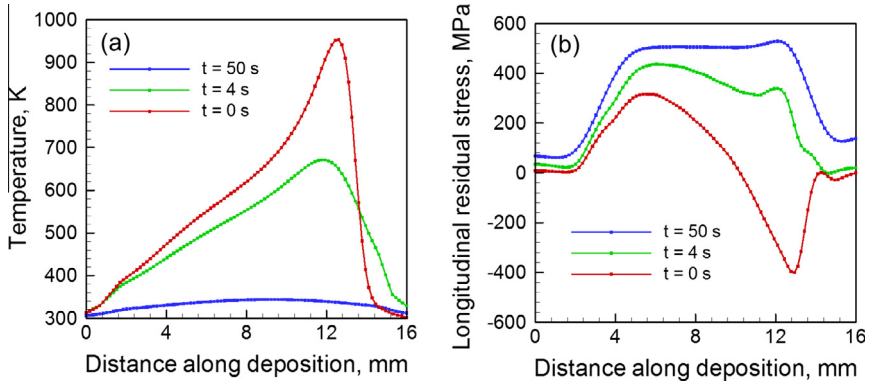

Fig. 7. Variation in (a) temperature distribution and (b) longitudinal stress distribution along path 1 with time after the laser beam extinguishes at the end of 2nd layer. This simulation is done for IN 718 powder deposited on IN 718 substrate with 300 W laser power and 15 mm/s scanning speed. "t" represents the time after the laser beam extinguishes at the end of the deposition.

higher temperatures. Therefore, the strain value increases continuously for the upper layers as shown in Fig. 6(a)–(f). The results indicate that thin-walled, taller structures are more susceptible to deformation than the shorter ones.

Evolution of the stresses depends on the transient temperature distribution especially during cooling of the deposit. Fig. 7(a) shows the temperature distribution along path 1 during cooling of the build. Fig. 7(b) represents the corresponding longitudinal

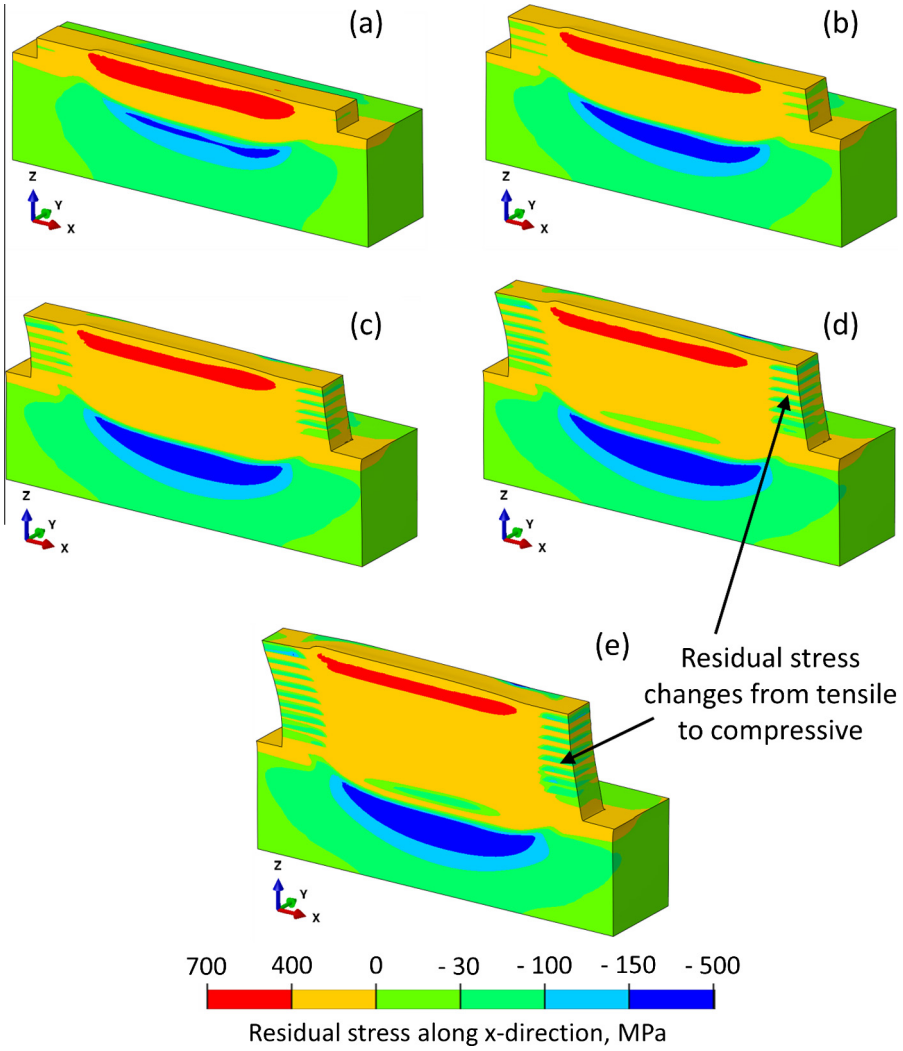

Fig. 8. Residual stress along x-direction (longitudinal) at the end of the deposition of (a) 2nd (b) 4th (c) 6th (d) 8th and (e) 10th layer of IN 718 powder on IN 718 substrate. Laser beam scanning direction is along the positive x-axis. This simulation is done for 300 W laser power and 15 mm/s scanning speed for the solution domain in Fig. 1. Deformation is magnified by 10×.

stress profile developed along path 1. At t = 0 s, i.e., just after the laser beam traverses the entire length and is switched off temporarily to prepare for the deposition of the next layer, the peak temperature of the deposit along path 1 (located at the substrate-deposit interface) is about 950 K. This high temperature softens the material locally. Therefore, the magnitude of the stress is relatively low as it is limited by the yield strength at the high temperature. The stress field evolves as the deposit continues to cool down further. After 50 s, the temperature of the deposit almost cools down to the room temperature and the longitudinal stress along path 1 is highly tensile, as shown in Fig. 7(b). If there was no additional layer deposited, the stress field at the end of cooling would not change further, thus corresponding to the residual stress field in the part.

Figs. 8–10 show the distribution of the residual stresses along x (longitudinal), y (transverse) and z (through-thickness) directions, respectively. The following major observations can be made from these results. The location of the maximum longitudinal and transverse (tensile) residual stresses are near the top of the deposit. For example, after the deposition of the 2nd layer the maximum stress accumulation is observed near the 2nd layer. However, this stress is relieved partially because of the reheating and cooling effects while depositing the upper layers. Therefore, after the deposition of the 4th layer the maximum stress accumulates near layer 4. Similar observations can be made after the depositions of 6th, 8th and 10th layers. Secondly, in both Figs. 8 and 9, the residual stresses change from tensile to compressive at the interfaces of the two successive layers as indicated in the figures. Finally, the through-thickness stress in Fig. 10 is compressive in the center of the deposit and tensile near the start and stop at the substrate deposit interface. These computed stress results can be useful in the future to study the delamination of deposit from substrate, separation of layers and warping.

Fig. 11 shows a fair agreement between the calculated residual stresses with the corresponding experimentally measured values [37] for a dissimilar metal deposition of IN 718 on a Ti-6Al-4V substrate. Fig. 11(a) and (b) represents the longitudinal and through-thickness components of the residual stresses, respectively. The stresses were measured at different locations along path 1 marked in Fig. 1. Several measurements were taken at the same location to estimate the error bar [37]. The reasons for the slight mismatch between the experimental and calculated values could be caused by the measurement difficulty and the assumptions used in numerical calculations; both are susceptible to some errors.

To understand the effect of alloy on the residual stresses, Fig. 12 compares the distribution of the residual stress components along

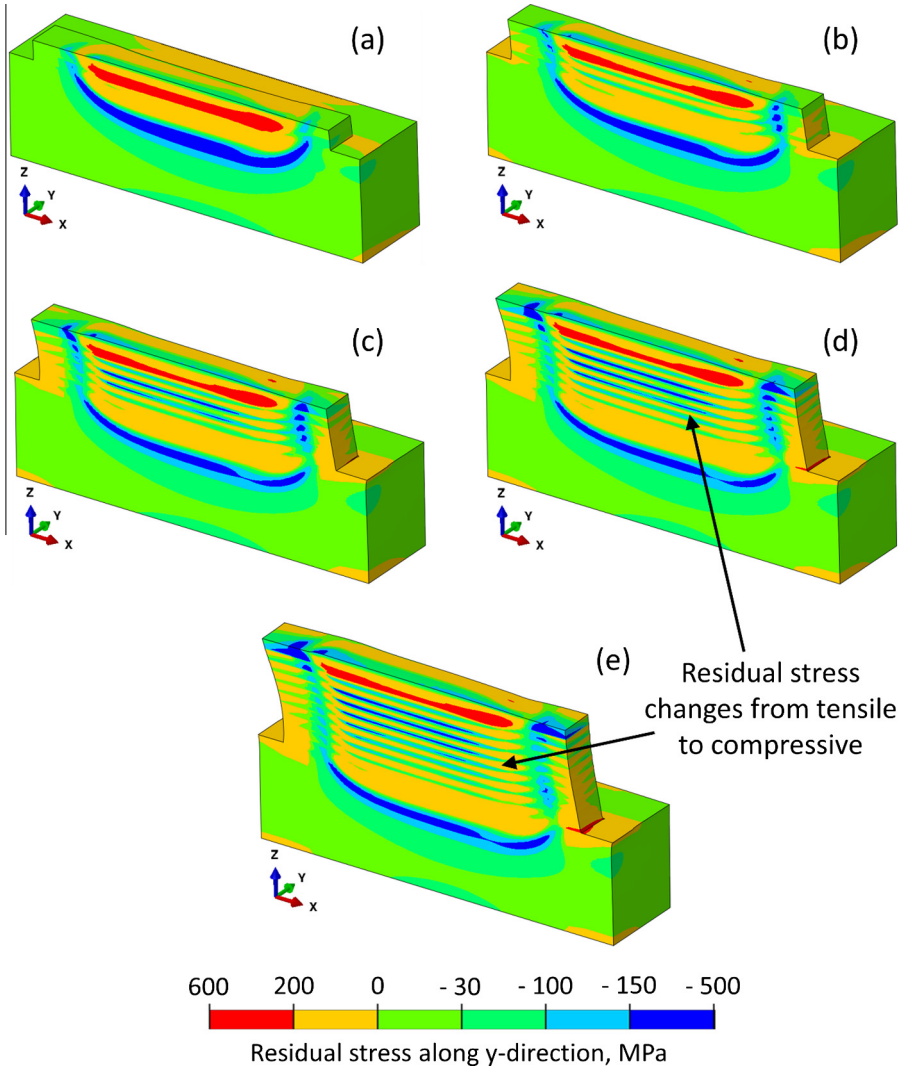

Fig. 9. Residual stress along y-direction (transverse) at the end of the deposition of (a) 2nd (b) 4th (c) 6th (d) 8th and (e) 10th layer of IN 718 powder on IN 718 substrate. Laser beam scanning direction is along the positive x-axis. This simulation is done for 300 W laser power and 15 mm/s scanning speed for the solution domain in Fig. 1. Deformation is magnified by 10×.

x, y and z directions at the end of the cooling of 2nd layer of IN 718 and Ti-6Al-4V deposits. All three residual stress components are highly non-uniform, as expected. The residual stresses in the substrate are mostly compressive. There also exists a sharp gradient of stresses at the substrate-deposit interface. For both alloys the longitudinal stress (x-direction) reaches the maximum at the mid length of the deposit and exhibits a sharp decrease toward both ends (free surfaces). A high gradient in through-thickness residual stress (z-direction) at substrate-deposit interface can potentially cause the separation of the component from the substrate (i.e., delamination). The yield strength of Ti-6Al-4V at room temperature is much higher than that of IN 718 (see Tables 2 and 3). Therefore, the residual stresses are much higher for Ti-6Al-4V as shown in Fig. 12.

Fig. 13(a) also shows that the longitudinal stress along path 1 for Ti-6Al-4V is higher than that for IN 718. However, susceptibility to warping and delamination depends not only on the magnitude of the residual stresses but also the yield strength of the alloy. Therefore, a normalized residual stress [38,39] expressed as the ratio of the longitudinal residual stress along path 1 to the room-temperature yield strength of the alloy is used for assessment of such problems. Fig. 13(b) shows that the normalized stress along path 1 is higher for IN 718 than that of Ti-6Al-4V. This is because of the lower yield strength of IN 718 than Ti-6Al-4V (Tables 2 and 3). Therefore, under same processing conditions, IN 718 is more susceptible to warping and delamination from the perspective of residual stresses. The high susceptibility to warping and delamination of additively manufactured Inconel 718 components is also reported by Prabhakar et al. [40]. It should also be mentioned that the through-thickness stress along path 2 is always lower than the yield strength of the alloy. For example, under the same conditions of Fig. 13, the maximum through-thickness stresses for IN 718 and Ti-6Al-4V are 100 MPa and 450 MPa, respectively.

The formation of tensile residual stresses has significant effects on the mechanical properties of the product. For example, Fig. 14, a plot based on independent literature data [41,42], shows that the fatigue cracks in additively manufactured Ti-6Al-4V parts grow faster in the presence of a higher tensile residual stress in the component. The maximum tensile residual stress values are estimated from the reported stress distributions [41,42]. The y-intercept of the curve is about 8×10^{-6} mm/cycle which corresponds to the crack growth rate with very low residual stresses (such as the traditionally processed Ti-6Al-4V parts) [43]. In the subsequent para-

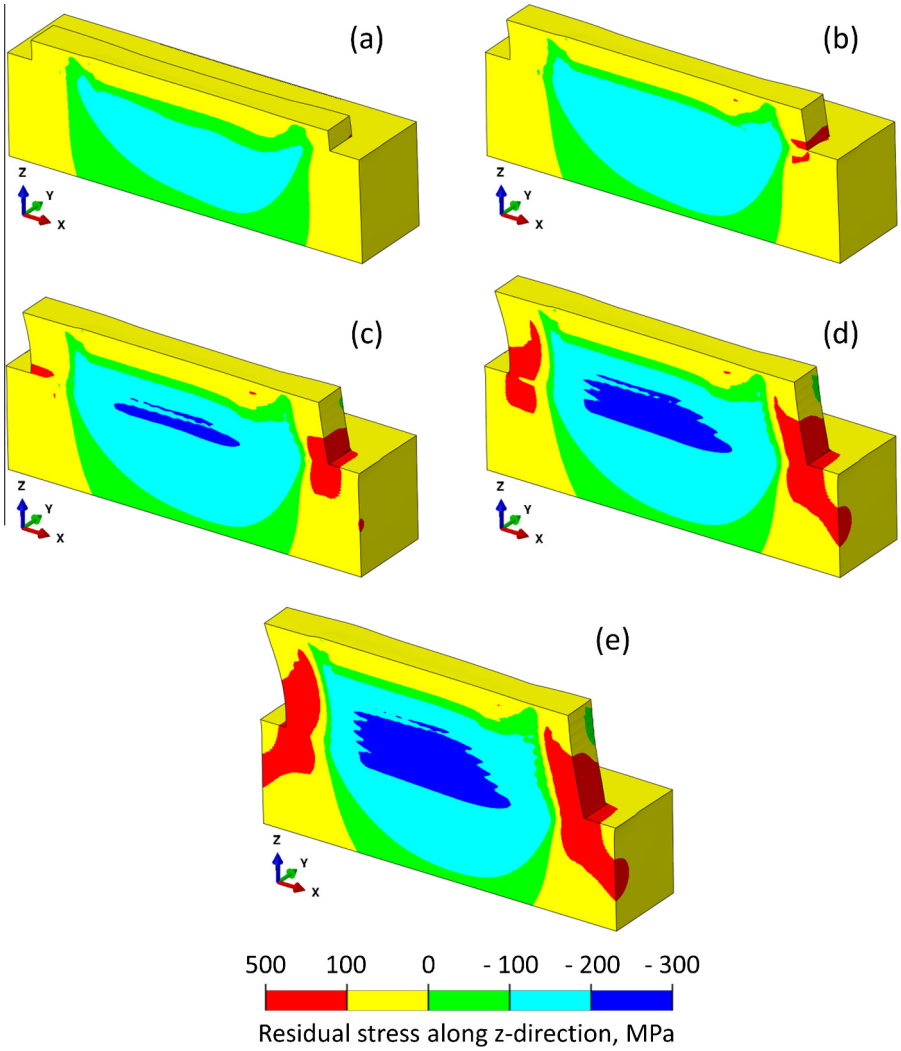

Fig. 10. Residual stress along z-direction (through-thickness) at the end of the deposition of (a) 2nd (b) 4th (c) 6th (d) 8th and (e) 10th layer of IN 718 powder on IN 718 substrate. Laser beam scanning direction is along the positive x-axis. This simulation is done for 300 W laser power and 15 mm/s scanning speed for the solution domain in Fig. 1. Deformation is magnified by 10×.

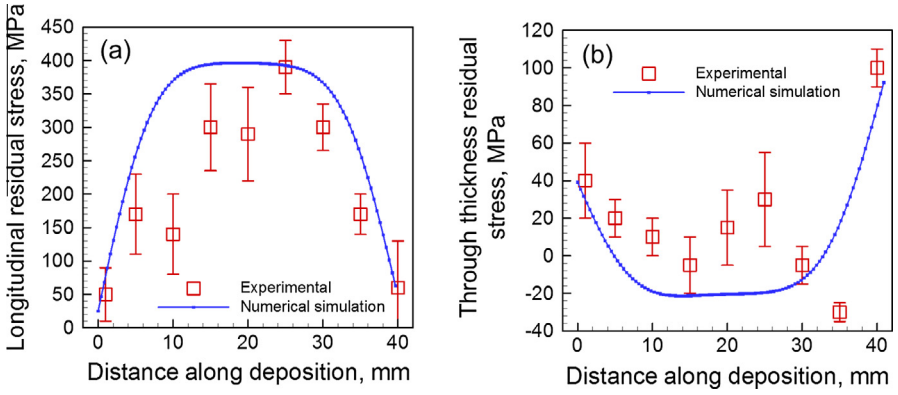

Fig. 11. Comparison of experimentally measured [37] and numerically computed (a) longitudinal residual stress and (b) through-thickness residual stress during the laser deposition of IN 718 powder on a Ti-6Al-4V substrate using process parameter set 2 in Table 5.

graphs the residual stresses resulting from different layer thickness and heat input are discussed to provide a preliminary assessment on the effect of processing parameters on the mechanical property of additively manufactured parts.

Fig. 15(a) and (b) shows the longitudinal and through-thickness residual stress distributions, respectively, during the deposition of a 0.8-mm-high wall using 2 and 4 layers. Building the same height using more layers requires a lower layer thickness. For the same

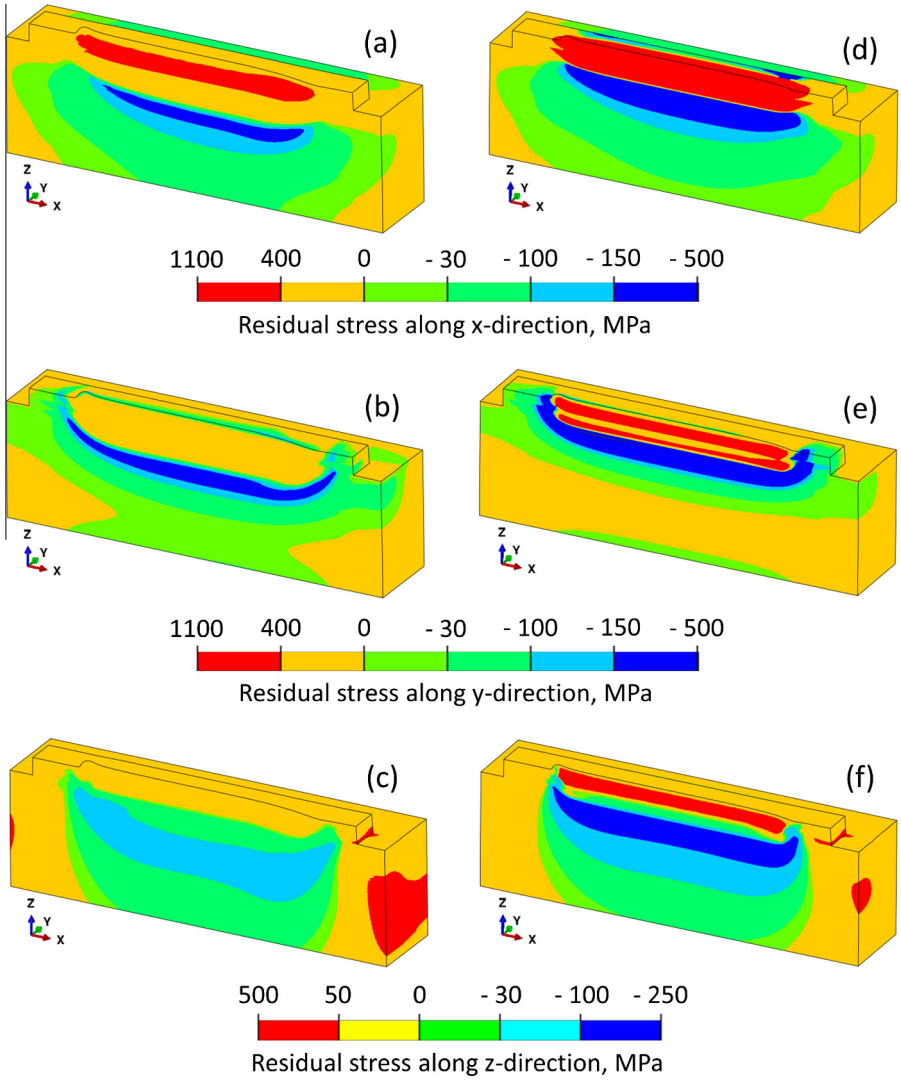

Fig. 12. Residual stress distribution for IN 718 along (a) x (b) y and (c) z directions, and for Ti-6Al-4V along (d) x (e) y and (f) z directions of the 2 layers deposit. Laser beam scanning direction is along the positive x-axis. The simulations are done for 250 W laser power and 15 mm/s scanning speed for the solution domain in Fig. 1.

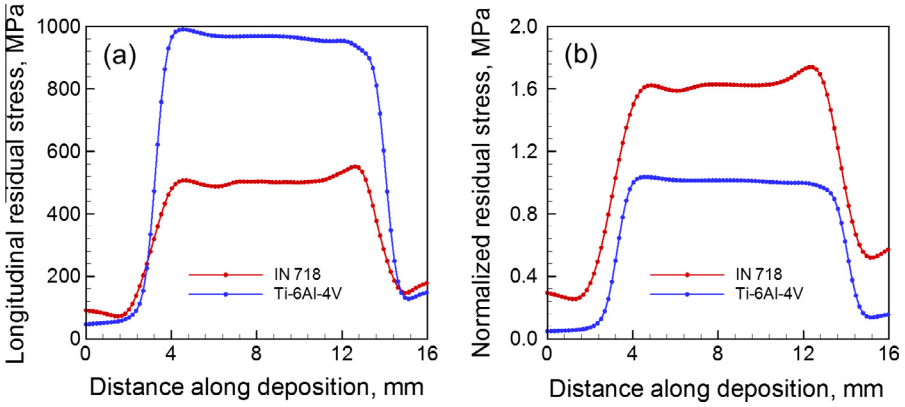

Fig. 13. (a) The longitudinal and (b) the normalized residual stress (longitudinal residual stress/yield strength) distributions along path 1 for IN 718 and Ti-6Al-4V for 250 W laser power and 15 mm/s scanning speed.

laser power and scanning speed, a lower layer thickness increases the volumetric heat flux intensity and hence the peak temperature. At the same time, it takes longer time to build the same height using thinner layers. Therefore, the total deposition time increases. Both the higher peak temperature and more exposure time tend to increase the distortion [44]. However, the deformation can reduce the residual stresses in the deposit. Therefore, both the longitudinal and the through-thickness residual stresses decrease with an increasing number of layers as shown in Fig. 15. For the deposition conditions studied here, the maximum longitudinal and through-

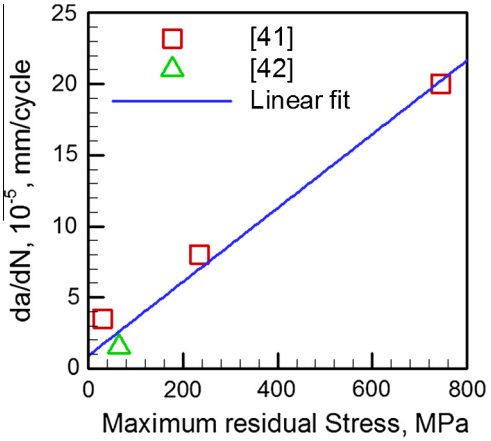

Fig. 14. Fatigue crack growth rate (da/dN) for additively manufactured Ti-6Al-4V components as a function of maximum tensile residual stress. The data are obtained from the crack growth rate curves reported in independent literature studies [41,42]. The stress intensity factor ratio is 0.1 and the stress intensity factor range is 10 MPa $m^{1/2}$.

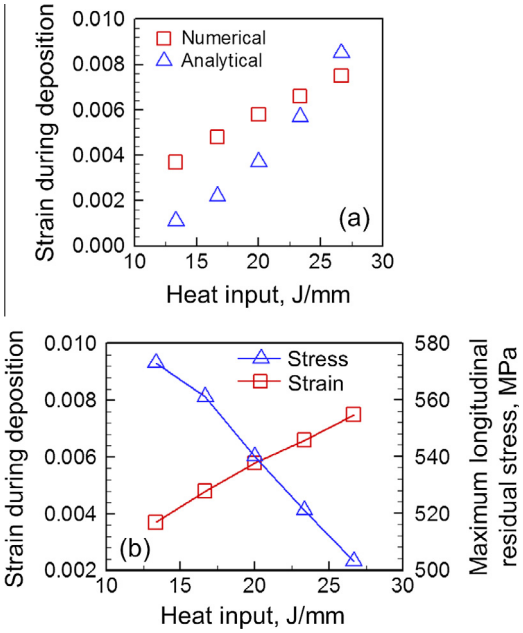

Fig. 16. (a) Variation of thermal strain during deposition as a function of heat input calculated both numerically and analytically, and (b) effect of heat input on maximum longitudinal stress and strain. Both the plots are drawn for 2 layers of IN 718 deposit on IN 718 substrate.

thickness residual stresses can be reduced by about 20% and 30%, respectively by using 4 layers to build the same height instead of 2 layers, as shown in Fig. 15.

To understand the effect of heat input and peak temperature on the distortion and strain, we have recently proposed [44] a strain parameter (ε^*) as an indicator of the susceptibility to distortion.

$$\varepsilon^* = \frac{\beta \Delta T}{EI} \frac{tH^{3/2}}{F_o \sqrt{\rho}} \tag{10}$$

where β is the volumetric coefficient of thermal expansion, ΔT is the maximum rise in temperature during the process, E is the elastic modulus, I is the moment of inertia of the substrate, t is the characteristic time, H is the heat input per unit length, F_o is the Fourier number, and ρ is the density of the alloy. The product, EI, is the flexural rigidity of the structure. Fourier number is the ratio of the heat storage rate to heat dissipation rate. The temperature rise and the Fourier number are both calculated using the heat transfer and fluid flow model. This strain parameter quantitatively represents the peak thermal strain encountered by the fabricated part [44]. Higher heat input increases the peak temperature as well as the pool volume [45]. Larger pools shrink more during solidification and exhibit more distortion. Therefore, strains increase with the heat input. Fig. 16(a) compares the peak thermal strains at the end of the deposition calculated both numerically using the thermo-mechanical model as well as analytically using Eq. (10). Eq. (10) does not consider the plastic strain, and this is probably the reason for the slight mismatch between the analytical and numerical results in Fig. 16(a).

Fig. 16(b) shows that doubling the heat input increases the strain by almost 2.5 times. However, the maximum longitudinal residual stresses can be reduced by about 20% by doubling the heat input. Distortion is often a crucial issue in AM as it affects the dimensional accuracy of the fabricated part [44,46]. On the other hand, the residual stresses can be reduced by post process heat treatment or by reducing the layer thickness. Therefore, an appropriate processing condition is to be carefully selected considering both the distortion and residual stresses. In Fig. 16(b), for example, a heat input of 20 J/mm seems to provide a strain of 0.0057 and a longitudinal residual stress of 540 MPa. This figure is useful to select a heat input considering both the maximum longitudinal residual stress and strain. In practice lower heat input can be achieved by low laser power and faster scanning speed. The layer thickness may also be kept low in order to minimize the residual stresses. This finding is consistent with the current industrial practice. For example, General Electric uses low heat input (100–500 W and 2000 mm/s) and low layer thickness of 40–100 μm to fabricate

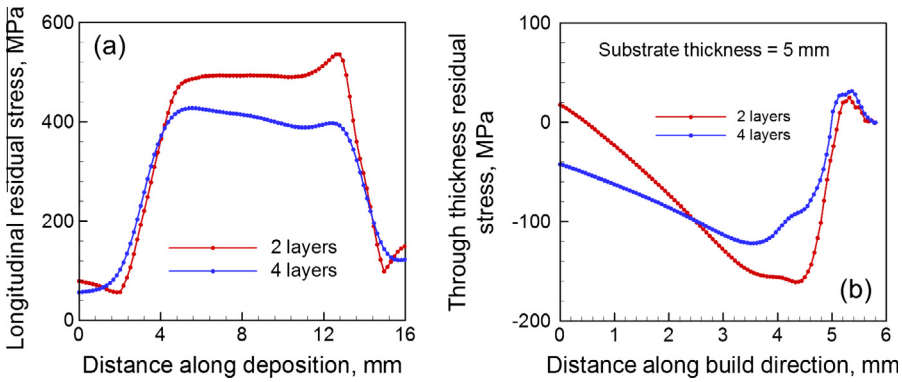

Fig. 15. (a) The longitudinal and (b) the through-thickness residual stress distributions of IN 718 deposit on IN 718 substrate for the process parameter set 3 in Table 5 using 2 and 4 layers deposition to build a 0.8-mm-high wall. The simulations are done for 250 W laser power and 15 mm/s scanning speed.

aero-engine fuel nozzles [47]. Such improved predictive models are essential to help select process parameters and evaluate other strategies such as preheating for mitigating residual stresses and distortion in the future.

4. Summary and conclusions

The evolution of the stresses and strains for Inconel 718 and Ti-6Al-4V and their dependence on important process parameters such as heat input and layer thickness are investigated using a coupled thermal, fluid flow and mechanical model. This model is used to estimate the appropriate heat input and layer thickness to fabricate dimensionally accurate components with low residual stresses. Below are the specific findings.

(1) Ti-6Al-4V components suffer higher residual stresses than IN 718 under the same processing conditions. However, IN 718 parts are more susceptible to warping, delamination and buckling because of their higher residual stress to yield strength ratio.
(2) The AM parts fabricated using thin layers encounter a high peak temperature and long exposure time under the laser beam. As a result, the residual stresses can be decreased as much as 30% by reducing the thickness of each layer to fabricate the component. This finding is consistent with the industrial practice of 40–100 μm layer thickness to produce aero engine fuel nozzles.
(3) Doubling the heat input can reduce the residual stresses by about 20%. However, the same condition enhances the thermal distortion by about 2.5 times. Therefore, an appropriate heat input selected by trading off both distortion and residual stresses will be helpful to fabricate a dimensionally accurate part with good mechanical properties.
(4) The longitudinal residual stress exhibits a steep gradient at the both ends of the deposit that makes the parts susceptible to buckling and warping. The through-thickness stress that is responsible for the possible delamination of a component changes sharply at the substrate deposit interface. The residual stress changes from tensile to compressive at the layer interfaces. In extreme cases, this behavior may result in the separation of layers.

It is hoped that the procedure proposed here will constitute a step forward in predictive modeling and results will be useful to assess residual stresses and make dimensionally compliant AM components.

Acknowledgement

This work was supported by the US Department of Energy NEUP [grant number DE-NE0008280]. One of the authors (T.M.) also acknowledges the support from American Welding Society research fellowship [grant number 179466].

References

[1] D.D. Gu, W. Meiners, K. Wissenbach, R. Poprawe, Laser additive manufacturing of metallic components: materials, processes and mechanisms, Int. Mater. Rev. 57 (2012) 133–164.
[2] W.J. Sames, F.A. List, S. Pannala, R.R. Dehoff, S.S. Babu, The metallurgy and processing science of metal additive manufacturing, Int. Mater. Rev. (2016) 1–46.
[3] J. Ding, P. Colegrove, J. Mehnen, S. Ganguly, P.M. Sequeira Almeida, F. Wang, S. Williams, Thermo-mechanical analysis of wire and arc additive layer manufacturing process on large multi-layer parts, Comput. Mater. Sci. 50 (2011) 3315–3322.
[4] P.H. Chang, T.L. Teng, Numerical and experimental investigations on the residual stresses of the butt-welded joints, Comput. Mater. Sci. 29 (2004) 511–522.
[5] D. Deng, H. Murakawa, Numerical simulation of temperature field and residual stress in multi-pass welds in stainless steel pipe and comparison with experimental measurements, Comput. Mater. Sci. 37 (2006) 269–277.
[6] R.J. Moat, A.J. Pinkerton, L. Li, P.J. Withers, M. Preuss, Residual stresses in laser direct metal deposited Waspaloy, Mater. Sci. Eng. A 528 (2011) 2288–2298.
[7] P. Rangaswamy, M.L. Griffith, M.B. Prime, T.M. Holden, R.B. Rogge, J.M. Edwards, R.J. Sebring, Residual stresses in LENS® components using neutron diffraction and contour method, Mater. Sci. Eng. A 399 (2005) 72–83.
[8] G. Bussu, P.E. Irving, The role of residual stress and heat affected zone properties on fatigue crack propagation in friction stir welded 2024-T351 aluminum joints, Int. J. Fatigue 25 (2003) 77–88.
[9] A.S. Wu, D.W. Brown, M. Kumar, G.F. Gallegos, W.E. King, An experimental investigation into additive manufacturing-induced residual stresses in 316L stainless steel, Metal. Mater. Trans. A 45 (2014) 6260–6270.
[10] J. Zhang, X. Wang, S. Paddea, X. Zhang, Fatigue crack propagation behaviour in wire + arc additive manufactured Ti-6Al-4V: effects of microstructure and residual stress, Mater. Des. 90 (2016) 551–561.
[11] A. Riemer, S. Leuders, M. Thöne, H.A. Richard, T. Tröster, T. Niendorf, On the fatigue crack growth behavior in 316L stainless steel manufactured by selective laser melting, Eng. Fract. Mech. 120 (2014) 15–25.
[12] L.M. Sochalski-Kolbus, E.A. Payzant, P.A. Cornwell, T.R. Watkins, S.S. Babu, R.R. Dehoff, M. Lorenz, O. Ovchinnikova, C. Duty, Comparison of residual stresses in Inconel 718 simple parts made by electron beam melting and direct laser metal sintering, Metal. Mater. Trans. A 46 (2015) 1419–1432.
[13] D. Qiao, W. Zhang, T.-Y. Pan, P. Crooker, S. David, Z. Feng, Evaluation of residual plastic strain distribution in dissimilar metal weld by hardness mapping, Sci. Technol. Weld. Join. 18 (2013) 624–630.
[14] P.J. Withers, H.K.D.H. Bhadeshia, Residual stress. Part 1 – measurement techniques, Mater. Sci. Technol. 17 (2001) 355–365.
[15] G.S. Schajer, Application of finite element calculations to residual stress measurements, J. Eng. Mater. Technol. 103 (1981) 157–163.
[16] V. Manvatkar, A. De, T. DebRoy, Heat transfer and material flow during laser assisted multi-layer additive manufacturing, J. Appl. Phys. 116 (2014) 124905.
[17] V. Manvatkar, A. De, T. DebRoy, Spatial variation of melt pool geometry, peak temperature and solidification parameters during laser assisted additive manufacturing process, Mater. Sci. Technol. 31 (2015) 924–930.
[18] S.A. David, T. DebRoy, Current issues and problems in welding science, Science 257 (1992) 497–502.
[19] A. Raghavan, H.L. Wei, T.A. Palmer, T. DebRoy, Heat transfer and fluid flow in additive manufacturing, J. Laser Appl. 25 (2013) 052006.
[20] A. Vasinonta, J.L. Beuth, M. Griffith, Process maps for predicting residual stress and melt pool size in the laser-based fabrication of thin-walled structures, J. Manuf. Sci. Eng. 129 (2007) 101–109.
[21] M.P. Mughal, H. Fawad, R.A. Mufti, M. Siddique, Deformation modelling in layered manufacturing of metallic parts using gas metal arc welding: effect of process parameters, Model. Simul. Mater. Sci. Eng. 13 (2005) 1187.
[22] A.H. Nickel, D.M. Barnett, F.B. Prinz, Thermal stresses and deposition patterns in layered manufacturing, Mater. Sci. Eng. A 317 (2001) 59–64.
[23] S. Ghosh, J. Choi, Three-dimensional transient finite element analysis for residual stresses in the laser aided direct metal/material deposition process, J. Laser Appl. 17 (2005) 144–158.
[24] P. Mercelis, J.P. Kruth, Residual stresses in selective laser sintering and selective laser melting, Rapid Prototyp. J. 12 (2006) 254–265.
[25] L. Wang, S.D. Felicelli, P. Pratt, Residual stresses in LENS-deposited AISI 410 stainless steel plates, Mater. Sci. Eng. A 496 (2008) 234–241.
[26] G. Vastola, G. Zhang, Q.X. Pei, Y-W. Zhang, Controlling of residual stress in additive manufacturing of Ti6Al4V by finite element modeling, Addit. Manuf. (2016), http://dx.doi.org/10.1016/j.addma.2016.05.010.
[27] Z. Nie, G. Wang, J.D. McGuffin-Cawley, B. Narayanan, S. Zhang, D. Schwam, M. Kottman, Y.K. Rong, Experimental study and modeling of H13 steel deposition using laser hot-wire additive manufacturing, J. Mater. Process. Technol. 235 (2016) 171–186.
[28] M. Alimardani, E. Toyserkani, J.P. Huissoon, A 3D dynamic numerical approach for temperature and thermal stress distributions in multilayer laser solid freeform fabrication process, Opt. Laser Eng. 45 (2007) 1115–1130.
[29] L.E. Svensson, B. Gretoft, H.K.D.H. Bhadeshia, An analysis of cooling curves from the fusion zone of steel weld deposits, Scand. J. Metall. 15 (1986) 97–103.
[30] K.C. Mills, Recommended Values of Thermo-Physical Properties for Selected Commercial Alloys, Woodhead Publishing, Cambridge, 2002.
[31] Abaqus Documentation, Version 6.14, Dassault Systems, 2015.
[32] A. Kamara, S. Marimuthu, L. Li, A numerical investigation into residual stress characteristics in laser deposited multiple layer waspaloy parts, Trans. ASME-B – J. Manuf. Sci. Eng. 133 (2011) 1–9.
[33] P. Scott, R. Olson, J. Bockbrader, M. Wilson, B. Gruen, R. Morbitzer, Y. Yang, C. Williams, F. Brust, L. Fredette, N. Ghadiali Battelle, The Battelle Integrity of Nuclear Piping (BINP), Program Final Report, Columbus, OH, 2005.
[34] T. Seshacharyulu, S.C. Medeiros, W.G. Frazier, Y.V.R.K. Prasad, Microstructural mechanisms during hot working of commercial grade Ti–6Al–4V with lamellar starting structure, Mater. Sci. Eng. A 325 (2002) 112–125.
[35] P. Rangaswamy, H. Choo, M.B. Prime, M.A. Bourke, J.M. Larsen, High temperature stress assessment in SCS-6/Ti-6Al-4V composite using neutron diffraction and finite element modeling, in: International Conference on Processing & Manufacturing of Advanced Materials, Las Vegas, NV, USA, 2000.

[36] F. Lia, R.M. Martukanitz, J.Z. Park, T. DebRoy, T. Mukherjee, J.S. Keist, S.N. Patankar, Process and microstructural validation of the laser-based directed energy deposition process for Ti-6Al-4V and Inconel 625 material, Mater. Sci. Technol. (2015) (Columbus, OH, USA), The abstract can be retrieved from: <http://www.programmaster.org/PM/PM.nsf/ApprovedAbstracts/A0DC8061FC54E5B785257E0A0073048E?OpenDocument>.
[37] K. Shah, I.U. Haq, S.A. Shah, F.U. Khan, M.T. Khan, S. Khan, Experimental study of direct laser deposition of Ti-6Al-4V and Inconel 718 by using pulsed parameters, Sci. World J. 2014 (2014).
[38] A.M. Al-Mukhtar, Residual stresses and stress intensity factor calculations in T-welded joints, J. Fail. Anal. Prevent. 13 (2013) 619–623.
[39] R. Jackson, I. Chusoipin, I. Green, A finite element study of the residual stress and deformation in hemispherical contacts, J. Tribol. 127 (2005) 484–493.
[40] P. Prabhakar, W.J. Sames, R. Dehoff, S.S. Babu, Computational modeling of residual stress formation during the electron beam melting process for Inconel 718, Addit. Manuf. 7 (2015) 83–91.
[41] S. Leuders, M. Thöne, A. Riemer, T. Niendorf, T. Tröster, H.A. Richard, H.J. Maier, On the mechanical behaviour of titanium alloy TiAl6V4 manufactured by selective laser melting: fatigue resistance and crack growth performance, Int. J. Fatigue 48 (2013) 300–307.
[42] P. Edwards, A. O'Conner, M. Ramulu, Electron beam additive manufacturing of titanium components: properties and performance, J. Manuf. Sci. Eng. 135 (2013) 061016.
[43] A.G. Gavras, F.C. Brendan, D.A. Lados, Effects of microstructure on the fatigue crack growth behavior of light metals and design considerations, Matéria (Rio de Janeiro) 15 (2010) 319–329.
[44] T. Mukherjee, J.S. Zuback, A. De, T. DebRoy, Printability of alloys for additive manufacturing, Sci. Rep. 6 (2016).
[45] H.L. Wei, J.W. Elmer, T. DebRoy, Origin of grain orientation during solidification of an aluminum alloy, Acta Mater. 115 (2016) 123–131.
[46] T. Mukherjee, V. Manvatkar, A. De, T. DebRoy, Mitigation of thermal distortion during additive manufacturing, Scripta Mater. 127 (2017) 79–83.
[47] P.M. Kenney, D.E. Lindley, General Electric Company, 2013, U.S. Patent Application 14/440, 154.

Appendix G:

Mitigation of thermal distortion during additive manufacturing

Scripta Materialia 127 (2017) 79–83

Contents lists available at ScienceDirect

Scripta Materialia

journal homepage: www.elsevier.com/locate/scriptamat

Regular article

Mitigation of thermal distortion during additive manufacturing

T. Mukherjee, V. Manvatkar, A. De, T. DebRoy *

Department of Materials Science and Engineering, The Pennsylvania State University, University Park, PA 16801, USA

ARTICLE INFO

Article history:
Received 28 May 2016
Received in revised form 26 July 2016
Accepted 3 September 2016
Available online xxxx

Keywords:
Additive manufacturing
3D printing
Laser deposition
Thermal strain

ABSTRACT

Additively manufactured parts are often distorted because of spatially variable heating and cooling. Currently there is no practical way to select process variables based on scientific principles to alleviate distortion. Here we develop a roadmap to mitigate distortion during additive manufacturing using a strain parameter and a well-tested, three-dimensional, numerical heat transfer and fluid flow model. The computed results uncover the effects of both the key process variables such as power, scanning speed, and important non-dimensional parameters such as Marangoni and Fourier numbers and non-dimensional peak temperature on thermal strain. Recommendations are provided to mitigate distortion based on the results.

Laser assisted additive manufacturing (AM) process produces 'near net shape' parts from a stream of alloy powders in a layer-by-layer manner for use in medical, aerospace, automotive and other industries [1,2]. The parts undergo repeated spatially variable heating, melting, solidification and cooling during AM [3,4]. Due to the transient heating and cooling, the fabricated parts exhibit thermal distortion [5–10]. Thermal distortion results in dimensional inaccuracy and adversely affects performance of the fabricated parts [11]. Previous work has shown that increase in net heat input [7] and reduction in dwell time [8] between deposition of successive layers can increase thermal distortion. It is also known that the alloy properties, the deposit and substrate dimensions, the laser scanning pathway, the hatch spacing between layers and the heating and cooling conditions significantly affect thermal distortion [9,12,13].

The existing AM literature does not provide any guidance for selecting process variables to minimize thermal distortion. A quantitative understanding of the effects of process variables on thermal distortion and a practical means to mitigate this problem based on scientific principles are needed but not generally available.

Here, we show for the first time how thermal distortion during AM can be minimized by back of the envelope calculations. The procedure involves evaluation of the effects of common process variables such as laser power and scanning speed on thermal strain. In addition, the non-dimensional parameters that are important for heat transfer and fluid flow phenomena in AM such as Fourier number, Marangoni number and non-dimensional temperature are correlated with thermal strain. Based on these results we provide recommendations to minimize distortion of the additively manufactured parts.

We have recently shown that thermal distortion is related to a strain parameter, ε^* [5]:

$$\varepsilon* = \frac{\beta}{E}\frac{\Delta T}{I}\frac{t}{F}\frac{H^{3/2}}{\sqrt{\rho}} \quad (1)$$

where β is the volumetric coefficient of thermal expansion, ΔT is the maximum rise in temperature during the process, E is the elastic modulus and I is the moment of inertia of the substrate, the product, EI, is the flexural rigidity of the structure, t is the characteristic time, H is the heat input per unit length, F is the Fourier number and ρ is the density of the alloy powder. Fourier number is the ratio of the heat dissipation rate to heat storage rate. The temperature rise and the Fourier number are both calculated using a well-tested heat transfer and fluid flow model [3,4]. The model solves the equations of conservations of mass, momentum and energy to provide three dimensional transient temperature and velocity fields as well as the shape and size of the molten pool [3,4]. Since the model and its applications are described in detail in the literature [3–5], they are not repeated here.

Fig. 1 shows the computed temperature and velocity fields, and the shape and size of molten pools for three alloys during the deposition of the second layer. The thermo-physical properties of the alloys [14] used for the calculations are presented in Table 1. Each color band in Fig. 1 represents a temperature range as shown in the legend. The melt pool is indicated by the red colored region where the temperature is above the liquidus temperature of the alloy. Likewise, the region where the temperature reaches between the solidus and liquidus temperature is indicated by the green color. The computed velocity fields result from the spatial gradient of surface tension on the surface of the molten pool, also known as the Marangoni stress. A reference vector is shown by an arrow and a comparison of the length of this arrow with

* Corresponding author.
E-mail address: rtd1@psu.edu (T. DebRoy).

http://dx.doi.org/10.1016/j.scriptamat.2016.09.001
1359-6462/

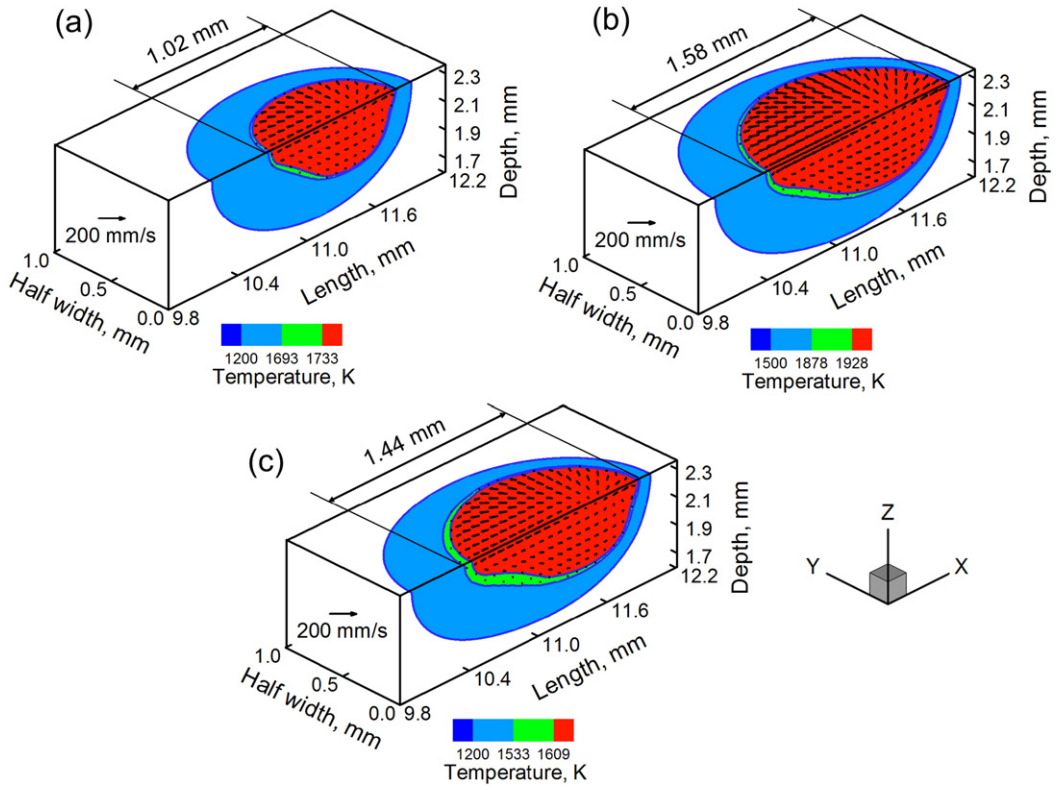

Fig. 1. Computed temperature and velocity fields at the mid length during the deposition of the 2nd layer of (a) SS 316 (b) Ti-6Al-4V and (c) IN 718. These results are for 210 W laser power and 12.7 mm/s scanning speed. Scanning direction is along the positive x-axis.

the vectors in the plots indicates the magnitudes of the computed velocities. Fig. 1 shows that the melt pool size of Ti-6Al-4V is the largest among the three alloys mainly because of its lowest density compared to those of the other alloys as shown in Table 1.

Eq. (1) does not consider any plastic deformation of the structure. However, the causative factors for plastic deformation are the same as those for the strain parameter, ε^*, expressed by Eq. (1). A quantitative relation between the maximum thermal strain encountered during deposition and the strain parameter ε^*, as shown in Fig. 2, was established in a recent paper [5]. It is observed that the maximum measured strain in multi-layer deposition correlates linearly with the strain parameter, ε^*, for several alloys and various processing conditions [5]. Thus, the strain parameter, ε^*, is considered to be a useful indicator of thermal distortion for the deposition of various alloys. This parameter embodies all causative factors for thermal distortion but, like all scaling analysis, does not provide an exact magnitude of strain. Valuable insight, not precision, is what the strain parameter provides. The measured strain is not zero at very low values of strain parameter because non-dimensional analysis is not meant to give the exact value. The strain parameter is important because it provides for the first time a clear understanding of how the strain will change with various factors as shown by Eq. (1).

Here we examine the non-dimensional thermal strain for the depositions of SS 316, Ti-6Al-4V and IN 718 alloys using Eq. (1) and parameters computed from a heat transfer and fluid flow model. The calculations were done for laser powers and scanning speeds in the commonly used ranges of 190 to 270 W and 12.7 to 25 mm/s, respectively. (See Table 2.)

Fig. 3(a) and (b) show that the strain parameter, ε^*, rises with increase in laser power and decrease in scanning speed. The peak temperature during AM increases with increasing laser power and decreasing scanning speed. The ratio of laser power to scanning speed is the heat input per unit length and higher heat input results in a larger melt pool and greater distortion on solidification. The higher peak temperature, in turn, enhances the thermal strain (Eq. (1)). The peak temperature also rises as the deposition moves to the upper layers away from the substrate and the rate of heat loss through the substrate reduces [16]. Hence, the thermal strain increases during the deposition of upper layers as indicated in Fig. 3(c). However, depending on the deposition conditions, the build may attain a steady state after many layers of deposition and the thermal strain may become almost constant, particularly for longer track lengths. For example, the thermal strain in a multi-layer build of SS 316 becomes almost constant after fifteen layers

Table 1
Thermo-physical properties of SS 316, Ti-6Al-4V and IN 718 [14].

Properties	SS 316	Ti-6Al-4V	IN 718
Liquidus temperature (K)	1733	1928	1609
Solidus temperature (K)	1693	1878	1533
Thermal conductivity (W/m K)	$11.82 + 0.0106\,T$	$1.57 + 1.6\times10^{-2}\,T - 1\times10^{-6}\,T^2$	$0.56 + 2.9\times10^{-2}\,T - 7\times10^{-6}\,T^2$
Specific heat (J/kg K)	$330.9 + 0.563\,T - 4.015\times10^{-4}\,T^2 + 9.465\times10^{-8}\,T^3$	$492.4 + 0.025\,T - 4.18\times10^{-6}\,T^2$	$36.04 + 0.026\,T - 4\times10^{-6}\,T^2$
Density (kg/m^3)	7800	4000	8100
Volumetric expansion co-efficient (/K)	5.85×10^{-5}	2.5×10^{-5}	4.8×10^{-5}
Viscosity (kg/m s)	7×10^{-3}	4×10^{-3}	5×10^{-3}
Co-efficient of surface tension (N/m)	1.5	1.52	1.82

Table 2
Process parameters used for calculations [15].

Laser power (W)	Beam radius (mm)	Scanning speed (mm/s)	Layer thickness (mm)	Substrate thickness (mm)	Powder flow rate (gm/s)
190–270	0.5	12.7–25	0.38	4	0.416

as shown in Fig. 3(c). The number of layers to attain a steady state when no further appreciable increase in thermal strain takes place depends on process parameters, build geometry and alloy properties. General Electric makes jet engine fuel nozzles in Auburn, Alabama in 20 μm thick layers and deposits thousands of layers at very high scanning speeds without any measurable distortion [17]. This practice is consistent with our results that lower heat input is effective in mitigating distortion.

Fig. 3 further shows that the thermal strain is relatively higher for IN 718 and Ti-6Al-4V deposits in comparison with that for SS 316 for a given processing condition. In order to understand the relative magnitudes of thermal strain for the alloys considered, their thermo-physical properties need to be considered. The Ti-6Al-4V melt pool is usually larger than that for the other alloys considered due to its lower density. Consequently, pronounced shrinkage of the pool and strain occurs in Ti-6Al-4V parts. Likewise, the deposits of IN 718 encounter high thermal strains due to its high coefficient of volume contraction. For a given set of processing conditions, IN 718 parts form large melt pools because of its low melting temperature. Shrinkage of large melt pools results in pronounced thermal strain.

Fig. 3 shows that in addition to laser power and scanning speed other factors such as the alloy properties, the number of deposited layers and processing conditions affect thermal strain significantly. In order to understand these effects, the thermal strain parameter is correlated with three important non-dimensional numbers, Fourier number, Marangoni number and the non-dimensional temperature. The Fourier number is the ratio of heat dissipation rate to heat storage rate. Marangoni number represents the strength of the convective transport of heat in melt pool and the non-dimensional temperature is an indicator of the extent of overheating of the melt pool [18].

Reduction of thermal strain and distortion requires efficient dissipation of heat to avoid localized accumulation of heat. A non-dimensional parameter that embodies both heat diffusion and accumulation of heat is the Fourier number (F):

$$F = \alpha\ \tau / w^2 \tag{2}$$

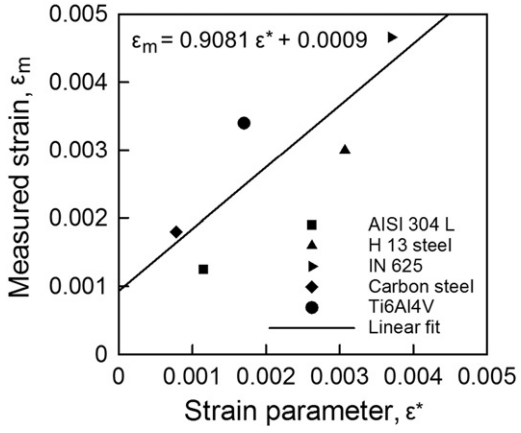

Fig. 2. Linear correlation between the experimentally measured thermal strain during deposition and the non-dimensional thermal strain for five alloys [5].

where α, τ and w refer to thermal diffusivity, characteristic time scale and length, respectively. The characteristic time can be expressed as L/V, where, L and V are the pool length and scanning speed respectively. Length of the molten pool is calculated using the heat transfer and fluid flow model as shown in Fig. 1. So, Eq. (2) can be re-written as:

$$F = \alpha / V\ L \tag{3}$$

Both rapid heat dissipation and reduction of heat accumulation result in lower peak temperature, higher Fourier number and smaller molten pool length. Therefore higher Fourier number results in lower thermal strain and distortion. In contrast, rigidity of the substrate can counter thermal distortion in AM [5] as shown in Eq. (1). Fig. 4(a) shows the variation of the strain parameter, ε^* as function of Fourier number and rigidity of the substrate for three different heat inputs. The thermal strain parameter reduces with increase in both the Fourier number and the rigidity, EI, of the structure. For a set of process variables, the effects of Fourier number and rigidity of the structure on thermal strain follow nearly the same trend for all three alloys, which is expected. The figure shows that the thermal strain increases with heat input. This behavior is attributed to more pronounced heat accumulation and decrease in Fourier number when the heat input is increased. Since decrease in laser power and smaller layer heights can reduce the rate of heat accumulation and thus, increase the Fourier number, they are practical means to control the thermal distortion in AM [3,4,19].

Convection is the primary mechanism of heat transfer in the molten pool during AM [3–5]. The convective transport of heat within the molten pool is driven primarily by the spatial variation of interfacial tension, also referred to as the Marangoni stress [20]. The shape and size of the molten pool is affected by the magnitude of the convective velocity of liquid metal that is expressed by the Marangoni number, Ma:

$$Ma = -\frac{d\gamma}{dT}\frac{L}{\eta}\frac{\Delta T}{\alpha} \tag{4}$$

where η is the viscosity, α is the thermal diffusivity of the alloy, L is the characteristic length of the molten pool, which is taken as the width of the molten pool, ΔT is the difference between the maximum temperature inside the pool and the solidus temperature of an alloy, and $\frac{d\gamma}{dT}$ is the sensitivity of surface tension with respect to temperature. For most alloys without any surface active elements, this quantity is negative. The overall molten pool volume is also affected significantly by the density of an alloy powder for a particular heat input. Lighter alloys tend to form larger molten pools and undergo greater volume contraction and thermal distortion. Therefore a combined effect of density of alloy powder and Marangoni number on the thermal strain parameter is examined.

Fig. 4b shows an increase in thermal strain with rise in Marangoni number and decrease in density of alloy powder for a particular set of process variables. The effect of Marangoni number and powder density follows a nearly similar trend for all the three alloys considered here for a particular processing condition. Increase in heat input leads to both higher peak temperature and Marangoni number, and higher thermal strain. Thus, reducing heat input by selecting either a lower laser power or a higher scanning speed or both, when possible, is a practical method to reduce thermal strain.

Eq. (1) shows that the strain parameter, ε^*, increases with rise in peak temperature and ΔT. In particular, higher peak temperature, T_P, results in greater volume shrinkage during solidification. A non-

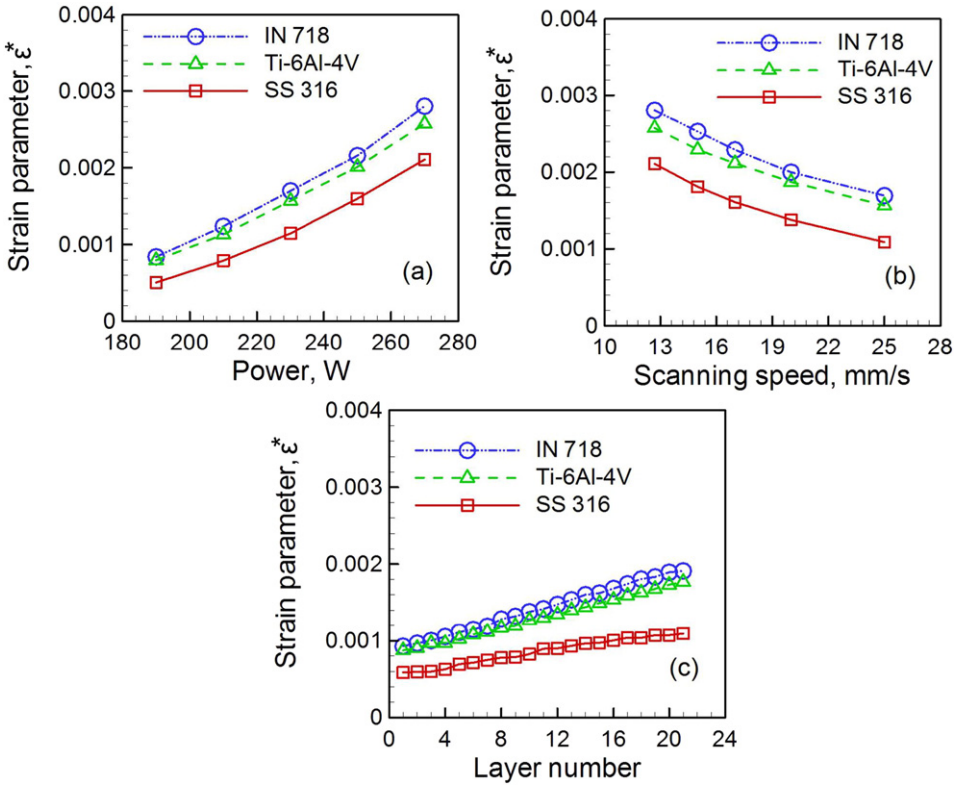

Fig. 3. Variation of non-dimensional strain as function of (a) laser power for a constant scanning speed of 12.7 mm/s and (b) scanning speed for a constant laser power of 270 W (c) layer number for a constant laser power of 230 W and scanning speed of 20 mm/s.

dimensional temperature T^* can reveal the effect of process variables on thermal strain due to rise in peak temperature:

$$T* = \frac{T_P - T_A}{T_L - T_A} \quad (5)$$

where, T_A and T_L are the ambient temperature and liquidus temperature, respectively. The term βT^* is a measure of the volumetric contraction. Since a lighter alloy and a larger liquid pool is more susceptible to thermal distortion, a combined effect of βT^*, pool length and alloy density on strain parameter is examined in Fig. 4c. It is clear that the thermal

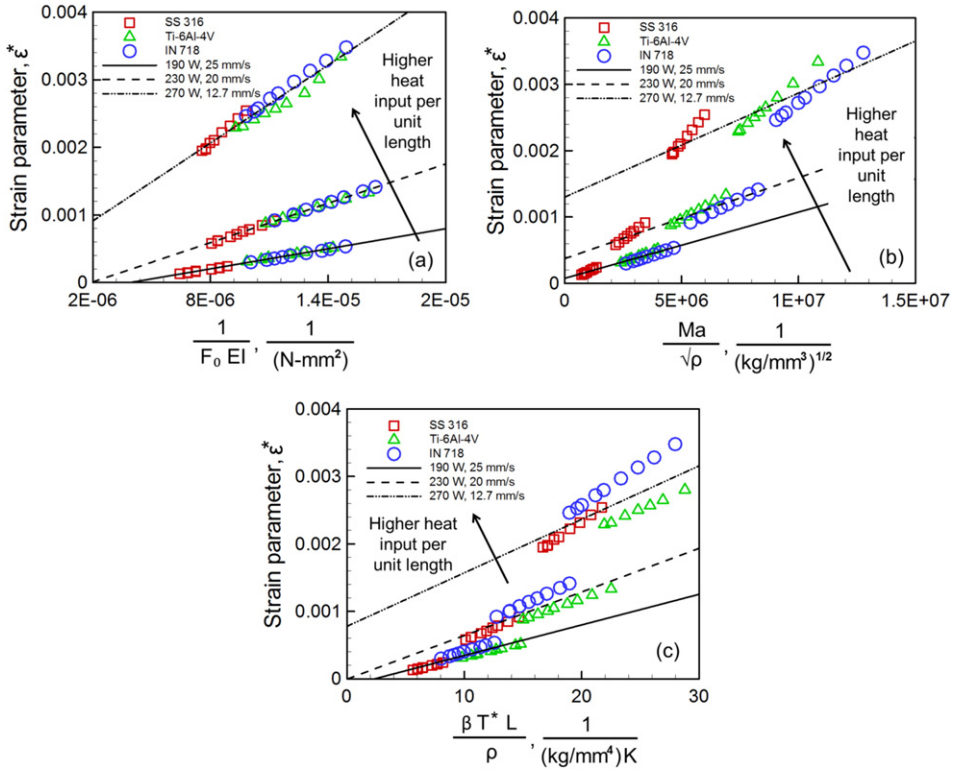

Fig. 4. Variation of non-dimensional strain as function of (a) Fourier number (b) Marangoni number, and (c) Non-dimensional temperature, for three heat inputs per unit length.

strain increases with βT^* and pool length and decreases with density, as expected. Low heat input and rapid heat dissipation can effectively reduce the peak temperature and pool dimension and reduce strain. The effect of the individual alloy properties such as viscosity and density at very high heat input and peak temperature appears to exhibit alloy specific trend as observed in Fig. 4(b) and (c). However, both 4(b) and 4(c), clearly show how the strain parameter is affected by Marangoni number and non-dimensional temperature.

Apart from distortion, process variables also affect microstructure and mechanical properties. For example, in 316 stainless steel parts made by AM, formation of detrimental δ-ferrite can be avoided and superior mechanical properties can be achieved by selecting low heat inputs [21–23]. It is also established that low heat input (100–500 W and 2000 mm/s) suppresses formation of intermetallic compounds and provides good mechanical properties of some nickel base superalloy builds [24,25]. Facchini et al. [26] reported martensite formation and limited ductility in additively manufactured Ti-6Al-4V parts for a wide range of processing conditions. However, Xu et al. [27] showed that martensite formation can be avoided and fine lamellar alpha and beta structure can be achieved by careful adjustment of focal offset (0 to 2 mm), travel speed (1029 mm/s) and laser power (375 W). Therefore, it would be important to examine the impact of process variables on distortion, microstructure and properties to achieve defect free, structurally sound and reliable components fabricated by AM.

In summary, the results presented here provide, for the first time, a quantitative basis for minimizing thermal distortion in AM based on scientific principles and important non-dimensional numbers. It is found that low heat input sufficient for maintaining adequate interlayer bonding is beneficial for the control of thermal strain. A decrease in laser power and layer height can also result in higher Fourier number and lower thermal strain. A reduction in laser power and an increase in scanning speed can reduce Marangoni number and non-dimensional temperature and decrease thermal strain. Likewise, alloys with lower heat capacity and higher thermal diffusivity will be susceptible to higher peak temperature, larger pool volume and higher thermal strain. Apart from careful selection of the process parameters to mitigate distortion, microstructural characterization and evaluation of mechanical properties of the components should be undertaken to produce high quality parts.

Acknowledgement

We acknowledge the support from US Department of Energy NEUP Grant DE-NE0008280. One of the author (T.M.) also acknowledges the support from American Welding Society research fellowship grant 179466.

References

[1] I. Gibson, D.W. Rosen, B. Stucker, Additive Manufacturing Technologies, Springer, New York, 2010.
[2] D.D. Gu, W. Meiners, K. Wissenbach, R. Poprawe, Int. Mater. Rev. 57 (2012) 133.
[3] V. Manvatkar, A. De, T. DebRoy, Mater. Sci. Technol. 31 (2015) 924.
[4] V. Manvatkar, A. De, T. DebRoy, J. Appl. Phys. 116 (2014) 124905.
[5] T. Mukherjee, J.S. Zuback, A. De, T. DebRoy, Sci. Rep. 6 (2016) 19717 Available at: http://www.nature.com/articles/srep19717.
[6] T. Mukherjee, J.S. Zuback, A. De, T. DebRoy, 7th International Symposium on High-Temperature Metallurgical Processing, TMS, Nashville, TN, 2016 469.
[7] J.C. Heigel, P. Michaleris, T.A. Palmer, J. Mater. Process. Technol. 220 (2015) 135.
[8] E.R. Denlinger, J.C. Heigel, P. Michaleris, T.A. Palmer, J. Mater. Process. Technol. 215 (2015) 123.
[9] P. Mercelis, J.P. Kruth, Rapid Prototyp. J. 12 (2006) 254.
[10] A. De, T. DebRoy, Sci. Technol. Weld. Join. 16 (2011) 204.
[11] C. Li, C.H. Fu, Y.B. Guo, F.Z. Fang, J. Mater. Process. Technol. 229 (2016) 703.
[12] L.M. Sochalski-Kolbus, E.A. Payzant, P.A. Cornwell, T.R. Watkins, S.S. Babu, R.R. Dehoff, M. Lorenz, O. Ovchinnikova, C. Duty, Metall. Mater. Trans. A 46 (2015) 1419.
[13] A.S. Wu, D.W. Brown, M. Kumar, G.F. Gallegos, W.E. King, Metall. Mater. Trans. A 45 (2014) 6260.
[14] K.C. Mills, Recommended Values of Thermo-Physical Properties for Selected Commercial Alloys, Woodhead Publishing, Cambridge, 2002.
[15] V.D. Manvatkar, A.A. Gokhale, G.J. Reddy, A. Venkataramana, A. De, Metall. Mater. Trans. A 42 (2011) 4080.
[16] H.L. Wei, J. Mazumder, T. DebRoy, Sci. Rep. 5 (2015) 16446 Available at: http://www.nature.com/articles/srep16446.
[17] M. LaMonica, GE, the world's largest manufacturer, is on the verge of using 3-D printing to make jet parts, MIT Technology Review, 2013 (Available at: http://www.technologyreview.com/s/513716/additive-manufacturing).
[18] V.E. Maarten, F.A. Bender, J.P. Kruth, Rapid Prototyp. J. 14 (2008) 15.
[19] J. Mazumder, A. Schifferer, J. Choi, Mater. Res. Innov. 3 (1999) 118.
[20] T. DebRoy, S.A. David, Rev. Mod. Phys. 67 (1995) 85.
[21] M.H. Farshidianfar, A. Khajepour, A.P. Gerlich, J. Mater. Process. Technol. 231 (2016) 468.
[22] K. Zhang, S. Wang, W. Liu, X. Shang, Mater. Des. 55 (2014) 104.
[23] A. Yadollahi, N. Shamsaei, S.M. Thompson, D.W. Seely, Mater. Sci. Eng. A 644 (2015) 171.
[24] P.M. Kenney, D.E. Lindley, General Electric Company, 2013, U.S. Patent Application 14/440, 154.
[25] H. Qi, M. Azer, A. Ritter, Metall. Mater. Trans. A 40 (2009) 2410.
[26] L. Facchini, E. Magalini, P. Robotti, A. Molinari, S. Höges, K. Wissenbach, Rapid Prototyp. J. 16 (2010) 450.
[27] W. Xu, M. Brandt, S. Sun, J. Elambasseril, Q. Liu, K. Latham, K. Xia, M. Qian, Acta Mater. 85 (2015) 74.

Appendix H:

Printability of alloys for additive manufacturing

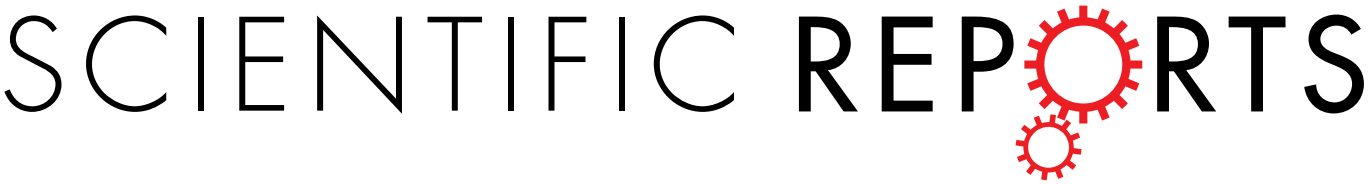

OPEN

Printability of alloys for additive manufacturing

T. Mukherjee, J. S. Zuback, A. De & T. DebRoy

Received: 30 September 2015
Accepted: 09 December 2015
Published: 22 January 2016

Although additive manufacturing (AM), or three dimensional (3D) printing, provides significant advantages over existing manufacturing techniques, metallic parts produced by AM are susceptible to distortion, lack of fusion defects and compositional changes. Here we show that the printability, or the ability of an alloy to avoid these defects, can be examined by developing and testing appropriate theories. A theoretical scaling analysis is used to test vulnerability of various alloys to thermal distortion. A theoretical kinetic model is used to examine predisposition of different alloys to AM induced compositional changes. A well-tested numerical heat transfer and fluid flow model is used to compare susceptibilities of various alloys to lack of fusion defects. These results are tested and validated with independent experimental data. The findings presented in this paper are aimed at achieving distortion free, compositionally sound and well bonded metallic parts.

Additive manufacturing (AM) allows for one-step fabrication of complex parts that are true to their designs. It eliminates the need for assembling multiple components, training a new workforce or setting up any new equipment while simultaneously minimizing manufacturing time and wastage of materials and energy. It is projected to become a 16 billion dollar industry over the next five years[1]. Its current applications include printing of tissues[2,3], implants and prosthesis[4], electronics[5], aero-engine components, compositionally graded parts[6] and corrosion resistant protective coatings[7]. Although AM is rapidly growing to produce metallic, polymeric and ceramic components, production of metallic parts is its fastest growing sector.

In order to successfully print a metallic part, an appropriate alloy must be selected. Parts should be dimensionally accurate, the chemical composition of the final product should be the same as that of the alloy powder and successive layers need to be adequately bonded by fusion. An understanding of printability, or the ability of an alloy to resist distortion, compositional changes and lack of fusion defects, is essential for both powder injection and powder bed based AM processes. What are needed and not currently available are quantitative scales to construct, test and validate the printability of different alloys in these processes.

During AM of metal parts, alloys undergo spatially-variable heating, melting, solidification and cooling of the entire part. Permanent deformation in various regions of a part can occur depending on thermo-physical properties of the alloy, the rigidity of the part and transient temperature fields[7]. An appropriate model for the estimation of strain can provide an assessment of the susceptibility of various alloys to distortion and the resulting dimensional inaccuracy of the final part in a quantitative scale.

Most engineering alloys contain multiple alloying elements that vaporize rapidly at high temperatures and can be selectively lost during AM. Consequently, the chemical composition of the part may be different from that of the original material. For all alloys, a reduction in peak temperature and a smaller surface-to-volume ratio of the molten pool will minimize pronounced changes of chemical composition during laser processing[8,9].

Lack of fusion defects originate from inadequate penetration of the molten pool into the substrate or previously deposited layer. Important variables include thermo-physical properties, characteristics of the heat source and processing parameters that determine the geometry of the melted region. Satisfactory penetration of the molten pool into the substrate or the previously deposited layer needs to be ensured to avoid this defect.

Here we report the development of theories to examine the propensities of common alloys to form the three most common defects during powder-based AM. These theories are tested using available independent experimental data. The methodology and results presented here are aimed at providing a quantitative basis for overcoming common defects in the AM of metallic parts.

Heat transfer and fluid flow modeling

Dimensional inaccuracy, loss of alloying elements due to vaporization and lack of fusion defects encountered during AM of metal parts depend on the geometry of the molten pool and temperature distribution. However, real

Department of Materials Science and Engineering, The Pennsylvania State University, University Park, PA 16802, United States. Correspondence and requests for materials should be addressed to T.D. (email: debroy@psu.edu)

time measurement of these quantities during AM is difficult. Therefore, a well-tested, 3D transient heat transfer and fluid flow model is used to calculate these quantities. The model solves equations of conservations of mass, momentum and energy to provide 3D transient temperature and velocity fields as well as the shape and size of molten pool. The methodology is well documented in the literature[10] and its implementation for an AM process has been described in the supplementary information.

For simplicity, a flat molten pool surface is assumed in the calculations. The flat surface assumption gives comparable values for pool dimensions as compared to free surface model. For example, Ha *et al.*[11] showed that the flat surface assumption resulted in about 3% difference in molten pool width and depth compared with the free surface model. It is estimated that the errors in strain owing to flat surface assumption is about 3%. An analysis of the error in estimation of thermal strain owing to flat surface assumption is included in the supplementary document.

Figure 1(a–d) show the 3D temperature and velocity field in a laser based AM process for Ti-6Al-4V during the deposition. Figure 1(e) shows that the calculated build shape and size are in fair agreement with experimental results[12]. The agreement between the computed and the experimental results indicates that the model can be used to estimate thermal strains, composition changes and lack of fusion defects with confidence.

Dimensional inaccuracy. Dimensional inaccuracy in AM parts due to thermal distortion is caused by non-uniform expansion and contraction of different regions of the part that experience changes in temperature. Thermal distortion during the deposition process depends on alloy properties, heat input, deposition time, substrate dimensions, part geometry, time delay between the deposition of successive layers and other variables. Propensity for thermal distortion is calculated from the maximum thermal strain. Using experimental data and dimensional analysis, the maximum thermal strain is estimated as a function of these important variables.

A non-dimensional thermal strain parameter (ε^*) is used to represent the maximum thermal strain. A relation between this parameter (ε^*) and the AM variables is developed based on the Buckingham π-theorem[13]. Table 2 provides a list of these variables along with their dimensions in MLTθ system. Since there are 4 fundamental dimensions and 8 variables, there are four ($8-4=4$) π terms. Non-repeating variables are chosen to be ρV, h, ΔT and k/C_P. Applying Buckingham π-theorem, the final four π terms can be written as

$$\pi_1 = \varepsilon^* \tag{1}$$

$$\pi_2 = \beta \Delta T \tag{2}$$

$$\pi_3 = \frac{\rho V H}{h^3 (k/C_P)^2} \tag{3}$$

$$\pi_4 = \frac{\rho V E I}{h^5 (k/C_P)^2} \tag{4}$$

From the above relationships, the thermal strain parameter can be expressed as a function of the AM variables as:

$$\varepsilon^* = \pi_1 = \frac{\pi_2 \pi_3^{3/2}}{\pi_4} = \frac{\beta \Delta T}{EI} \frac{\sqrt{h(\rho V)}}{(k/C_P)} H^{3/2} = \frac{\beta \Delta T}{EI} \frac{\sqrt{Vh}}{\alpha \sqrt{\rho}} H^{3/2} \tag{5}$$

The heat transfer in AM processes is transient in nature which is best characterized by the Fourier number (F) given as $\alpha\tau/w^2$ where α, τ and w refer to thermal diffusivity, characteristic time scale and length through which the heat conduction occurs, respectively. The Fourier number (F) can be rewritten as α/vw considering v as the beam scanning speed and w as the length of the molten pool. The term $\sqrt{Vh}$ in equation (5) is dimensionally equivalent to w^2. Therefore, the thermal strain parameter, ε^*, can be expressed in terms of the Fourier number (F) as

$$\varepsilon^* = \frac{\beta \Delta T}{EI} \frac{t}{F\sqrt{\rho}} H^{3/2} \tag{6}$$

Equation (6) indicates that high strains result from large volumetric change ($\beta\Delta T$), long deposition time (t) and high rates of heat input per unit length (H). In contrast, terms in the denominator of equation (6) indicate factors that are helpful to reduce thermal strain. For example, a high flexural rigidity (EI) of a structure resists deformation. Similarly, a high Fourier number (F) indicates faster diffusive heat transfer relative to heat accumulation and a high rate of heat transfer reduces the peak temperature and thus, the thermal strain.

Figure 2(a) shows the maximum thermal strains (ε) obtained from the experimentally measured thermal distortions[14–18] as a function of the thermal strain parameter (ε^*), which is estimated using equation (6). A sample calculation for the estimation of the thermal strain parameter (ε^*) for Ti-6Al-4V is shown in the supplementary document. Figure 2(a) indicates that the maximum thermal strain (ε) for an AM part can be expressed as a linear function of the thermal strain parameter (ε^*). Based on the trend of the data points presented in Fig. 2(a), the maximum thermal strain (ε) can be expressed as

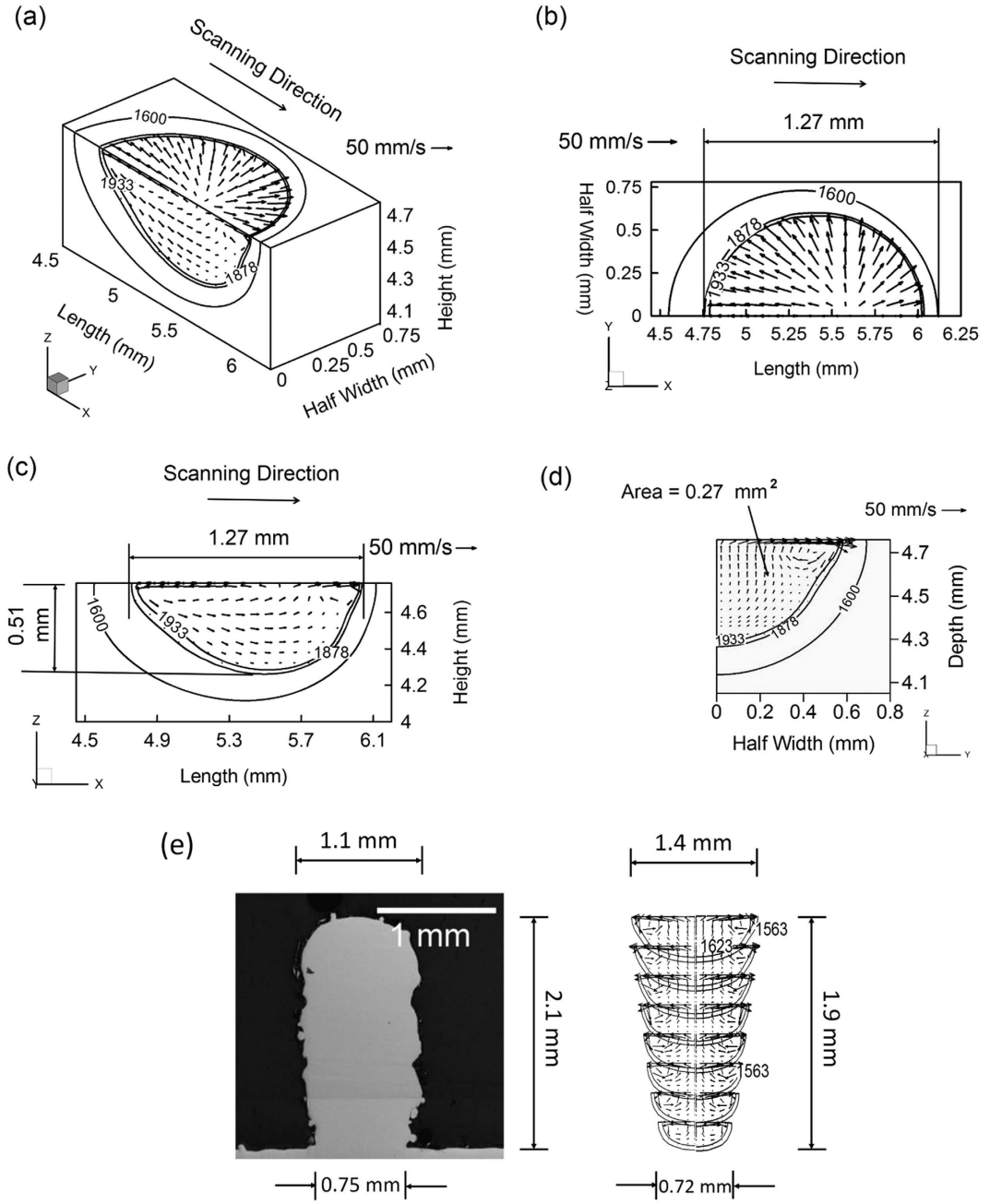

Figure 1. Computed 3D transient temperature and velocity field in laser based AM process using Parameter Set 1 in Table 1 for second layer deposition of Ti-6Al-4V (**a**) Isometric view where 1933 K and 1878 K represent liquidus and solidus temperatures, respectively. The isotherm of 1878 K represents the molten pool boundary. Half of the pool is shown due to the symmetric nature of the pool about the x–z plane. A reference velocity vector of 50 cm/s has been shown to comprehend the liquid metal flow velocity in the molten pool. (**b**) Measurement of the length of the pool on top view. (**c**) Measurement of depth of penetration of the pool on longitudinal cross-sectional view. (**d**) Transverse cross-sectional view to measure the area of the pool perpendicular to the scanning direction using Parameter Set 2 in Table 1 for IN625 (**e**) Pool shape and size comparison for single track 8 layers deposition between numerically calculated pool and experimentally obtained pool taken from literature[12].

$$\varepsilon = \frac{0.9081\beta\Delta T}{EI}\frac{t}{F\sqrt{\rho}}H^{3/2} + 0.0009 \tag{7}$$

Heat input per unit length (H) and volumetric change ($\beta\Delta T$) are two important variables in AM and equation (7) shows that these affect the maximum thermal strain (ε) in direct proportion. Equation (7) is validated by examining the effects of heat input and volumetric change on the maximum thermal strain using independent

Parameter Set	Laser power (W)	Beam radius (mm)	Scanning speed (mm/s)	Layer thickness (mm)	Substrate thickness (mm)
1	190	0.5	12.5	0.38	4
2	600	0.5	7.5	0.25	7
3	1000	0.5	12.5	0.38	4

Table 1. Process conditions used in numerical calculations.

Variable	Dimension
Volumetric thermal expansion coefficient, β	θ^{-1}
Temperature gradient, $\Delta T = T_P - T_S$, where T_P and T_S refer respectively to peak and surrounding temperature	θ
Deposition layer thickness, h	L
Thermal diffusivity, $\alpha = k/\rho C_P$, where k, ρ and C_P are thermal conductivity, density and specific heat, respectively of deposit material	L^2T^{-1}
Heat input per unit length, $H = \eta P/v$, where η, P, and v refer to absorption coefficient, beam power and scanning speed, respectively	MLT^{-2}
Melt pool volume, V	L^3
Flexural rigidity of the substrate plate, EI, where E and I refer respectively to elastic modulus and second moment of inertia	ML^3T^{-2}
Thermal strain parameter, ε^*	$M^0L^0T^0\theta^0$

Table 2. Variables used in dimensional analysis in the MLTθ system.

experimental data[14,15,19,20]. Figure 2(b,c) show that both $H^{3/2}$ and $\beta\Delta T$ influence thermal strain linearly, regardless of the alloy. The linearity of the plots is indicated by the correlation coefficients of 0.92 and 0.98 for Fig. 2(b,c), respectively. Figure 2(a) through 2(c) show that equation (7) can estimate the maximum thermal strain (ε) to provide a direct measure of the expected thermal distortion. Equation (7) is valid for the heat input range of 150–2800 J/mm, which is widely used for major AM applications[7,21]. Figure 2(a) presents independent experimental data which includes strains due to phase transformations. Tool paths during AM can have significant effects on thermal distortion. Wei *et al.*[22] showed that the heat transfer pattern and pool dimensions change depending on the tool path. Therefore, the Fourier number also depends on the tool path, which is accounted for in equation (7).

Equation (7) provides a usable scale to estimate and compare the maximum thermal strain in laser-based AM for different alloys. A relatively high value of thermal strain calculated using equation (7) signifies more thermal distortion and a lower printability of the corresponding alloy. Figure 3 shows that increasing the number of layers increases thermal strain. This is caused by lower heat conduction from the molten pool into the substrate resulting in higher temperature difference (ΔT). Thermal strain is the highest for Ti-6Al-4V, which can be attributed to its relatively low density and thermal diffusivity. The ranking of the alloys in Fig. 3 provides a relative scale of their printability considering their susceptibility to thermal distortion. For alloys that are highly susceptible, appropriate AM variables like laser power, layer thickness and scanning speed need to be adjusted based on equation (7) to reduce thermal strain and distortion.

Composition change. At high temperatures encountered during AM, significant vaporization of alloying elements occur from the molten pool. Since some alloying elements are more volatile than others, selective vaporization of alloying elements often results in a significant change in the composition of the alloy. For example, during laser welding of aluminum alloys, losses of magnesium and zinc result in pronounced changes of their concentrations. The composition change, in turn causes degradation of hardness, corrosion resistance and tensile properties.

The vaporization fluxes of alloying elements, J_i, can be estimated from the Langmuir equation[8]:

$$J_i = \frac{\lambda P_i}{\sqrt{2\pi M_i T}} \tag{8}$$

where P_i is vapor pressure over the alloy, M_i is the molecular weight of element i, T is temperature and λ is a positive fraction accounting for the condensation of some vaporized atoms. Temperatures of the molten pool are calculated using a three-dimensional heat transfer and fluid flow model and the equilibrium vapor pressures of all alloying elements are estimated from available thermodynamic data. The amount of material vaporized, Δm_i, can be estimated as

$$\Delta m_i = \frac{LA_s J_i}{v} \tag{9}$$

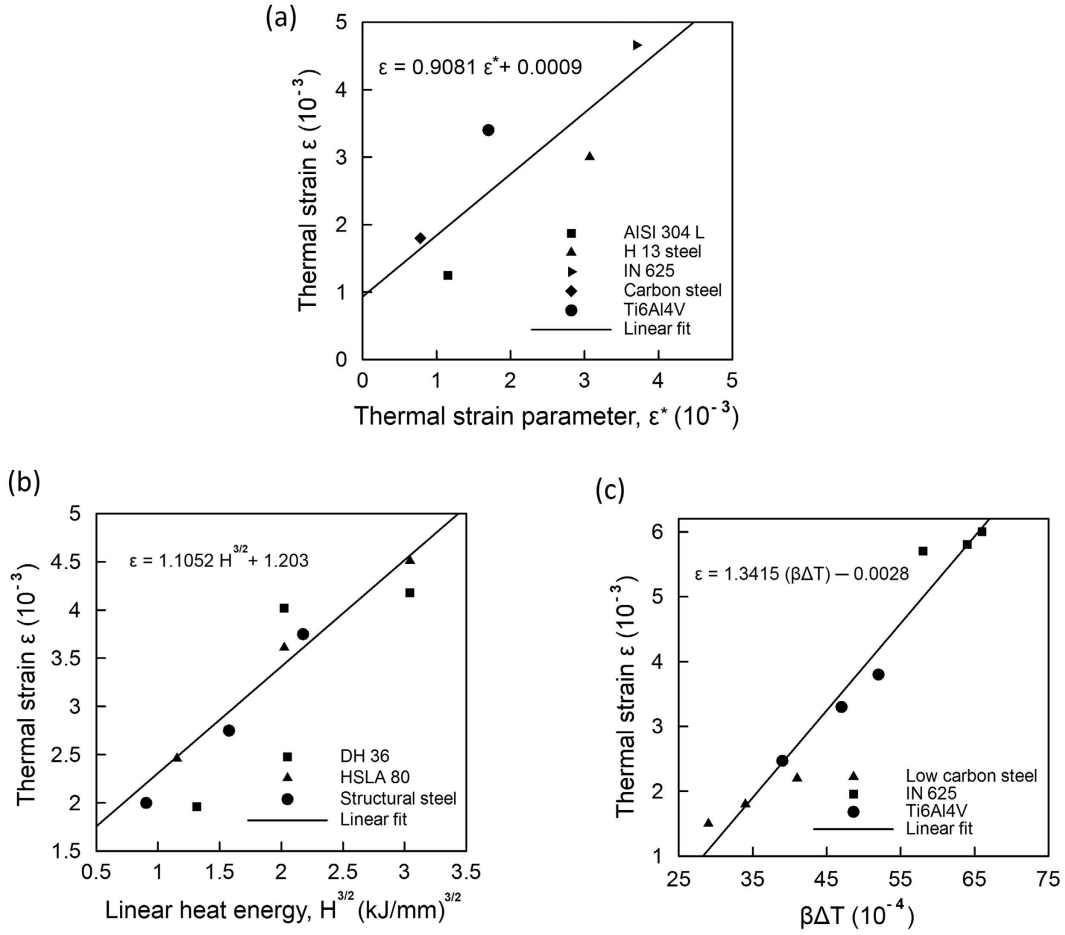

Figure 2. Values of maximum thermal strain ε (**a**) as a function of the thermal strain parameter for five alloys[14–18] showing a linear relationship (**b**) as a function of $H^{3/2}$ for structural steel[19], tool steel[20] and high strength low alloys steel[20] in welding (**c**) as a function of $\beta\Delta T$ for low carbon steel[15], IN 625[14] and Ti-6Al-4V[14] in AM.

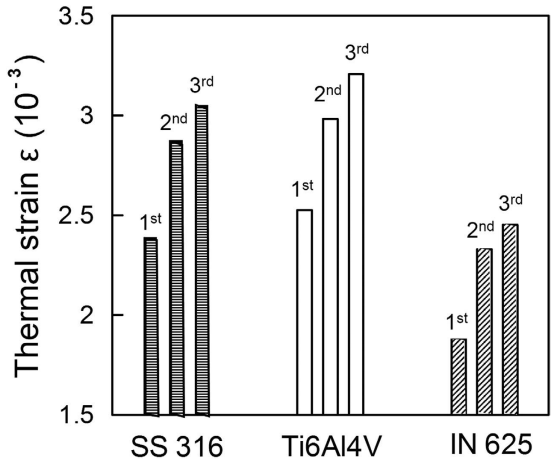

Figure 3. Values of maximum thermal strain ε in laser additive manufacturing (LAM) of a single-track three-layer deposition of SS 316, Ti6Al4V and IN 625 powder materials using Parameter Set 1 in Table 1.

where v is scanning speed, L is the track length and A_s is surface area of the molten pool. The volume of material V deposited can be approximated by

$$V = A_t L \tag{10}$$

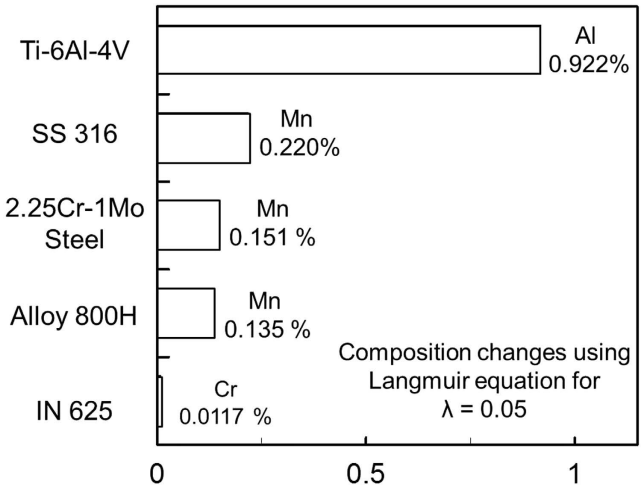

Figure 4. Composition change in wt% of the most volatile elements due to vaporization for five alloys using Parameter Set 3 in Table 1.

where A_t is transverse cross sectional area of the molten pool perpendicular to the scanning direction at the point of highest depth. The weight percentage of element i after vaporization, W_f, can be calculated using

$$W_f = \frac{V\rho W_i - \Delta m_i}{V\rho - \sum_i \Delta m_i} \tag{11}$$

where W_i is the initial weight percentage of element i in the powder. The composition change is the difference in weight percentages of element i in the powder and deposited material.

Figure 4 shows the most volatile alloying elements to be manganese in 2.25Cr-1Mo steel, Alloy 800H and SS 316, chromium in IN 625, and aluminum in Ti-6Al-4V. Figure 4 shows that Ti-6Al-4V is the most susceptible and IN 625 is the least susceptible to change in composition, respectively.

Results from Brice *et al.*[23] show an average composition change of about 0.9 wt% Al for electron beam deposition of Ti-6Al-4V. Temperatures of the molten pool are higher for Ti-6Al-4V than the other alloys for the same heat input per unit length due to its relatively low thermal conductivity and density. High temperatures and the high equilibrium vapor pressure of aluminum result in a larger composition change for Ti-6Al-4V compared to the other alloys for identical process parameters.

A scale has been developed to rank the printability of common alloys by considering composition change. Figure 4 shows that IN 625 will experience the smallest composition change and Ti-6Al-4V will experience the largest. Therefore, IN 625 and Ti-6Al-4V will be the least and most susceptible to composition change among the alloys considered. For alloys highly susceptible to composition change, care should be taken to adjust appropriate AM variables such as laser power density and scanning speed to reduce loss of volatile alloying elements.

Lack of fusion defects. Lack of fusion is caused by inadequate penetration of the molten pool of an upper layer into either the substrate or the previously deposited layer. Inadequate penetration can cause voids to form in the final product which are typically larger than 10 micrometers in equivalent diameter. These voids can also be generated by gas entrapment during the atomization of the powder particles and the shape of the deposit. For example, omega shape deposits create much more inter layer porosity compared to lens shape deposits[24]. These macro-pores are much larger than the micro-pores caused by surface moisture absorption, oxidation and dissolved gases. Penetration depth depends on the physical properties of the alloy powder and processing conditions like laser power, scanning speed and deposition strategy. However, various alloys exhibit different depths of penetration for identical AM processing conditions depending on their thermo-physical properties. Therefore, alloys differ in their susceptibilities to lack of fusion defects.

Adequate fusion and inter-layer bonding for different alloys can be examined by considering a non-dimensional lack of fusion index, *LF*, defined by

$$LF = \frac{d}{h} \tag{12}$$

where d is the penetration depth of the molten pool and h is the thickness of a layer of material deposited onto the substrate or previously deposited layer. In order for a deposited layer to bond properly with a previous layer, the penetration depth of the molten pool, d, should exceed the layer thickness, h, and adequately remelt the previously deposited layer. The minimum possible value of LF for establishing contact between two successive layers is 1, indicating a penetration depth (d) equal to layer thickness (h). However, this contact is inadequate for good bonding. Carroll *et al.*[25] reported a 99.999% dense part for direct energy deposition AM of Ti-6Al-4V, indicating

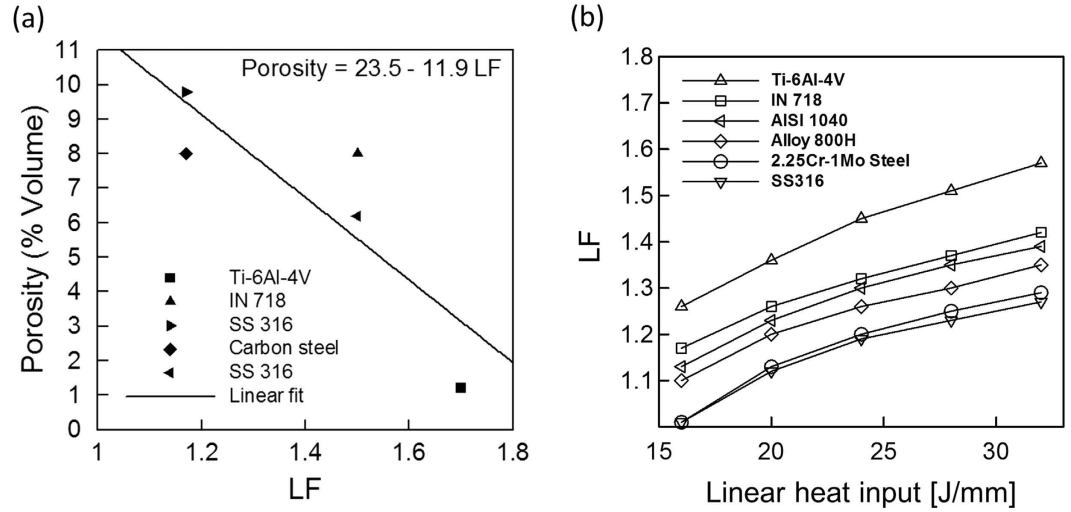

Figure 5. Correlation between LF and (a) macro-porosity for Ti-6Al-4V[26], IN 718[27], SS 316[28], carbon steel[29] and SS 316[30] and (b) linear heat input for six different alloys with a constant layer thickness of 0.38 mm.

proper inter-layer bonding. A corresponding LF index was estimated as 1.15. So, a penetration of 15% of the layer thickness into the previous layer signifies good interlayer bonding.

The three-dimensional heat transfer and fluid flow model is used to estimate penetration depths for six alloys over a range of linear heat inputs. Figure 1(c) shows the computed molten pool for Ti-6Al-4V, as an example, and similar results for the other five alloys are shown in the supplementary document. Figure 5(a) shows an inverse relationship between the macro-porosity resulting from lack of fusion defects[26–30] and the corresponding estimated LF values. For larger values of LF, the molten pool penetrates deeper into the previously deposited layer to provide adequate inter-layer bonding. Figure 5(b) shows the susceptibilities of various alloys to lack of fusion defects are unaffected by the heat input. Also, Fig. 5(b) shows that for a given heat input, Ti-6Al-4V will have the highest value of LF while SS 316 will have the lowest. Therefore, Ti-6Al-4V and SS 316 are the least and most susceptible to lack of fusion defects, respectively, among the alloys considered. For alloys that are highly susceptible to lack of fusion defects, AM variables like laser power, scanning speed and powder feed rate should be appropriately adjusted to attain an adequate depth of penetration.

Conclusion

In summary, relative susceptibilities of various alloys to thermal distortion, loss of alloying elements and lack of fusion defects that determine their printability have been examined quantitatively and validated with independent experimental data. Results show that Ti-6Al-4V is most susceptible to thermal strain and distortion during AM compared to IN 625 and SS 316. Ti-6Al-4V and IN 625 are the most and least susceptible to composition change, respectively. The computed lack of fusion index shows that SS 316 and Ti-6Al-4V have the highest and lowest vulnerability to lack of fusion defects, respectively. The results provide an understanding of the printability of various powder materials based on their physical properties and how they would behave under commonly used process conditions in AM.

Methods

A computer code that solves the equations of conservation of mass, momentum and energy has been developed to calculate transient temperature and velocity fields and the geometry of the molten pool. The governing equations are discretized by following a control volume method and solved using tri-diagonal matrix algorithm (TDMA) with appropriate boundary conditions and temperature dependent material properties. The material database for thermo-physical and chemical properties of the alloys are created using JMatPro® V8 software. The three components of velocity and enthalpy are iterated at each time step. The total computational time depended on the part dimensions, process conditions and the alloy. For example, for the deposition of a 1 cm long slab of Ti-6Al-4V using 141,075 grid points and the data set 1 in Table 1, 6 minutes and 48 seconds was needed in a personal computer with 3.20 GHz Intel Pentium 4 processor and 2 GB RAM. Typically a total of about 5 billion linear equations need to be solved cumulatively for all time steps for each layer.

References

1. Mitchell, J. W. What a 100-year-old foundry shows us about how 3D printing will shape the future of manufacturing. *Global Trade*. pp. 101–104 (August-September 2015).
2. Murphy, S. V. & Atala, A. 3D bioprinting of tissues and organs. *Nature Biotechnol.* **8,** 773–785 (2014).
3. Miller, J. S. *et al.* Rapid casting of patterned vascular networks for perfusable engineered three-dimensional tissues. *Nature Mater.* **11,** 768–774 (2012).
4. He, Y., Xue, G. & Fu, J. Fabrication of low cost soft tissue prostheses with the desktop 3D printer. *Sci. Rep.* **4,** 6973; doi: 10.1038/srep06973 (2014).

5. Zheng, Y., He, Z., Gao, Y. & Liu, J. Direct desktop printed-circuits-on-paper flexible electronics. *Sci. Rep*. **3,** 1786, doi: 10.1038/srep01786 (2013).
6. Hofmann, D. C. *et al.* Developing gradient metal alloys through radial deposition additive manufacturing. *Sci. Rep*. **4,** 5357; doi: 10.1038/srep05357 (2014).
7. Gibson, I., Rosen, D. & Stucker, B. *Additive Manufacturing Technologies: 3D Printing, Rapid Prototyping and Direct Digital Manufacturing Ch.10* (Springer, New York, 2015).
8. DebRoy, T. & David, S. A. Physical processes in fusion welding. *Rev. Mod. Phys*. **67(1),** 85–112 (1995).
9. David, S. A. & DebRoy, T. Current issues and problems in welding science. *Science*. **257,** 497–502 (1992).
10. Manvatkar, V., De, A. & DebRoy, T. Heat transfer and material flow during laser assisted multi-layer additive manufacturing. *J. Appl. Phys*. **116,** 124905; doi: 10.1063/1.4896751 (2014).
11. Ha, E. J. & Kim, W. S. A study of low-power density laser welding process with evolution of free surface. *Int. J. Heat Fluid Flow*. **26,** 613–621 (2005).
12. Dinda, G. P., Dasgupta, A. K. & Mazumder, J. Laser aided direct metal deposition of Inconel 625 superalloy: Microstructural evolution and thermal stability. *Mater. Sci. Engg. A*. **509,** 98–104 (2009).
13. Bird, R. B., Stewart, W. E. & Lightfoot, E. N. *Transport phenomena* (John Wiley & Sons, New York, 2002).
14. Denlinger, E. R., Heigel, J. C., Michaleris, P. & Palmer, T. A. Effect of inter-layer dwell time on distortion and residual stress in additive manufacturing of titanium and nickel alloys. *J. Mater. Process. Tech*. **215,** 123–131 (2015).
15. Grum, J. & Znidarsic, M. Microstructure, microhardness, and residual stress analysis of laser surface cladding of low-carbon steel. *Mater. Manuf. Process*. **19,** 243–258 (2004).
16. Alimardani, M., Toyserkani, E. & Huissoon, J. P. A 3D dynamic numerical approach for temperature and thermal stress distributions in multilayer laser solid freeform fabrication process. *Opt. Las. Eng*. **45,** 1115–1130 (2007).
17. Heigel, J. C., Michaleris, P. & Palmer, T. A. *In situ* monitoring and characterization of distortion during laser cladding of Inconel® 625. *J. Mater. Process. Tech*. **220,** 135–145 (2015).
18. Farahmand, P. & Kovacevic, R. An experimental–numerical investigation of heat distribution and stress field in single- and multi-track laser cladding by a high-power direct diode laser. *Opt. Laser Technol*. **63,** 154–168 (2014).
19. Okano, S., Mochizuki, M., Toyoda, M. & Ueyama, T. Effect of welding conditions on reduction in angular distortion by welding with trailing heat sink. *Sci. Technol. Weld. Joi*. **17,** 264–268 (2012).
20. Yang, Y. P., Dull, R., Castner, H., Huang, T. D. & Fanguy, D. Material strength effect on weld shrinkage and distortion. *Weld. J*. **93,** 421-430-s (2014).
21. Gu, D. D., Meiners, W., Wissenbach, K. & Poprawe, R. Laser additive manufacturing of metallic components: materials, processes and mechanisms. *Int. Mater. Rev*. **57,** 133–164 (2012).
22. Wei, H. L., Mazumder, J. & DebRoy, T. Evolution of solidification texture during additive manufacturing. *Sci. Rep*. **5,** 16446; doi: 10.1038/srep16446 (2015).
23. Brice, C. A. *et al.* 4th International light metals technology conference. Broachbeach, QLD, Australia (2009).
24. Steen, W. M. & Mazumder, J. *Laser material processing* (Springer-Verlag, London, 2010).
25. Carroll, B. E., Palmer, T. A. & Beese, A. M. Anisotropic tensile behavior of Ti-6Al-4V components fabricated with directed energy deposition additive manufacturing. *Acta Mater*. **87,** 309–320 (2015).
26. Kong, C. J., Tuck, C. J., Ashcroft, I. A., Wildman, R. D. & Hague, R. High density Ti6Al4V via SLM processing: microstructure and mechanical properties. *International Solid Freeform Fabrication Symposium*. **36,** 475–483 (2011).
27. Jia, Q. & Gu, D. Selective laser melting additive manufacturing of Inconel 718 superalloy parts: Densification, microstructure and properties. *J. Alloy Compd*. **585,** 713–721 (2014).
28. Spierings, A. B. & Schneider, M. Comparison of density measurement techniques for additive manufactured metallic parts. *Rapid Prototyping J*. **17(5),** 380–386 (2011).
29. Taha, M. A., Yousef, A. F., Gany, K. A. & Sabour, H. A. On selective laser melting of ultra high carbon steel: Effect of scan speed and post heat treatment. *Mat.-wiss.u. Werkstofftech*. **43(11),** 913–923 (2012).
30. Mertens, A. *et al.* Microstructures and mechanical properties of stainless steel AISI 316L processed by selective laser melting. *Mater. Sci. Forum*. **783-786,** 898–903 (2014).

Acknowledgements

We thank Dr. Allison Beese and Dr. Wei Zhang for helpful comments and acknowledge the support from US Department of Energy NEUP Grant DE-NE0008280.

Author Contributions

T.D. and A.D. conceived the idea. T.M., J.S.Z. and A.D. performed the computer simulations and calculations. T.M. and J.S.Z. analyzed the data and interpreted the results under the direction of A.D. and T. D. All authors contributed to preparing the manuscript.

Additional Information

Supplementary information accompanies this paper at http://www.nature.com/srep

Competing financial interests: The authors declare no competing financial interests.

How to cite this article: Mukherjee, T. *et al.* Printability of alloys for additive manufacturing. *Sci. Rep*. **6**, 19717; doi: 10.1038/srep19717 (2016).

Appendix I:

Fabrication of compositionally graded test specimens using laser based additive manufacturing

Fabricating initial test specimens

Initial experiments were undertaken to fabricate compositionally graded transition joints using custom-blended powder compositions to investigate as-deposited microstructures, microhardness changes and carbon diffusion. A multiple nozzle, high energy high deposition (HEHD) machine was used for building the samples. The advantage of this machine is its ability to deposit material quickly by using relatively high laser powers and fast travel speeds. The scanning pattern used in both experiments is schematically shown in Figure 1. Each layer consisted of 5 passes, all scanned in the same direction. For the next layer, the scanning direction was opposite of the previous layer. Based on the experience of the technician, this strategy gives the best results in terms of the target geometry.

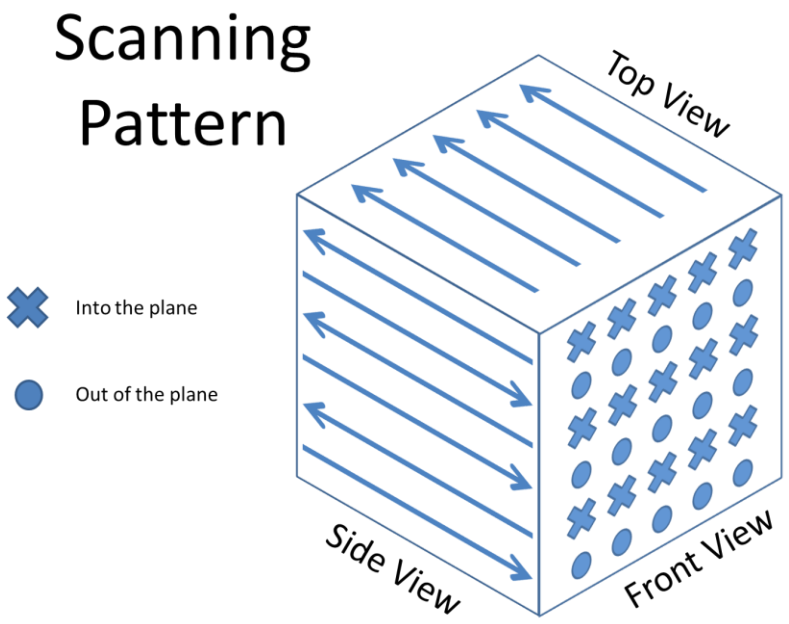

Figure 1. Scanning pattern used for experiments

In the first experiment, various mixtures of pure iron and chromium powders were blended to different compositions and deposited onto a 2.25Cr-1Mo substrate. The purpose of building these

samples is to study carbon diffusion through an iron matrix with different concentrations of chromium. A total of 9 samples were built on the substrate. Seven different blends were mixed having compositions ranging from 1 to 10 wt% Cr with the remaining wt % being Fe. In all, there were 3 distinct types of samples built as shown in Figure 2. Type 1 is a uniform blend of a single composition capped with a few layers of Pyromet 800 powder (Alloy 800H). Types 2 and 3 were gradients, which contained a few layers of each of the 7 different compositions from the substrate to the Pyromet 800 cap. The difference between Types 2 and 3 is that Type 2 contains 2 layers of Inconel 625 as a butter to mimic conventional welding practices. A small cap of Pyromet 800 was put on the samples so diffusion can be studied from both ends of the build simultaneously.

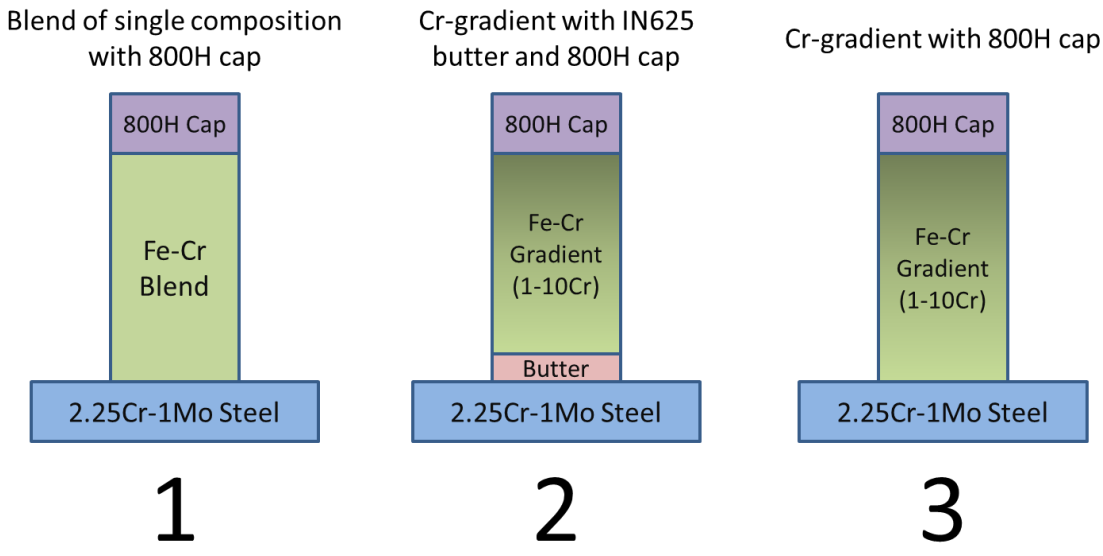

Figure 2. Schematic diagram of the various sample types fabricated

Figure 3 below shows a photograph of the nine different Fe-Cr builds. The small spherical balls that appear on the sides of the build are a result from partially melted particles that came in contact with the build shortly after solidification. Since the purpose of the experiments is to study

diffusion through the bulk of the material, these partially melted particles are not a concern. Figure 4 and Figure 5 show the dimensions of the Fe-Cr builds. A total of 32 layers were deposited for each build with four of those being Alloy 800H. The layer thickness was about 0.9 mm. Therefore, 28 layers of the custom blends were deposited to give a height of about 25.4 mm (1 inch). The width of each layer was about 2.54 mm, so a total of 5 passes per layer made the width of the build approximately 12.7 mm (1/2 inch) thick.

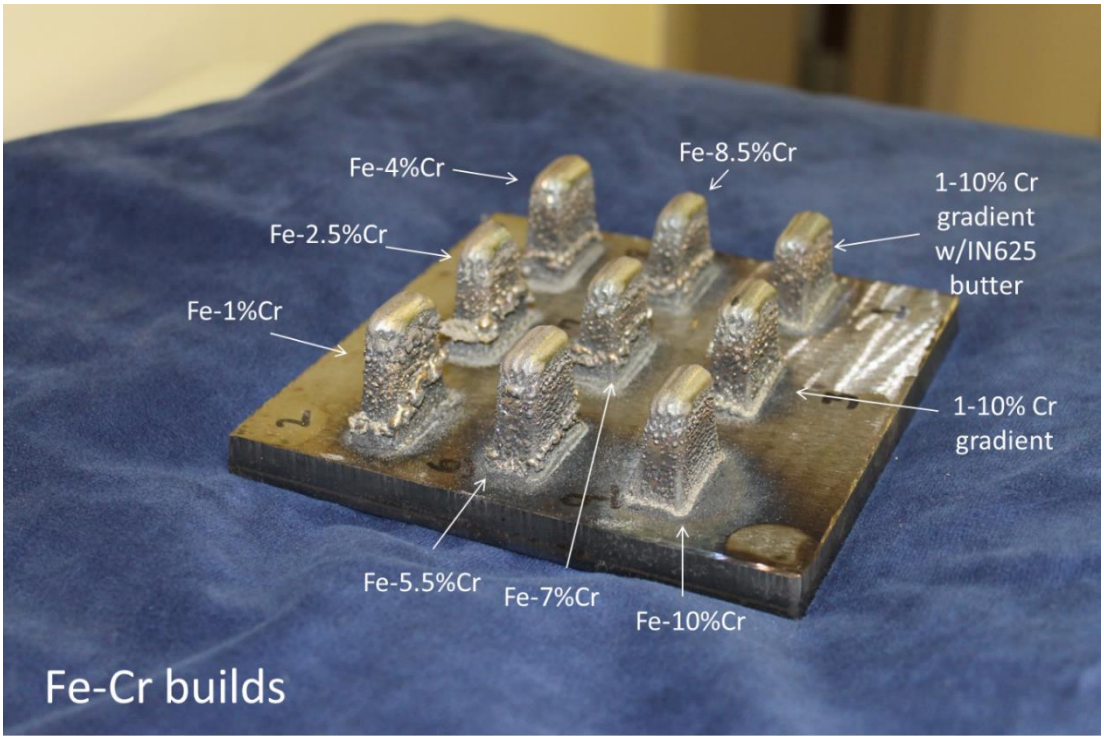

Figure 3. Fe-Cr builds on a 2.25Cr-1Mo steel substrate

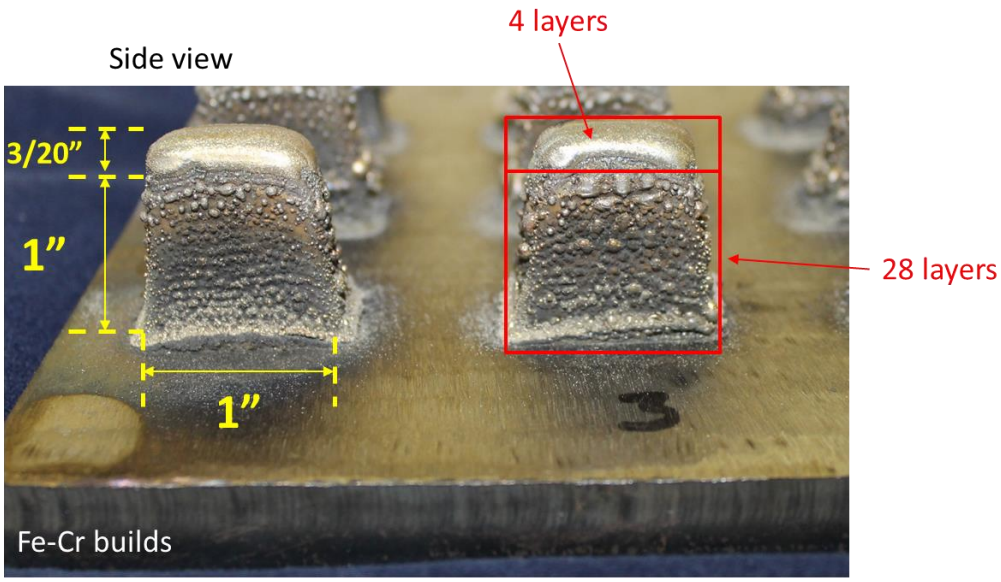

Figure *4*. A front view of the Fe-Cr builds showing dimensions

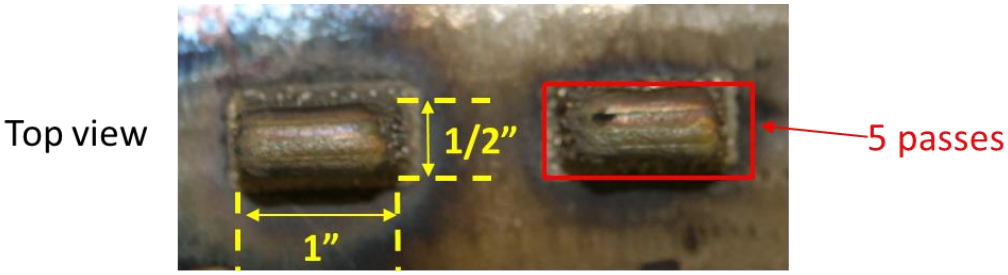

Figure 5. Top view of Fe-Cr builds with dimensions

The second experiment was similar in setup to the first experiment. However, the second experiment focused on a mixture of a Fe-Cr blend with Pyromet 800 powder. First, Fe and Cr were blended to a composition of 2.25 wt% Cr and 97.75 wt% Fe. This mixture was then blended with Pyromet 800 powder. The amount of 800H of the mixture ranged from 10 to 100 wt% in increments of 10 wt%.

The three different sample types are shown in Figure 6. Similar to the previous experiment, Type 1 is a single composition blend capped with 800H whereas Type 2 and 3 are gradient blends ranging from 10 wt% to 100 wt% 800H. Type 2 contains a two-layer butter of Inconel 625.

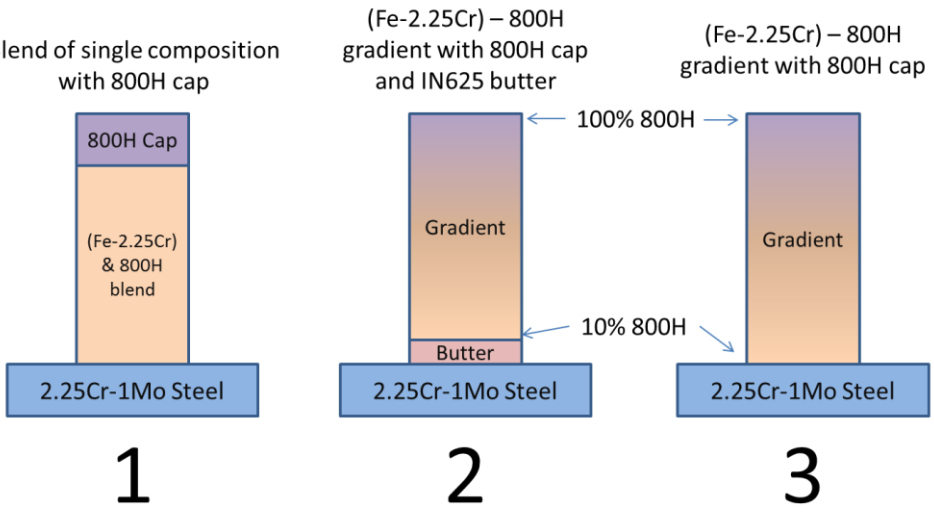

Figure 6. Schematic diagram of the various sample types fabricated

Nine samples were deposited onto a 2.25Cr-1Mo steel substrate as shown in Figure 7. After building a Type 1 sample (starting with 10% 800H), four layers were added to the gradient samples (Types 2 and 3) to vary the composition in the build. Although only seven Type 1 samples were built ranging from 10 to 70 wt% 800H, blends of 80 and 90 wt% 800H were prepared and added to the Type 2 and 3 samples to cover the full range of variation from 100% (2.25Cr-1Mo) steel to 100% 800H. The process parameters for the experiments are shown in Table 1.

Parameter (units)	Value
Laser power (W)	2000
Travel speed (mm/s)	10.6
Powder flow rate (g/min)	~ 15
Focus head standoff (mm)	10
Beam diameter (mm)	~ 4

Table 1. Process parameters used for fabricating compositionally graded test specimens

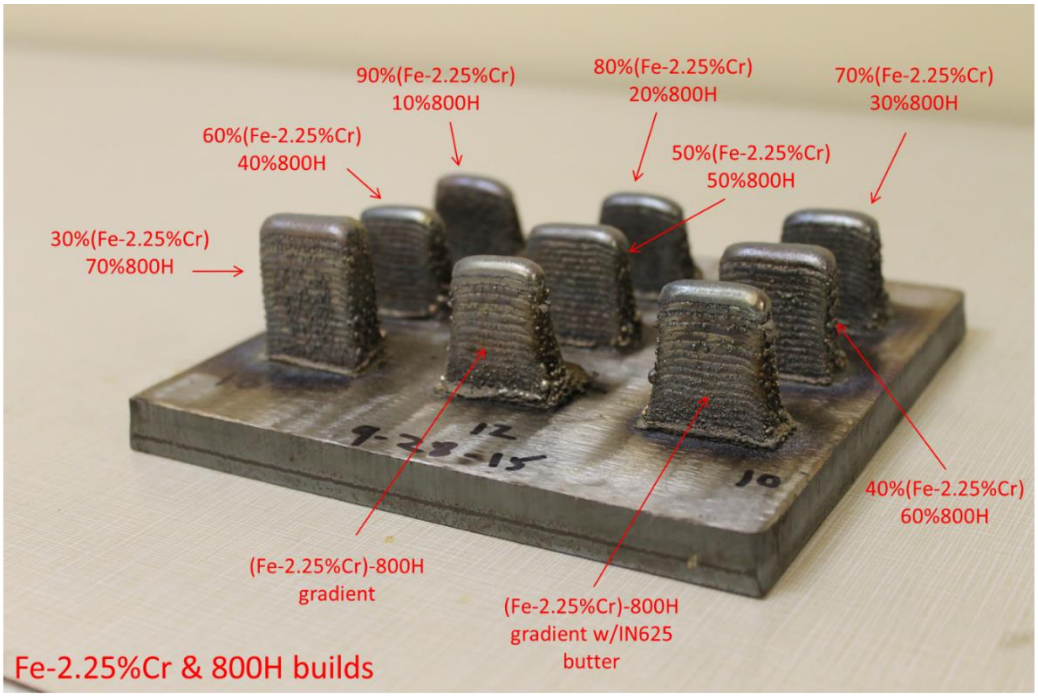

Figure 7. Various builds with custom blends of Alloy 800H and (2.25% Cr-Fe)

Due to their relatively small size, the samples were sent to an outside vendor to be cut by electrical discharge machining (EDM). The benefit this type of sectioning is the minimal material lost, the precision of the cuts and the capability of providing multiple cross sections of the same sample.

In order to test whether the compositionally graded samples being developed will achieve the overall goal of extending creep lifetime compared to dissimilar metal welds, it is imperative that the amount of AM process induced defects is minimized or completely eliminated. After fabrication of the initial samples, multiple lack of fusion defects vertically aligned in the build direction have been observed, which is shown in Figure 8. The most probable reason for these types of periodic defects is due to the choice of improper hatch spacing. As the composition varies greatly from one end of the gradient to the other, the thermos-physical properties also change. It

is predicted that these changes in properties ultimately have a significant impact on the shape and size of the molten pool.

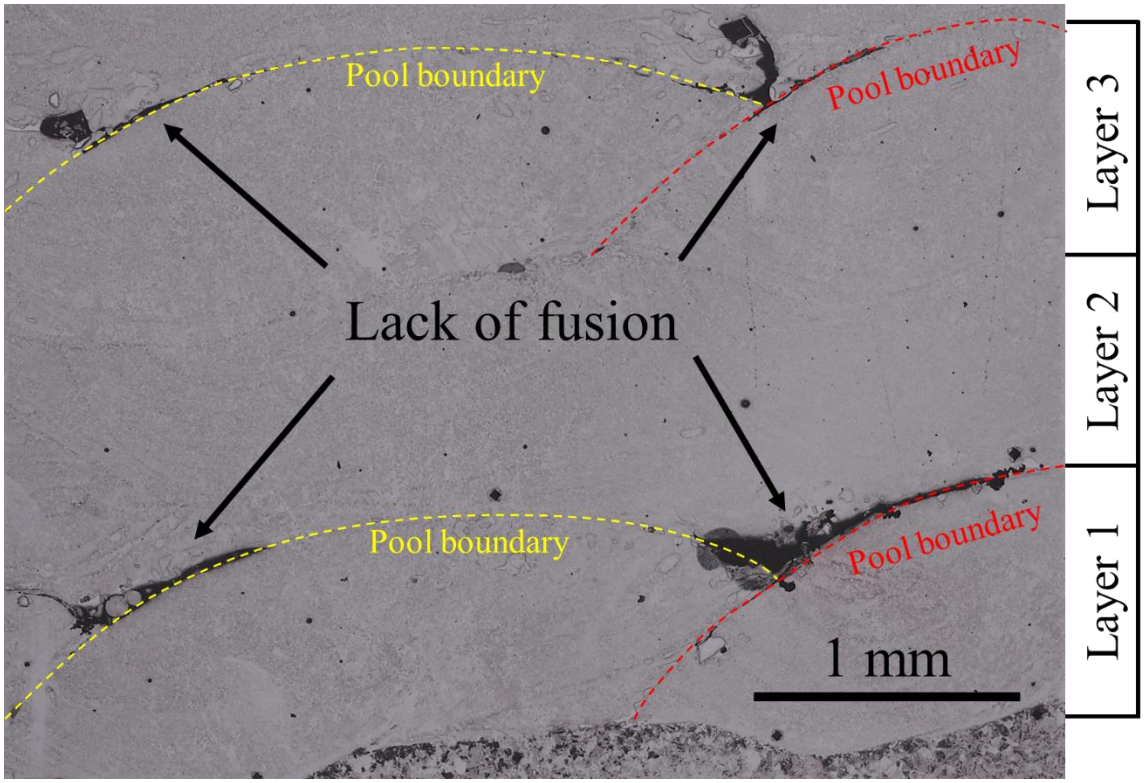

Figure 8. *Vertically aligned lack of fusion defects in the 10% 800H region of a ferritic/austenitic FGM*

Fabricating single layer deposits to study molten pool dimensions

To understand how the changes in composition effect the molten pool geometry along the composition gradient, a series of single track, single layer beads were deposited onto an SAE387 Grade 22 steel substrate. A total of 44 tracks consisting of 11 different chemical compositions were deposited using the process parameters displayed in Table 1, except a total of 4 different laser powers (1500, 2000, 2500, 3000W) were used for each composition. The samples were sectioned into smaller transverse cross sections and mounted in epoxy. Each sample was grinded with a series of SiC papers and a mirror-finish was achieved from final polishing using 0.04 µm colloidal

silica. Measurements of the cross section width and height were taken using ImageJ, available at PSU. Results from the measurements are shown in Figures 9 and 10. It can be seen that there are significant differences in the deposit dimensions as a function of chemical composition.

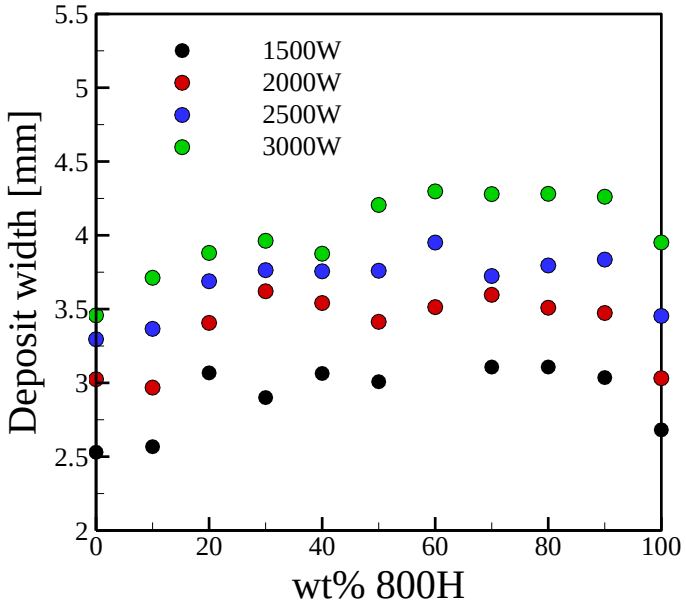

Figure 9. Measured deposit width for single track, single layer beads for compositions varying from 2.25Cr-1Mo steel (0 wt% 800H) to 100 wt% 800H

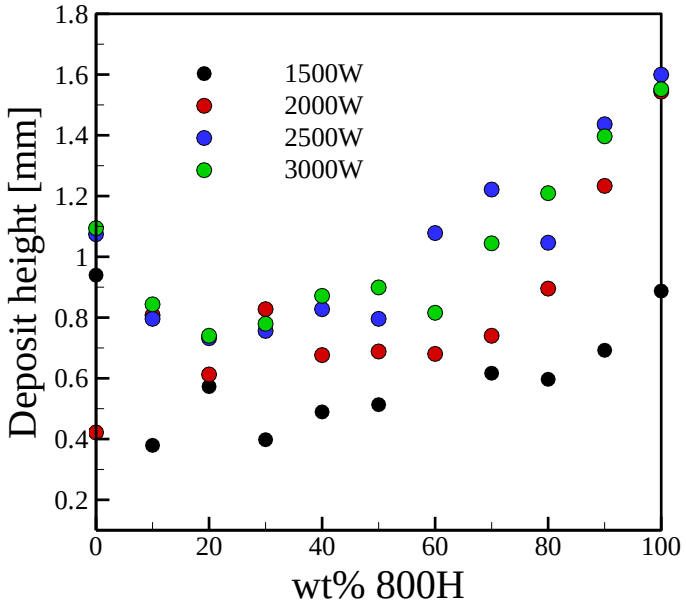

Figure 10. Measured deposit height for single track, single layer beads for compositions varying from 2.25Cr-1Mo steel (0 wt% 800H) to 100 wt% 800H

It was concluded from the experiments that changes in chemistry on compositional grading significantly affect the molten pool geometry. In general, as the chemical composition

changed from the ferritic steel to the austenitic alloy, the molten pool grew larger in volume. Representative micrographs of selected compositions highlighting the observed changes are shown in Figure 11. These important findings provide insight that the use of constant process parameters during compositional grading may not be sufficient for obtaining target geometry and can lead to the formation of internal defects if the spacing between passes is not carefully controlled.

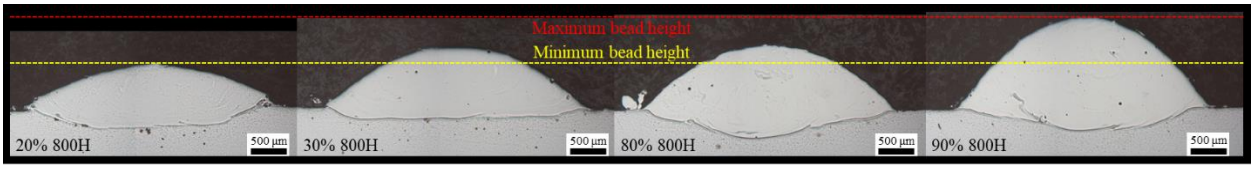

Figure 11. Transverse cross sections of single pass deposits with different compositions showing significant changes in geometry, notably width and height

Fabrication of specialized creep test specimen

A compositionally graded test specimen approximately 152.4 mm (~6 in.) in length was fabricated at PSU using the in-house HEHD laser-based deposition system. The parameters used for the depositions are shown in Table 2. The target dimensions of the specimen were 152.4 mm (6 in.) in height, 38.1 mm (1.5 in.) in width and 101.6 mm (4 in.) in length. The sample has been sectioned into smaller slices, as shown in Figure 12. The different slices will be subjected to aging and other heat treatments as well as for characterization of the as-deposited microstructure.

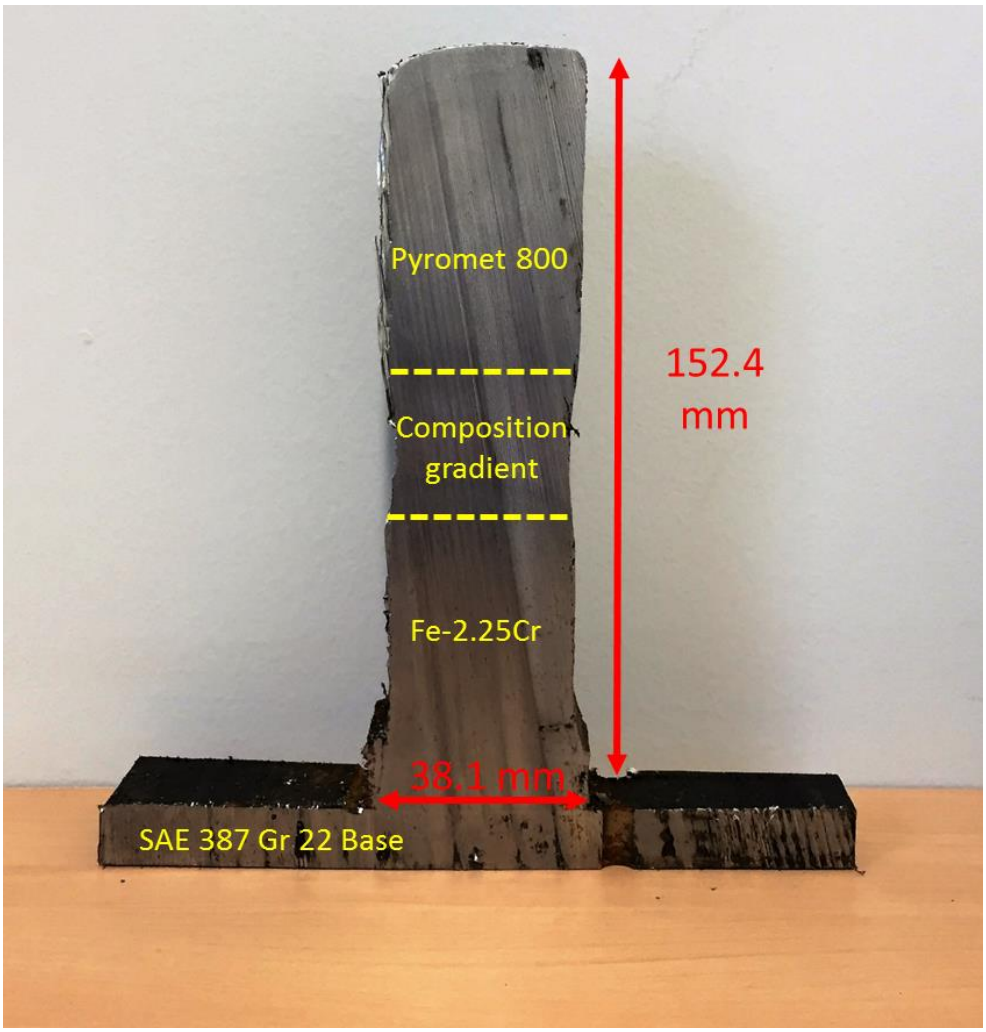

Figure 12. Transverse section of 152.4 mm build

The sample was fabricated by first building to a height of about 63.5 mm (2.5 in.) with a custom powder blend with a composition of Fe-2.25Cr to resemble the SAE 387 Grade 22 baseplate (Cr-Mo Steel). Then, a 25.4 mm (1 in.) compositionally gradient region was deposited in increments of 9 different powder blends. From the measured layer height and vertical step distance, two layers of each blended composition were deposited before switching the powder to a new composition. Finally, a 63.5 mm (2.5 in.) region was deposited on top of the compositionally gradient region using Pyromet® 800 powder (Alloy 800H).

Parameter (units)	Value
Laser power (W)	2500
Travel speed (mm/s)	10.6
Powder flow rate (g/min)	~ 15
Focus head standoff (mm)	10
Beam diameter (mm)	~ 4

Table 2. Process parameters used for 152.4 mm specimen

Upon sectioning the larger build into smaller slices, a large crack extending most of the way across the sample was noticed near the beginning of the compositionally graded region. As a result, the sample was unable to withstand the high forces of water jet cutting, and a fracture of the specimen occurred as depicted in Figure 13. There are a few possible reasons the crack could have resulted. The deposition took place over two business days, as the large dimensions were unable to be completed in one working day. It appears that the fracture occurred at the interface between the last layer deposited on the first day and the first layer deposited the next day. As a result, it is possible that unwanted oxides could have formed, which could prevent adequate fusion between layers. Also, the sample was able to cool to room temperature overnight, which may have had a negative effect on penetration of the successive layer.

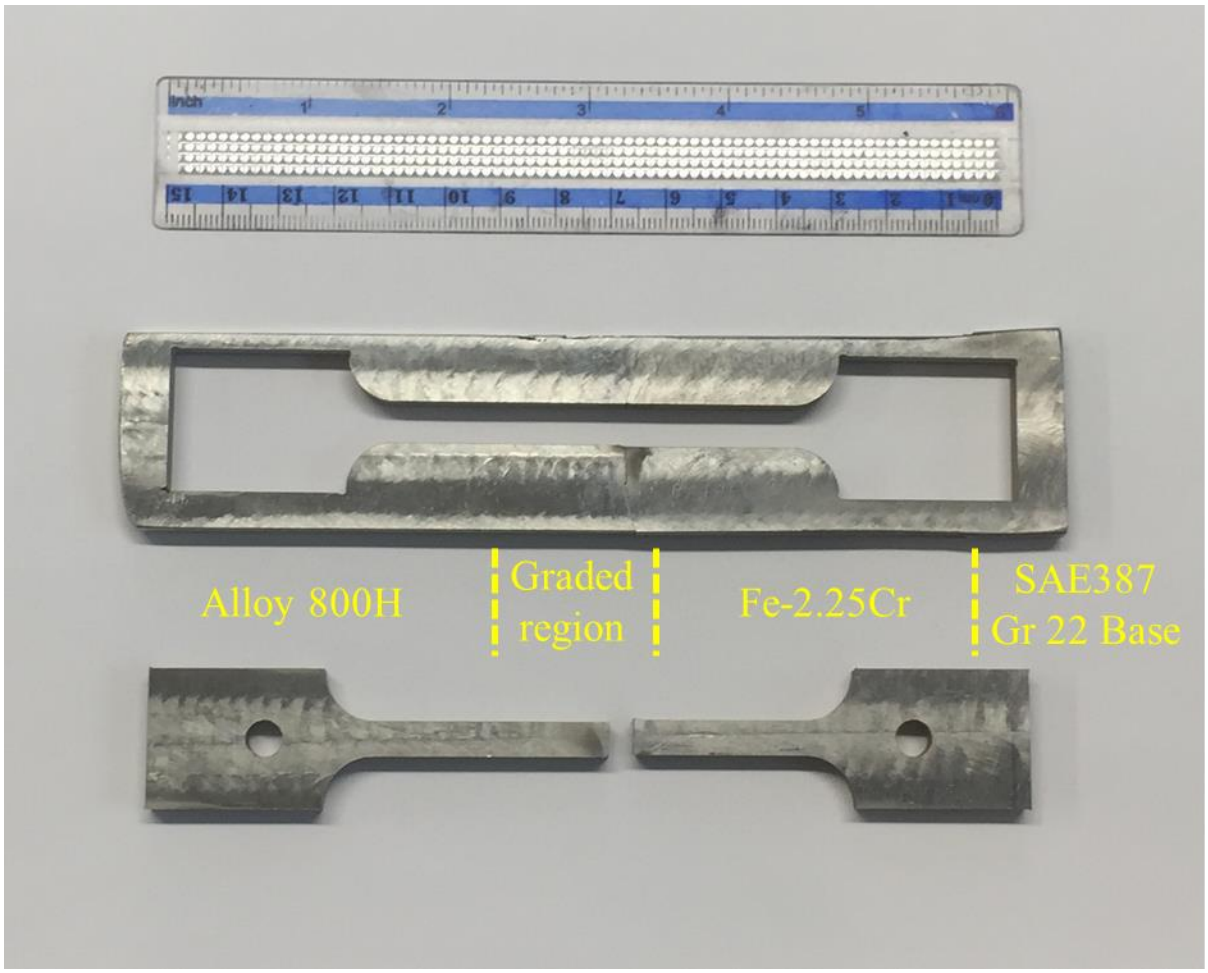

Figure 13. Photo showing fractured flat dog bone creep sample extracted from AM deposit

To address this issue, the remaining sections were sent to an outsider vender for hot isostatic pressing (HIP). This process uses high temperatures and pressures to close internal openings in metallic parts such as gas induced porosity, lack of fusion defects and micro-cracks. Due to the inhomogeneity of the sample material and based on the suggestion from the vender, a common HIP procedure for stainless steels was chosen. It was concluded that the compositions found in the compositionally graded specimen most resembled that of high nickel stainless steels, such as SS316L. The samples were first heated to 1150°C at a rate of 15°C/minute, then held at this temperature for about 4 hours. Following this treatment, the samples were then cooled to room

temperature at 200°C/minute. However, it was revealed that the crack was too large to be closed by HIP.

Therefore, another experimental deposition was undertaken using similar process parameters. However, much care was taken to prevent cracking and ensure a build with no large detrimental defects. To do so, each previously deposited layer was preheated by using low laser power and high scanning speed between stopping and starting the process. It was expected that this method would keep the build at an elevated temperature in order to promote better bonding between layers. The specimen was sent for HIP to an outside vendor in order to close gas pores. Two types of samples were extracted from the large block. In one type, the flat face of the dog bone sample was perpendicular to the scanning direction while in the other type, the flat face was parallel. In each of the samples, the long dimension of the dog bone was oriented with the build direction. Figure 14 shows that 8 samples were able to be extracted from the large build. Of these, two exhibited noticeable internal porosity.

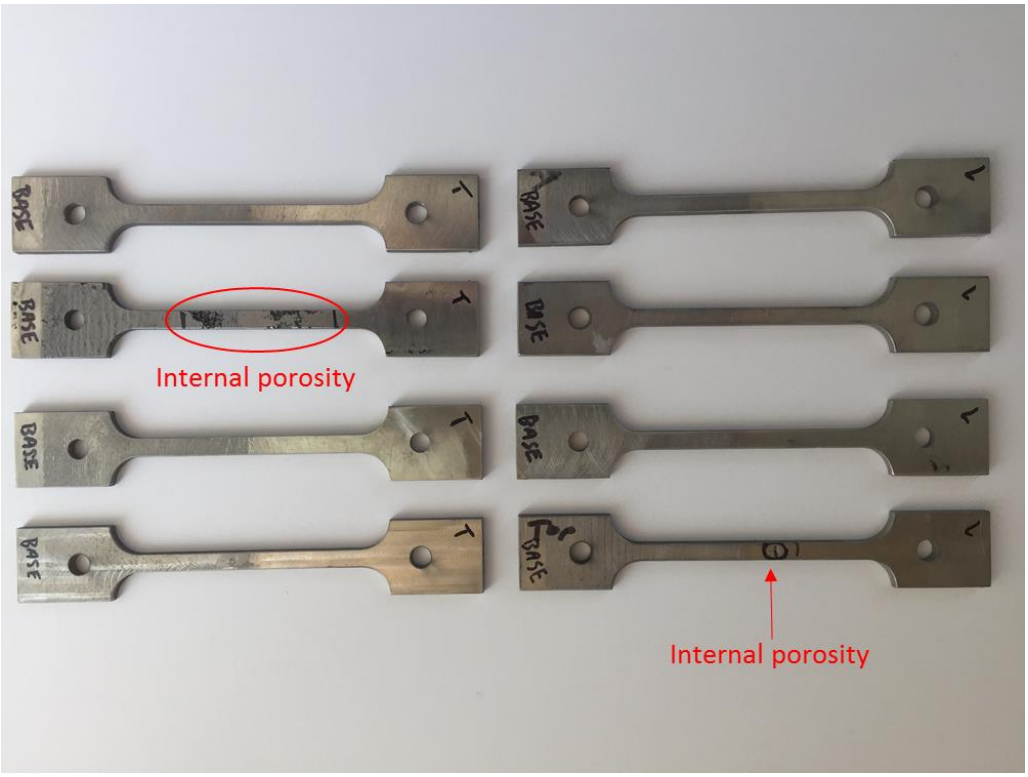

Figure 14. Flat dog bone graded test specimens for specialized creep testing at ORNL

The purpose of this deposition can be summarized in the following takeaways. First, we have demonstrated the ability to scale-up our processing of sub-size samples to scales more typical of application. Next, a specimen has been fabricated where tensile bars meeting the required dimensions were extracted and sent to ORNL for specialized creep testing in which local deformation within the compositionally graded transition region can be characterized.

Appendix J:

Creep testing at Ohio State University and Oak Ridge National Laboratory

Traditional Creep Testing at OSU

The goal of this task was to provide baseline creep data for dissimilar metal welds between 2.25Cr-1Mo steel and Alloy 800H. The welding machine used at OSU is a robotic gas metal arc welding (GMAW) machine. As a first step, single bead-on-plate tests were performed to find the parameters which resulted in a bead with the best surface appearance. The purpose of this study was to find optimal parameters for producing a high quality weld. The parameters varied in the study were wire feed speed, stick out distance, travel speed and dragging angle. The results from the study are summarized in a supplementary document entitled "OSU-DMWs Testing."

The initial dissimilar metal welds were made between 2.25Cr-1Mo steel and Alloy 800H using an Alloy 800H backing plate. The filler metal used was IN82, which has been previously been reported in available literature. A preheat temperature of 280°C was used. A total of six beads were necessary to complete the weld: one bead in the first layer, two beads in the second layer and three beads in the final layer. After completion, the welds showed noticeable angular distortion and cross-sectional macrographs showed lack-of-fusion defects, as shown below in Figures 1 and 2. The results of this study indicated that future work needed to be done to optimize welding parameters to eliminate lack of fusion defects and to modify the fixtures in order to reduce angular distortion. More information and results can be found in the attached document entitled "DMW Experiment I."

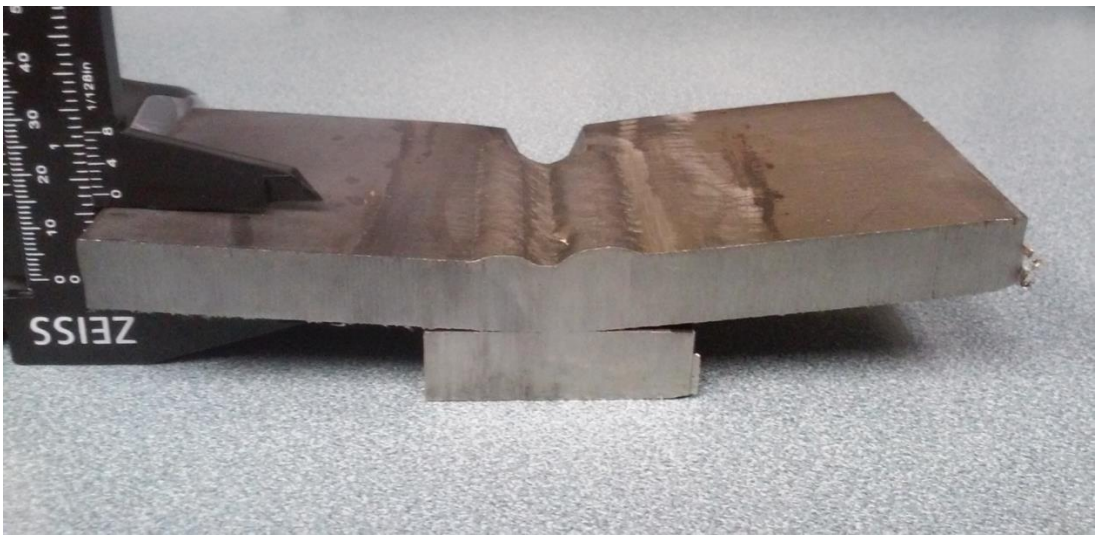

Figure 1. Angular distortion in initial DMW between 2.25Cr-1Mo steel and Alloy 800H

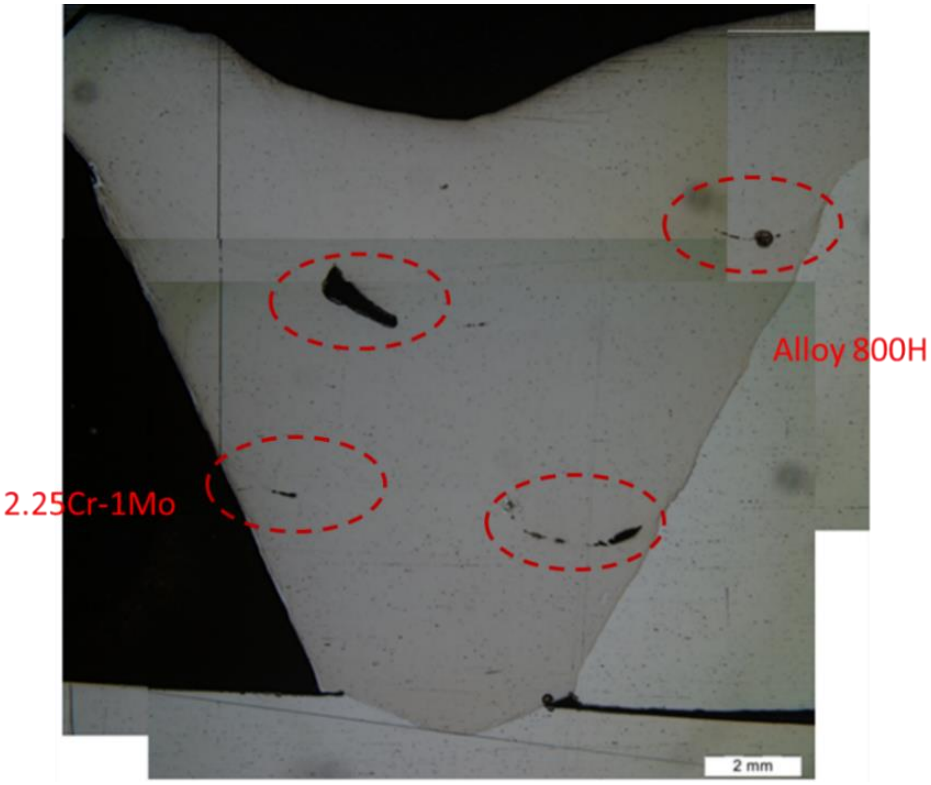

Figure 2. Lack of fusion present in initial DMW between 2.25Cr-1Mo steel and Alloy 800H

Lack of fusion defects can serve as stress concentrators under an applied load and therefore are detrimental to the mechanical properties of the DMW. Thus, it is imperative that the number and size of these voids is completely eliminated or minimized in order to truly test the properties of the weld. In the second DMW experiment, welding parameters were adjusted to eliminate the lack of fusion defects that were found in the first experiment. Figure 3 shows that the number of voids was reduced and only a small gas pore could be seen. The weld design, parameters, setup and results of the weld can be found in the accompanying document, "DMW Experiment II."

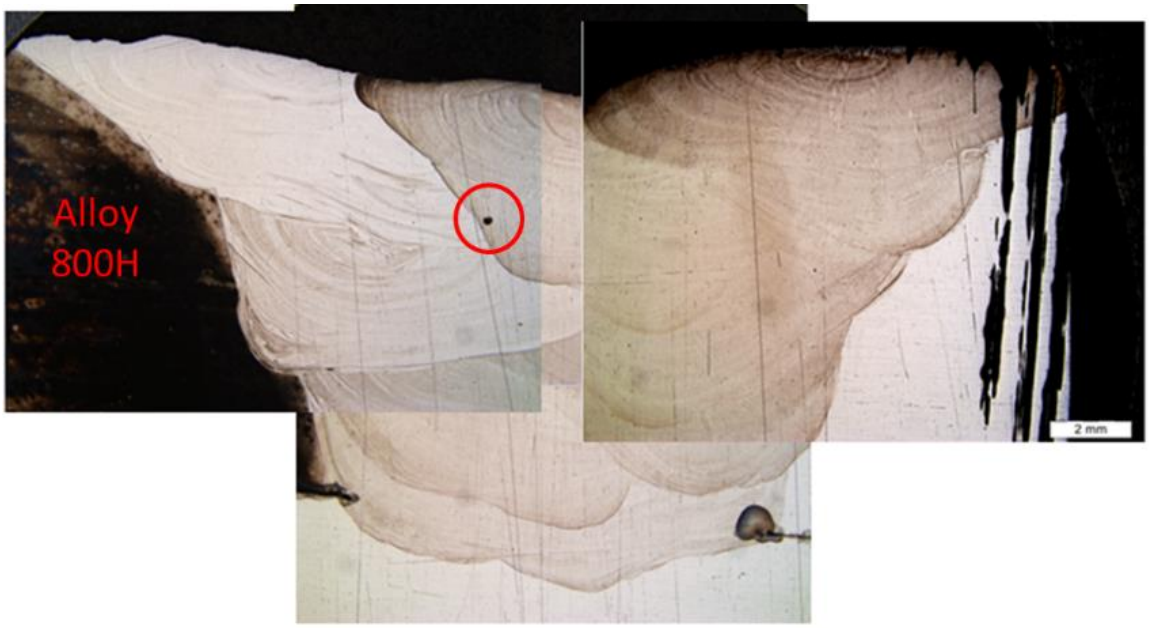

Figure 3. Macrograph of the second DMW showing no observable lack of fusion defects and one small gas pore (red circle)

A post weld heat treatment (PWHT) of 700°C for 3 hours has been chosen to alleviate residual stresses. Two cross sections of the weld perpendicular to the welding direction were taken for microstructural characterization: one before and one after PWHT. The sample configuration used for the testing is shown below in Figure 4. According to the literature, the main area of concern that accounts for the poor creep performance of DMW between 2.25Cr-1Mo steel and Alloy 800H is near the fusion line of the steel and filler metal. For this reason, the middle of the sample gauge was centered around the fusion line between 2.25Cr-1Mo steel base and the IN82 filler metal, as depicted in Figure 5.

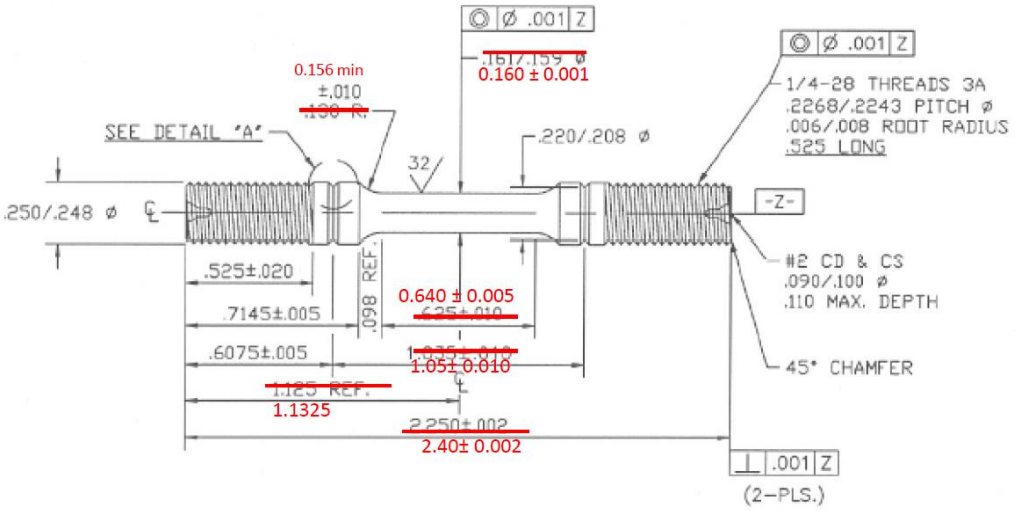

Figure 4. Sample configuration for traditional creep testing

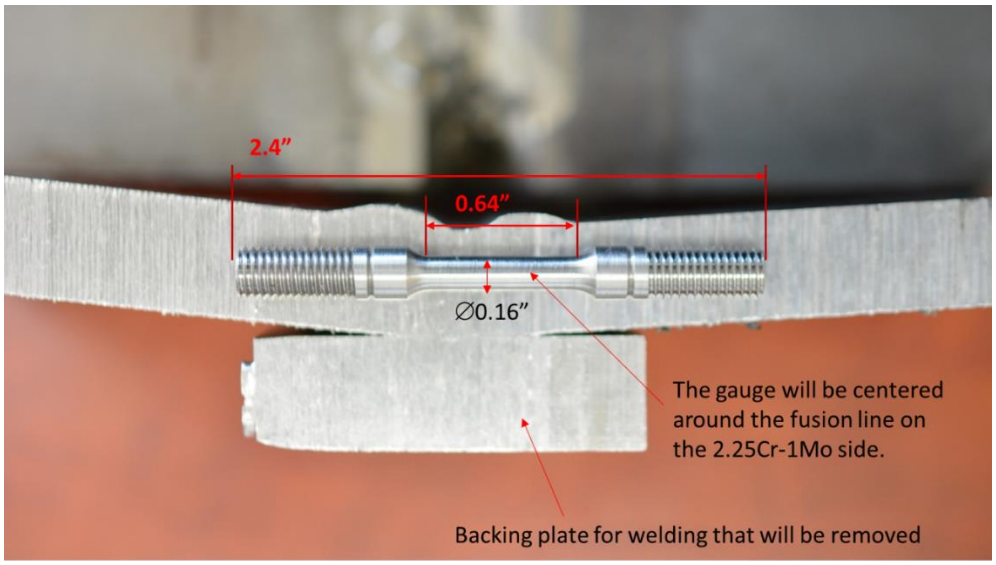

Figure 5. Photograph showing the dimensions and location of the sample along the DMW

Two creep specimens were machined from the PWHT dissimilar metal weld. Each was tested at a stress level of 220 MPa (31.9 ksi) at a temperature of 550°C (1022°F). The strain behaviors of the tests are shown Figures 6 and 7. In Figure 6, the extrapolation was done using the data between 10 and 11.4 hours. Using this extrapolated data, the rupture strain at 20.4 hours is approximately 2.89%. While testing creep specimen 2, the extensometer ran out of travel at 60 hours. The rupture strain at 72.4 hours was about 3.18%.

The data obtained from the creep tests were compared with data from the literature, which were also taken for a dissimilar metal weld between 2.25Cr-1Mo Steel and Alloy 800H. Figure 8 shows that the data obtained in this study is comparable with that of the literature. The results serve as a baseline for dissimilar metal welds that will later be compared with results from creep testing graded transition joints.

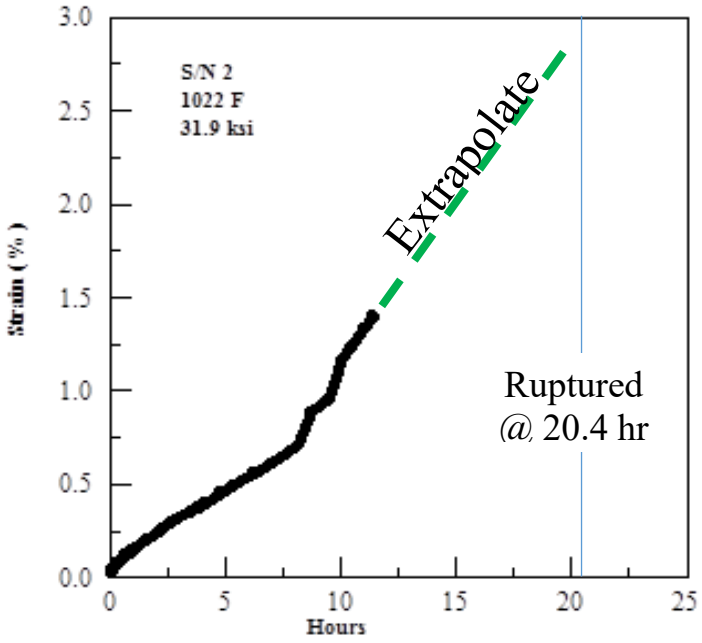

Figure 6. Strain vs. time for creep specimen 1 during creep test at 31.9 ksi (220MPa) and 1022°F (550°C)

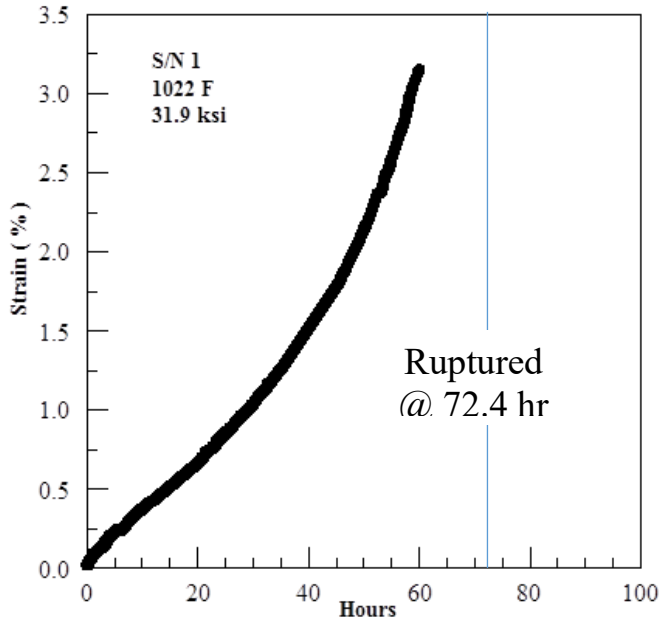

Figure 7. Strain vs. time for creep specimen 2 during creep test at 31.9 ksi (220MPa) and 1022°F (550°C)

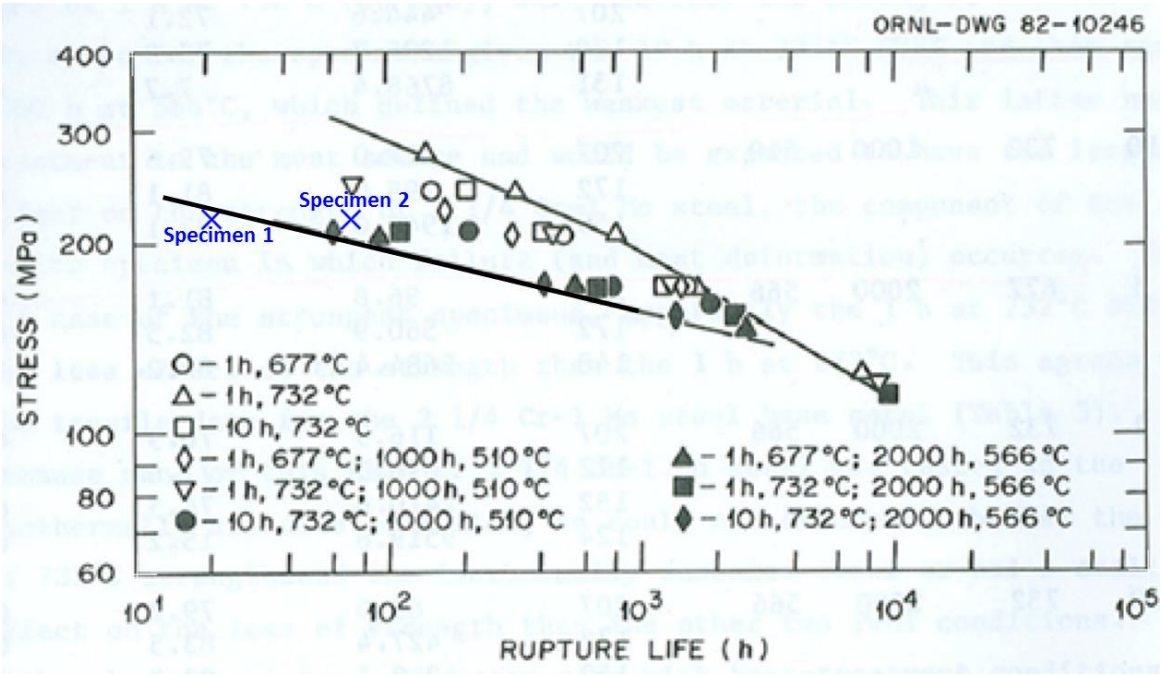

Figure 8. Comparison of baseline creep data with literature data from Klueh, K. L. and King, J. F. *Elevated temperature Tensile and Creep-Rupture Behavior of Alloy 800H/ERNiCr-3 Weld Metal/2.25Cr-1Mo Steel Dissimilar-Metal Weldments.* (ORNL, 1982).

Specialized Creep Testing at ORNL

One of key issues of premature failure in dissimilar metal weld (DMW) is localized deformation in a very narrow region in the weld and HAZ of ferritic steels and near the interface of a DMW. It has been long recognized that, due to the sharp microstructure and property gradients in the weld and HAZ, standard stress-to-rupture testing procedures that simply measure overall strain can produce erroneous results. ORNL team developed a new weld creep testing technique, using high-temperature digital image correlation (DIC), to measure the localized non-uniform deformation of a cross-weld specimen. This new technique has been proven to be very effective to determine the localized creep deformation and failure in the highly non-uniform weld region of creep resistance steels.

Tensile creep-rupture tests of the weld cross-sections were performed using a GleebleTM thermal mechanical simulator. Samples were machined according to the dimensions shown in Figure 9. The sample was heated to 650°C at 5°C/s and then a constant stress of 70MPa was applied. The creep-rupture tests were interrupted at 90 hours. During testing, an in-situ optical image correlation method was used to measure displacement on the surface of an object by tracking random patterns on the samples. Random speckles were created by painting techniques. Digital cameras (Point Grey GRAS-50S5C-C) linked with a computer were used for image acquisition. Sigma lenses (28-300mm f/3.5-6.3 DG) were used for zooming purposes. Since the thermal radiation from the hot sample at elevated temperature will lessen image contrast, resulting in large errors in DIC, the current study adopted monochromatic light illumination and narrow bandpass filter. 3x4 high-brightness green LED array (Visual Instrumentation model 900405, wavelength 530±5nm) and Edmund 532nm hard-coated bandpass filter (Part number 65155) were used. Images were taken at 1-minute intervals for the first 12 hours and then at 5-minutes intervals for the subsequent 78 hours. Images were post-processed by the Vic-3D software developed by Correlated Solutions and the strain maps were obtained. Figure 10 shows a creep strain map of a Grade 91 cross-weld sample. The current weld creep testing technique captured localized deformation in the heat affected zone of a cross-weld specimen.

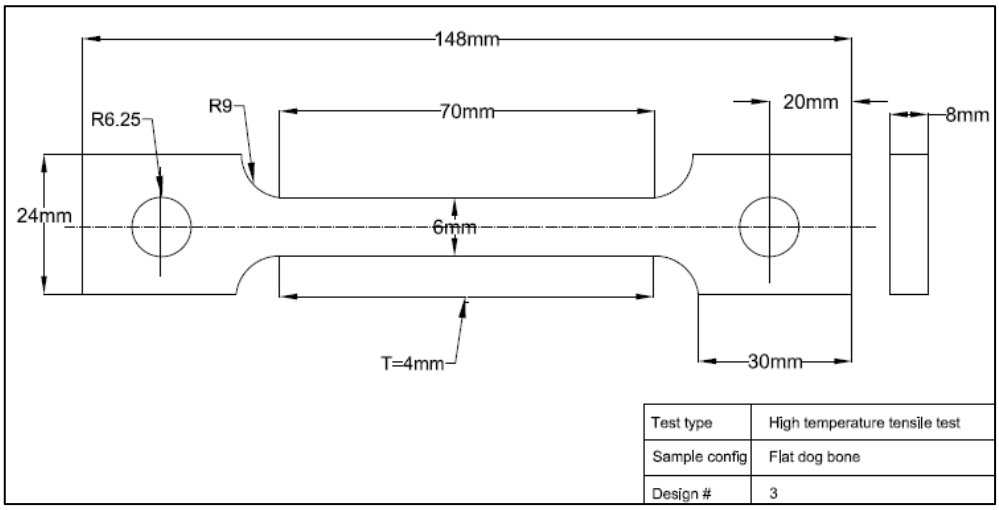

Figure 9. Sample configuration for digital image correlation creep testing

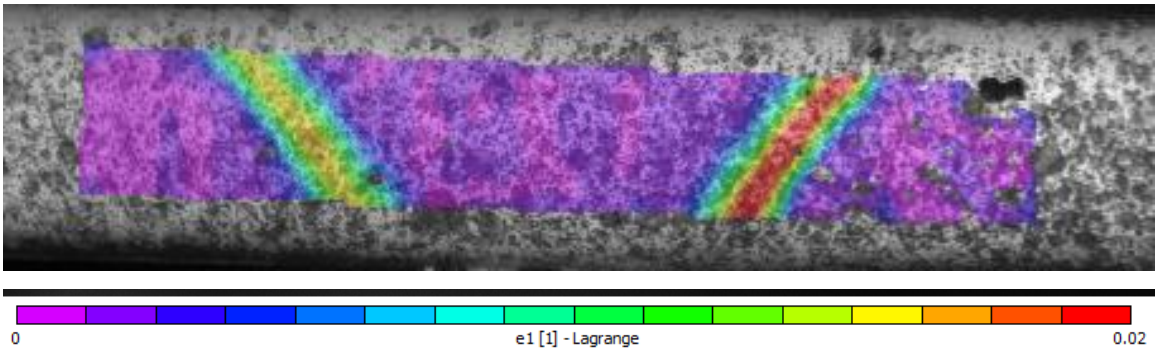

Figure 10. Creep strain map of a cross-weld sample showing localized deformation in heat-affected zone.

The weld creep testing technique is also applied to evaluate creep behavior of a DMW specimen (stainless steel 316L joined with 2.25Cr1Mo steel with Alloy 82 filler wire, as shown in Figure *11*). Testing temperature is 700°C. Temperatures of 3 distinct alloys were monitored by thermocouples and shown in Figure 12. Initial tests showed the temperatures of stainless steel 316L and Alloy 82 are well-controlled. However, the temperature of 2.25Cr1Mo is about 200°C lower than testing temperature. Joule heating and conduction heating are the major heating mechanisms for current testing. Low electrical resistance and high thermal conductivity of

2.251Mo steel resulted in lower temperature. ORNL team is working on finding alternative heating method to ensure uniform temperature distribution in a DMW specimen.

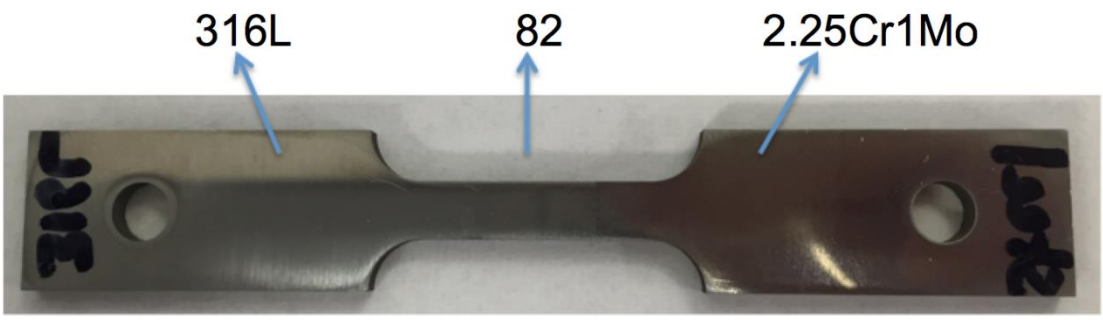

Figure 11. Test specimen of stainless steel 316L and 2.25Cr1Mo DMW.

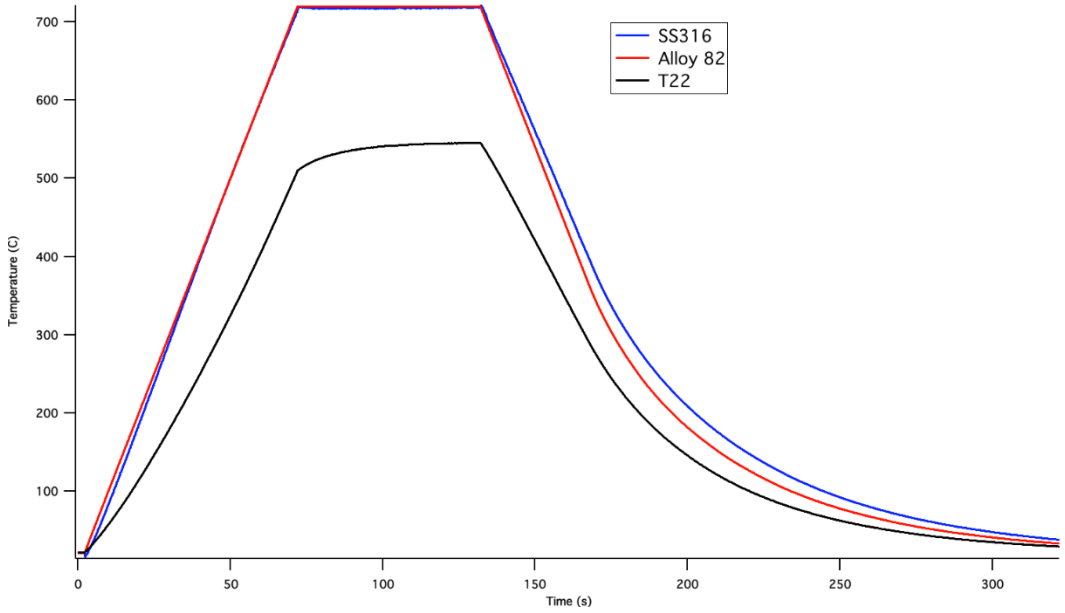

Figure 12. Temperature history of stainless steel 316L, Alloy 82 and 2.25Cr1Mo

Due to the significant difference in resistance and thermal conductivities between carbon steel and nickel alloy or stainless steels, there is a great temperature gradient in DMW when the sample was tested in Gleeble, whose heating mechanism is Joule heating. As a result, current study was seeking alternative testing techniques to study the localized creep deformation in DMW. A direct loading creep testing system at ORNL was used to perform stress to rupture test. A T22/Alloy 82/SS316 DMW flat dog-bone sample were painted with high temperature

resistance paint for digital image correlation (DIC). Several digital images were taken on both sides of the sample before testing as reference images. The test was performed at 100MPa and 600°C in pure argon environment. Three thermocouples were attached on the sample to monitor the temperature distribution across the weld as shown in Figure 13.

The creep test was stopped manually after 378 hours. Even with argon protection, surface paint showed significant degradation. The contrast between the white background and black speckles on tested sample is much less than the reference of untested sample (Figure 14) and this may reduce the accuracy in DIC analysis. In addition, some spallation of paint was observed, especially on the back size of the sample. We think the spallation of paint is due to formation of brittle oxide between paint and sample surface. As a result, there are two ways to mitigate the spallation: 1. Create better bonding between sample surface and paint to prevent oxygen penetration and 2 reduce oxygen exposure on sample. These two methods will be evaluated in the future.

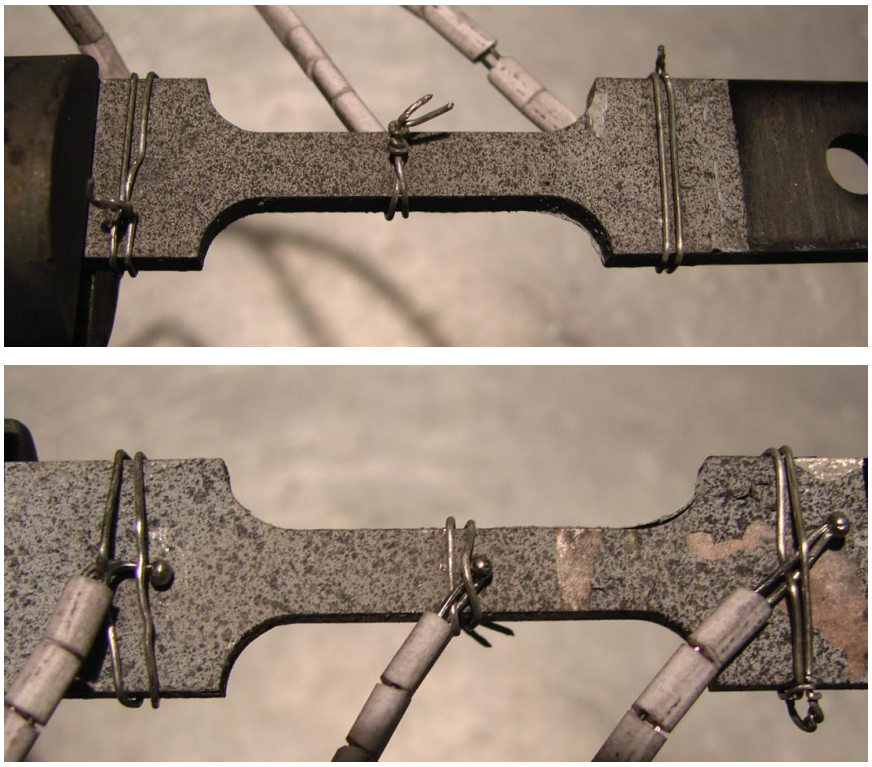

Figure 13. DMW sample image after 378 hours creep testing; SS316 is on the left and T22 is on the right (a) front side that was used for DIC analysis (b) back side showing spallation of surface paint

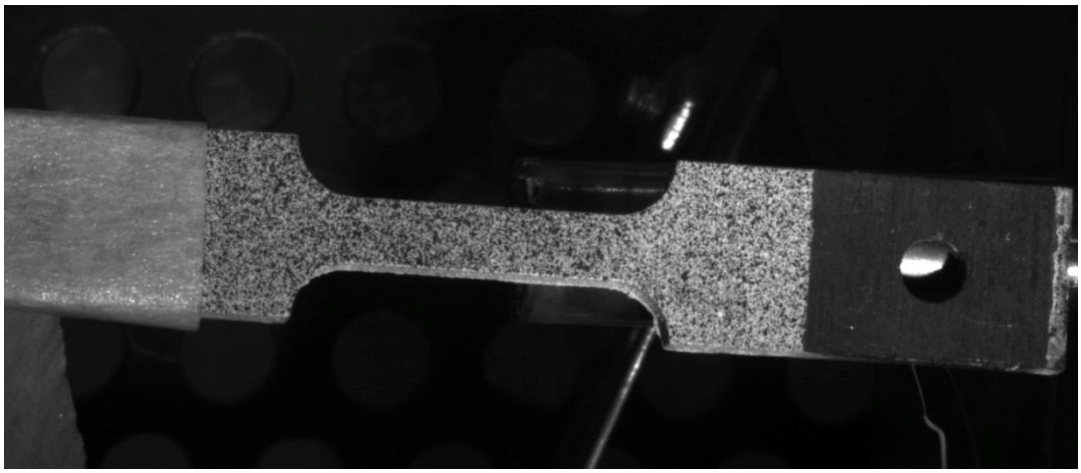

Figure 14: DMW sample image before creep testing showing speckle patterns with good contrast; SS316 is on the left and T22 is on the right

A digital image of tested sample was captured using the same camera setup as used for reference image to insure the consistency in measurement. Correlation between reference sample image and tested sample image could be performed by Vic-3D® software even with contrast difference. The region of Interest (ROI), as shown in Figure 15, was selected, which included 9mm of Inconel-82 material, 10mm of 2.25Cr-1Mo material and 10mm of 316 Stainless steel material. Figure 15 shows creep strain distribution across the DMW after 378 hours of testing. Localized creep deformation was observed in T22 heat-affected zone and base metal. The highest strain was found at a location 5mm from T22/Alloy 82 interface in T22 with a value of 0.035.

The current study demonstrated the feasibility of using DIC on interrupted creep test to determine the localized creep deformation of DMW. However, even when the test ran less than 400 hours, some paint degradations were observed. Future work will be focused on improving paint contrast sustainability at high temperature for long-term exposure. In addition, it is also very important to perform continuous creep testing with real time strain distribution measurement. Special designed creep testing system will be designed and built later to incorporate digital image recording in real time.

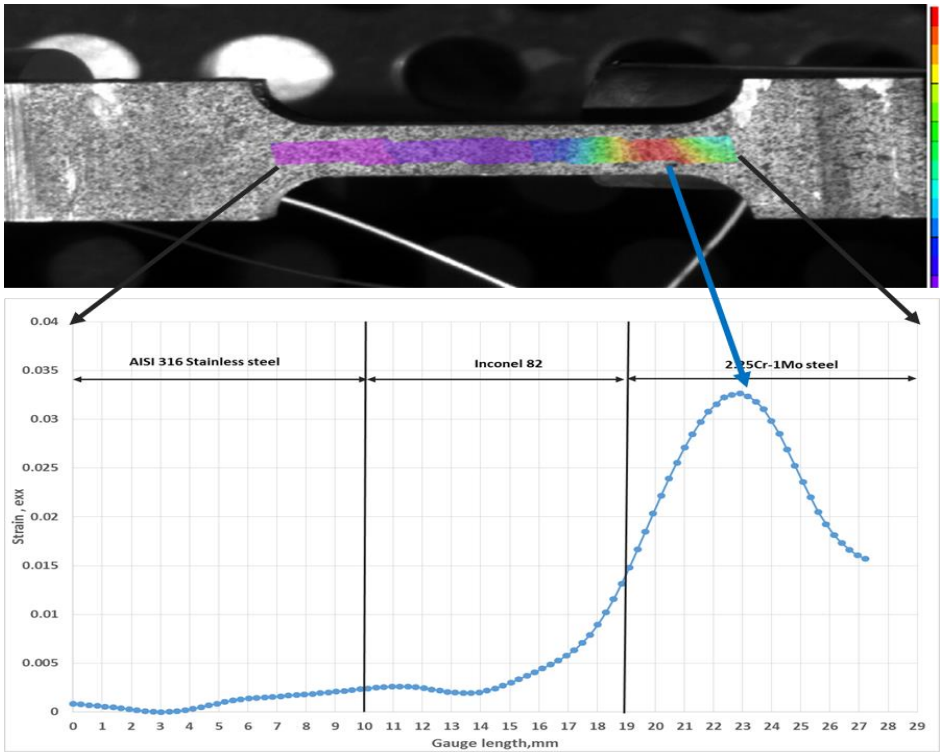

Figure 15. Spatial variation of strain measured over the selected 29mm of Region of Interest (ROI) for DIC